University of Southampton
School of Engineering and Applied Sciences
Materials Research Group

Fatigue Life Prediction of Nickel Base Superalloys

by
Mark Miller

Thesis Submitted for the degree of Engineering Doctorate

July 2007

University of Southampton

Abstract

School of Engineering and Applied Sciences
Materials Research Group

Engineering Doctorate

Fatigue Life Prediction of Nickel Base Superalloys

By Mark Miller

Neural networks have been used extensively in material science with varying success. It has been demonstrated that they can be very effective at predicting mechanical properties such as yield strength and ultimate tensile strength. These networks require large amounts of input data in order to learn the correct data trends. A neural network modelling process has been developed which includes data collection methodology and subsequent filtering techniques in conjunction with training of a neural network model. It has been shown that by using certain techniques to 'improve' the input data a network will not only fit seen and unseen Ultimate Tensile Strength (UTS) and Yield Strength (YS) data but correctly predict trends consistent with metallurgical understanding. Using the methods developed with the UTS and YS models, a Low Cycle Fatigue (LCF) life model has been developed with promising initial results.

Crack initiation at high temperatures has been studied in CMSX4 in both air and vacuum environments, to elucidate the effect of oxidation on the notch fatigue initiation process. In air, crack initiation occurred at sub-surface interdendritic pores in all cases. The sub-surface crack grows initially under vacuum conditions, before breaking out to the top surface. Lifetime is then dependent on initiating pore size and distance from the notch root surface. In vacuum conditions, crack initiation has been observed more consistently from surface or close-to-surface pores - indicating that surface oxidation is in-filling/"healing" surface pores or providing significant local stress transfer to shift initiation to sub-surface pores. Complementary work has been carried out using PWA 1484 and Rene N5. Extensive data has been collected on initiating pores for all 3 alloys. A model has been developed to predict fatigue life based upon geometrical information from the initiating pores. A Paris law approach is used in conjunction with long crack propagation data. The model shows a good fit with experimental data and further improvements have been recommended in order to increase the capability of the model.

Contents

Figures

Acknowledgements

I would like to thank QinetiQ for the sponsorship of my Engineering Doctorate. The financial support of EPSRC is also gratefully acknowledged. Thanks also go to Alstom Power and GE for supply of raw materials.

Thanks are extended to my academic tutor Dr Philippa Reed and colleague Dr Mark Joyce (University of Southampton) and industrial tutors Ian Wilcock and Dr Irene Di Martino (QinetiQ) for their support and guidance.

I would also like to thank Dr Xijia Wu (CNRC Canada), Dr Mark Joyce, Amira Kawar and Irene Lee (University of Southampton) for their contributions to this work.

Finally special thanks to my fiancée Nicky and my academic tutor Dr Philippa Reed who showed great patience as I procrastinated over my final write up and without whom I would have certainly have never finished.

Nomenclature and Acronyms

σ'_f	-	Fatigue strength coefficient
ε'_f	-	Fatigue ductility coefficient.
Π_0	-	Potential energy of an un-cracked plate
Π	-	Potential energy supplied by internal strain energy and external forces
Υ_e	-	Surface energy of the material
σ_f	-	Fracture stress
Υ_p	-	Plastic work term
σ_y	-	Yield stress
ε	–	Strain
E	-	Elastic modulus
E	-	Energy
J	-	J integral
K	-	Stress intensity factor
K_{IC}	-	Fracture toughness (mode I)
K_{th}	-	Threshold stress intensity factor
N_f	-	Number of cycles to failure
Nv		Valence-electron concentration
W_s	-	Work required to create new surfaces.

APB	-	Anti Phase Boundary
ARD	-	Automatic Relevance Determination
BEI	-	Backscattered Electron Image
CRP	-	Collaborative Research Project
CRS	-	Creep Rupture Strength
DOE	-	Design of Experiments
DS	-	Directionally Solidified
EDM	-	Electronic Discharge Machining
EDX	-	Energy Dispersive X-ray
EPSRC	-	Engineering and Physical Sciences Research Council
FBTA	-	Finite Body Tessellation Analysis
FCC	-	Face Centre Cubic
FEA	-	Finite Element Analysis
FEG	-	Field Electron Gun
HCF	-	High Cycle Fatigue
HU	-	Hidden Unit
LCF	-	Low Cycle fatigue
LEFM	-	Linear Elastic Fracture Mechanics
LPE	-	Log Predictive Error
MLP	-	Multi Layer Perceptron

MSE	-	Mean Squared Error
NN	-	Neural Network
NRC	-	National research council (Canadian partners in CRP)
OA	-	Orientation A
OB	-	Orientation B
ORT	-	Orientation
OX	-	Orientation X
PM	-	Powder Metallurgy
PX	-	Polycrystalline
QQ	-	QinetiQ
RMS	-	Root Mean Square
RR	-	Rolls Royce
SEI	-	Secondary Electron Imaging
SEM	-	Scanning Electron Microscope
SEN	-	Single Edge Notch
SENB	-	Single Edge Notch Bend
SSE	-	Sum Squared Error
SX	-	Single Crystal
TE	-	Test Error
UTS	-	Ultimate Tensile Strength
YS	-	Yield Stress

Alloys

CM247	Cannon-Muskegon alloy CM247
CMSX-4	Cannon-Muskegon alloy CMSX-4
IN939	INCOLOY alloy 939
Inconel 617	INCONEL Alloy 617
M21	Alloy M21
M313	Alloy M313
MERL 76	Pratt and Whitney Alloy MERL 76
Nim739	Nimonic Alloy 739
Nimonic 901	Nimonic Alloy 901
PWA 1480	Pratt and Whitney Alloy 1480
PWA 1484	Pratt and Whitney Alloy MERL 1484
U720	Udimet 720

1 Introduction

This thesis is presented in two distinct but linked sections. Both pieces of work have been carried out as part of an Engineering Doctorate sponsored by QinetiQ. A theme of fatigue in nickel base superalloy runs throughout and other strong links can be drawn between the chapters. Literature reviews of neural networks and Ni based superalloys are pertinent to the neural network modelling and are therefore both included before the neural network modelling section. An introduction to the second section on fatigue life and crack initiation in notch bend bars is included in section 6

1.1 Neural Networks for Fatigue Life Prediction

Nickel based super alloys were developed initially for their high temperature resistance. Creep and oxidation resistance are major design considerations for turbine blades whereas turbine discs require high strength to cope with forces at high rotational speed. Fatigue performance of superalloys is becoming increasingly important as aero engine lives are extended and there is a push to extend intervals between inspections and overhauls. Fatigue lifing of aero engines is normally based on a safe life approach where lives are determined by physical test programs.

Much is known about how alloying additions affect the microstructure and therefore the mechanical properties of a superalloy and new alloying combinations can be formulated with reasonable confidence of the expected material performance. As superalloys get closer to the limit of their performance due to extreme heat, corrosive atmospheres and high rotational forces further improvements in mechanical performance are generally small.

A modelling technique that allows predictions to be carried out on multiple combinations of alloying conditions, processing routes and heat treatment temperatures will provide a powerful tool in the evolution of new alloys.

Neural networks have been used extensively in material science with varying success. It has been demonstrated that they can be very effective at predicting mechanical properties such as yield strength, ultimate tensile strength and even crack growth rates given the correct information. These networks require large amounts of input data in order to learn the correct data trends and tensile strength related data is relatively easy and cheap to accumulate. Fatigue life data on the other hand is costly and time consuming to generate and not normally provided by the material manufacturer.

The development of a neural network modelling process which includes data collection from a variety of sources and subsequent filtering of said data in conjunction with training of a neural network model will provide a framework to develop such a tool.

2 Neural Network Design and Architecture

2.1 What is a Neural Network?

Neural networks can be used to analyse trends in data or be trained to predict results for previously unseen data. A neural network is composed of simple computational elements called nodes, whose behaviour is based upon the function of the animal neuron. The processing ability of the network is stored in the weights associated with the interconnecting units[i]

The following sections will describe the construction of a Multi Layer Perceptron network as used by Neuromat. Reference has been made to other types of network comparing their respective advantages and disadvantages.

2.2 McCulloch-Pitts Neuron

The history of neural networks can be traced back to the work of trying to model the neurons in the human brain. The first model of a neuron was created by physiologists, McCulloch and Pitts (1943). The model they created has two inputs and a single output. McCulloch and Pitts noted that a neuron would not activate if only one of the inputs was active. The weights for each input are equal, and the output is binary. Until the inputs sum to a certain threshold level, the output remains zero (Figure 1). The McCulloch-Pitts neuron has limitations. It cannot solve the "exclusive or" function (XOR) or the "exclusive nor" function (XNOR).

2.3 Perceptron

Frank Rosenblatt, using the McCulloch-Pitts neuron, went on to develop the first perceptron[ii]. This perceptron, which could learn through the weighting of inputs, was instrumental in the later formation of neural networks. A basic perceptron is represented in Figure 2.

If the perceptron is used to look at a simple linear problem the activation of the neuron is defined by:[iii]

$$a = \sum_i w_i x_i + \phi \qquad \textbf{Equation 1}$$

Where W are the weights, X is inputs and ϕ the bias value. The output, Y, is then given by applying a threshold to the activation

$$Y = 0 \text{ if } a < output$$
$$Y = 1 \text{ if } a \geq output$$

Equation 2

Given a set of inputs and results, the perceptron can be trained to predict the results by adjusting the weights and bias accordingly. In order to do this a random set of inputs and weights is chosen and an output is recorded. The difference between the output and the real data is calculated in an error function. The weights and bias are then systematically changed until the error is minimised. The choice of starting values and weights along with the algorithms required to minimise the error function are a whole area of research in themselves.

In order to model more complex non linear problems the summation function within the hidden unit can be changed. The activation function is often chosen to be the logistic sigmoid (Equation 3) or the hyperbolic tangent (Equation 4).

$$1/(1+e^{-x})$$ **Equation 3**

$$\tanh(x)$$ **Equation 4**

These functions are used because they are mathematically convenient and are close to linear near origin while saturating rather quickly when getting away from the origin. This allows MLP networks to model well both strongly and mildly nonlinear mappings. For example, a hidden unit utilising a hyperbolic tangent would contain two contain two functions:

$$y = \sum w^{(2)} h + \phi^{(2)}$$ **Equation 5**

$$h = \tanh\left(\sum_j w_j^{(1)} x_j + \phi^{(1)} \right)$$ **Equation 6**

The input data x_j are multiplied by weights $w_j^{(1)}$, the sum of all these products form the argument of the hyperbolic tangent. The output y is described by the function h multiplied by another weight $w^{(2)}$, the product of which is then added to a second bias $\theta^{(2)}$. Combining these equations gives the output y as a non-linear function of $w_j^{(1)}$. Varying the weights will change the shape of the hyperbolic tangent.

The neuron, or perceptron, is the base upon which neural networks are built. A single neuron cannot do very much. However, several neurons can be combined into a layer

or multiple layers that have greater power. A neural network has a layer of input nodes and a hidden layer comprised of neurons which then in turn feed one or more output nodes. There may be more than one hidden layer. Each node in each layer is connected to all nodes in preceding and following layers (Figure 3). The equations for a multiple hidden unit network are the same as for a single unit. The parameters must now be summed over all hidden units as well as inputs.

2.4 Multi-layer perceptron

This is perhaps the most common network architecture in use today. This class of network consists of multiple layers of computational units, typically interconnected as a feed-forward network. In this case each neuron in one layer is directly connected to all neurons of the subsequent layer (Figure 4). Each unit performs a biased weighted sum of inputs and passes this activation level through a transfer function to produce an output. Such networks can model functions of almost arbitrary complexity, with the number of layers, number of units in each layer and type of function within each hidden unit determining the model complexity.

Multi-layer networks use a variety of learning techniques, the most common being back propagation. Output values are compared with known data in order to calculate a predefined error-function. Using this information, the algorithm adjusts the weights of each connection in order to reduce the value of the error-function. This is an iterative process which seeks to minimize the error function value. The danger is that the network over fits the training data and fails to capture the true statistical process generating the data. An example of over fitting is given in Figure 5, where the red line represents a well trained model and the black line demonstrates over fitting. A simple heuristic, called early stopping, often ensures that the network will generalize well to examples not in the training set.

Other typical problems of the back-propagation algorithm are the speed of convergence and the possibility of ending up at local minimum rather than the global minimum of the error function.

2.5 Backpropagation

As the algorithm's name implies, the errors (and therefore the learning) propagate backwards from the output nodes to the inner nodes. A summary of the backpropagtion technique is as follows

- Present a training sample to the neural network.
- Compare the network's output to the desired output from that sample. Calculate the error in each output neuron.
- For each neuron, calculate what the output should have been, and a scaling factor, how much lower or higher the output must be adjusted to match the desired output. This is the local error.
- Adjust the weights of each neuron to lower the local error.
- Assign "blame" for the local error to neurons at the previous level, giving greater responsibility to neurons connected by stronger weights.
- Repeat the steps above on the neurons at the previous level, using each one's "blame" as its error.

Backpropagation neural networks are good at prediction and classification.

2.6 Early stopping

Early stopping has two main advantages; it enables fast training of neural networks and it can be applied successfully to networks in which the number of weights far exceeds the sample size. The technique involves the following stages:

- Divide the available data into training and validation sets.
- Use a large number of hidden units.
- Use very small random initial values.
- Use a slow learning rate.
- Compute the validation error rate periodically during training.
- Stop training when the validation error rate begins to increase

There are still several unresolved practical issues in early stopping

- How many cases should be assigned to the training and validation sets
- Should the split into training and validation sets be carried out randomly or by an algorithm?
- What constitutes an increase in validation error, over and above natural fluctuation during training?

2.7 Fitting and over-fitting.

A neural network is able to fit an extremely complex function given that it has a sufficiently large number of hidden units. Problems are caused when the neural

network fits the data so well it is modelling noise in the data rather than the underlying trend, this process is known as overfitting. An example of overfitting is given in Figure 5, the black dots represent the training data and the model prediction is the solid black line. When the unseen test data is added (x) it is apparent that the model does not fit to this data and that the red line (simpler model) would provide a much better fit.

2.8 Regularization

Regularization is any method of preventing overfitting of data by a model. Most regularization methods work by implicitly or explicitly penalizing models based on the number of their parameters. Regularization is discussed in more depth with respect to Neuromat software in a later chapter.

2.9 Other types of network

Recurrent network

Recurrent network (RN) is a model with bi-directional data flow. While feed forward network propagates data linearly from input to output, RN also propagates data from later processing stages to earlier stages.

A simple recurrent network (SRN) is a variation on the multi-layer perceptron, sometimes called an "Elman network". A three-layer network is used, with the addition of a set of "context units" in the input layer. There are connections from the middle hidden layer to these context units fixed with weight 1. At each time step, the input is propagated in a standard feedforward fashion, and then a learning rule, usually backpropagation, is applied. The fixed back connections result in the context units always maintaining a copy of the previous values of the hidden units (since they propagate over the connections before the learning rule is applied). Thus the network can maintain a sort of state, allowing it to perform such tasks as sequence-prediction that are beyond the power of a standard multi-layer perceptron.

Hopfield network

The Hopfield net is a recurrent neural network in which all connections are symmetric, this network has the property that its dynamics are guaranteed to converge. If the connections are trained using Hebbian learning then the Hopfield network can perform robust content-addressable memory, robust to connection alteration.

As a consequence there is no separate input or output layer but instead each node receives input signals and every node has an output. The connection weights between

each pair of nodes are symmetrical; that is, they are equal for messages passed in either direction.

Input signals are applied to all nodes simultaneously. Random starting connection weights are used to generate an output signal which is then immediately fed back to all nodes as a new input. This process is repeated until the network reaches a stable state. The final outputs are taken as the response of the network.

The trained network contains multiple patterns stored in the coded form of the connection weights. When an input is presented to the trained network, the output given is the stored pattern that is closest to the input pattern. This is a type of associative memory.

Boltzmann machine

The Boltzmann machine can be thought of as a noisy Hopfield network. Invented by Geoff Hinton and Terry Sejnowski (1985), the Boltzmann machine was important because it was one of the first neural networks in which learning of latent variables (hidden units) was demonstrated. Boltzmann machine learning was slow to simulate, but the Contrastive Divergence algorithm of Geoff Hinton (introduced in about 2000) allows models including Boltzmann machines and Product of Experts to be trained much faster.

Support vector machine

A support vector machine (SVM) is a recently developed form of machine learning algorithm. The training of SVMs is based on quadratic programming, a form of optimization that (usually) has only one global minimum. Therefore, and because SVMs have means to reduce the danger of overfitting, some practitioners prefer SVM training to neural network training.

Self-organizing map / Kohonen Net

A Kohonen network is a two-layered network, much like the Perceptron. But the output layer for a two-neuron input layer can be represented as a two-dimensional grid, also known as the "competitive layer". The input values are continuous, typically normalized to any value between -1 and +1. Training of the Kohonen network does not involve comparing the actual output with a desired output. Instead, the input vector is compared with the weight vectors leading to the competitive layer. The neuron with a weight vector most closely matching the input vector is called the winning neuron.

Only the winning neuron produces output, and only the winning neuron gets its weights adjusted. In more sophisticated models, only the weights of the winning neuron and its immediate neighbours are updated.

After training, a limited number of input vectors will map to activation of distinct output neurons. Because the weights are modified in response to the inputs, rather than in response to desired outputs, competitive learning is called unsupervised learning, to distinguish it from the supervised learning of Perceptrons.

Instantaneously trained networks

Instantaneously trained neural networks (ITNN) are also called "Kak networks" after their inventor Subhash Kak. They were inspired by the phenomenon of short-term learning that seems to occur instantaneously. In these networks the weights of the hidden and the output layers are mapped directly from the training vector data. Ordinarily, they work on binary data but versions for continuous data that require small additional processing are also available.

Spiking neural networks

The Spiking (or pulsed) neural networks (SNN) are models which explicitly take into account timing of inputs. The network input and output are usually represented as series of spikes (delta-function or more complex shapes). SNNs have an advantage of being able to continuously process information. SNNs are often implemented as recurrent networks.

2.10 Analysis of Significance of Inputs.

This is often called sensitivity analysis. The basic principle of it is that on a trained system the test data is changed for each input while keeping the other inputs fixed. The relative effect on the output is recorded for each variation in input.. With this information, the relative importance of the inputs can be calculated.

Neural nets are non-linear by nature, so their sensitivities are non-linear as well. There is no such thing as a significance factor for an input - there's a non-linear significance function that may or may not depend on other input values[iv]. A selection of methods and their relative advantages and disadvantages are discussed by Sarle[v] but no recommendation is given to which method performs best. The methods used depend on the type of network and training algorithm in use.

Neuromat uses Automatic Relevance Determination (ARD) to associate significances with the inputs.

2.11 Neural Networks to Predict Material Properties

Neural networks have been used extensively in the literature to look at mechanical and compositional properties of steels[vi] and welds[vii] and to model/control[viii] casting processes.

Evans[ix] compared a number of well known parametric models and a multilayer neural network to determine whether the latter can produce improved long term rupture life predictions for 2.25Cr-1Mo steel. Even the more complex non-linear models (e.g. Manson-Haferd) produced implausible extrapolations. In contrast, the optimised neural network was able to identify general patterns in the training data that were useful for extrapolation purposes and this, as reflected in an average error of some 4-5%.

Huang and Blackwell have successfully trained and tested a neural network with mechanical property variables relating to the temperatures and strain rates used when hot forming IN718 sheet[x]. Model inputs were temperature, strain and strain rate with stress as an output. The output of the model was used to define a constitutive relationship for this material that could be used in the finite element modelling of the sheet forming process. A model with 5 hidden units was trained on 70 lines of input data and tested against a further 60. Tests against randomly selected unseen data produced good results within tight error bounds.

H. Badeshia[xi] has written a useful review of neural networks in material science, initially concentrating on steels, but going on to talk about work in Ni base superalloys, ceramics and composites. Most relevant papers concerned with mechanical properties of superalloys are mentioned in further detail bellow.

Schooling, Brown and Reed[xii] have developed a neural network model for prediction of fatigue behaviour. The model has 6 inputs; temperature, yield strength Young's modulus, ultimate tensile strength and Nv number (number of valence. electrons divided by the number of atoms). 64 sets of input data were used constructing the model although there is no mention to which alloys were included. It was shown that that is possible to model trends in fatigue crack growth behaviour with variation in material properties. A trend for increased stage II fatigue life with increased instability to sigma-phase formation was shown to exist, although the observed effect was small due to the small range of Nv in Ni-based superalloys.

Jones and Mackay[xiii] have modelled YS and UTS of wrought polycrystalline Ni base superalloys. Inputs consisted of chemical composition and test temperature and totalled 16. The training dataset consisted of 200 datapoints and utilised a 50/50 split for training and testing. Performance was quantified by calculating RMS error values between training and testing data. The model performs well predicting the YS of a "γ/γ' superalloy". The physical significance of the models was investigated by varying compositional and temperature. Alloy compositions for Astroloy and Waspalloy were used.

Ward and Knowles[xiv] have modelled the yield strength of Ni based superalloys using a neural network within a Bayesian framework based on work by Mackay. Although there is no reference to the exact program used, a network employing 6 or 7 hidden nodes was developed. Automatic Relevance Determination was used to influence the importance of inputs. A database with around 200 datapoints ranging over 36 different alloys was used to train the network. Significance values for inputs were generated post testing and largely agreed with the literature.

Predictions against Nimonic 115 were good, error bars were shown to predict an uncertainly level of +/_ 50MPa. It is assumed that Nim115 was previously unseen data although the paper does not state this categorically. Further studies looking at the theoretical effect of changing γ' volume fraction showed sensible results. The most influential parameters were found to be temperature, followed by the γ' and γ'' formers Al, Ti, Tl/AI and Nb and the refractory elements Mo W and Ta. The other elements included were found to have little influence on yield strength.

Further work by Warde and Knowles[xv] looks at the use of neural networks to aid alloys design. Two neural network models (YS and UTS) were used in the optimisation of a number of Ni based superalloys. The number and range of input variables was increased so that the compositional window for new alloys was within the bounds of the neural network.

Elements Cr. Co, Mo, Ta, Al, Ti were set at 3 different levels; min, max and average, based upon values in the training dataset. All other additions were held at a constant level. The neural network model was then run for every combination of alloying element resulting in 729 new alloys. This list was narrowed down on the basis of the predicted YS and UTS follower by the use of MTDATA[1] to evaluate thermal stability of the alloys.

At the time of writing, the authors had no facility to predict Fatigue or CRS values

Tancret and Badhesia have produced three papers looking at mechanical properties modelling[xvi], phase diagram and segregation simulation[xvii] and experimental results[xviii] of an alloy design process incorporating neural network modelling. Results are summarised in a final paper[xix]

Neural network modelling was used to predict mechanical properties: yield stress, ultimate tensile stress, tensile ductility, creep rupture stress and the γ and γ' lattice parameters a_γ and $a_{\gamma'}$. The training data was collected from industrial sources and from the scientific literature. The databases contain information on the alloy compositions, on the heat and/or mechanical treatments, and on test conditions temperature and lifetime in the case of creep rupture.

Models are shown to perform well against known data (examples are given for UTS and tensile ductility models) and selected unknown data (CRS model shown).

The aim of the work was to come up with a new alloy composition avoiding expensive alloying elements such as Co, Mo, Ta, Nb, Hf and Re. Neural network models were used to test new alloy compositions in order to find suitable compositions that met the design requirements. However, because undesirable phases may form in these new alloy compositions, a phase diagram and chemical segregation simulation method was used in parallel with the neural network models[217].

Once the new alloy was cast, the results of mechanical tests were compared with initial property predictions made using the neural network models. Experimental results agree

[1] **MTDATA** - Windows software and thermodynamic databases for the calculation of chemical speciation phase diagrams and mechanical properties.

well with the averaged predictions achieved from neural network models (Figure 6 & Figure 7).

Fuji, Mackay and Badheshia[xx] used a neural network for the prediction of crack propagation rate in Ni-based superalloys, using up to 51 input variables with 1894 combinations of fatigue crack growth. Input variables included ΔK, composition, temperature, grain size, heat treatment, loading condition, atmosphere, R-ratio, load, waveform sample thickness and yield strength. All data for the database was collected from published literature. It was found that using a committee of models reduced the test error by ~3% over the best single model for this type of problem. The effect of grain size alone was evaluated, confirming that an increase in grain size should lead to a decrease in the fatigue crack growth rate.

A software package called NEUROMAT based on the work of Mackay has been developed by Badhesia, Ward, Knowles . (currently being used at QinetiQ as part of its NN capability) information available at Neuromat website[xxi].

A cut down version of the software is also available online[xxii] and allows for CRS, UTS and YS of Ni-based superalloys to be calculated. The input variables include composition and four heat treatments, of which temperature and duration have to be specified.

A neural network for life prediction was developed and demonstrated for predicting the elevated temperature (0.7–0.8 *T*m) creep–fatigue behaviour of Ni-base alloy INCONEL 690[xxiii].

A design of experiments method was used to select a test matrix which would provide a statistically significant variation in fatigue life over the testing region. A 2^{5-2} factorial design required 16 tests to be carried out at each test temperature containing 5 extrinsic parameters at 2 levels.

The back-propagation neural network technique, when based upon a statistically designed training set, was shown to have the potential for achieving superior creep–fatigue life cycle predictions when compared to the modified Coffin–Manson, linear life fraction and hysteresis energy methods, with 100% of the predictions at 1000°C and 90% of the predictions at 1100°C lying within an error band of $^{+}/_{-}$ 2.

2.11.1 Summary of Literature

Neural networks have been used extensively in material science for material property predictions. Models range from process modelling with a small number of inputs (generally mechanical properties and processing parameters) through to material property prediction from chemical composition and heat treatment of the alloy.

It has been shown that for a single alloy system a training dataset can be generated experimentally using design of experiments method to insure that results are statistically significant. Training neural networks on this dataset provided accurate predictions for the creep fatigue behaviour of Inconel 690.

Increasing the size and complexity of models requires a large and carefully selected dataset. Results from more complex models are often quoted as a function of training test error rather than using them to predict properties of unseen alloys.

Models based upon chemical compositions and heat treatments have been used to assess the significance of inputs. This can be done by looking at the automatic significance output from some models or by systematically varying inputs recording the effect on the output of the model. Presented results have shown good correlation between model significances and actual metallurgical theory.

Neural network models have been used as a tool in the design of a completely new alloy in combination with phase / chemical segregation simulations. The resulting alloy has been shown to have mechanical properties close to those originally predicted by the neural network model.

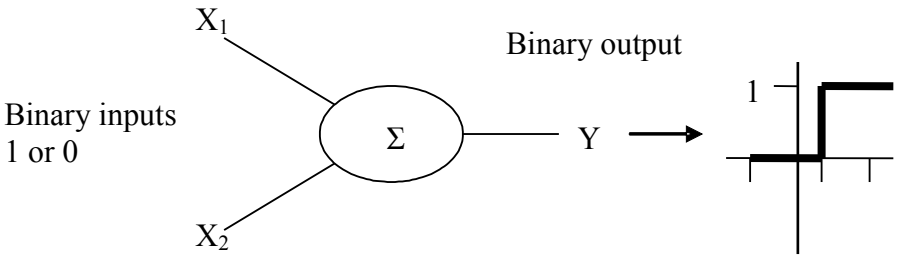

Figure 1 - McCulloch - Pitts Neuron

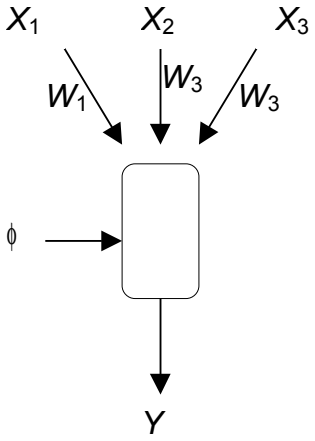

Figure 2 - A single neuron

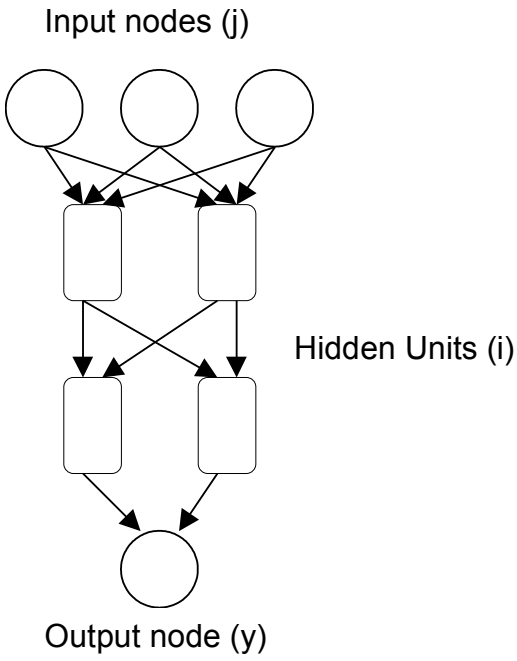

Figure 3 - A basic network

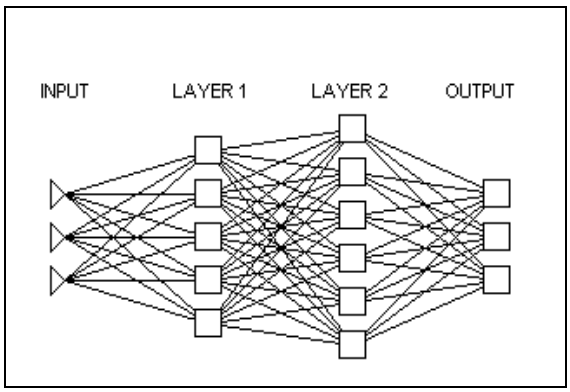

Figure 4 a typical feed forward network

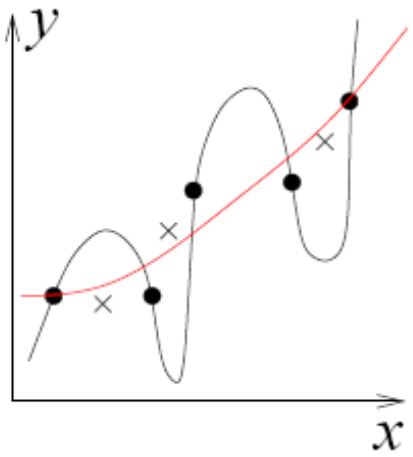

Figure 5 An example of overfitting *(after Neuromat reference manual)*

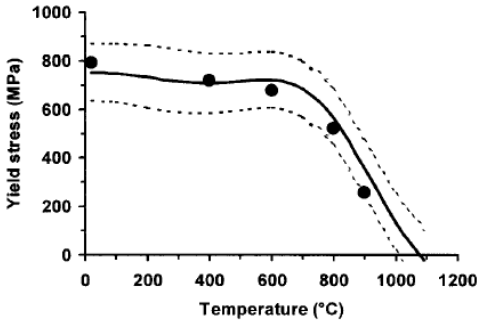

Figure 6 Evolution of yield stress as a function of temperature

solid circles indicate measurements; solid line indicates mean Gaussian processes predictions; broken lines indicate predicted error bounds (after Tancret Badhesia)

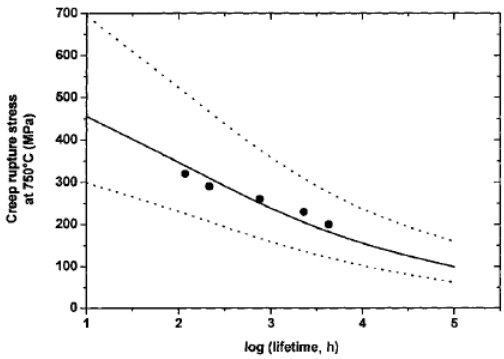

Figure 7 Evolution of creep rupture stress as function of temperature

solid circles indicate measurements; solid line indicates mean Gaussian processes predictions; broken lines indicate predicted error bounds (after Tancret Badhesia)

3 Fatigue

3.1 Introduction to Fatigue

It is rare that a component is simply subjected to static loads that do not vary with time. More commonly, loads fluctuate in intensity or alternate between tension and compression. It is possible for these fluctuating loads to cause cumulative damage to a component even when load levels are well below the yield stress of the material. The term fatigue is used to describe this damage accumulation effect. There are different stages of fatigue damage, the progression of which can be broadly classified into the following stages[xxiv].

- Sub-structural and microstructural changes which cause nucleation of permanent damage.
- The creation of microscopic cracks.
- The growth and coalescence of microscopic flaws to form 'dominant' cracks, which may eventually lead to catastrophic failure.
- Stable propagation of the dominant crack.
- Structural instability or complete fracture.

This report looks in more detail at the first three stages of fatigue damage as classified by Suresh218 as they deal with the areas defined within the project aims.

3.2 Total Lifetime Approaches

The standard method of recording the fatigue performance of a material is through the use of an S-N curve (Figure 10). An S-N curve relates the applied cyclic stress (or cyclic strain) to the number of cycles to failure of a component. At low stresses/strains the cycles to failure of a material can run into millions of cycles whereas at very high stresses/strains failure can be within a few cycles. Cycles to failure are therefore plotted on a logarithmic scale. Typically fatigue lifetimes of 100,000 cycles and below are considered to be Low Cycle Fatigue (LCF) compared to High Cycle Fatigue (HCF), when components last for 100,000 cycles up to 100,000,000 cycles. The strain life approach can be adopted for LCF. Strain life data can be fitted to Equation 1 from the work of Coffin[xxv] and Manson[xxvi].

$$\frac{\Delta\varepsilon}{2} = \frac{\sigma'_f - \sigma'_m}{E}(2N_f)^b + \varepsilon'_f(2N_f)^c \qquad \text{Equation 7}$$

Where N_f is number of cycles to failure, E is elastic modulus, *a* and *b* are constants, σ'_f is the fatigue strength coefficient and ε'_f is the fatigue ductility coefficient. The first and second terms on the right hand side are the elastic and plastic components, respectively, of the total strain amplitude.

3.3 Introduction to Fracture Mechanics

The above fatigue characterisation approaches are total lifetime approaches. They encompass number of cycles to initiation, as well as number of cycles for propagation, of the initiating defect, until component failure occurs. Most engineering components contain an existing defect distribution, as such damage tolerant fatigue lifing approaches have been developed which allow the propagation of an existing defect to be assessed. A flaw, such as internal porosity, a scratch or a microcrack in a component will act as a stress concentrator, raising stresses locally in the vicinity of the flaw-tip. Fracture mechanics allows the characterisation of these local crack tip stresses and can therefore be used to characterise crack propagation through a given material. When using fracture mechanics methods it is important to understand the assumptions and limitations upon which the methodology is based – a brief introduction of the basics follows.

3.3.1 Linear Elastic Fracture Mechanics

Linear elastic fracture mechanics (LEFM) was developed by Griffith218 and is the most widely used fracture mechanics approach to characterise fatigue crack growth. LEFM assumes that a material behaves in a linear elastic fashion i.e. that stress is a linear function of strain and all deformation is recoverable. The local stresses near the crack tip can be calculated using this approach. For example, consider a sharp, through thickness crack, length of 2a, in a thin elastic plate (Figure 11). The local stresses close to the crack tip are given to a first approximation by the following equations, where the polar co-ordinates r and θ have their origin at the crack tip and the stresses tend to infinity as r tends to zero (This does not occur in reality due to plastic yielding of the material at the crack tip218).

$$\sigma_{xx} = \sigma \left(\frac{a}{2r} \right)^{1/2} \left[\cos \frac{\theta}{2} \left(1 - \sin \frac{\theta}{2} \sin \frac{3\theta}{2} \right) \right] \qquad \textbf{Equation 8}$$

$$\sigma_{yy} = \sigma\left(\frac{a}{2r}\right)^{1/2}\left[\cos\frac{\theta}{2}\left(1+\sin\frac{\theta}{2}\sin\frac{3\theta}{2}\right)\right] \qquad \textbf{Equation 9}$$

$$\sigma_{xx} = \sigma\left(\frac{a}{2r}\right)^{1/2}\left[\sin\frac{\theta}{2}\left(\sin\frac{\theta}{2}\cos\frac{\theta}{2}\cos\frac{3\theta}{2}\right)\right] \qquad \textbf{Equation 10}$$

The Griffith Energy Balance approach states that a crack can form, or an existing crack can grow, only if such a process causes the total energy to decrease or remain constant. Thus the critical conditions for fracture can be defined as the point where crack growth occurs under equilibrium conditions, with no net change in total energy[xxvii].

Consider a plate subject to constant stress as described previously (Figure 11), plate width >>2a and plane stress conditions apply. In order for this crack to grow, sufficient potential energy must be available in the plate to overcome the surface energy of the material. The Griffith energy balance for an incremental increase in the crack area, *dA*, under equilibrium conditions can be expressed as:

$$\frac{dE}{dA} = \frac{d\prod}{dA} + \frac{dW_s}{dA} = 0 \qquad \textbf{Equation 11}$$

Where E is the total energy, $\prod$ is the potential energy supplied by the internal strain energy and external forces, and W_s is the work required to create new surfaces. For a cracked plate (Figure 12) Griffith used the stress analysis of Inglis[xxviii] to show that:

$$\prod = \prod_0 - \frac{\pi\sigma^2 a^2 B}{E} \qquad \textbf{Equation 12}$$

Where $\prod_0$ is the potential energy of an un-cracked plate and B is the plate thickness. Since formation of a crack requires the creation of two surfaces, W_s is given by:

$$W_s = 4aB\gamma_e \qquad \textbf{Equation 13}$$

Where Υ_e is the surface energy of the material, giving:

$$-\frac{d\prod}{dA} = \frac{\pi\sigma^2 a}{E} \qquad \textbf{Equation 14}$$

and

$$\frac{dW_s}{dA} = 2\gamma_e \qquad \textbf{Equation 15}$$

Equating 7 and 8 and solving for fracture stress gives:

$$\sigma_f = \left(\frac{2E\gamma_e}{\pi a}\right)^{1/2} \qquad \textbf{Equation 16}$$

This is a good approximation as long as the material is brittle, for example it works well with glass and some plastics. Rearranging the equation gives:

$$\sigma_f \sqrt{\pi a} = \sqrt{2E\gamma_e} \qquad \textbf{Equation 17}$$

Indicating that as the crack length (a) increases, the fracture strength (σ_f) decreases. Above σ_y in a real material plastic flow occurs. LEFM predicts that local crack tip stresses are greater than σ_y hence we expect yield at the crack tip over a certain area. This area is called the plastic zone. If the crack tip extends, a new plastic zone has to form at the crack tip and plastic work is done. In order for the criterion to be suitable for more ductile solids, a plastic work term Υ_p must be incorporated in the original equation.

$$\frac{\pi \sigma_f^2 a}{E} = 2(\gamma_e + \gamma_p) \qquad \textbf{Equation 18}$$

Where the term on the left is the force driving crack growth and the term on the right is the overall work done in fracture ($\Upsilon_e + \Upsilon_p$). In most engineering materials the term Υ_p is several orders of magnitude larger than Υ_e.

The stress intensity factor, K, is the fundamental parameter used to describe the stress intensity at the crack tip. The local stresses close to the crack tip are given to a first approximation by the following equations, where the polar co-ordinates r and θ have their origin at the crack tip, the stresses tend to infinity as r tends to zero218. This does not occur in reality due to plastic yielding of the material at the crack tip. The general equation relating the crack length, applied stress and K is given by:

$$K = \sigma \sqrt{\pi a} f\left(\frac{a}{W}\right) \qquad \textbf{Equation 19}$$

Where σ is the far-field applied stress, a is the flaw size and f(a/W) is the compliance function to take into account the different component geometry and crack shapes. If two cracks of different geometry have the same value of K, then in theory the stress fields around the crack tips are identical assuming the elastic approximation holds.

K can also be equated with the left-hand term in Equation 11, i.e. at fracture there is found to be a critical value of K, which is a materials parameter, the fracture toughness. (This is true as long as there is sufficient constraint to ensure predominantly

plane strain conditions are operating and hence LEFM holds). More generally K is normally given a subscript to denote the mode of loading (Figure 13) i.e. K_I, K_{II} or K_{III}.

$$K_{I,II,III} = Y\sigma \sqrt{\pi a} \qquad \textbf{Equation 20}$$

Where σ is the applied stress, a is a characteristic crack dimension and Y is a dimensionless constant that depends on mode and loading conditions (including component and crack geometry). K can therefore be relatively easily calculated from specimen geometry, loading conditions and defect size, and gives a measure of the magnitude of the crack tip stress field.

ΔK is therefore a suitable parameter for the characterisation of fatigue crack growth where the crack growth mechanisms are assumed to be primarily controlled by the range of crack tip stresses. Such crack propagation data is typically obtained from test coupons of materials containing a pre-existing, relatively large, defect (typically of the order of millimetres long). To this defect, defined stress states are applied, allowing both ΔK and crack growth rate to be calculated. Log-log plots of the crack growth rate per cycle (da/dN vs. ΔK) typically show a sigmoidal relationship divided into three distinct regions (Figure 14). Regime A shows that at very low ΔK, the crack growth rate is negligible. Below the threshold stress intensity factor, ΔK_{th}, crack growth is arrested or imperceptible. Stage I crack growth is usually predominant in this regime and there is a large influence of microstructure, mean stress, crack length and environment.

Regime B is denoted the Paris regime, because at intermediate ΔK values, the relationship between da/dN and ΔK is given by the Paris equation:

$$\frac{da}{dN} = C\Delta K^m \qquad \textbf{Equation 21}$$

Where C and m are materials constants. This behaviour is relatively microstructure insensitive and less affected by mean stress levels (or minimum to maximum load ratios (R-ratios)). If crack growth is predominantly in the Paris regime, and both the initial crack length, and the final crack length (e.g. the crack length giving fast failure or undue compliance such as general yield in the un-cracked ligament) are known, then the number of cycles required for the initial defect to grow to the final crack length can be calculated using integration approaches based on Equation 18. Regime C is where monotonic failure processes are contributing heavily to the fatigue crack growth as K_{max}

approaches the fracture toughness (K_{IC}) and the crack growth rate rapidly increases with increasing ΔK due to increasing bursts of monotonic failure, until final failure occurs. This regime is also heavily influenced by microstructure and mean stress levels, but as it contributes to so few cycles of the overall fatigue lifetime is generally considered to be of minor importance.

The use of K to define crack tip stresses assumes elastic behaviour, i.e. that the crack tip plasticity is sufficiently limited that K still characterises the near crack tip stress field (i.e. that the linear elastic behaviour assumption gives a reasonable approximation). If a significant amount of plastic deformation has taken place, alternative parameters such as the J-integral have been employed to characterise the fatigue crack growth[218]. ΔK is still valid however if there is limited plastic deformation occurring at the crack tip and there is sufficient material around the plastic zone which is behaving elastically providing constraint.

3.4 Initiation of fatigue cracks

The principal sites of fatigue crack initiation in engineering components include voids, slag or gas entrapments, inclusions, dents, scratches, forging laps and folds, macroscopic stress concentrations, as well as regions of microstructural and chemical non uniformity[218]. Studies on a range of superalloys have identified high temperature crack initiation at slip bands[xxix], inclusions[xxx], pre-cracked carbide particles and preferentially oxidised carbides[xxxi,xxxii].

3.5 Stage I / II / III crack growth

Several fatigue propagation modes have been observed which can be generally linked to the three regimes of da/dN versus ΔK behaviour shown in Figure 14.

Stage I

Stage I crack growth behaviour occurs at low ΔK levels (near threshold) for large defects and during early stages of small (e.g. freely initiating) crack growth. When the crack and the zone of plastic deformation surrounding the crack tip are confined to a few grain diameters, crack growth occurs predominantly by single shear in the direction of the primary slip systems[218]. Stage I crack growth is characterised by faceted fracture surface appearance and is often referred to as crystallographic crack growth, as cracks grow along the crystallographic slip planes e.g. {111} in face-centred cubic (FCC) materials. Stage I crack growth persists while the crack tip plastic zone size

remains smaller than some microstructural feature. It is most pronounced in those materials which exhibit highly planar slip.

Stage II

Stage II crack growth occurs when the plastic zone size becomes larger than the afore-mentioned microstructural feature. Crack propagation is now perpendicular to the applied stress and several slip systems are acting at once. Examination of the fracture surface at a microscopic level may reveal parallel ridges which have formed parallel to the crack front. These closely spaced ridges are called striations, where each ridge represents one fatigue cycle. Striations may not however always be visible on a fatigued fracture surface.

Stage III

Stage III crack growth typically occurs under high ΔK values, and rapidly accelerating crack growth rates, up to final failure of the component. On observation of the resulting fracture surface there is often evidence of significant plastic collapse of the material. A component spends the shortest proportion of its life in stage III crack growth.

3.6 Extrinsic shielding effects (closure mechanisms)

Crack propagation rates can be significantly affected by shielding effects, these can be due to changes in the locally experienced crack tip stresses due to crack deflection (resolved crack tip stresses alter), changes in local materials properties (e.g. stiffness as a secondary particle is encountered) or crack closure. Crack closure is the term used to describe load transfer in the wake of a growing crack due to contact between the crack faces behind the crack tip. Crack closure could arise from (1) surface roughness/crack path tortuousity (coupled with a degree of mode II shear irreversibility), (2) oxide debris entrained in the crack or (3) plasticity ahead of the crack tip, leading to significant plastic wake material existing along the crack flanks. All three mechanisms can cause contact of the crack surfaces behind the crack tip at a stress intensity factor ($K_{closure}$) greater than the applied minimum stress intensity factor (K_{min}) and therefore the crack tip sees an effective ΔK that is less than the applied ΔK i.e. a reduced crack tip driving force. Closure effects are most significant in the near-threshold regime, where applied ΔK levels are low and K_{min} may be less than $K_{closure}$. For all of these crack wake effects to build up the cracks need to have grown a significant distance.

3.7 Short crack behaviour

Initiation and so-called short crack growth behaviour is technically important for superalloy components (e.g. turbine discs and blades). A large part of the overall fatigue life may be spent in initiation and so-called short crack growth phases at the high stress levels experienced in service. Useful definitions of what constitutes a short crack are given by Suresh[218].

- *Microstructurally* short cracks, where the crack length is similar to a characteristic microstructural dimension such as grain size in monolithic materials.
- *Mechanically* short cracks, where the crack length is similar to the crack tip plastic zone for smooth specimens, or cracks that are engulfed by the plastic strain field of a notch.
- *Physically* short cracks, which may be larger than any microstructural dimension or plastic zones, but small in relation to the size of the component in which they have occurred.
- *Chemically* short cracks, which are nominally amenable to LEFM analyses, but exhibit apparent anomalies in the propagation rates below a certain crack size as a consequence of the dependence of environmental stress corrosion fatigue effects on crack dimensions.

It is important to note the difference between short and long cracks as there are observed differences in the propagation behaviour when compared on a nominal ΔK basis. Generally, short cracks propagate at higher rates than long cracks when compared at similar ΔK ranges, as shown schematically in Figure 15. This indicates that ΔK is no longer characterising the crack tip stress state for both long and short cracks. Various arguments have been put forward as to why we see this anomalous behaviour for small defects. Clearly mechanically short cracks do not experience LEFM conditions and parameters such as ΔJ have been used as correlation parameters with some success[218]. The early stages of short crack growth (at apparent low ΔK ranges) are also very scattered; this wide variation in crack growth rates is due to the strong influence of microstructure for such small defects. Temporary crack arrests at obstacles to slip such as grain boundaries and second phase particles are typically seen. The occurrence of such obstacles will vary from crack to crack, leading to the widely varied crack growth rates typically observed. At nominally similar low ΔK ranges for large defects (near-threshold), locally, such arrest events are also seen. These effects

are averaged along the length of the defect, thus showing little scatter from crack to crack.

In the long crack case, significant closure effects are also expected to arise near threshold, which have not developed in short cracks that have developed insufficient crack wake. At longer crack lengths the short crack behaviour starts to approach the crack growth rates seen in long crack specimens. This is believed to be a combination of more typical LEFM conditions being attained, along with the evolution of similar closure levels as the crack length increases.

3.8 Creep and Environmental Interactions

Creep is a thermally activated process and is therefore significant in elevated temperature fatigue behaviour. Creep is a time-dependent inelastic deformation and hence significant creep can render the standard LEFM approach invalid. Creep damage processes can also synergistically interact with the damage process at the fatigue crack tip. To characterise creep-fatigue, crack growth rates can be partitioned into fatigue and creep components, or the crack growth driving forces can be split into elastic and inelastic components. This is further complicated by the influence creep may have in the plastic zone ahead of the crack, possible crack tip blunting by creep, and environmental interactions. Oxidation processes (particularly intergranular attack) can become more significant at higher temperatures.

3.9 Creep-Fatigue

The characterisation of fatigue crack growth incorporating creep is complicated, as the interactions of these effects cannot be described by a straightforward summation of the individual effects. Creep and environmental effects can combine to accelerate crack growth, or, oppose each other, slowing the crack growth and in some cases even contributing to crack arrest[xxxiii].

The most simplistic method to characterise crack growth in the mixed cycle and the time-dependent regime, is the summation of the individual effects of fatigue and creep components of the crack growth.

$$\frac{da}{dN} = \left(\frac{da}{dN}\right)_{CR} + \left(\frac{da}{dN}\right)_{F} \qquad \textbf{Equation 22}$$

Where $(da/dN)_{CR}$ and $(da/dN)_F$ are the crack growth rates due to creep and fatigue components respectively. This approach only holds true if there is no interaction

between the creep and fatigue crack growth, giving a total crack growth rate equal to the sum of the individual fatigue and creep components of the crack growth. When creep-fatigue interactions occur at the crack tip, the crack growth could either be accelerated due to creep crack growth, or slowed due to stress relief from creep deformation. Environmental effects are not taken into account if there are any, as this is a simple approach. The crack growth rate in the mixed crack growth mode regime would be underestimated by linear superposition as creep and environment effects tend to accelerate crack growth.

Other research has shown that using a more sophisticated approach of the time integration method proved to be more successful. The general form of the equation is

$$\frac{da}{dN} = \left(\frac{da}{dN}\right)_f + \left(\frac{da}{dt}\right) dt \qquad \textbf{Equation 23}$$

Where (da/dN)f is the crack growth rate due to simply fatigue unaffected by creep or environment effects. This is obtained by testing at high frequencies in a vacuum environment. Data from sustained load tests under conditions that are similar to creep-fatigue tests is required in order to calculate the integral term of the equation.

4 Nickel Based Super Alloys

4.1 Development of Nickel Based Alloys

Nickel based super alloys were developed initially for their high temperature resistance. As engine materials have to operate at higher and higher temperatures other materials are no longer appropriate. Aluminium alloys, although used in high percentages throughout the airframe have a service temperature of around 200°C making them unsuitable for any aero engine components. Stainless steels can operate at up to 700°C but are very heavy and corrosion is an issue at elevated temperatures. Titanium is often used in compressors and is a good mid temperature material, useful up to 500°C. Nickel based alloys (superalloys) have good high temperature mechanical properties such as resistance to creep, fatigue, creep-fatigue and good strength at high temperature. They can operate at temperatures up to 1200°C but are very heavy. The weight penalty of these materials is an acceptable compromise for their very high operating temperature.

4.2 Microstructure

A typical nickel based superalloy consists of a γ matrix, a solid solution strengthened matrix consisting of mostly nickel with additions of molybdenum, tungsten and chromium. It is a Face Centred Cubic (FCC) matrix. The main strengthening precipitate γ' consists of $Ni_3(Ti,Al)$, it is also FCC but ordered and coherent with the γ matrix. At smaller sizes it is spherical but at larger sizes it adopts a cuboidal structure (Figure 16) to minimise lattice misfit strain. Increases in the γ' fraction bring about an increased yield strength with blade alloys typically having a γ' fraction of 70-80%.

Grain boundary carbides also play a role in strengthening cast and wrought forms of polycrystalline superalloy but are not relevant to single crystals. Alloying additions are used to improve the performance of nickel based alloys even further. Aluminium and titanium, as mentioned previously, provide precipitate strengthening and are key to the formation of γ'. Chromium additions increase the corrosion resistance of the alloy by forming a protective Cr_20_3 layer. The addition of chromium limits the amount of titanium and aluminium additions possible due to the combination of solubility of each element being affected by each of the other additions. A balance has to be struck between strength and corrosion resistance. Turbine blades typically contain lower percentages of chromium and high percentage of titanium and aluminium. Other

alloying elements are also used, the additions and reasons for use are discussed further when looking at the metallurgy of CMSX-4 in section 4.5.1.

4.3 Deformation of Nickel Base Alloys

Nickel base superalloys have a tendency towards planar slip. As dislocations cut through the γ' precipitate they reduce the effective area of the precipitate blocking their path. Successive dislocations therefore have to cut through less and less precipitate thus favouring slip along that plane. However, as the γ' precipitate is ordered, the passage of a single dislocation sets up an anti-phase boundary (APB) with a high associated energy. This state is short lived as the passage of a second dislocation removes the anti-phase boundary. It is therefore energetically favourable for dislocations to pass though the γ' in pairs (super dislocations). In FCC materials, dislocations commonly dissociate into two partial dislocations. If these dislocations separate out the area between then becomes known as a stacking fault. The stacking fault has a stacking fault energy (SFE) associated with it, proportional to the stacking fault area. This dissociation into partial dislocations makes cross slip (a dislocation crossing from one slip plane to another) difficult. All these factors promote planar slip at low temperatures. More intense slip bands mean that stage one crack growth along the slip bands is enhanced, and highly faceted fatigue fracture surfaces are often observed where the crack has grown along the {111} slip planes.

As temperature increases, thermally activated processes such as cross-slip are initiated, more wavy slip is promoted and a second cubic slip system also starts to operate. When a superdislocation (the double pairs of partial dislocations separated by the APB) cross-slips from a {111} onto a {100} plane, the APB energy is reduced. If the first dislocation then cross-slips back onto a {111} plane (favourable for lowering the SFE between the two partials), it is unfavourable for the APB to follow it due to the lower APB energy on {100}, and the superdislocation becomes locked into position. This is known as Kear-Wilsdorf locking[xxxiv], (Figure 17), and is thought to be the mechanism responsible for the anomalous yield behaviour of γ' (increasing σ_y is observed with increasing temperature). This complex dislocation locking is the mechanism behind the high strength of nickel-base superalloys at high temperatures.

4.4 Single Crystals

The presence of grain boundaries and the average grain size in polycrystalline alloys is an important factor in the fatigue and creep behaviour of nickel based superalloys. In

turbine blades of aircraft jet engines, it is known that the elimination of transverse grain boundaries promotes substantial improvements in creep and fatigue lives. As a result, directionally solidified and single crystalline superalloys are widely used as materials for turbine blades in gas turbine engines.

Single crystals are cast using a process called directional solidification. This process requires the controlled withdrawal of a mould from an electrically heated furnace. A multiple turn constriction called a 'pigtail' is used at the bottom of the mould, this constriction only allows one grain orientation to grow up through the pigtail as the mould is withdrawn from the furnace. During casting, the alloy is cooled through portions of the phase diagram where liquid and solid phases co-exist. This zone is called the mushy zone. If the mushy zone is extensive it allows convection currents to form as the casting solidifies. These convection currents can cause the tips of solidifying dendrites to be broken off and swirl away to cause randomly occurring grain initiation sites ahead of the solidification front. These inclusions are called freckling. An extensive mushy zone can also cause compositional segregation within the solid and liquid phases, leading to significant variations in composition between dendrite cores and interdendritic regions. Both of these processes are deleterious to material properties, segregation can be removed with subsequent heat treatment, but extensive segregation can lead to locally varying melting points, with the risk of incipient melting during solution heat treatment. Both processes can be minimised by using a sharp temperature gradient during the casting process. Single crystals have highly anisotropic mechanical properties, both in terms of stiffness and plasticity. The highest stiffness is measured along the close packed <111> direction and the lowest being along the <001> direction. Anisotropic plasticity is caused by slip systems with the highest resolved shear stresses experiencing the most intense plastic deformation, with obvious implications for both creep and fatigue behaviour (higher order plastic deformation phenomena).

4.5 CMSX-4

4.5.1 Microstructure and Physical Properties

CMSX-4 is a second generation single crystal superalloy containing 3% rhenium in particular, and other alloying additions to provide solid solution strengthening. Rhenium is found predominantly in the γ matrix, it retards coarsening of the γ' strengthening phase and increases γ/γ' misfit. Rhenium clusters act as efficient

obstacles to dislocation movement in the γ matrix, more so than isolated solute atoms, and therefore are believed to contribute significantly to the high strength of the alloy[xxxv]. Rhenium has been linked to enhanced strain ageing, since its large atomic radius promotes the trapping of dislocations[xxxvi]. Rhenium has also been shown to reduce creep[xxxvii]

Chromium provides corrosion and oxidation resistance due to the formation of the non-porous surface oxide Cr_2O_3. However the chromium levels are lowered to allow increased aluminium and titanium levels. Also at high temperatures Al_2O_3 scales provide additional resistance to oxidation. Cobalt, when added to Nickel-base superalloys, reduces the solubility of aluminium and titanium in the nickel-chromium γ matrix. This encourages the formation of the γ' phase. Cobalt can also reduce creep by lowering the stacking fault energy, thereby hindering dislocation cross-slip and climb. Molybdenum, niobium, tungsten and tantalum are added to the monocrystalline nickel base superalloys to solid-solution strengthen the γ and γ' phases and can help reduce creep deformation. The addition of carbon removes the detrimental elements such as sulphur and oxygen. Molybdenum can reduce creep at high temperatures since it reduces self-diffusivity.

The addition of molybdenum, tantalum, tungsten, rhenium and cobalt has been shown to strongly affect the γ/γ' lattice misfit due to their large atomic radii. In particular rhenium additions have been shown to produce a more negative misfit[xxxviii].

It has also been shown that the lattice misfit is severely affected by the dendritic structure, since the refractory elements are prone to segregation[xxxix].

4.5.2 Heat Treatment

Cast superalloys (such as CMSX-4) are given heat treatment to strengthen, improve ductility and homogenize their structure. In outline they receive a lengthy, staged solution heat treatment to reduce dendritic segregation effects, followed by a single stage ageing heat treatment to optimise the γ' distribution.

4.5.3 Oxidation behavior

CMSX-4 has a low chromium content and therefore has relatively poor oxidation resistance. This is an accepted trade off in order to gain improved mechanical properties by using a higher percentage of aluminium and titanium. Turbine blades are manufactured with a protective coating to prevent oxidation at high operating

temperatures thus allowing for the low chromium content. The literature reflects this in that there is very little written about the oxidation of uncoated CMSX-4.

4.5.4 Creep

Creep behaviour of CMSX-4 is well documented. Tests are normally conducted at higher temperatures (750°C to 1000°C). CMSX-4 exhibits excellent creep resistance at elevated temperature due to hardening by γ' precipitates. At high temperatures, and in particular, low stresses, rafting is observed[xl]. Rafting occurs when the γ' begins to deform under stress and high temperature. Each cubical particle shortens along the [001] direction and expands along the [100] and [010] directions. When deformation of the particles reaches 15%, adjacent particles may weld together to produce an elongated (rafted) γ' structure along [100] or [010] directions. Multiple crack initiation is common in creep failure[xli].

4.5.5 Fatigue Behaviour

At room temperatures in polycrystalline nickel base superalloys, cracks can initiate from slip bands, grain boundaries, carbides, due to cracking of inclusions/precipitates, or at defects. Cracks that have initiated at inclusions or precipitates usually arise due to differences in the thermal expansion coefficients or the strength between the inclusions and the matrix.[xlii].

Casting micropores have been found to initiate LCF cracks early in the life of MAR-M200 and CMSX-2 single crystals at 650°C[xliii]. The initiating pore was either at the surface or sub-surface and when crack initiation occurred at the surface in CMSX-2, the replica record showed that life was mainly spent in crack growth. Fatigue failure in CMSX-2 was found to occur by the growth of a single crack that initiated at porosity and in MAR-M200, several cracks that initiated at pores coalesced to final failure.

Crack initiation in CMSX-4 appears to be controlled by porosity and oxidation spikes219. Oxidation is also suggested to be a dominant factor in crack growth[xliv] Oxidation at the crack tip becomes important at higher temperatures with oxide induced closure causing crack tip blunting and reducing crack growth rates[xlv.]

Ott et al carried out fatigue tests on CMSX-4 and CMSX-6. Samples were pre-strained in the [001] direction in either tension, resulting in a raft structure perpendicular to the applied stress, or in compression, providing a rafted structure parallel to the applied stress, at 1100°C in vacuum to develop a rafted microstructure.

Fatigue tests were then carried out on these samples at 950°C in air under strain control to assess the effects of rafting parallel and perpendicular to the applied stress compared to an unstrained baseline. The tests were performed with a total strain amplitude of 1.2%. It was found that this produced a stress of ~500MPa irrespective of the rafting orientation. Fatigue tests with the tensile axis parallel to the [001] direction were carried out, short cracks were seen to initiate at either surface pores or from cracks in the brittle oxide layer.

Schubert et al[219] carried out fatigue tests on CMSX-4 at 750°C and 1000°C in air and in vacuum. Testing single edge notch (SEN) type samples with small corner or edge cracks simulated small cracks in turbine blades. Tests were carried out at a load ratio of 0.1 and a frequency of 5Hz. In addition creep fatigue tests were carried out with a trapezoidal 0.1-300-0.1-1 waveform. Pre-cracking was performed at test temperature at 10Hz. Specimens were orientated such that the tensile axis was parallel to the <001> direction, whilst the nominal crack growth direction was either in the <100> or the <110> direction. Fatigue cracks grown in air at 750°C were seen to propagate along γ channels in the nominal mode I direction zigzagging between the {111} and {100} planes at low and medium ΔK levels. At higher ΔK a change in the surface crack growth mechanism to the {111} planes was observed together with cutting of the γ' phase. At 1000°C no cutting of the γ' occurred and hence propagation was via cross sliding on the {100} planes along the γ channels.

The difference between secondary notch orientations was much more pronounced at 750°C than at 1000°C. In both cases the change was only evident at low ΔK levels (<20 MPa√m). Similarly the effect of environment on fatigue crack growth rates was only evident at low ΔK levels (<20 MPa√m).

4.5.6 Summary of CMSX-4 findings

Creep behaviour of CMSX-4 is well documented between 750°C-1000°C where it exhibits excellent creep resistance due to hardening by γ' precipitates. At high temperatures, and in particular, low stresses, rafting is observed. Multiple crack initiation is common in creep failure. Fatigue behaviour of CMSX-4 is less commonly investigated. The literature suggests that initiation is controlled by porosity and oxidation spikes. Oxidation is suggested to be a dominant factor in crack growth with oxidation induced closure effects retarding crack growth. Oxidation also causes crack tip blunting, this is more apparent at higher temperatures.

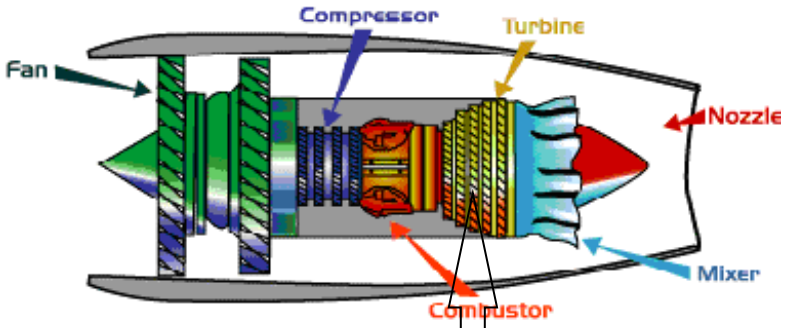

Figure 8 - Anatomy of a Jet Engine

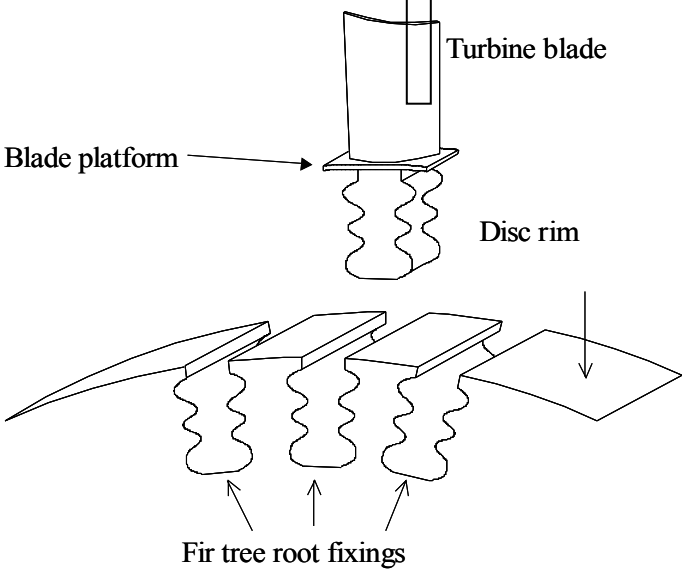

Figure 9 - Fir tree root fixing for turbine blade

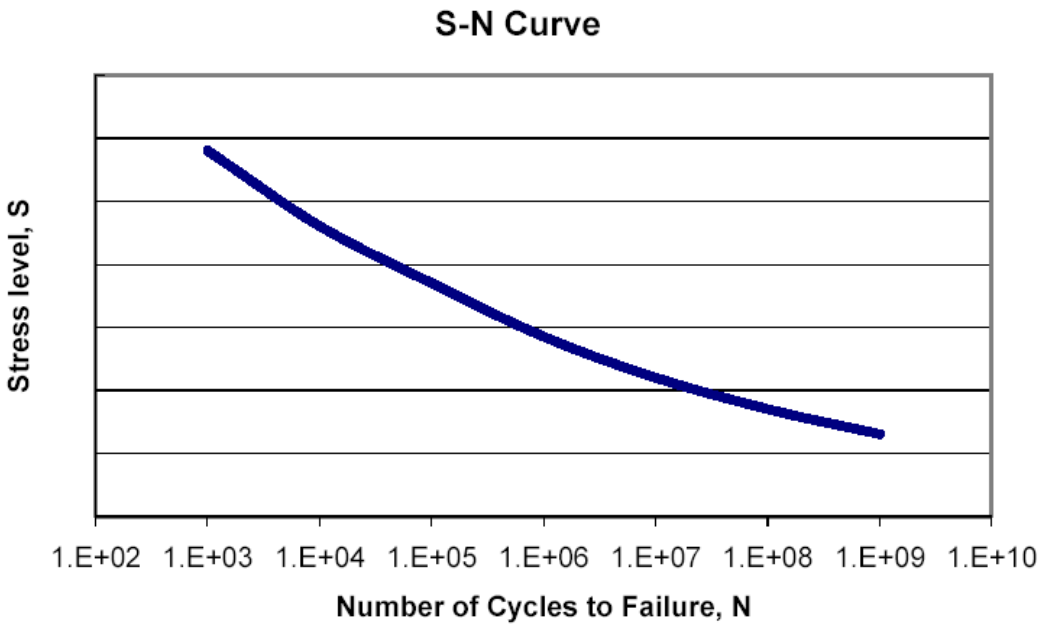

Figure 10 - A typical S-N curve

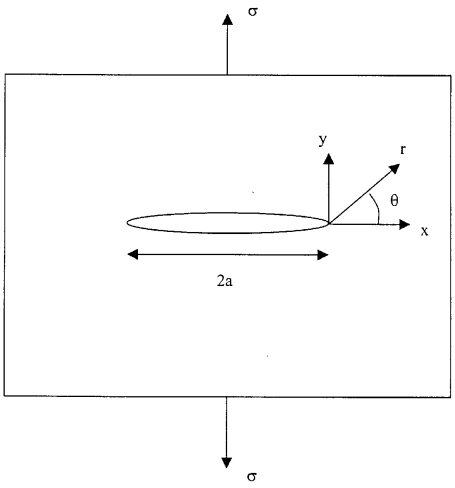

Figure 11 - Sharp crack length 2a in a thin elastic plate, with a nominal applied stress σ

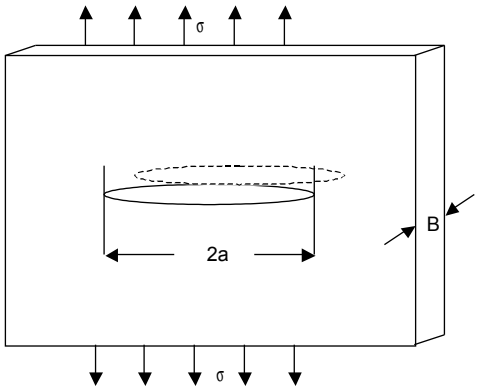

Figure 12 - Sharp crack length 2a in an elastic plate, with a nominal applied stress σ

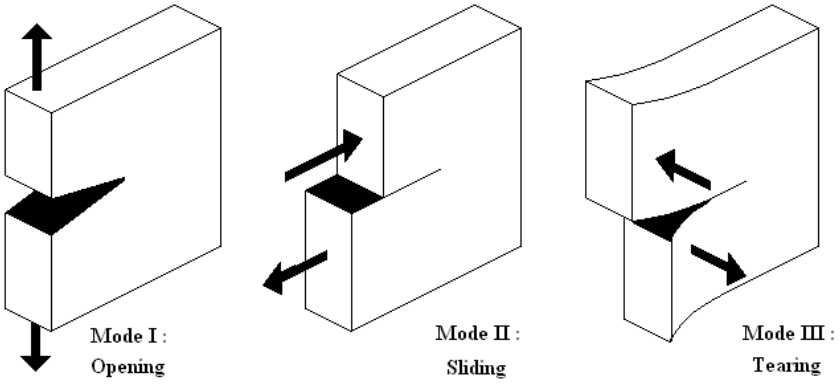

Figure 13 - Typical opening modes

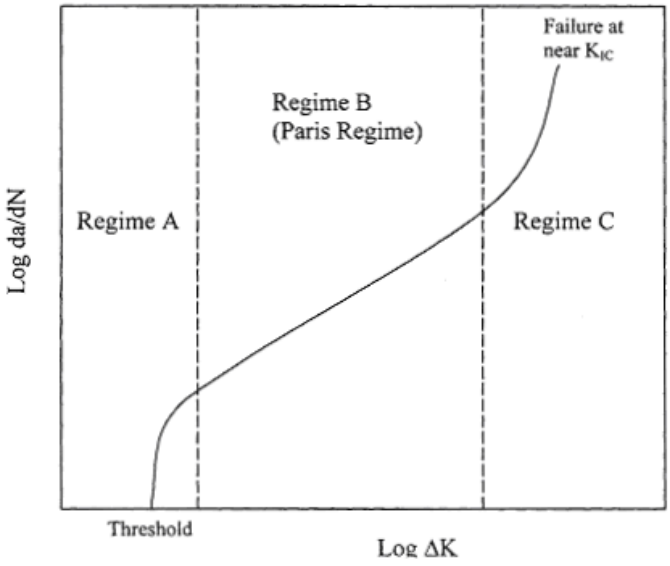

Figure 14 - Typical da/dN versus ΔK curve

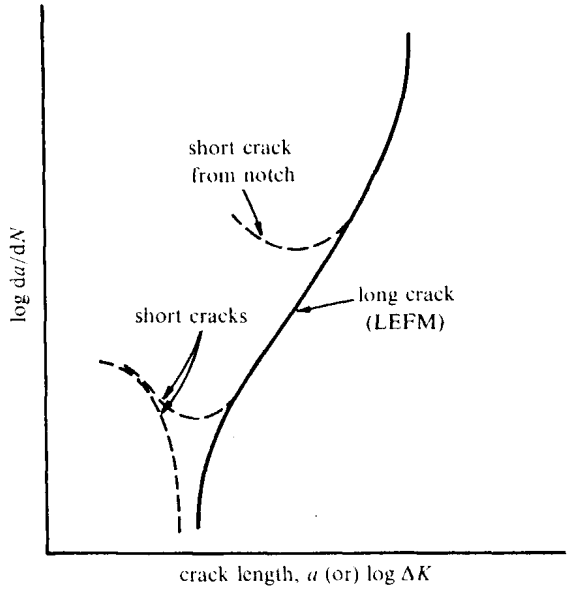

Figure 15 - Typical long crack/short crack behaviour (after Suresh218)

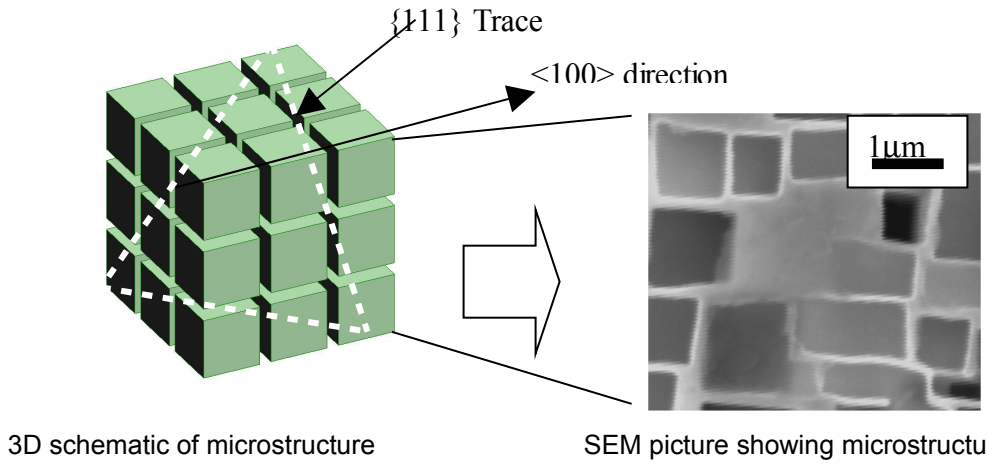

Figure 16 - Cuboidal γ'

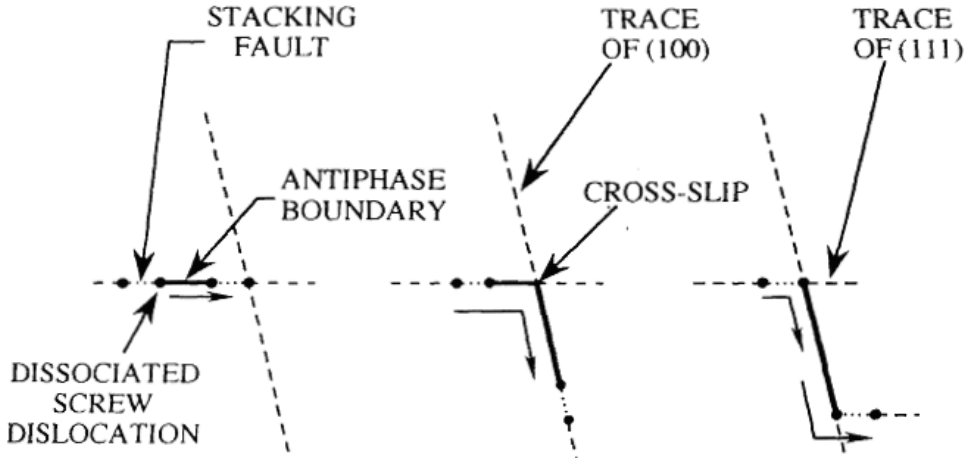

Figure 17 - Cross-slip pinning mechanism, the dislocation cross-slips onto (010) due to lower APB energy and is locked in this configuration

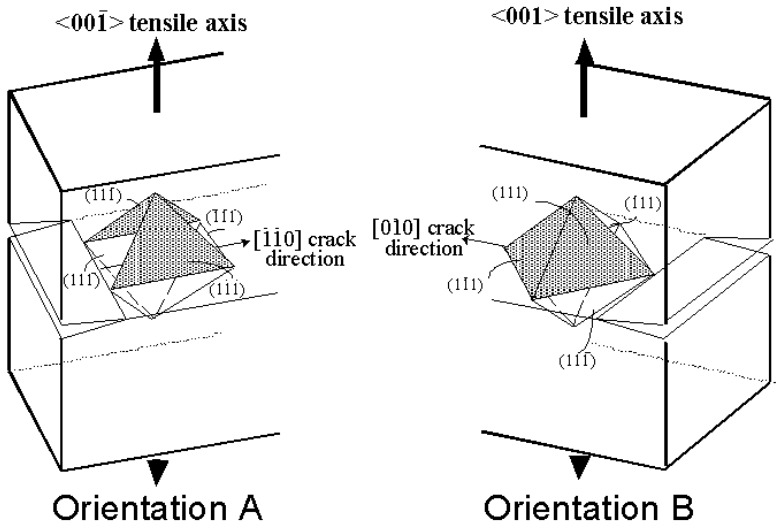

Figure 18 - Definition of secondary orientations A and B and their nominal crack growth directions

5 Neural Network Modelling

5.1 Program of Work

Fatigue performance of nickel based superalloys is an increasingly important consideration when designing new alloys. Producing a new alloy and carrying out a fatigue testing program is an expensive and time consuming process. The ability to predict fatigue performance or trends based upon the alloy composition and processing routes would provide a powerful tool in alloy development and could help narrow down the combinations of alloying elements before raw material is produced. Such a tool would help reduce costs during an alloy development program.

This work follows on from an initial program of work within the Engine Materials Lifing group at QinetiQ, Farnborough. Neural network modelling has already been used within QinetiQ to model YS, UTS and CRS of alloys based on their chemical composition and processing root. This work has been used as a precursor to developing a modelling technique for predicting fatigue life. The main aims of this work are:

- Using current neural network models as a starting point, develop a methodology of collection and screening of input data.
- Develop guidelines for training and validation of neural network models for prediction of mechanical properties of Ni-based superalloys.
- Search literature and in house QinetiQ data for LCF data to populate a new neural network model.
- Use experience gained from work with current models to develop and validate a model for prediction of alloy fatigue life. Model development should include justification of selection of inputs

The first few sections of this chapter discuss work performed with YS and UTS models. Large datasets were already available and some initial work had already been carried out, this work has been built upon further and reported. YS and UTS models are much simpler to analyse as results are presented as a function of test temperature only for each alloy. They therefore presented good subjects to further develop modelling techniques and strategies which could then be applied to an LCF model.

The development of the YS and UTS neural network models was supported with statistical analysis of the data, first using examination by Excel spreadsheet then

progressing onto Minitab statistical analysis software. Results from the models have been compared with unseen test data.

The second section of this work applies the methodologies developed for, and lessons learned from, development of YS and UTS models to the development of a fatigue life prediction model. Further work has been carried out to establish the correct inputs for the model and initial models have been compared with unseen test data.

The modelling process employed in this work is of a cyclic nature where the process of learning from data is seen as a continuous process. Once a dataset has been established and trained, the results have been used to suggest improvements either in the modelling process or by modifying the input data. The modelling process is then repeated and observations recorded.

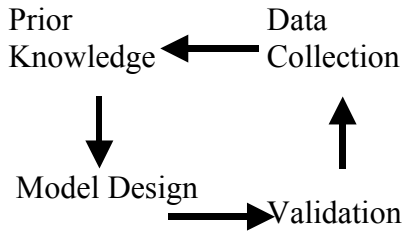

Care has been taken not to implement too many changes at once so the effect of each one can be established.

5.2 Software Approaches

5.2.1 Neuromat Overview

Neuromat Model Manager is a user friendly neural network modelling software package that is available for Linux RedHat. It is commercially available software supplied by Neuromat Ltd in conjunction with Cambridge University.

Neuromat performs the training of multiple models, selection of models to form committees and ranks their performance. Models comprising of committees can then be re-trained and used to predict against unseen data with reference to the levels of confidence of the prediction and significances of individual inputs. The key advantages of Neuromat are the ability to generate error bars when predicting data and the inclusion of an algorithm to determine the significance of inputs to the model. The methods used in Neuromat software are described in more technical detail in the following sections.

5.2.2 Bayesian learning

The neural network used in Neuromat is a feed forward network consisting of two layers. The activation function of the neurons in the hidden layer is a *tanh* function. The second layer neuron performs a linear combination of each hidden unit output. The algorithm used to train the models has been written by D.J.C. Mackay219. It implements a particular learning method using Bayesian statistics to choose the most probable distribution for the weights given the data. Training of the model is based on Bayesian probability theory and treats learning as an inference problem. Rather than trying to identify the best set of weights, the algorithm infers a probability distribution for the weights from the data presented. The training method tries to minimise an error function M(w) (Equation 24).

$$M(w) = \beta E_D + \alpha E_w \qquad \textbf{Equation 24}$$

where E_D is the sum squared error between the target and the predictions for a given choice of weights, and E_w is a regulariser, that is a term which favours small values of the weights:

$$E_w = \tfrac{1}{2} \sum_i w_i^2 \qquad \textbf{Equation 25}$$

When making predictions, the variety of solutions corresponding to different possible sets of weights are averaged using the probabilities of these sets of weights, a process called marginalising.

An advantage of this process is the ability to quantify the uncertainty of fitting. If the probability distribution assigned to a weight set is sharply peaked, the most probable values will give the largest contribution to the prediction. Alternative solutions will have little importance and the prediction will be associated with a small uncertainty. If, the data is such that different sets of weights are all similarly probable (a wide distribution of probabilities) all predictions will contribute in similar proportions and the error bar will be large. Large error bars signify sparse or noisy data and provide a good reminder when the network is trying to predict outside the training space (extrapolate data).

5.2.3 Ranking models

Rankings can be performed by Log Predictive Error (LPE) or Test Error (TE). TE uses a sum of squared errors with regularisation constants α and β to control influence of ED and E_w (Equation 24). Where Ed is given as:

$$E_D(w) = \frac{1}{2}\sum [y(x^m; w) - t^m]^2 \qquad \textbf{Equation 26}$$

LPE attaches less importance to points which are outliers i.e. badly predicted/erroneous data.

$$LPE = \sum_m \frac{1}{2}(t_m - y_m)^2 / \sigma_y^{m2} + \log(\sqrt{2\pi\sigma_y^m}) \qquad \textbf{Equation 27}$$

Where σ_y^m is an error bound. Penalty for bad predictions is much less if that prediction is accompanied by appropriately large error bars.

5.2.4 Data Preparation

The training database is first 'rearranged' with every second line being placed at the end of the dataset. The next step is the normalisation of the data. Data is normalized between −0.5 and 0.5 using Equation 28.

$$X_N = \frac{x - x_{\min}}{x_{\max} - x_{\min}} - 0.5 \qquad \textbf{Equation 28}$$

5.2.5 Training models

Neuromat takes steps to avoid the overfitting problem by dividing the data into a training set and a test set. Figure 19 shows an example of a model (the black line) overfitting to the training data. When the rest of the data is presented (Figure 20) to the model it is associated with large test errors as the model does not generalise well. Figure 21 shows the relationship between training and test error as the complexity of the model increases. There reaches a point when the model begins to over fit to the data and although the training error continues to decrease, the ability to predict unseen data reduces.

For most of the experiments detailed in this chapter, data is split 50/50 for training and selecting models and committees (NB - New version of software allows this ratio to

be changed). The first half of the database is used to train a number of models. The numbers of models trained is set by the maximum number of hidden units and seeds selected. Neuromat has the capacity to create models with up to 25 hidden units. During the training process, Neuromat creates a model for every combination of hidden unit and seed. For example selecting a maximum of 10 hidden units and 5 seeds would require the creation of 50 models. Every combination of 1 to 10 hidden unit models starting at any one of 5 seed points will be trained. The remaining percentage of the data is then used to test and rank each model in turn

5.2.6 Committees of models

The complexity of a model depends on its number of hidden units. Therefore, models with different numbers of hidden units will give different predictions. Committees generally perform better than single models, especially in areas of uncertainty due to sparse or noisy data.

In Neuromat, committees are constructed using the best performing models ranked on either LPE or TE basis. Predictions are then made using an average from all models in the committee. A graph of combined test error against number of models in committee can be plotted (Figure 22). This information can then be used to select the optimum number of models with which to construct a committee. The process of selecting models is done by hand.

5.2.7 Significance of inputs.

Significance values for all inputs are generated during training. Neuromat uses Automatic Relevance Determination (ARD) which was developed by Mackay[xlvi]. The aim of ARD is to discover which hidden variables are relevant in explaining the dynamics of the system of interest. The ARD is implemented as a form of Bayesian structure learning where a prior Gaussian distribution is placed on the weights, favouring small magnitudes. The essence of ARD is that each input unit has its own prior variance parameter. Small variance suggests that all weights leaving the unit will be small, so the unit will have little influence on subsequent values. A large variance indicates that the unit is important in explaining the data.

5.2.8 Neuromat Notation

Neuromat uses letter and number notation to reference individual models within a committee. The letter is used to define the number of hidden units within the model; a=1, b=2, c=3 etc. The number represents which initial seed point was used to train the model. For example H3 would refer to an 8 hidden unit model that was seeded with seed number 3.

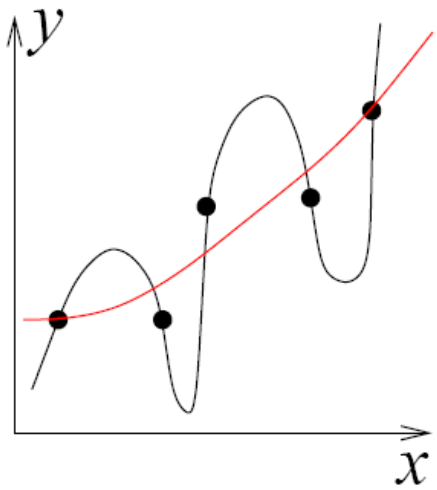

Figure 19 Examples of two possible data fits *(after Neuromat reference manual)*

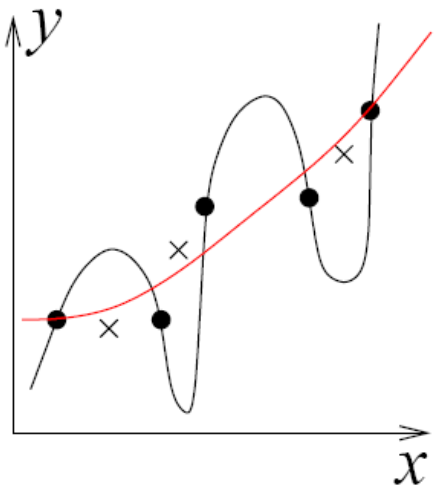

Figure 20 Addition of test data to indemtify model overfitting *(after Neuromat reference manual)*

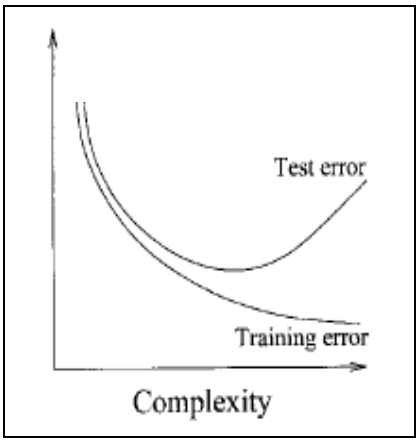

Figure 21 Effect of complexity (number of HU's) on test and training error

Figure 22 – Test error vs. number of models in a committee

5.2.9 Matlab

Much of the work done with Neuromat has been mirrored using Matlab. This was not so much an exercise in rewriting Neuromat in Matlab script but using Matlab to run experiments to investigate trends in the data and understand how the neural network modelling process works. The Matlab modelling process provides greater transparency of Neuromat thus allowing assumptions and methods to be checked in greater detail. Matlab also allows much simpler and therefore quicker analysis of network models to be performed.

The Neural Network Toolbox is a powerful collection of MATLAB functions for the design, training, and simulation of neural networks. It supports a wide range of network architectures and training methods including: supervised training of feedforward networks using the perceptron learning rule, Widrow-Hoff rule, several variations on backpropagation (including the fast Levenberg-Marquardt algorithm), and radial basis networks; supervised training of recurrent Elman networks; unsupervised training of associative networks including competitive and feature map layers; Kohonen networks, self-organizing maps, and learning vector quantization.

The Neural Network Toolbox has comprehensive help files which detail the theory and use of all the functions mentioned in this chapter. The Toolbox is delivered as MATLAB M-files, enabling users to see the algorithms and implementations, as well as to make changes or create new functions to address a specific application.

Scripts have been written as part of this work to aid the training and prediction process and can be found in APPENDIX 2.

The models written to date are currently using ‘trainbr’ function which utilises Bayesian Regularisation Backpropagation much the same as Neuromat. This allows small tests to be carried out quickly and simply without having to train a full Neuromat model. It also seemed a sensible starting point as the writers of Neuromat have spent time choosing a sensible training method for this sort of problem.

The basis of this work is to investigate how to collect, process and use data to train models, not to investigate neural network models themselves.

Matlab Scripts have been written to pre process the data, train the Networks and produce graphs of results and predictions all in one run. Matlab scripts have been written to implement the following processes:

During the training process, a graph of training Sum of Squared Errors (SSE) vs test SSE is produced (Figure 23). The test dataset has to be specified before training. The training vs test SSE can be used to stop the training process at a certain point (a form of early stopping).

All the models to date have been trained for a set number of Epochs. An epoch represents the presentation of the set of training (input and/or target) vectors to a network and the calculation of new weights and biases.

Generation of a graph showing each target data-point vs the predicted value from the trained model (Figure 24). The line Y=X signifies a perfect prediction. The graph is one of many ways to see how well the model has fit the training data. A similar graph can be produced for prediction against unseen data

Predictions from each individual model are plotted against the actual test data (Figure 25). At the time of writing, no script has been written to select the optimum combination of models for one or multiple values of hidden units.

A first attempt has also been made at assigning significances to the input variables of the trained model. The example chart shown in Figure 26 is generated calculating the sum product of each input weight and all the subsequent weights of hidden units between a particular input and the output. This method is a rather crude treatment of analysis of input variables and requires refinement.

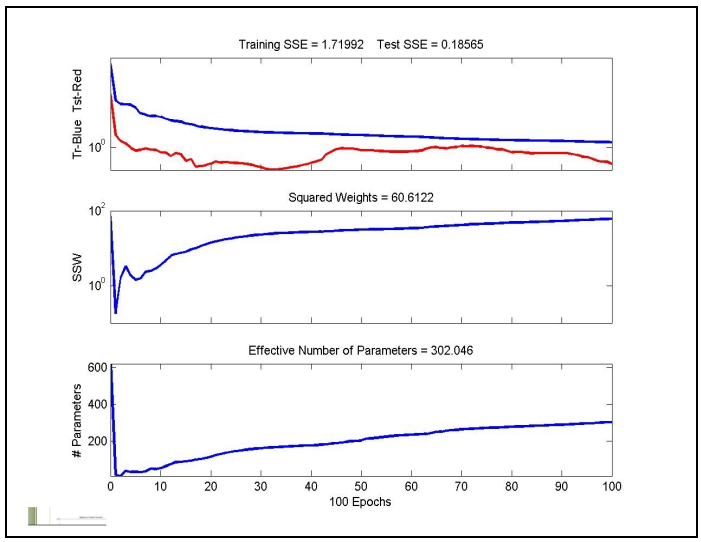

Figure 23 – Example of Matlab output during training

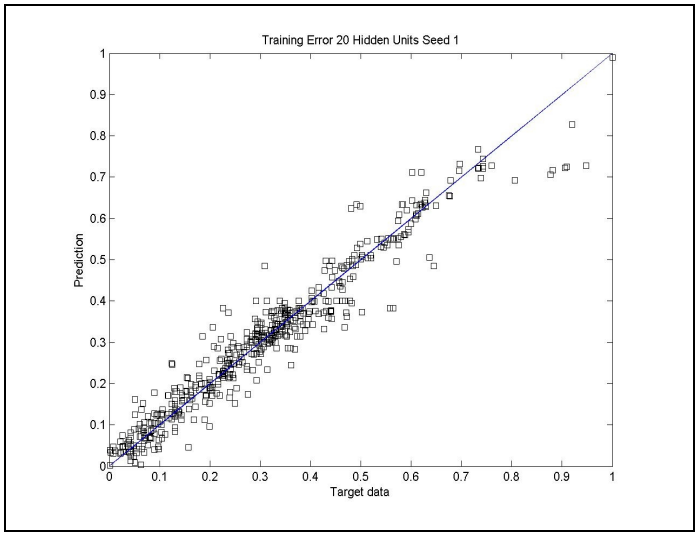

Figure 24 – Example of test vs training error graph generated using Matlab

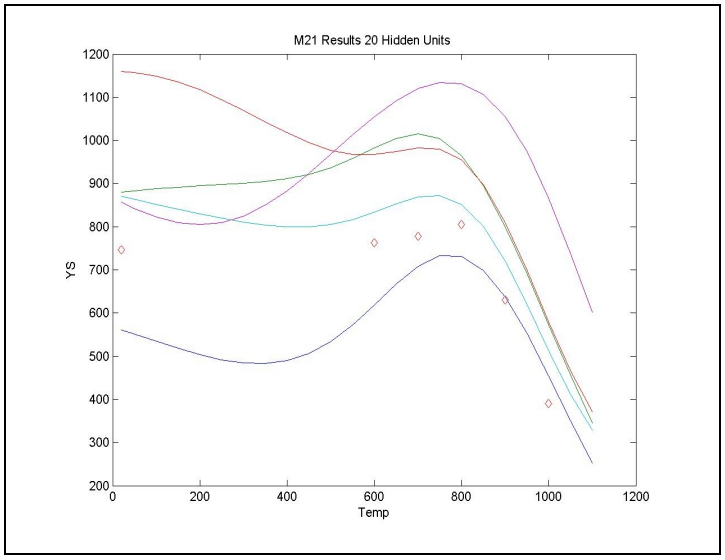

Figure 25 – Example of Matlab neural network predictions vs. actual data

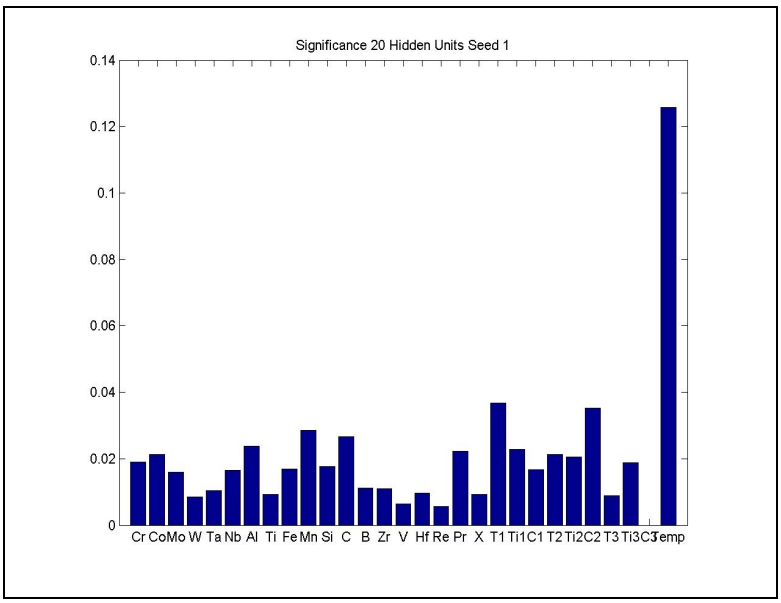

Figure 26 – Example of Significances related to input weights generated by Matlab

5.3 Initial Modelling Work using UTS Database

QinetiQ currently have 3 neural network models based around the Neuromat neural network program supplied by Cambridge University. Each Model uses its own database comprising of in house data and data available in the literature.

At the time of writing, the UTS database comprises of 1288 lines of data and 32 inputs shown below.

Nickel	Hafnium
Chromium	Rhenium
Cobalt	Lanthanum
Molybdenum	Process
Tungsten	Crystallography
Tantalum	Solution Temp
Niobium	Solution Time
Aluminium	Solution Cooling type
Titanium	Ageing Temp 1
Iron	Ageing Time 1
Manganese	Ageing Cooling type 1
Silicon	Ageing Temp 2
Carbon	Ageing Time 2
Boron	Ageing Cooling type 2
Zirconium	Test Temperature °C
Vanadium	UTS (MPa)

5.4 Data Collection Methodology

5.4.1 Data Sources

An initial search through the literature and QinetiQ internal databases was carried out to investigate the amount, and more importantly, the quality of data available. Data sources include:

- Superalloys conference proceedings
- Nickel Development Institute (NiDI) Handbook
- QinetiQ reports such as MANDATE Brite EuRam FPIV Programme
- INCO Alloy Datasheets

The first steps taken were to take existing QinetiQ data and build a Microsoft Access database. An extra field was included for the full reference source for each record with hyperlinks to electronic journal papers where applicable. This is particularly valuable information to QinetiQ and proved useful when checking the data for spurious results.

5.4.2 Selection of Inputs

Inputs have been selected to describe the chemical composition, processing route and heat treatment as they all affect the microstructure and therefore strength of the alloy. The roles of alloying additions and processing routes are discussed in section 4.2. Selecting the right number of inputs depends on several factors:

1. There must be enough inputs to adequately describe the alloy composition and other processes that are commonly documented.
2. As the number of inputs increases, so does the complexity of the neural network and the amount of data required to train it.
3. Input data must be consistently recorded for each record used.

Initial models have used the full chemical composition of the alloy with further work being carried out to determine if some elements could be left out of future models. Inputs were chosen based upon information that was readily available in data sources, such inputs could only be used if that particular piece of information was recorded for every alloy. Missing data is difficult to represent in a neural network, a cell cannot simply be left blank. A value of zero is generally not an accurate representation for unknown data. Blank cells can be filled with the average value for that input but this is not desirable as it is not a true result and could be very different from the actual missing value. A better solution is to remove the record containing the missing data.

With this in mind, if the list of inputs was over defined many sources of data would be unusable. The input data has been divided up into 3 categories; Composition, Processing and Heat Treatment. Varying data in each category will have a measurable effect on the strength of the alloy.

5.4.3 Alloy composition

Alloying elements that are included specifically to strengthen the superalloy are discussed in the literature review. To start off with, full compositional information was recorded for each alloy. The initial list comprised of 19 elements: Ni, Cr, Co, Mo, W, Ta, Nb, Al, Ti, Fe, Mn, Si, C, B, Zr, V, Hf, Re, and La.

It is expected that the most important elements will be those that are included for γ' formation and solid solution strengthening. The removal of some of these elements as

inputs is discussed later in the chapter. Alloy compositions are recorded as weight percent to an accuracy of 2 decimal places.

5.4.4 Processing parameters

Information about the processing route of each alloy was limited to; Cast or cast and wrought as the first input and Polycrystalline (PX), directionally solidified (DS) or single crystal (SX) as the second. These parameters are the only ones which are regularly recorded and they all have a significant effect on material properties which cannot be described by composition and heat treatment alone. Processing parameters are recorded by allocating a number to each parameter as shown:

	Process		Crystallography
Cast	0	PX	0
Wrought	1	DS	1
PM	2	SSX	2

The disadvantage with this method is that it infers some sort of numerical ranking to the processes which may adversely affect the model. An alternative method could be used as shown:

	P1	P2	P3		C1	C2	C3
Cast	1	0	0	PX	1	0	0
Wrought	0	1	0	DS	0	1	0
PM	0	0	1	SSX	0	0	1

The problem here lies in the creation of 4^2 more input columns in this case. It was decided to use the first method for initial modelling attempts in order to keep the number of inputs to a minimum.

[2] Whichever method is used to describe level information for processes should also be used for cooling rate information (see heat treatments) so the increase in inputs would be by 7 and not 3.

5.4.5 Heat Treatments

The heat treatment used will determine the γ/γ' microstructure and grain size (where applicable) thus having a large effect on the strength of the alloy. The most common heat treatment cycle is normally a combination of a solution treatment and one or two ageing treatments. Heat treatment information has therefore been split into 9 inputs. Information on heat treatments is recorded with 3 critical parameters (Temperature, Time and Cooling type). Cooling rate is also important but was not often included in papers and specifications and was therefore left out. It is also a function of the cooling method used, so this parameter should adequately describe the process.

Temperature and time inputs are simply recorded in °C and hours respectively. Cooling methods are recorded in much the same way as processing information and are subject to the same decision as to how to record the levels.

	Cooling Method
Air cool	0
Furnace cool	1
Water Quench	2
Oil Quench	3

Some alloys have a multi step heat treatment that does not fit the structure of the input database. For these alloys, a method of reducing complex multi step treatments into one equivalent step was used. A single step was calculated to give an equivalent amount of diffusion of Al and Ti in Ni. An example for the treatment of alloy CM247LC DS is given.

The solution heat treatment for CM247LC DS is 1221°C for 2 hours + 1232°C for 2 hours + 1246°C for 2 hours + 1260°C for 2 hours then rapid fan quench in argon. Diffusion of aluminium in nickel (k) has been calculated using the Arrhenius equation.

$$k = Ae^{-E_a/RT} \qquad \textbf{Equation 29}$$

Where A and E_a are material constants from the literature[xlvii], R is the gas constant and T the temperature in °Kelvin. The diffusion distance is then calculated:

$$\text{Distance} = \sqrt{(k.t)} \qquad \textbf{Equation 30}$$

Where k has been calculated in Equation 29 and t is the time in seconds. The time required for each step, at the maximum temperature (1260°C) instead of the actual temperature, to give an equivalent diffusion distance was then calculated. An example

is given for diffusion of aluminium in nickel (Figure 27). Values for titanium were very similar.

		Constants						
Temp (°C)	Temp (°K)	R	A	Q	D	Time (s)	Diffusion distance (cm)	Eqiv Time @ 1553°K
1221	1494	1.987	4.41	73160	8.737E-11	7200	0.000793115	3846.2925
1232	1505	1.987	4.41	73160	1.046E-10	7200	0.000867861	4605.438
1246	1519	1.987	4.41	73160	1.311E-10	7200	0.000971433	5770.2683
1260	1533	1.987	4.41	73160	1.635E-10	7200	0.001085128	7200
								Total
							Seconds	21421.999
							Hours	5.9505552

Figure 27 – Excel calculations for solution heat treatment approximation

The 4 step solution treatment is therefore substituted with 1 solution treatment step at 1260°C for 6 hours.

5.5 Predictions using UTS_IW7_Test database.

The IW7 test database represents the initial database of raw data, as inherited from QinetiQ for this work. The data has been collected by a combination of undergraduate students and researchers over the period of several years The following set of results represents a summary of the work completed prior to any raw data analysis and subsequent data clean-up. The model was trained using a maximum of 18 hidden units and 9 seeds. A maximum of 60 models was selected to train committees.

- Best LPE committee comprises of 4 models.
- Best TE committee comprises of 8 models.
- Best LPE and TE committees had no models in common.

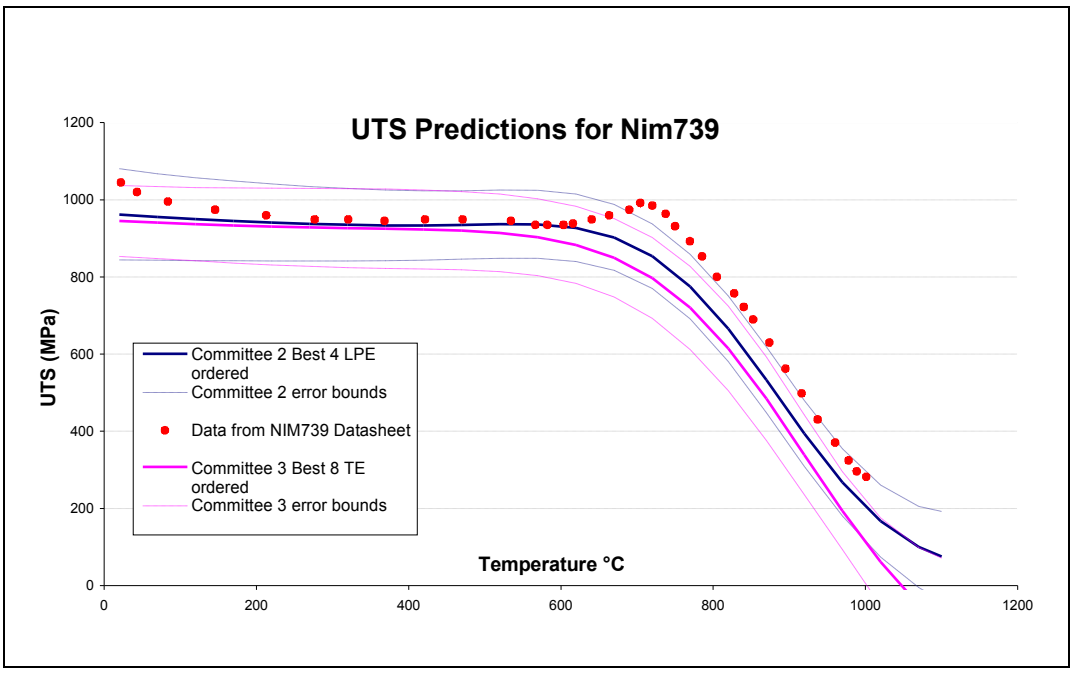

Figure 28 - UTS predictions for Nim739 using UTS_IW7_Test

Both the LPE and TE committees gave good results when tested against unseen Nim739 data (Figure 28). The best LPE committee prediction was closer to the test data. Test data was very close to staying within error bounds throughout the temperature range. Maximum predicted error was 118 MPa with an average error of +/- 84MPa

When tested against data for M313 the LPE committee prediction was very close to the test data again. (Figure 29). The model had significantly wider error bounds than the prediction for Nim739 with an average error +/- 468MPa for the best LPE committee. The best TE model committee was not tested using this data.

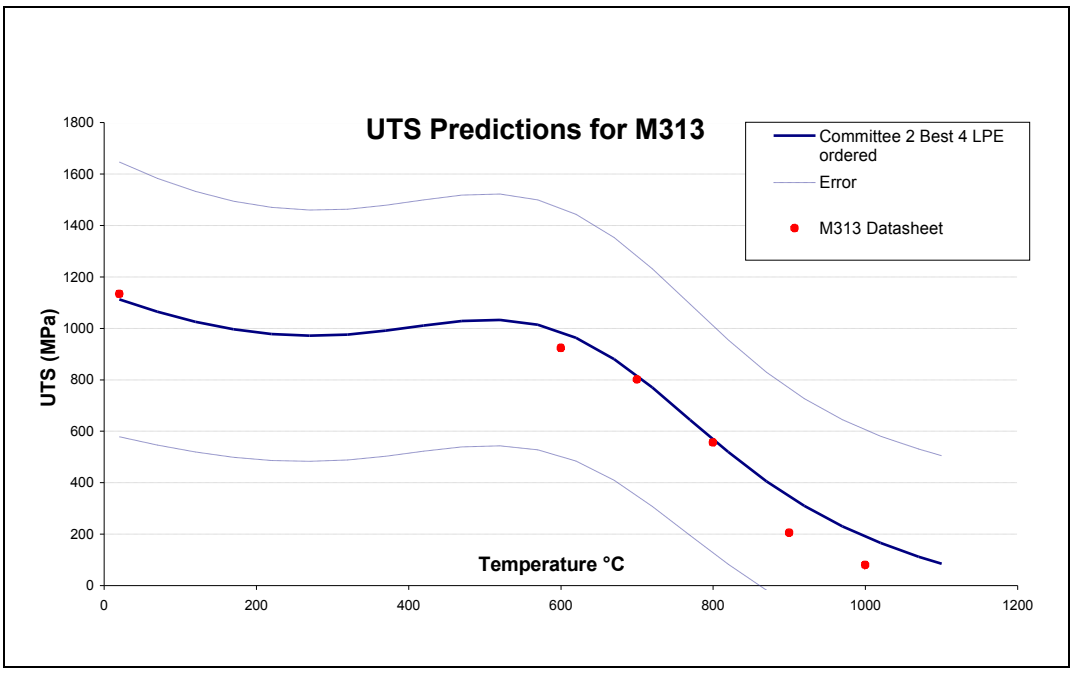

Figure 29 - UTS predictions for M313 using UTS_IW7_Test

The training database was checked for data that is similar to data used to test the models. Although there is no Nim739 data in the database there is IN939 which has an almost identical composition. The IN939 data in the training database has been plotted with the 'unseen' Nim739' data and the predicted values for Nim739 (Figure 30).

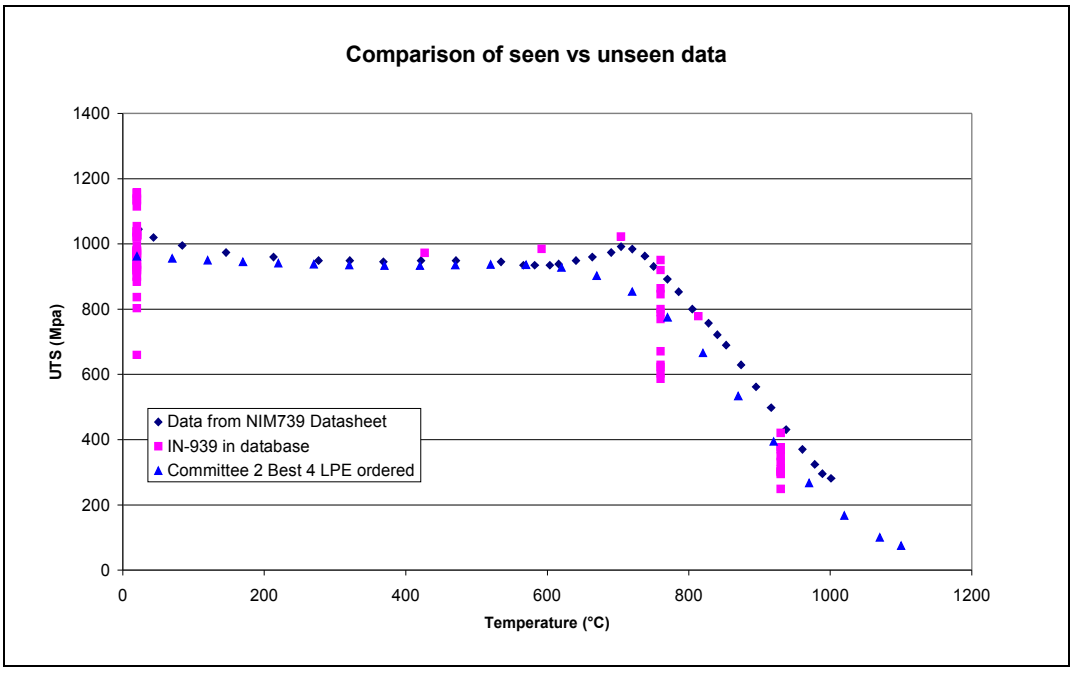

Figure 30 - Comparison of data for Nim739 and IN939 + Neuromat prediction

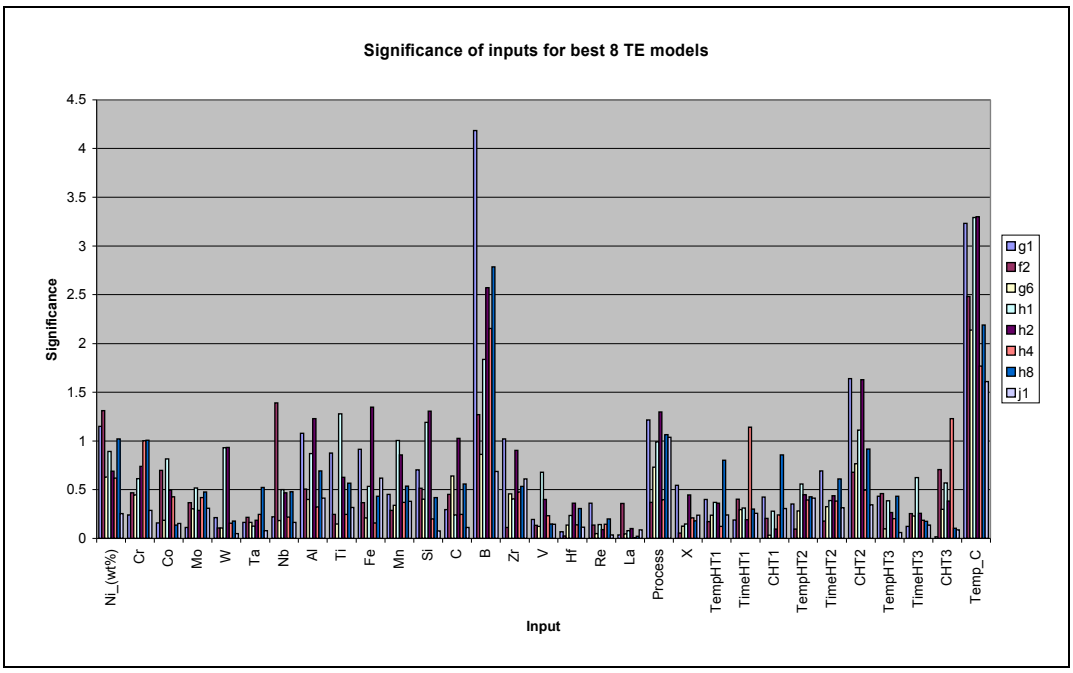

Figure 31 - Significance of inputs for best TE committee

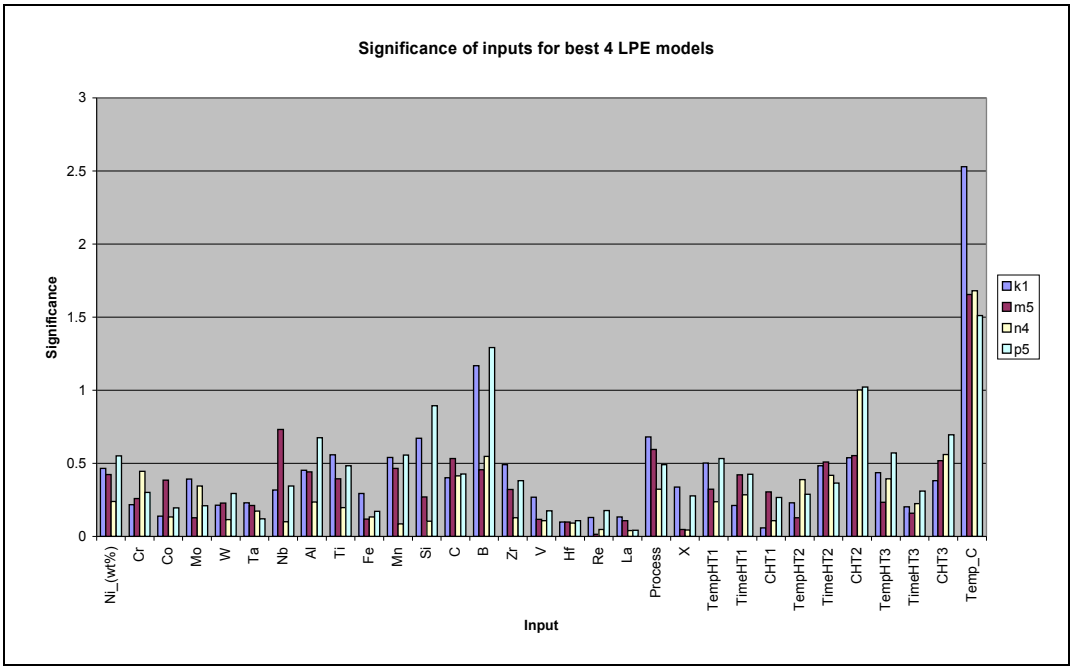

Figure 32 - Significance of inputs for best LPE committee.

Significance plots for both committees (Figure 31 & Figure 32) show that the most significant data inputs to the models are; test temperature, cooling rate from heat treatment 2 and weight percentage of boron. It is expected that test temperature should be the most significant input but the relative high significances of heat treatment 2 and boron in comparison to additions such as Al and Ti is not expected.

5.6 Supporting work using Matlab

Initial work with Matlab for this dataset produced results that were not repeatable. A network that was trained and gave reasonable predictions could be retrained from scratch with the same data in an identical manner and yet give very different results.

This was found to be due to the way that the model chooses its starting weights. One of the first lines in the code which 'initialised' the network randomly selects the starting weights and biases (or 'seeds'). To make the training process repeatable the starting weights and biases can be recorded and re-used to yield similar training results.

The effect of changing initial weights is well illustrated in Figure 33 where each line represents the prediction from a single 25 hidden unit model started with random seeds on identical training datasets.

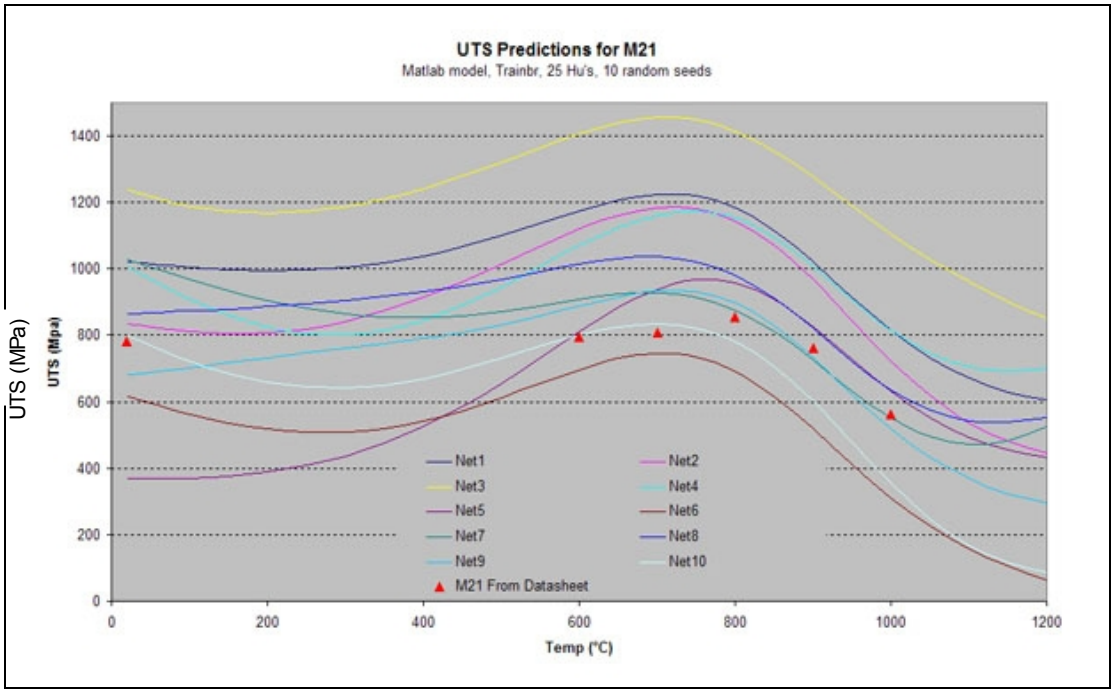

Figure 33 – Models trained using the same training in Matlab using different initial values

The first attempts using Matlab to generate models were run by hand with no extra scripting. The results in Figure 34 show UTS predictions for alloy Nimonic 739 from single models against seen data.

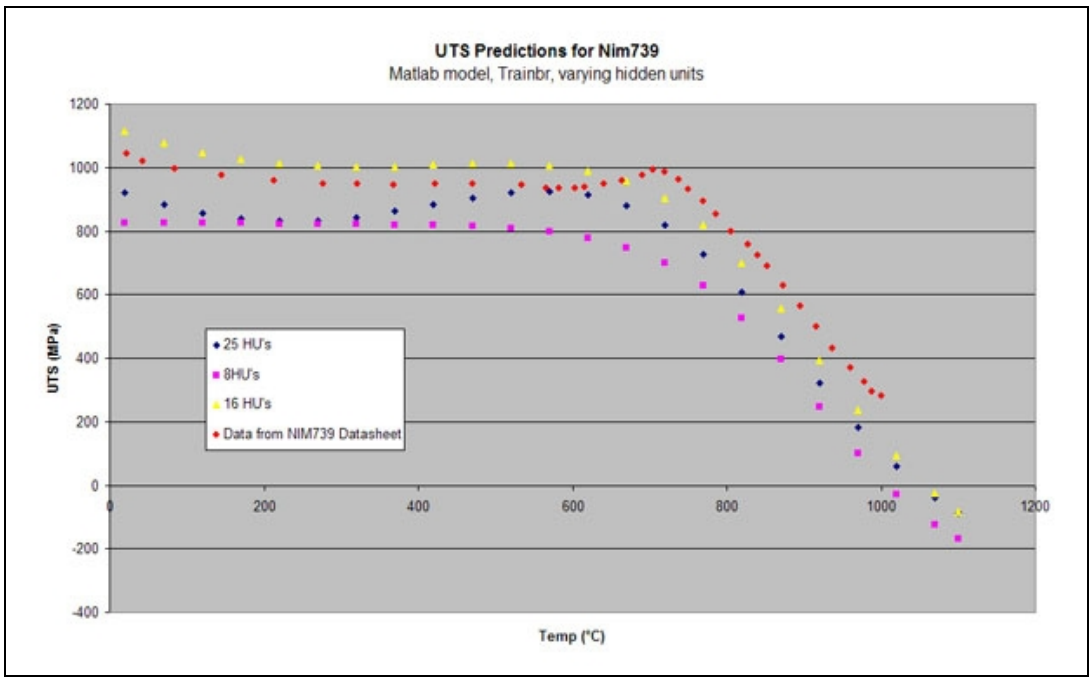

Figure 34 – Predictions for Nim739 UTS, varying number of HU's

5.7 Summary of Preliminary Results

Matlab models have shown that a large number of seed points will give the network the best chance at finding an optimum fit to the UTS data and the difference between networks trained from different seeds can be very large. It is advisable to select the maximum number of seeds points in Neuromat before training the model to give it the best chance of arriving at a globally optimised solution

Initial Matlab models have shown that a single model in the region of 16 to 25 hidden units can provide a reasonable fit to seen data. No one model fitted all seen test alloys well.

Although the first results from the "raw" database proved encouraging, it was found that for one 'unseen' alloy (Nim739) there was a very similar alloy present in the database so this was not a critical test of the model's predictive ability. More importantly, the results of the significance analysis showed that the model was relying heavily on inputs that are believed to be metallurgically less important than others. The predictions shown are the best results achieved for this particular model/database combination.

With this in mind, statistical analysis of the input data was conducted before further models were trained.

- Data spread for each input within the database
  - Maxima, Minima, Mean, Distribution etc..
- Analysis of data in large subsets
- Number of data points per alloy
- Scatter of subsets for alloys with a large number of data points (Alloys with >10 data points have been identified and results for each alloy plotted)
- Any repeat tests within database
- Wt% Totals were checked

5.8 Data Preparation and Analysis

Data was stored within a Microsoft Access database in order to make data analysis and data sorting more straightforward. Datasets were exported to Excel or .txt files for analysis or to train a neural network model when required. This insures that the very latest database was always used when producing statistical analysis of data or training a neural network.

Each database was exported to a spreadsheet in Excel. The excel data analysis tool for 'Descriptive Statistics' was used to analyse the data. The Descriptive Statistics tool generates the following information:

- Mean
- Standard Error
- Median
- Mode
- Standard Deviation
- Sample Variance
- Kurtosis
    - *Returns the kurtosis of a data set. Kurtosis characterizes the relative peakedness or flatness of a distribution compared with the normal distribution. Positive kurtosis indicates a relatively peaked distribution. Negative kurtosis indicates a relatively flat distribution*
- Skewness
    - *asymmetry of a distribution around its mean. Positive skewness indicates a distribution with an asymmetric tail extending toward more positive values. Negative skewness indicates a distribution with an asymmetric tail extending toward more negative values.*
- Range
- Minimum
- Maximum

In addition to the analysis performed automatically by Excel, two more calculations were performed.

1. The percentage of data points for each input that are non zero. E.g. The column for Ni contains 100% non zero values.
2. The distribution above and below 100% for the total weight percent for each alloy.

When looking at analytical results for; Process, Crystallography (X) and the three cooling rates (CHT1, CHT2 and CHT3) it must be taken into account that these inputs are coded 0,1,2,3.

UTS Data	Ni_(wt%)	Cr	Co	Mo	W	Ta	Nb	Al	Ti	Fe	Mn
Mean	57.83	15.67	10.34	3.57	1.85	0.91	1.06	2.81	2.60	2.87	0.07
Standard Error	0.19	0.13	0.20	0.10	0.08	0.06	0.05	0.05	0.05	0.18	0.00
Median	57.27	16.00	11.00	3.00	1.00	0.00	0.00	2.50	2.60	0.00	0.00
Mode	57.27	16.00	0.00	3.00	0.00	0.00	0.00	2.50	5.00	0.00	0.00
Standard Deviation	6.68	4.61	7.25	3.60	2.93	2.03	1.75	1.91	1.68	6.48	0.15
Sample Variance	44.64	21.30	52.52	12.96	8.56	4.11	3.06	3.64	2.81	41.94	0.02
Kurtosis	0.59	0.58	-1.20	17.76	3.63	10.17	1.15	-1.01	-1.29	2.90	8.96
Skewness	0.60	-0.32	-0.23	3.58	2.07	3.04	1.61	0.35	0.06	2.11	2.94
Range	36.00	30.00	25.15	25.00	12.20	11.90	6.50	8.00	5.50	27.16	0.80
Minimum	40.00	0.00	0.00	0.00	0.00	0.00	0.00	0.00	0.00	0.00	0.00
Maximum	76.00	30.00	25.15	25.00	12.20	11.90	6.50	8.00	5.50	27.16	0.80
Number of records	1288										
Percentage of non zero values	100.0%	99.5%	76.4%	86.0%	52.4%	28.3%	44.3%	97.7%	91.9%	38.5%	35.2%

	Si	C	B	Zr	V	Hf	Re	La	Process	X
Mean	0.07	0.08	0.01	0.05	0.02	0.08	0.05	0.00	0.61	0.11
Standard Error	0.00	0.00	0.00	0.00	0.00	0.01	0.01	0.00	0.02	0.01
Median	0.00	0.06	0.01	0.04	0.00	0.00	0.00	0.00	0.00	0.00
Mode	0.00	0.01	0.02	0.00	0.00	0.00	0.00	0.00	0.00	0.00
Standard Deviation	0.14	0.08	0.03	0.10	0.12	0.30	0.37	0.00	0.72	0.42
Sample Variance	0.02	0.01	0.00	0.01	0.01	0.09	0.14	0.00	0.51	0.18
Kurtosis	12.30	15.04	45.45	65.17	57.14	17.98	53.57	179.71	-0.74	13.01
Skewness	3.23	3.13	6.28	7.61	7.59	4.28	7.42	13.47	0.73	3.74
Range	0.95	0.60	0.25	1.00	1.00	2.00	2.90	0.02	2.00	2.00
Minimum	0.00	0.00	0.00	0.00	0.00	0.00	0.00	0.00	0.00	0.00
Maximum	0.95	0.60	0.25	1.00	1.00	2.00	2.90	0.02	2.00	2.00
Number of records										
Percentage of non zero values	36.7%	98.2%	83.6%	64.5%	2.1%	9.5%	2.2%	0.5%	47.3%	7.7%

	TempHT1	TimeHT1	CHT1	TempHT2	TimeHT2	CHT2	TempHT3	TimeHT3	CHT3	Temp_C	UTS_MPa
Mean	969.30	2.94	0.36	707.91	13.95	0.10	407.20	8.59	0.02	498.01	998.36
Standard Error	10.21	0.06	0.02	8.78	0.30	0.01	10.24	0.20	0.01	9.61	10.38
Median	1100.00	2.00	0.00	760.00	16.00	0.00	620.00	8.00	0.00	609.05	1050.00
Mode	1100.00	4.00	0.00	20.00	24.00	0.00	20.00	2.00	0.00	20.00	1050.00
Standard Deviation	366.31	2.00	0.86	315.12	10.87	0.40	367.46	7.26	0.26	344.73	372.35
Sample Variance	134185.98	4.01	0.74	99301.06	118.09	0.16	135025.68	52.73	0.07	118840.20	138646.36
Kurtosis	2.72	17.90	3.01	0.72	13.37	32.74	-1.90	-0.96	124.29	-1.29	-0.28
Skewness	-2.09	2.73	2.14	-1.25	1.84	5.34	-0.06	0.55	11.23	-0.29	-0.60
Range	1295.00	18.83	3.00	1140.00	119.00	3.00	1020.00	32.00	3.00	1080.29	1647.38
Minimum	20.00	0.17	0.00	20.00	1.00	0.00	20.00	0.00	0.00	19.71	35.00
Maximum	1315.00	19.00	3.00	1160.00	120.00	3.00	1040.00	32.00	3.00	1100.00	1682.38
Number of records											
Count - zero values	0	0	1089	0	0	1195	0	1	1278	0	0
Percentage of non zero values	100.0%	100.0%	15.5%	100.0%	100.0%	7.2%	100.0%	99.9%	0.8%	100.0%	100.0%

Table 1 Data analysis of UTS database

Analysis shows that there is a good population of data for boron within that database and the data is not particularly skewed or have any large outliers (Table 1).

Data for heat treatment 2 (CHT2) shows that 99% of the values are set at 0 which corresponds to air cool. Weight percentage totals show that only 507 entries have a total weight percentage that equates to 100% exactly. Furthermore, there are 135 alloy entries outside 100 $^{+}/_{-}$ 0.5% and 22 entries that are less that 99%.

This data does not represent mistakes during data entry but is representative of actual data published. A lot of data is quoted as nominal values within ranges which quite often do not add up to 100%.

A form within Microsoft Access was used with an underlying query to automatically generate graphs to show spread of data points within one alloy type or a group of alloys. Figure 35 shows the full spread of data points within the original database. Clusters of data are observed at common test temperatures 0°C, 550°C, 650°C etc. Large amounts of scatter are visible at these temperatures and require closer inspection on an alloy by alloy basis. Presenting Neuromat with data with such a large

spread will cause it to use large error bars in area where there is actually a lot of data. Some obvious outliers are visible at 20°C with UTS values of between 400 and 600MPa.

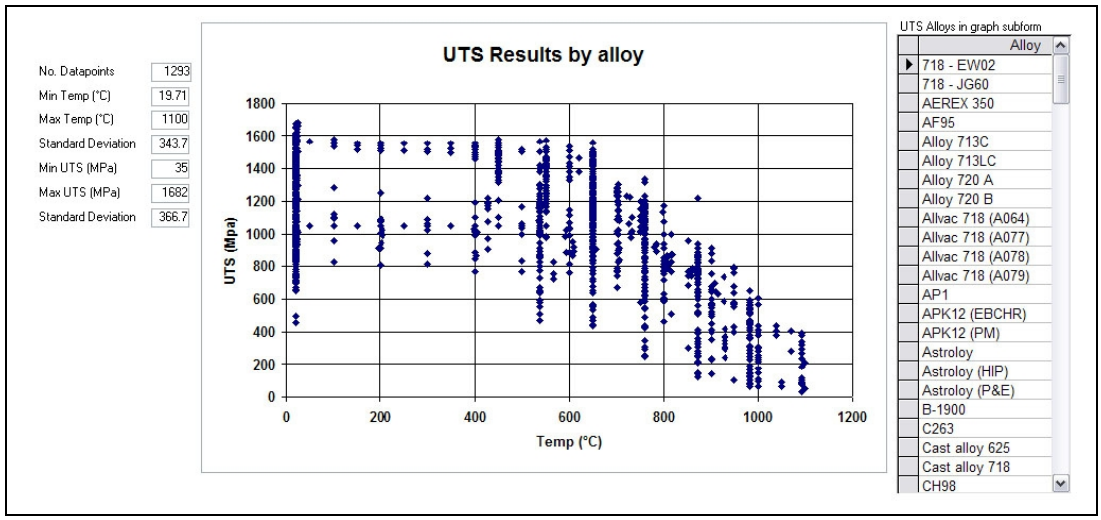

Figure 35 – Full spread of UTS data by alloy (UTS vs. Temp)

The two distinct clusters of data can be separated out further by plotting with respect to alloy type / process (Figure 36). It can be seen that the higher cluster is generally comprised of powder metallurgy alloys. Some outliers that have been removed during the checking process have also been circled on this graph.

Alloys were examined on an alloy by alloy basis in order to identify incorrect data points. An example of a typical alloy curve within the database is shown in Figure 37. Figure 38 shows U720 and all its derivatives which exhibit a high amount of scatter due to the subtle alloy variations within the group and the large amount of test data from a variety of sources.

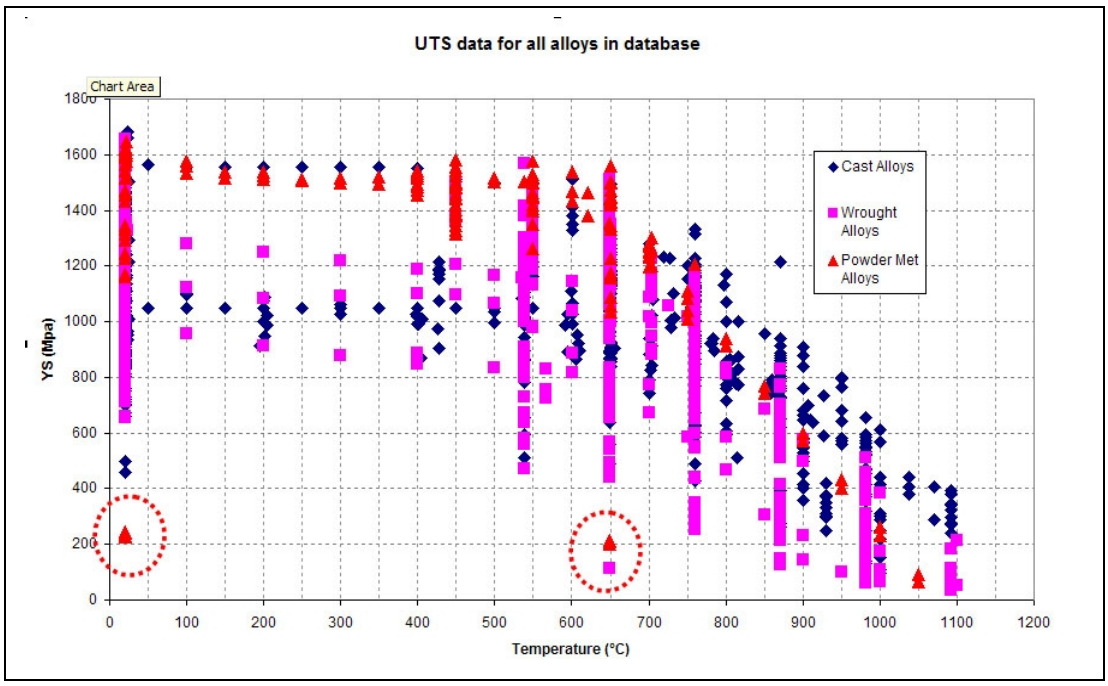

Figure 36 – Identification of outliers in UTS database

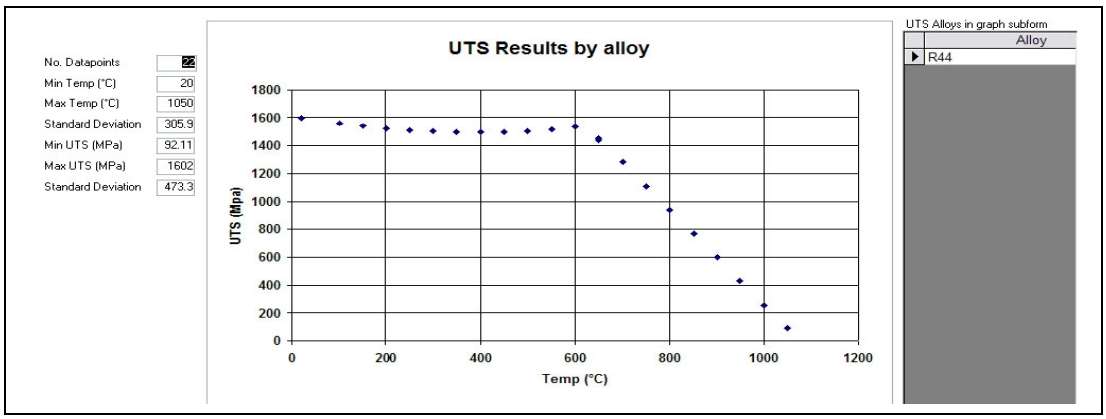

Figure 37 – Material curve for alloy R44

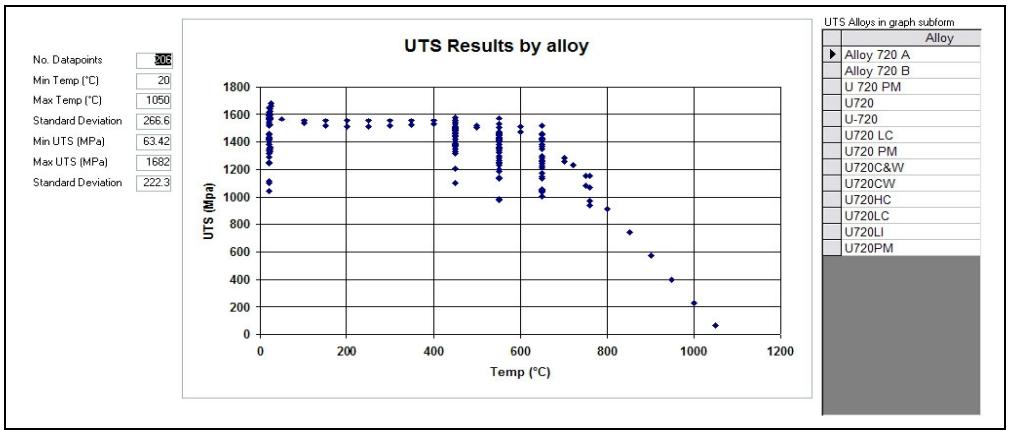

Figure 38 – Data for U720 exhibiting large amounts of scatter at common test temperatures

5.9 Modifications to database.

Heat Treatments

When the data was initially input into the database, heat treatment columns were filled from left to right depending on how many heat treatments the alloys received. Each heat treatment step is added for a particular reason and can have different effects on the microstructure. The model should benefit from each treatment (solution and age) being identified in its own column.

The heat treatment columns in the database have now been rearranged so that the significance's would correspond to different types of heat treatment. Column TempHT1 has been reserved for solution treatments (high temperature relatively short duration). All heat treatments in column TempHT1 that were identified as ageing treatments were moved to columns TempHT2 and TempHT3 with single ages in TempHT2.

Weight Percentages & Inclusion of Ni

The Nickel column can be calculated as a function of all the rest of the alloying elements, it is therefore unnecessary to include this information in order to train the neural network. The removal of this column also generates the assumption that all weight percentage totals are now 100%.

Removal of outliers

The graphs for each alloy were used to identify clear outliers. Data was amended when type errors were identified. Some data was removed when it was believed that it was clearly wrong i.e. differed by an order of magnitude from the next nearest result.

5.10 Models Using refined UTS Database

UTS models trained with full database including test alloys (UTS_17_01_05)

- LPE committee comprises of 15 models (Figure 39) Models range between 5 and 14 hidden units.
- TE committee comprises of 12 models (Figure 40) Models range between 5 and 9 hidden units.

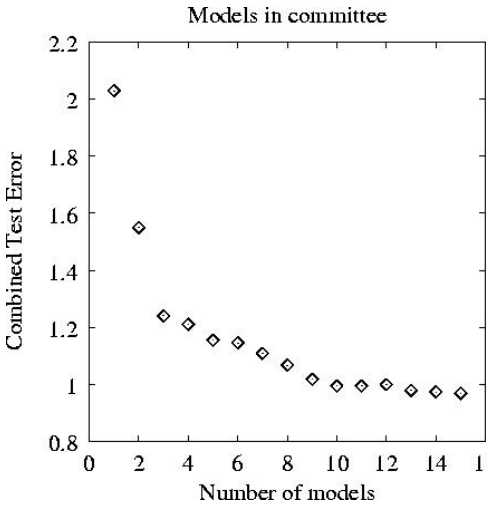

Figure 39 - Committee based on LPE ranking

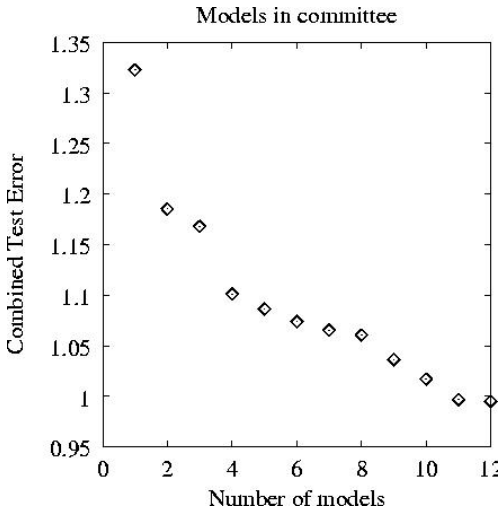

Figure 40 - Committee based on TE ranking

The committee models were exported so that they can be run on a as a standard PC as a standalone application. A single text file has been created with all test alloys and all variations for sensitivity analysis so that model only needs to be run once in order to generate all data required.

Predictions against test alloys (seen data)

Graphs show that the LPE committee performs better with test alloys 617 (Figure 41) and 901 (Figure 42) with very little difference between the two for MERL 76 (Figure 43). LPE predictions appear to be lower than TE based prediction.

Error bands for MERL 76 predictions show decreased confidence levels at higher temperatures which correlate well to the spread of data in the database.

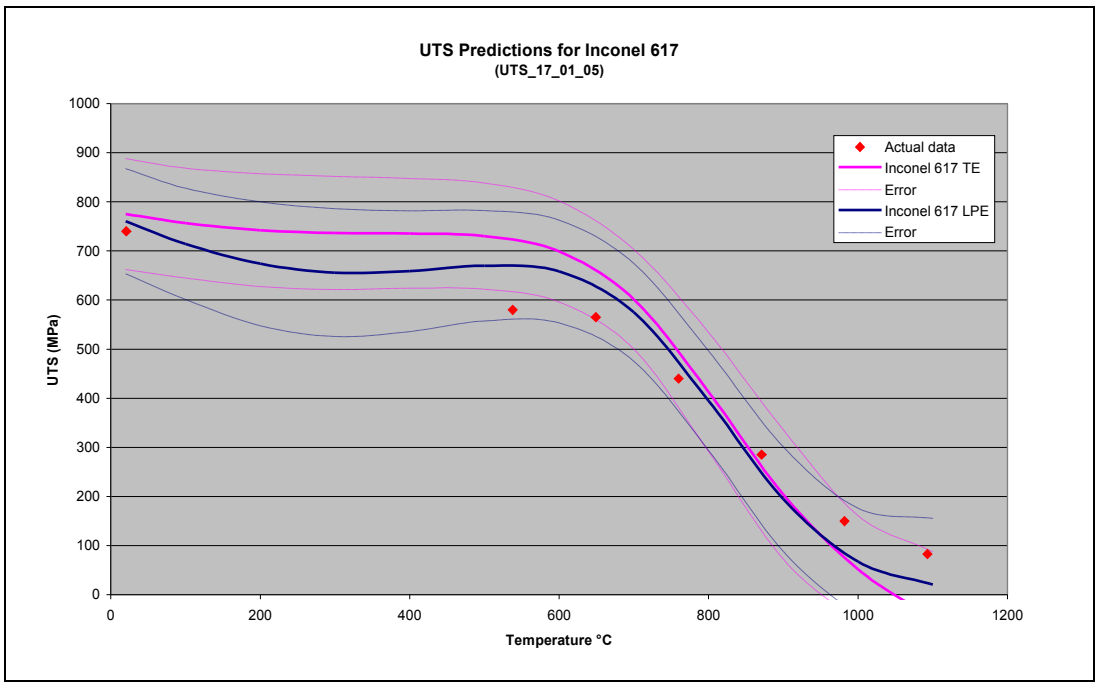

Figure 41 – Neuromat predictions for Inconel 617 UTS

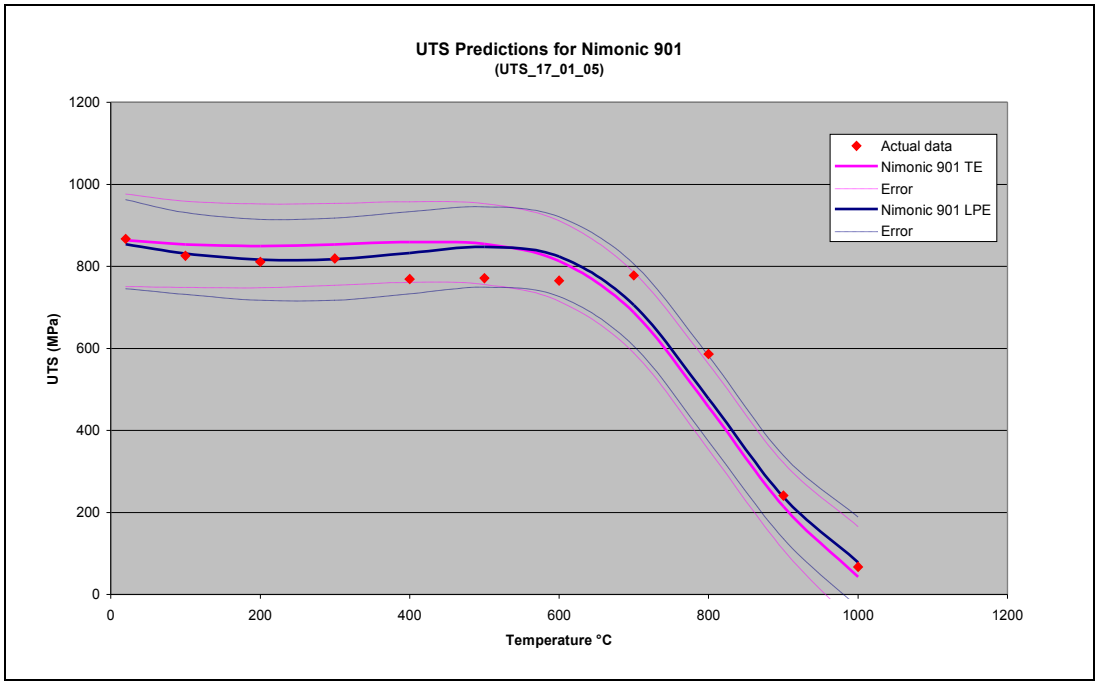

Figure 42 – Neuromat predictions for Nimonic 901 UTS

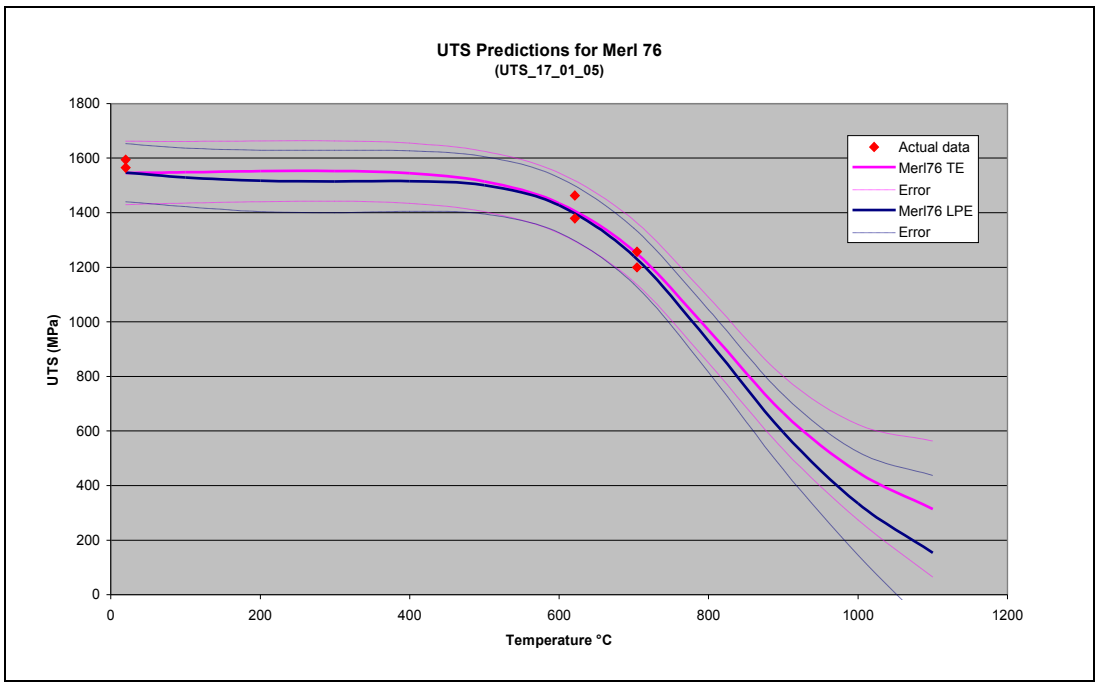

Figure 43 – Neuromat predictions for MERL 76 UTS

Significance of input variables.

Significance values from each model in each committee have been recorded. The following graph shows the average significance values for each committee model (Figure 44).

Significance values for composition inputs appear more consistent with metallurgical understanding than previous models using raw data. Boron is no longer considered to be the element that has most effect on UTS. The significances of heat treatment steps are however less believable with cooling rate of the first ageing treatment (CHT2) appearing to have the most effect. It has however been shown in the literature that, in the case of U720, there is significant influence of quenching medium on the properties of the alloy due to the effect on tertiary γ' formation[xlviii].

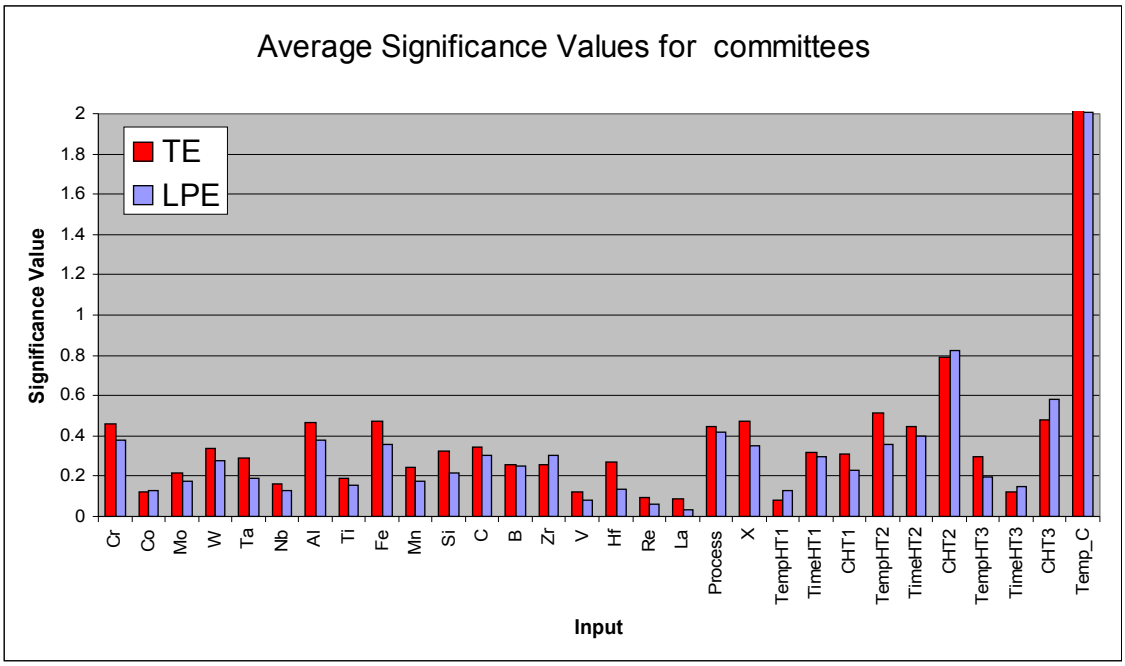

Figure 44 – Significance of inputs for input dataset UTS_17_01_05

Sensitivity Analysis

Inconel 617 is present in the training dataset. The prediction is carried out for an ageing treatment at 650°C for 8 hours and shows an average increase in UTS of ~300MPa (Figure 45).

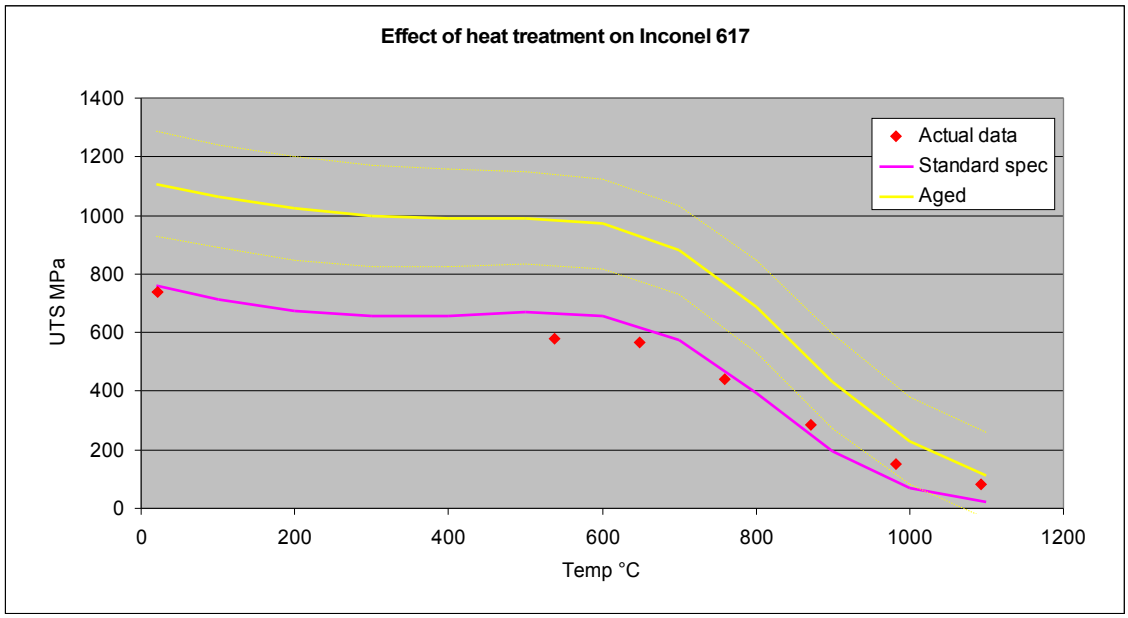

Figure 45 – Sensitivity of UTS model to change in heat treatment for Inconel 617

MERL 76 was chosen as an example of a high strength disk alloy within the database. The prediction for MERL 76 without any ageing treatments (Figure 46) showed a small increase in UTS although error bounds have increased from $^{+}/_{-}$ 100MPa to $^{+}/_{-}$ 400MPa. Decreasing the 1st ageing temperature produced a small increase in UTS whereas

increasing the 1st ageing temperature produced a small decrease in UTS – these predictions were accompanied by tighter error bounds (+/- 100MPa).

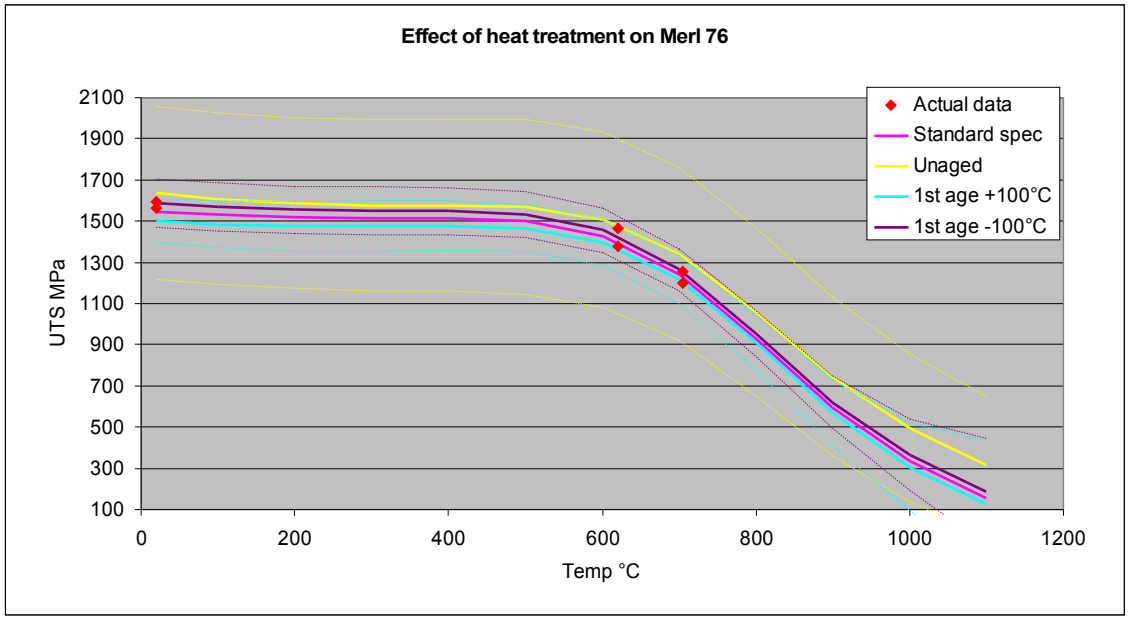

Figure 46 - Sensitivity of UTS model to change in 1st age temperature for MERL 76

Making changes to the second age rather than the first ageing treatment had no real effect on the UTS values over the prediction for the standard spec alloy (Figure 47).

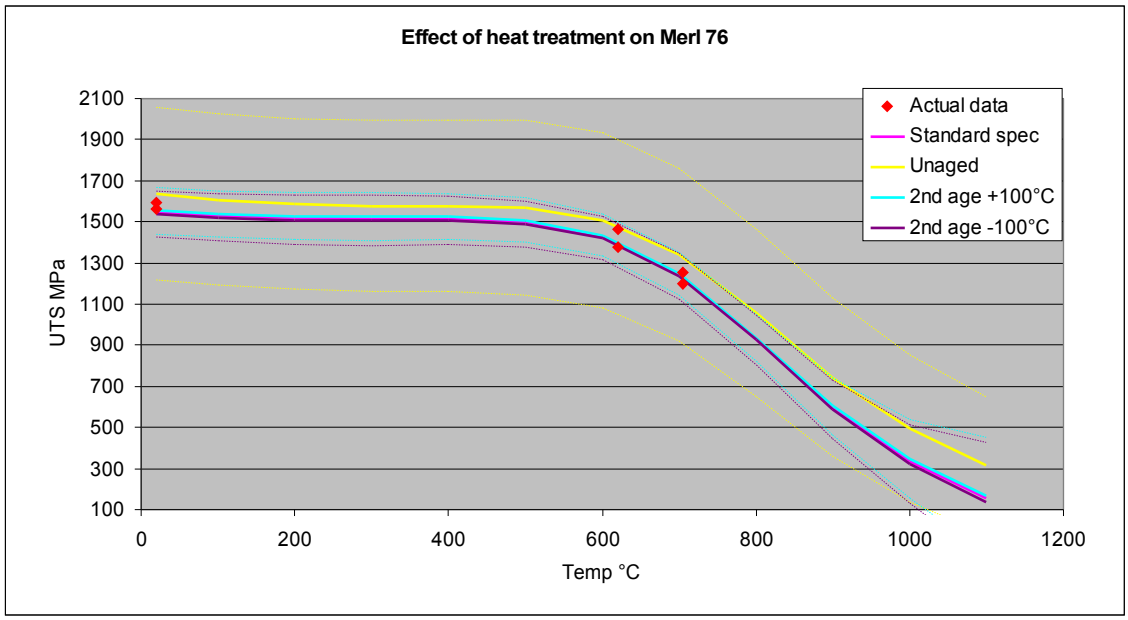

Figure 47 - Sensitivity of UTS model to change in 2nd age temperature for MERL 76

Predictions for un-aged Nimonic 901 (a medium strength disk alloy) suggested a decrease in UTS on average. The error bounds accompanying this prediction are huge (+/- 1350 MPa). The effect of altering the ageing temperature was negligible (Figure 48) but the model does not have sufficient data to predict for this case.

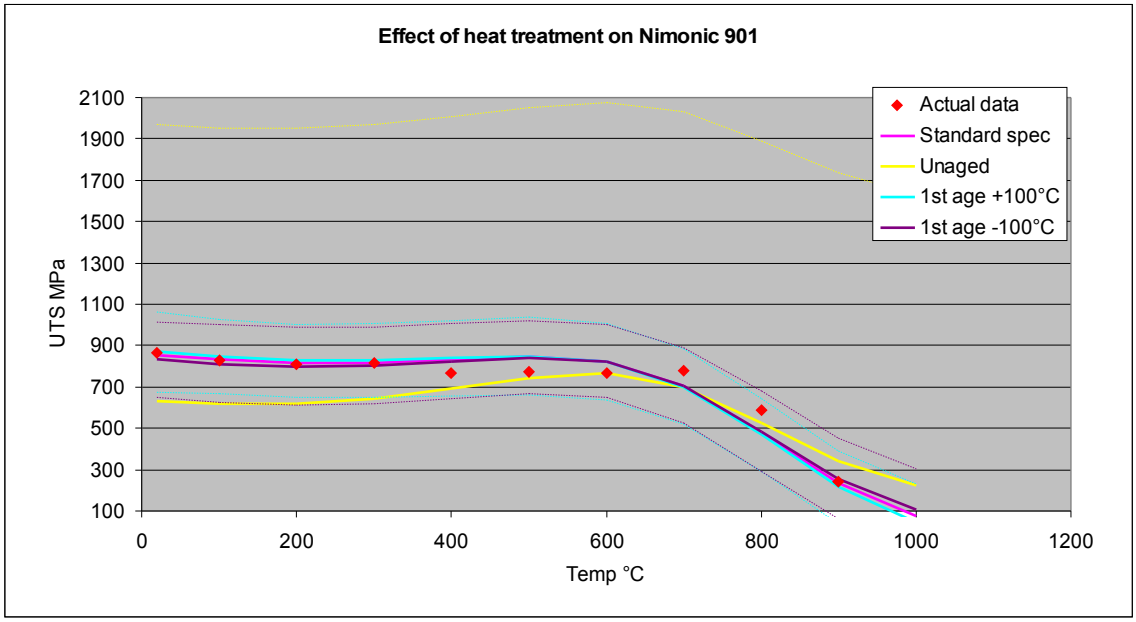

Figure 48 Sensitivity of UTS model to change in 1st age temperature for Nimonic 901

Compositional variations

Increasing both aluminium and titanium by 0.5% brought about a predicted decrease in UTS. Decreasing the amount of aluminium and titanium showed a predicted increase in UTS. Error bounds remained roughly the same as for the standard specification of the alloy. The changes in UTS, although small, occurred in the opposite directions to what was expected as Al and Ti are γ' formers. A 1% increase in niobium content showed an increase in UTS of ~30MPa (Figure 49).

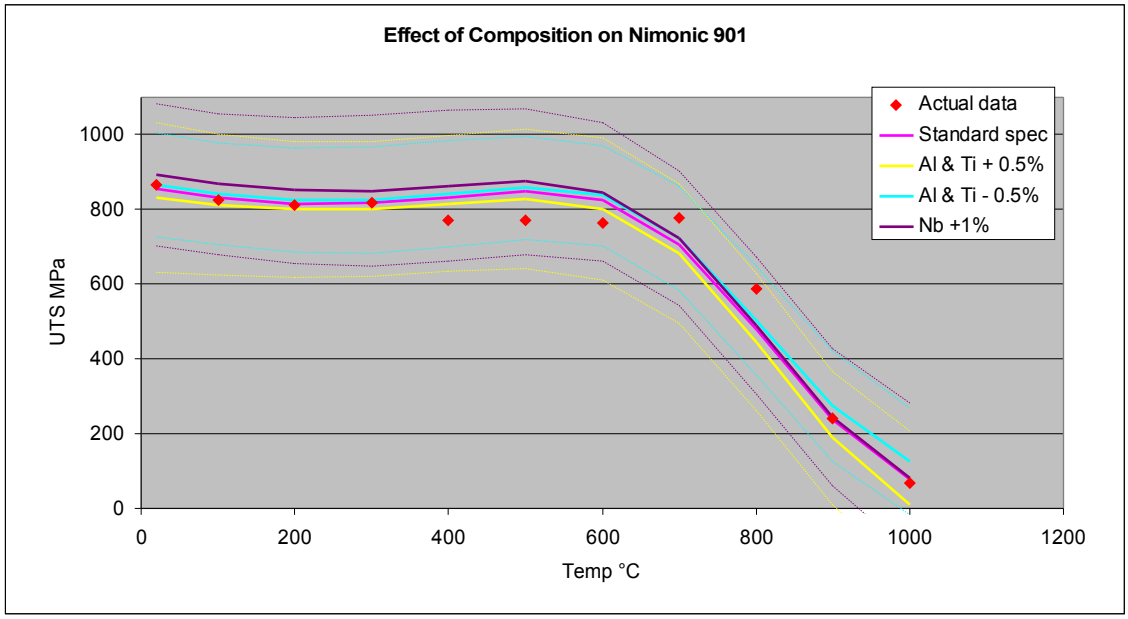

Figure 49 Sensitivity of UTS model to change in composition for Nimonic 901

UTS models trained with database <u>without</u> test alloys (UTS_19_01_05)

- LPE committee comprises of 5 models (Figure 50) Models range between 7 and 12 hidden units.

- TE committee comprises of 4 models (Figure 51) Models range between 7 and 11 hidden units.

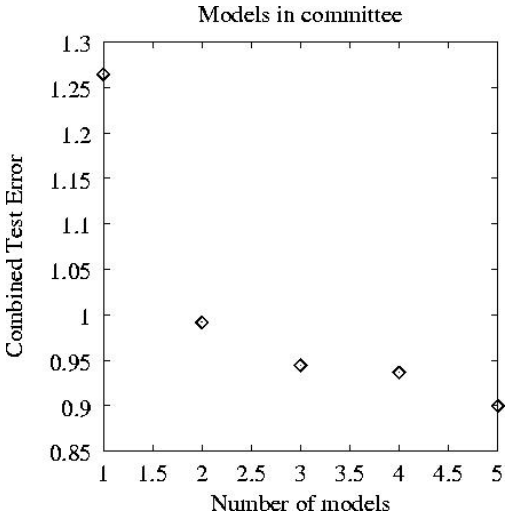

Figure 50 - Committee based on LPE ranking

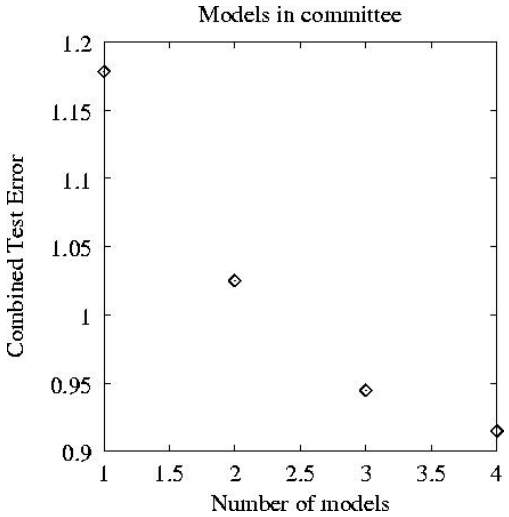

Figure 51 - Committee based on TE ranking

The suggested committees are very different for only a small change in the database, The LPE committee has reduced from 15 to 5 models. Extra models in a committee improve generalisation but the test error for the 5 model committee was lower (9.0) compared with 9.5 for the 15 model committee.

The following predictions are tests against unseen data (red and blue lines) previous predictions (seen data) have also been added to the graph to compare how much worse (if at all) predictions are when test alloy data is not included in the training database.

Predictions for UTS made without Inconel 617 in the database are not as close as those made when Inconel 617 was present. Predictions are better between 800 and 1000°C for all models. The difference between models was negligible in this temperature range although error bounds were tighter for models based upon seen data (Figure 52).

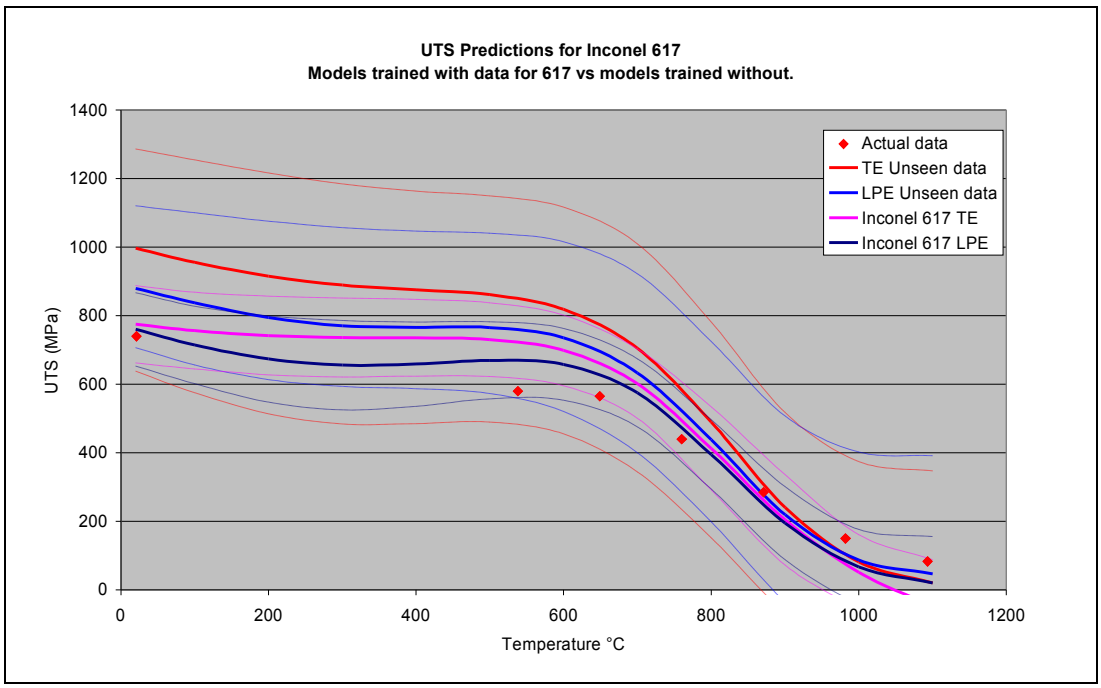

Figure 52 – Predictions for Inconel 617 using models trained with and without the test data set.

All predictions for MERL 76 UTS lie within 50MPa of each other and lie on existing data points for the alloy (Figure 53).

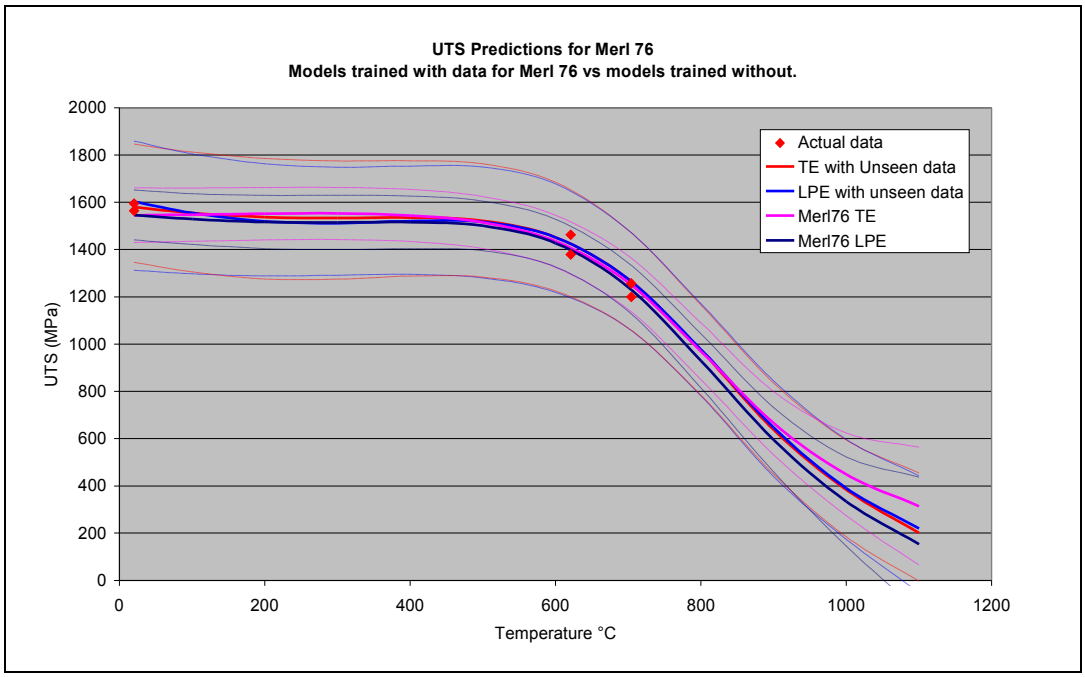

Figure 53 - Predictions for MERL 76 using models trained with and without the test data set

Predictions made for Nimonic 901 with unseen data are ~500MPa of the target values. Only the error bounds for the LPE committee actually include the target data. Original predictions for seen data were very close to actual data in the database (Figure 54).

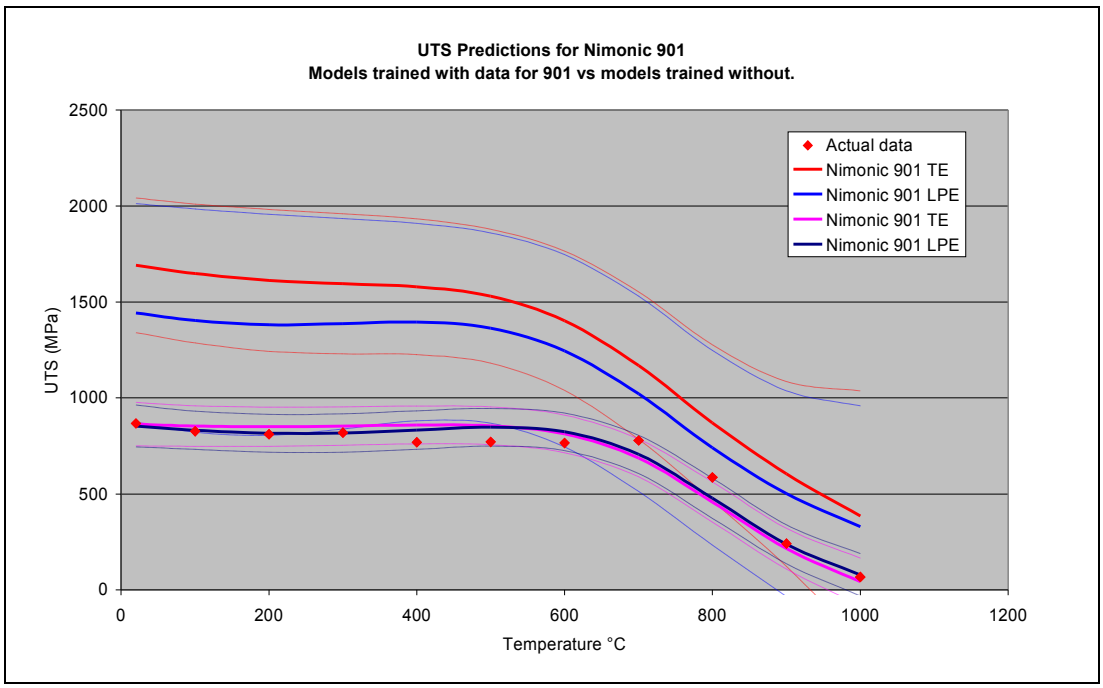

Figure 54- Predictions for Nimonic 901 using models trained with and without the test data set

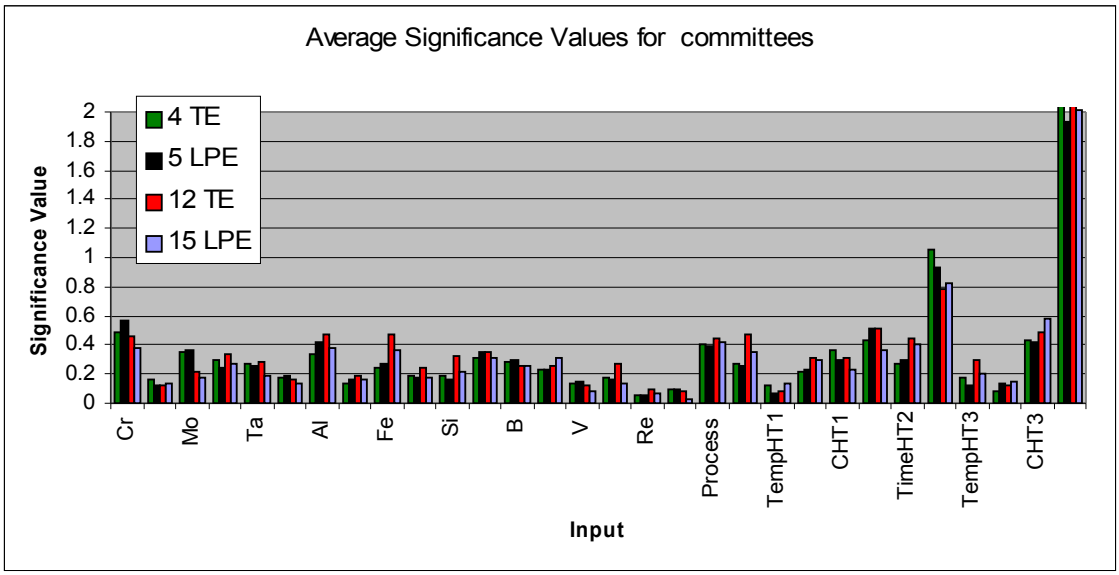

Figure 55 – Significance values for UTS model committees.

Significance analysis shows little difference between committees comprising of a small or large number of models (Figure 55). The significance of Fe is noticeably higher when the test alloys are present. This may be due to the inclusion of Nimonic 901 (35% Fe).

<u>Comparison of new UTS models with UTS models trained with old test data</u>

Comparisons have been made between UTS_17_01_05 (current models based on full database) and UTS_01_11_04 (Old models – including Ni and some minor data errors). Predictions have been made using old test alloys which were not in the old database but

are included in the new database therefore new models should give results comparable to, if not better than previous results.

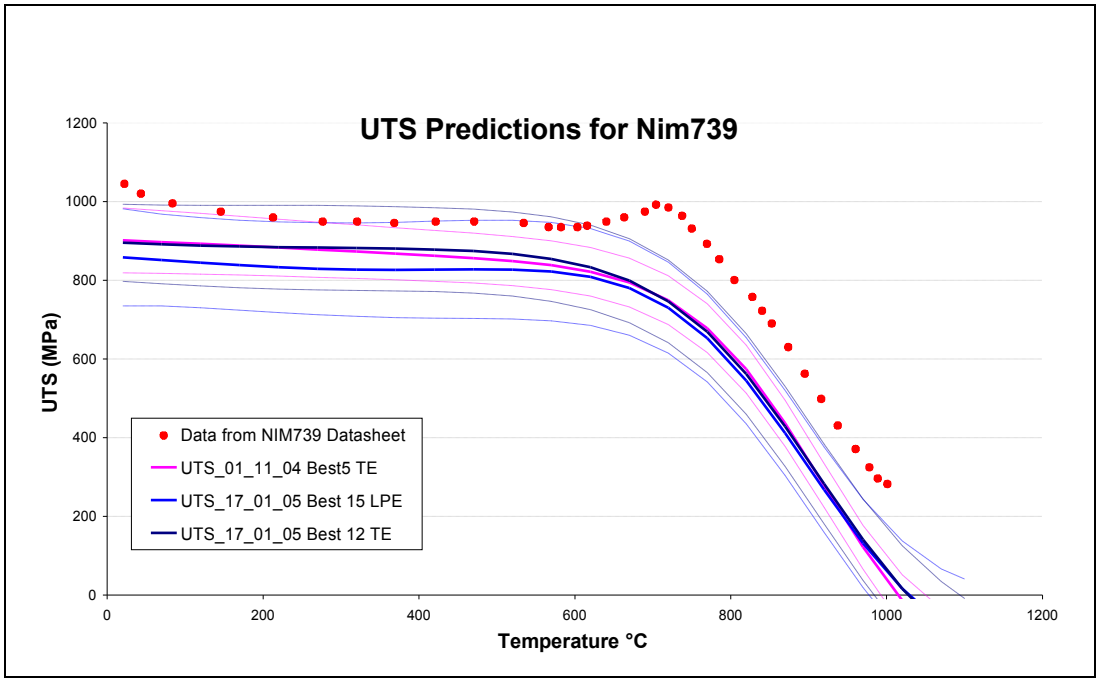

Figure 56 – UTS predictions for Nimonic 739 (comparison of old and new models

Predictions for Nimonic 739 remain relatively unchanged to previous models (Figure 56). Error bounds are wider for the new models at low test temperatures despite the inclusion of the test alloy in the database.

Results for test alloy M313 show the new models to give less accurate predictions but with tighter error bounds (Figure 57). The LPE committee gave best results for both old and new models.

Results for test alloy M21 show the new models to give slightly less accurate predictions but with tighter error bounds (Figure 58). The LPE committee gave best results for both old and new models.

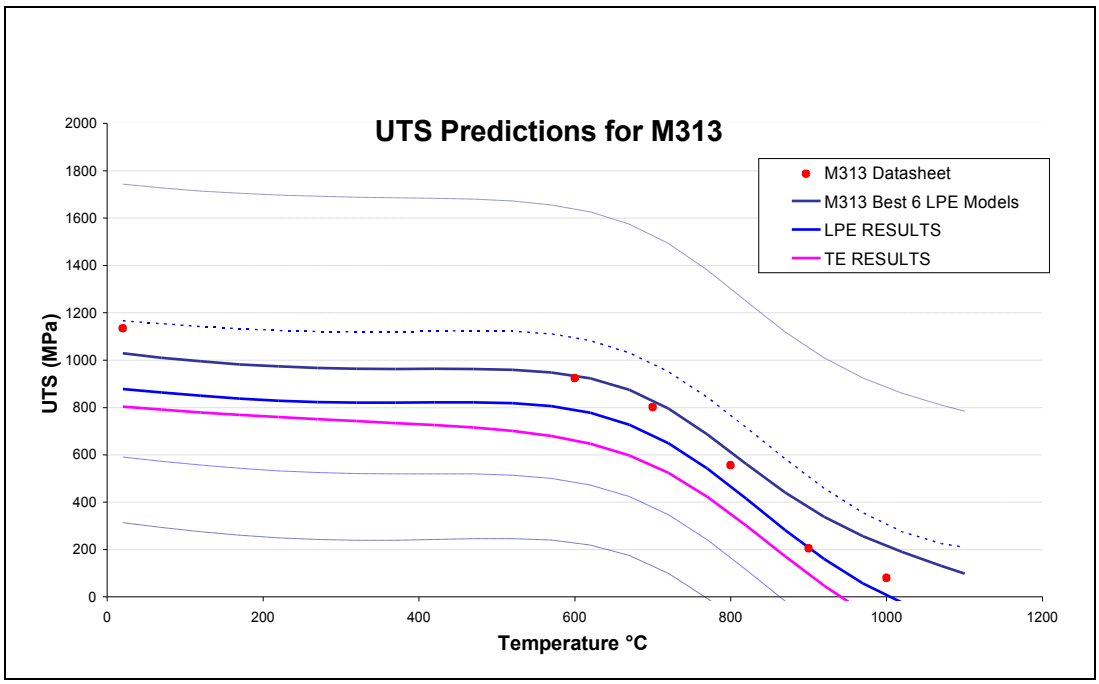

Figure 57– UTS predictions for M313 (comparison of old and new models

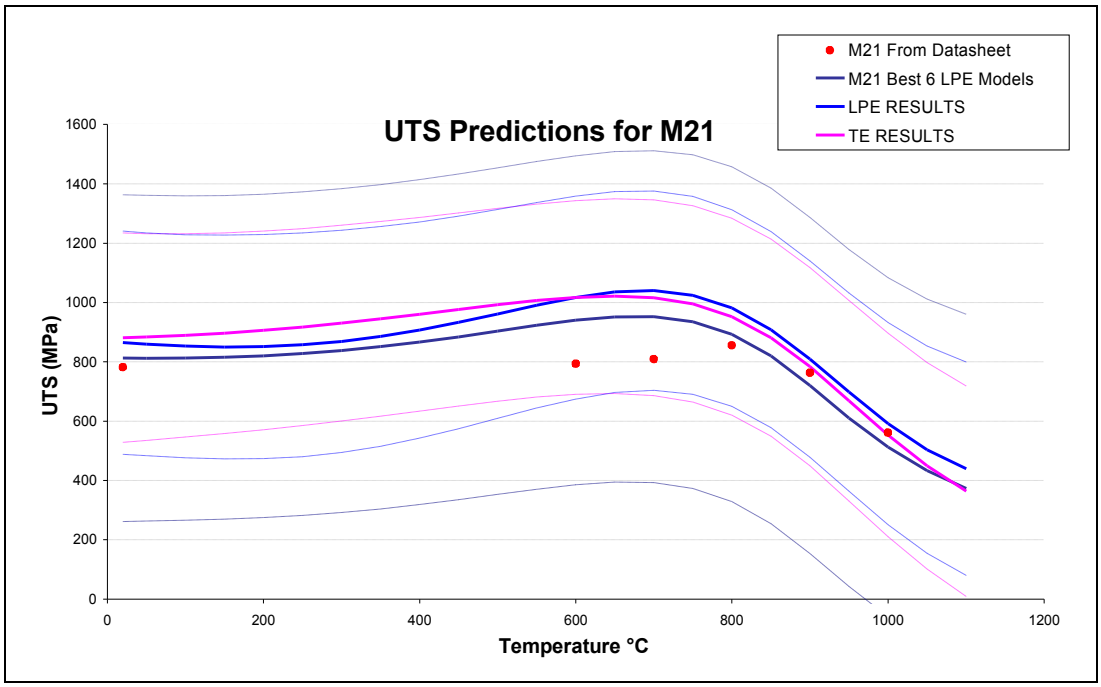

Figure 58– UTS predictions for M21 (comparison of old and new models

5.10.1 Discussion

New models perform well against all 3 test alloys (In617, Nim901, MERL 76) when test alloy data is included in the training dataset. With the test alloy data removed from the dataset predictions were as follows:

- MERL 76 remained unchanged (Figure 53)
- Inconel 617 - less accurate predictions in 0-800°C temperature range (Figure 52)
- Nimonic 901 – predictions out by 100-500MPa with the smaller errors at higher temperatures (Figure 54)
- In all cases error bounds were wider when predicting for unseen data

Input significance values have improved over previous models they conform much more closely with metallurgical theory of which additions improve alloy strength. Significances for compositional inputs no longer show Boron content to be most significant. On average, the most significant inputs (in order) are:

Cr	Al	Fe	C	W	Mo	B

Where Cr provides oxidation resistance and solid solution strengthening and Al is a γ' former. Fe has two functions, in most alloys it is an impurity and therefore has no effect but it is present in the Inconel alloys as a γ'' former and therefore directly linked to UTS.

The cooling rate of the second ageing treatment is still found to be a significant input to the model and it has been found in the literature to have a pronounced effect on strength due to its effect on the formation of the finest γ' 220. Some additional points of note were:

- The effect of changing ageing temperature and Al and Ti additions appears to have the opposite effect to that expected (in most cases the effect is only small)
- Addition of Nb increases UTS.
- Ageing 617 increases UTS

The processes of removing outlying data poses the question as to whether scatter is useful to the modelling process or not. Reducing alloy data to a smooth data curve such as Figure 37 could improve the 'accuracy' of the predictions. Keeping the extra data in

gives the model information on scatter and will affect the generation of scatter bands within Neuromat.

The information within the model database is a mixture of data from papers; where data scatter will occur between repeat tests by the same author or between different authors, and data from alloy specification sheets where one curve is normally given. It could be assumed that the manufacturers curve will often represent the optimum strength of the alloy.

The anticipated use of the neural network models is to investigate new alloy combinations based upon extrapolation from existing test data. With this in mind, the scatter band should represent uncertainty in the model due to lack of information in the training dataset for certain alloying combinations.

5.10.2 Conclusions

Removing a small amount of erroneous data has had a positive effect on the models. There is generally a smaller difference between predictions by LPE ranked and TE ranked models. This is likely to be due to the different ways in which LPE and TE rankings treat outlying data.

Some models appear to be insensitive to changes in ageing treatment and composition. Changes in UTS values are generally small for a given composition or heat treatment variation and in a lot of cases values move in the opposite direction to that which is expected.

The significance value for the input Fe is artificially high when Nimonic 901 is present. Removing Nimonic 901 (35% Fe by weight) is detrimental to subsequent predictions for that alloy (Figure 54). This suggests that the model is trying to fit very small variations in composition to the large scatter in the data. In reality, a major cause of this scatter can be put down to the testing conditions or small variations in the material that are not captured in the chemical composition e.g. levels of porosity. For any given composition and heat treatment UTS values can vary depending on the processing route and desired application.

There is a large spread of data points containing Fe in the database – 140 data points for IN718 variants alone (Figure 59). With this amount of information the model should be able to predict relatively well for Nimonic 901 whether the small amount of 901 data is present or not.

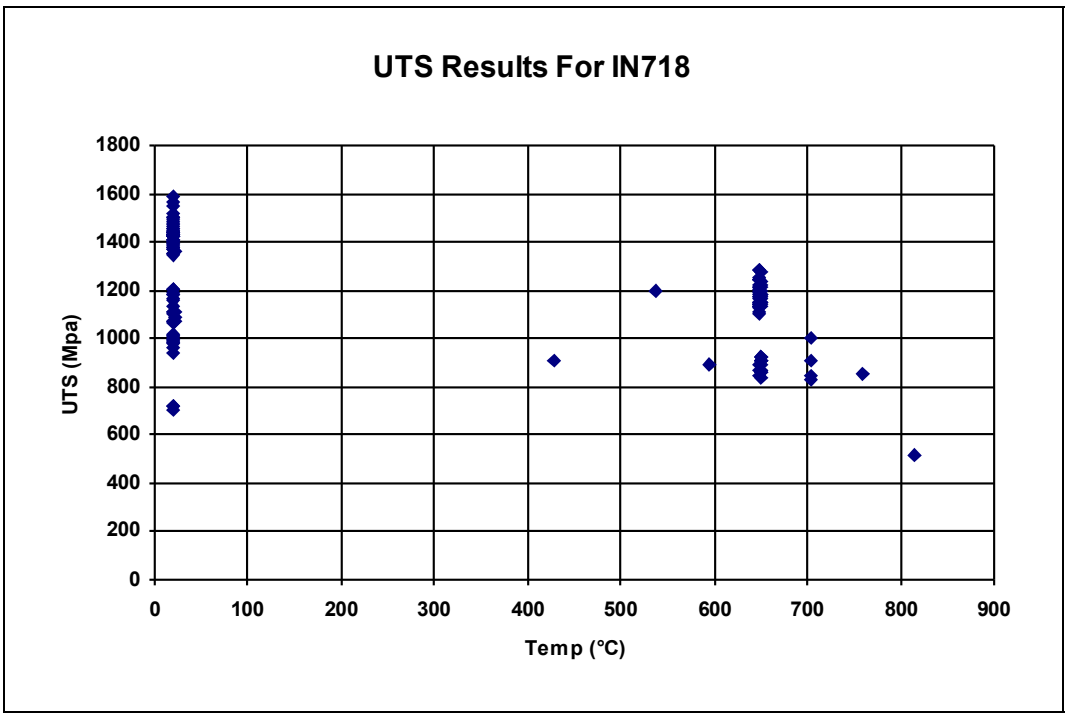

Figure 59 – Spread of data in UTS database for IN718

It has been proposed that alloys with a large data spread such as In 718 (Figure 59) should be re-examined. Where alloys are all within nominal composition and heat treatment, results spread will reduce through averaging values and a standard composition will be adopted. For alloys such as In718 where there are several variants such as cast and wrought, these distinctions will remain.

Data from tests where the composition or heat treatment has been varied will be checked on a case by case basis. Baseline data from these tests can be compared with expected values to assess whether the UTS, YS etc. at the starting point was consistent with other known data before any compositional changes have been made.

More data is required for most alloys in the 100 – 500°C temperature range. If this is achieved by extrapolating from existing data for each alloy it is thought that this should help the model make predictions in this temperature range.

5.11 YS database

Using the work with the UTS dataset as a guideline the following approach was used for analysis and subsequent training using the YS data set:

- Cleaning' of the database was performed – Some data was removed where there was a very large spread
- A standard composition was adopted for each alloy. Only tests that were specifically investigating effect of compositional changes were allowed to remain unchanged.
- Statistical analysis was used to check input data spread and start looking at candidates for removal from the input dataset.

5.12 Statistical analysis of YS input database.

Minitab software was used to generate information about every input variable to check for spread of data and incorrect data entries (Figure 60). The graphs also proved useful in explaining some trends within the network later on. Graphs of YS vs. temperature were also plotted for each alloy as described previously in order to identify outliers and areas of large scatter.

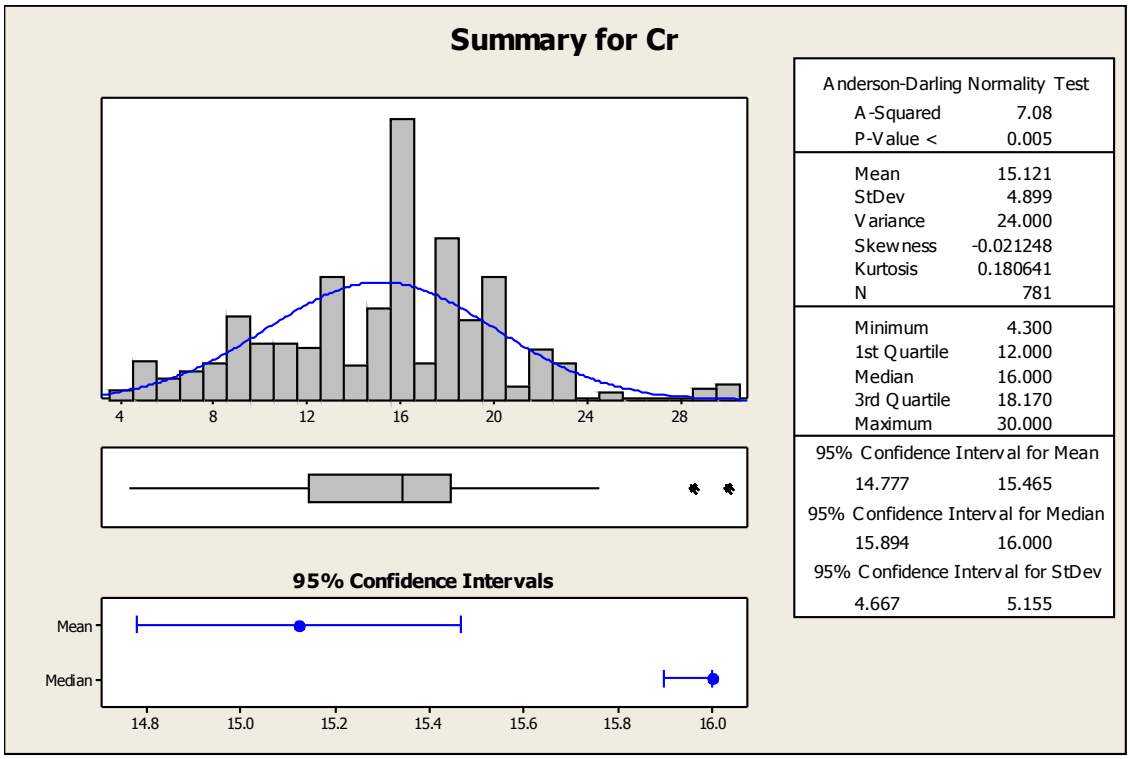

Figure 60 – Input data spread for Cr in the YS database

Distribution of data for coded inputs; process, crystallography and cooling rates is presented in Table 2. Input CHT2 contains very little data for cooling rates type 2,3 and 4 and is a possible candidate for removal.

	Process		X		CHT1	CHT2
Cast	36.5%	**PX**	89.8%	**Air**	84.5%	96.8%
Wrought	42.1%	**DS**	3.6%	**Furnace**	0.5%	2.2%
PM	21.4%	**SX**	6.6%	**Oil**	9.8%	1.0%
	-		-	**Water**	5.2%	0.0%

Table 2

The input space for each variable vs. test temperature is presented in Figure 61. Cr and Co (top left) exhibit a good spread with respect to test temperature and no sign of correlation. Cooling rate 3 shows no variation at all. The bottom right graph is test temperature and therefore shows 100% correlation.

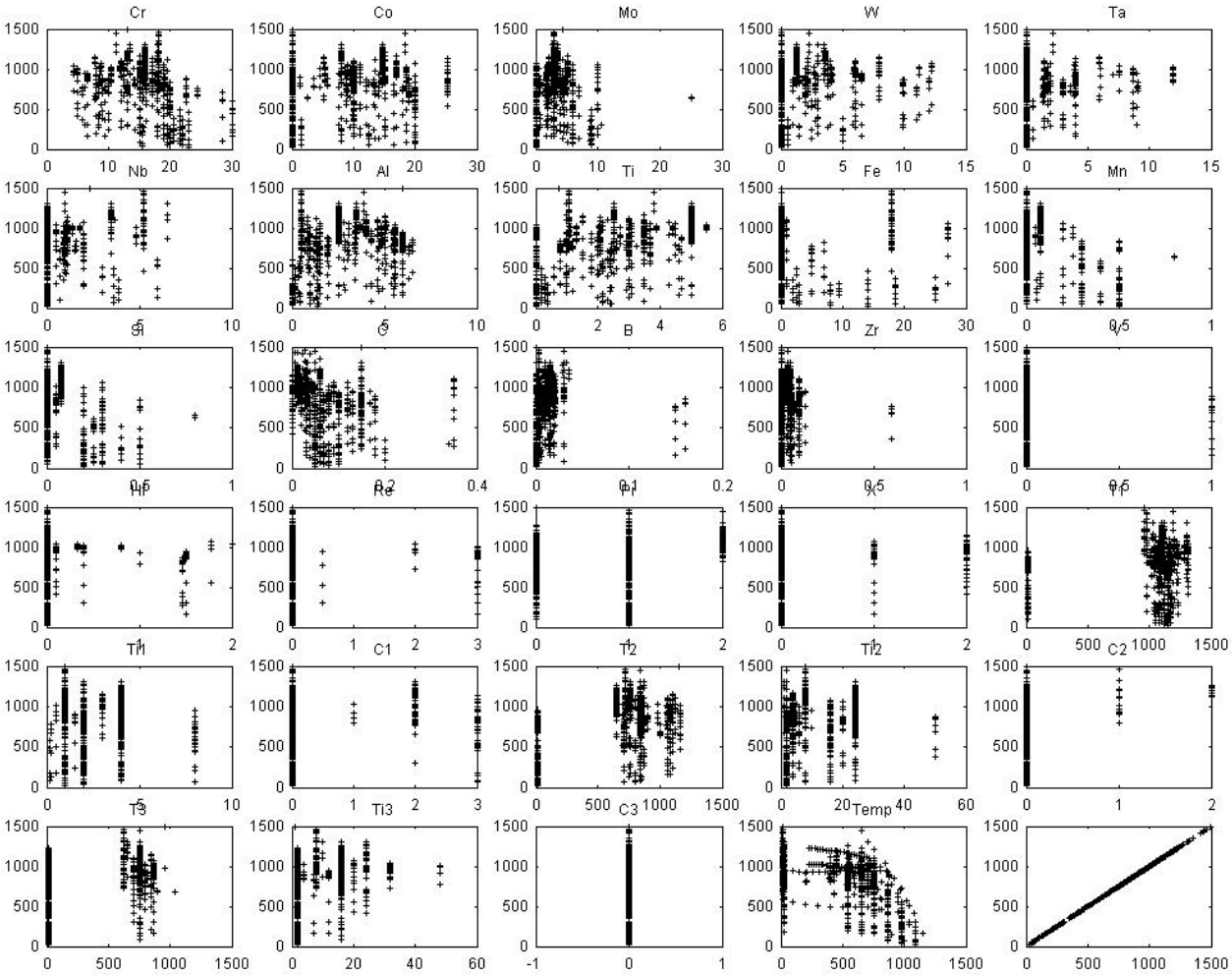

Figure 61 – YS database. All inputs with respect to test temperature

5.13 Results from models trained on 'clean' YS dataset

YS_26_04_05

The original model trained on the clean YS database was presented with all data (786 lines, 28 inputs, 1 output) in the order found in the dataset. The input column for La was removed as part of the dataset cleaning process. The model always performs well against seen data (Figure 62 & Figure 63) and generally performed well against unseen data (Figure 64). The model struggles to predict well against unseen Nimonic 901 (Figure 65).

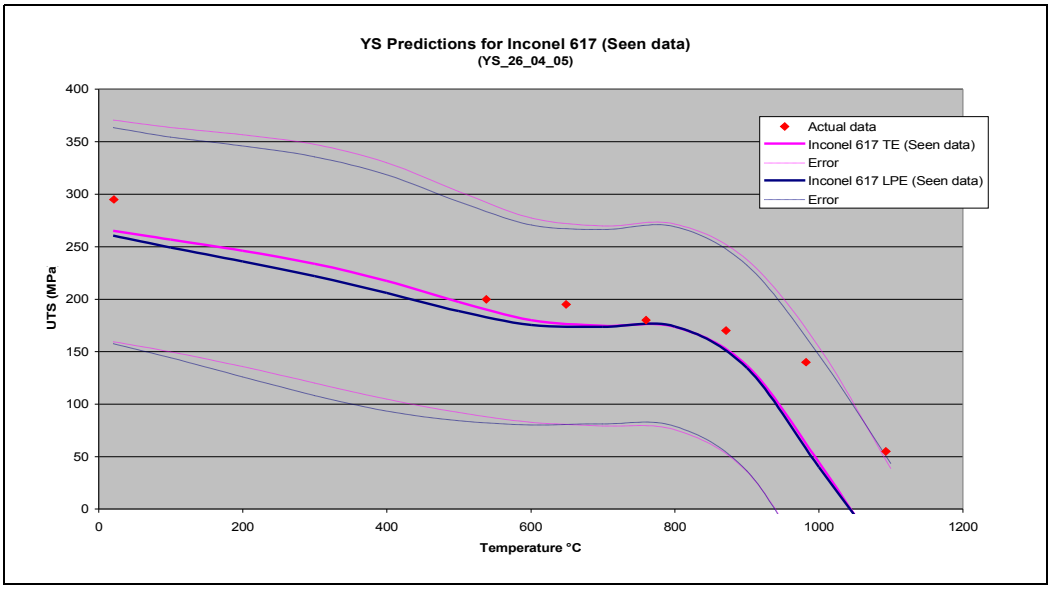

Figure 62 – YS prediction for Inconel 617 (seen data)

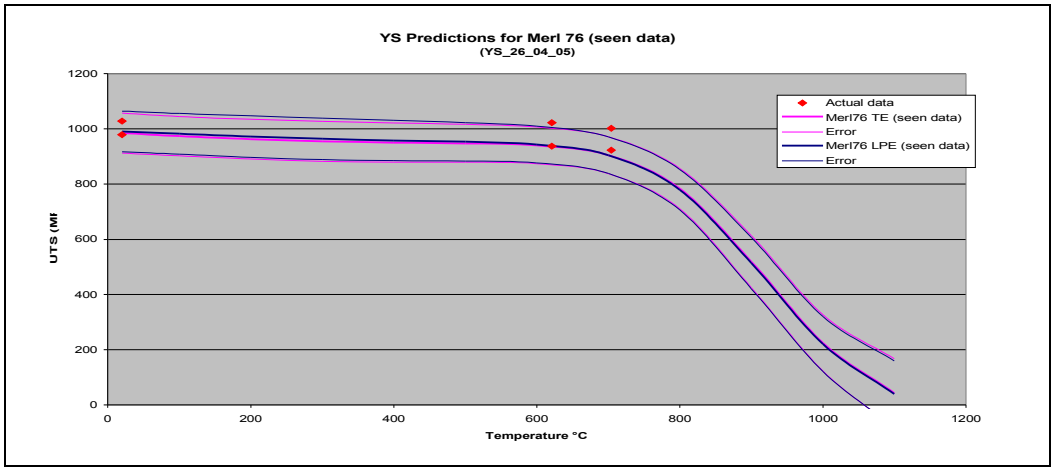

Figure 63 YS prediction for MERL 76 (seen data)

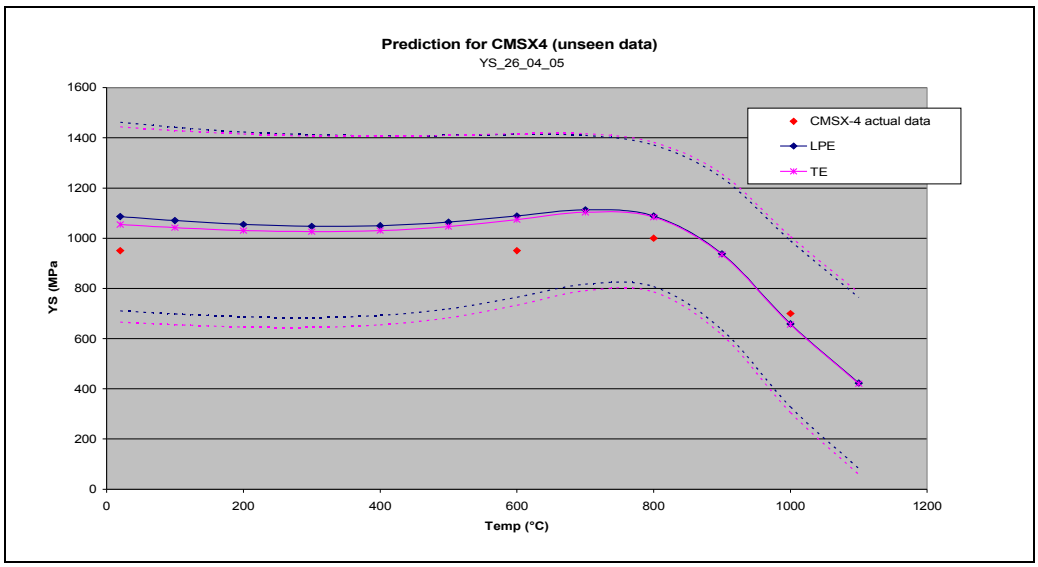

Figure 64 YS prediction for CMSX-4 (unseen data)

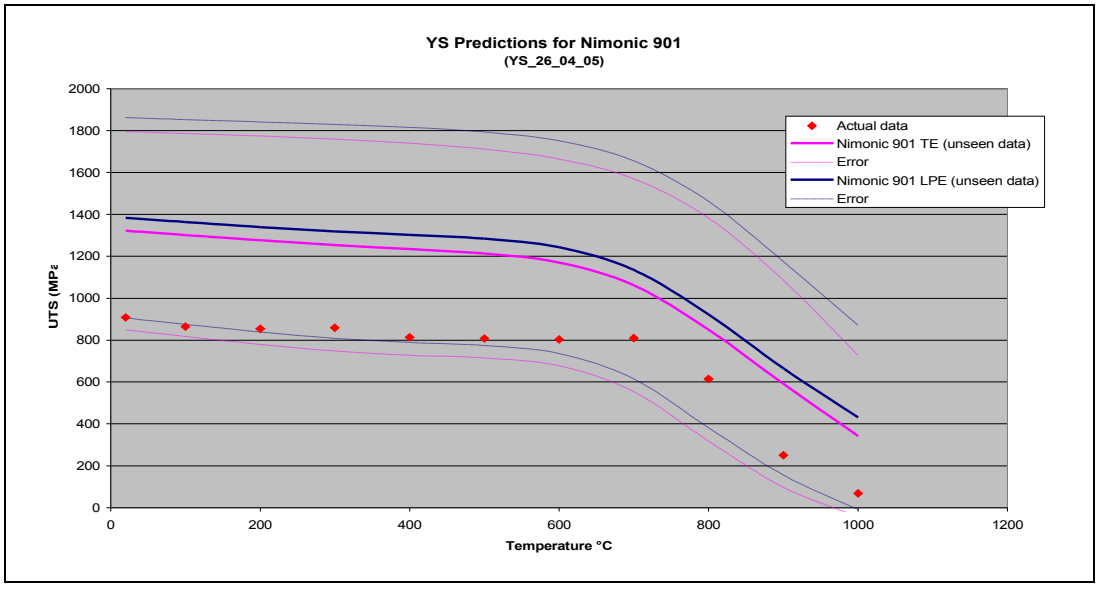

Figure 65 YS prediction for Nimonic 901 (seen data)

Significance analysis for both committees shows good agreement with metallurgical understanding (Figure 66). The model has assigned the largest significance to test temperature, with the solution heat treatment temperature and γ' formers Al and Ti also being assigned relatively high significance values.

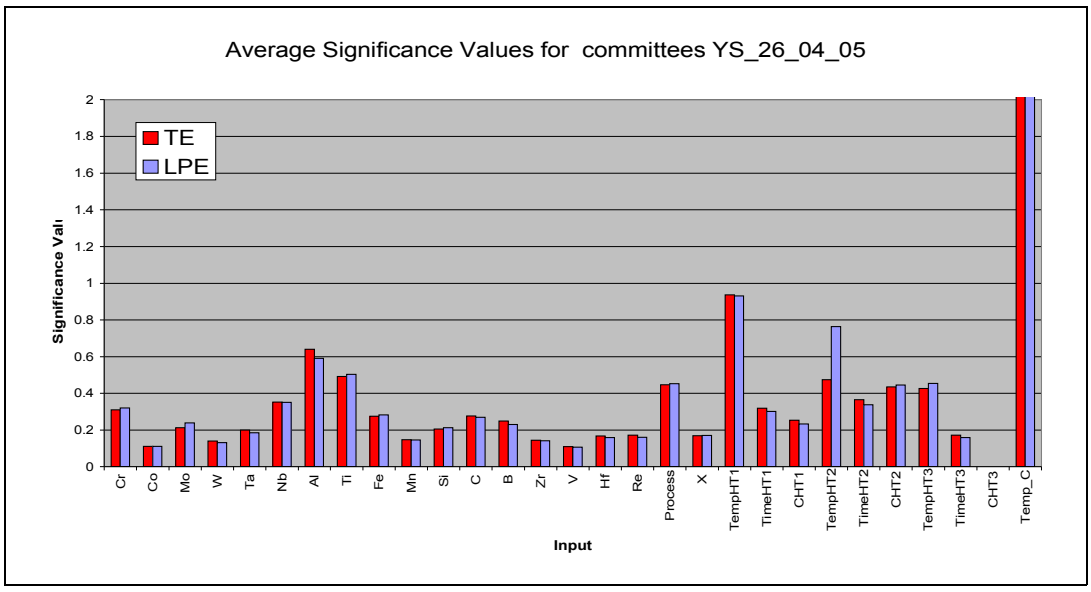

Figure 66 – significance of inputs for YS model

Sensitivity analysis using CMSX-4 (Figure 67) and MERL 76 (Figure 68) as test alloys shows that the model results move in the correct direction with variation of inputs such as process, some alloying inputs and variations on heat treatment. In practical terms, these changes are not actually possible to the extent used in the example but do give a good indication that the model behaves in the correct way. For example, a large increase in aluminium gave a large increase in strength in CMSX-4 (aluminium is present as a γ' former). A polycrystalline version of CMSX-4 is predicted to have increased strength (which in not inconceivable) polycrystalline disk alloys are some of the strongest. Water quenching gives the biggest reduction in strength – rapid cooling allows less time for formation of γ'. MERL 76 shows a reduction in strength without the artificial ageing process. Changes in the ageing temperature have virtually no effect although this is probably too subtle an effect for the model to pick out.

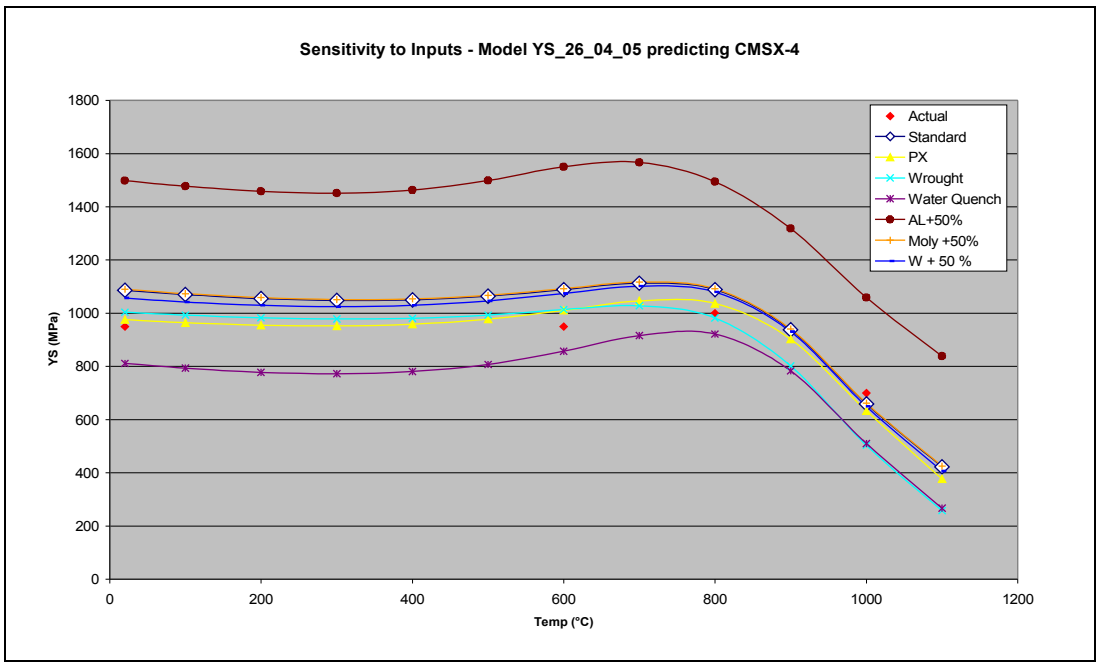

Figure 67 – Sensitivity to inputs YS model – CMSX-4 example

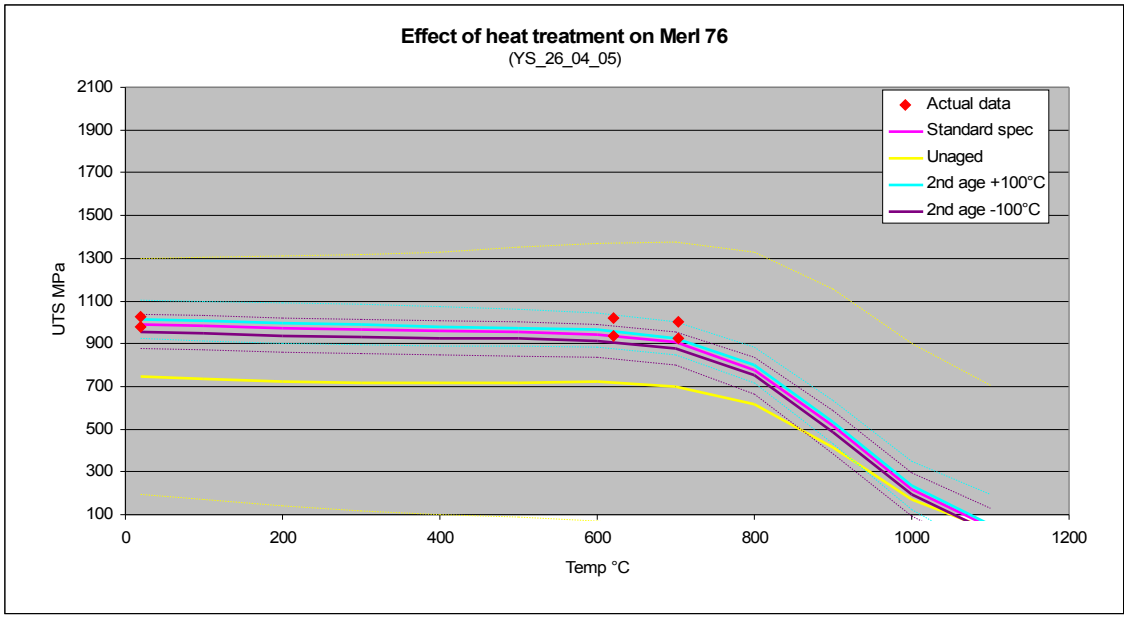

Figure 68 - Sensitivity to inputs YS model – MERL 76 example

YS_02_05_05

This model has been trained using the same YS database but this time data has been split into 90% training data and 10% test data to investigate new functionality made available in the Neuromat software. Test errors were similar to those achieved with the 50/50 data split. The sensitivity example using CMSX-4 also shows very similar results between models.

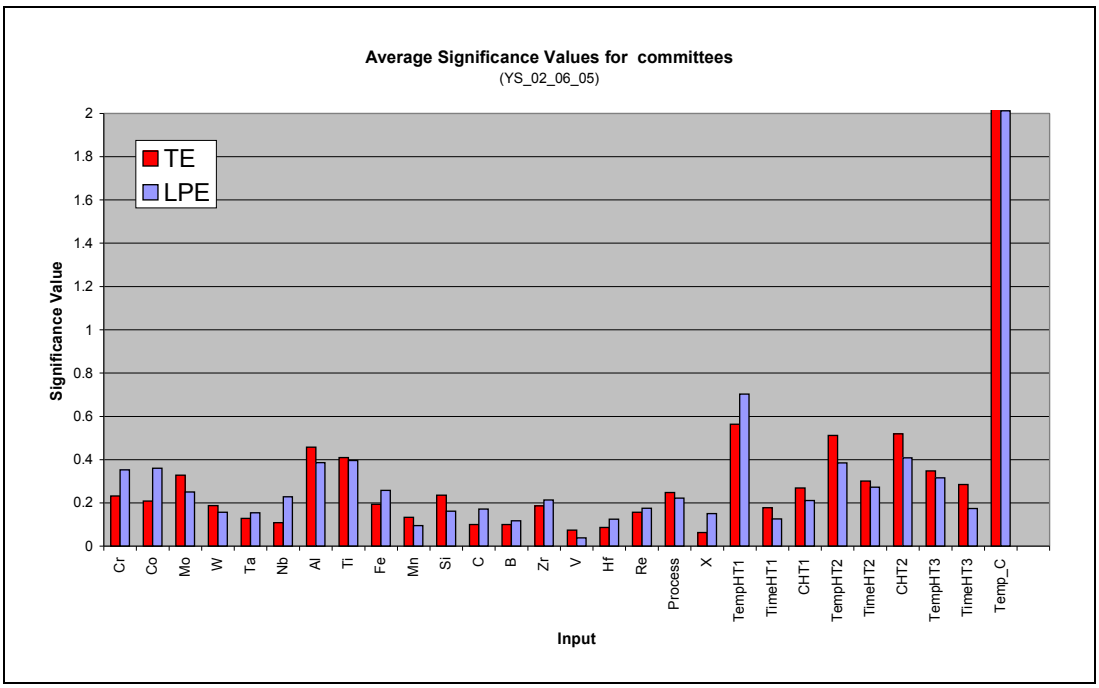

Figure 69 Significance of YS input values after training with 90/10 split

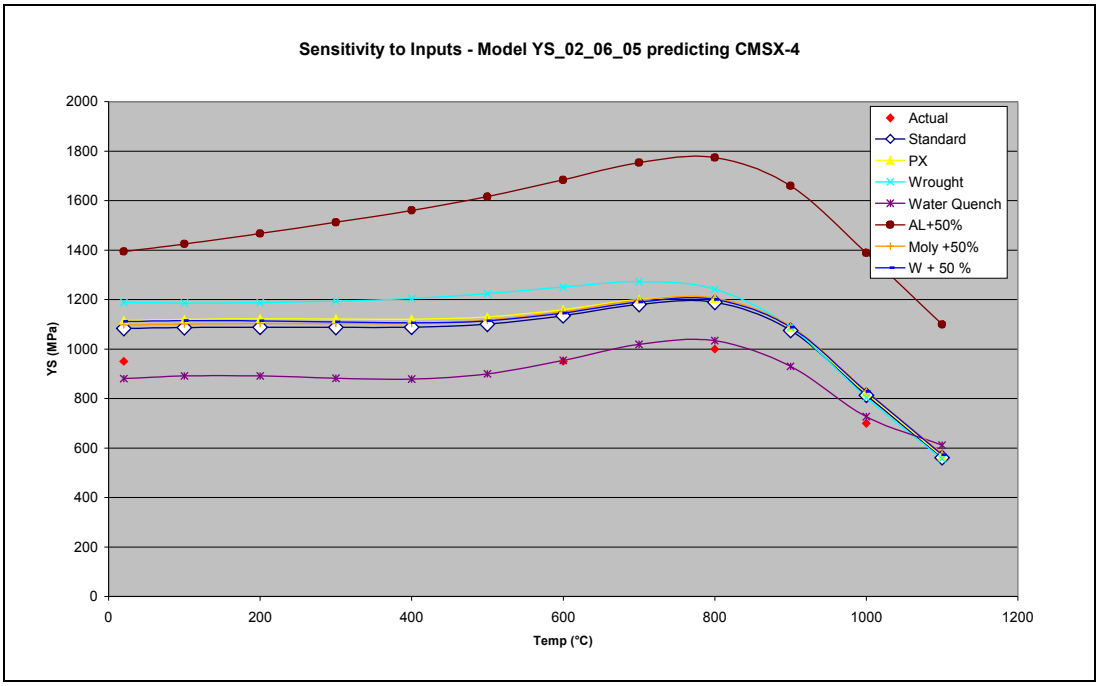

Figure 70 Sensitivity to inputs YS (90/10 split) model – CMSX-4 example

5.13.1 Supporting Work with Matlab Neural Network Models

All work conducted so far using Neuromat has used committees of models. The effect of the seed point (where the model starts off) has not been looked at in detail either. Matlab neural network models have been used to investigate the effect the seeding of the neural network models on the fit achieved.

Using seen data as examples, there is a large difference between the fit achieved between different alloys. Using M313 M21 and M22 as examples, the effect of seeding has a different effect on each alloy. All three alloys have roughly the same number of data points in the database. All predictions for M22 are very close to actual data for all 10 networks (Figure 71). M313 alloy predictions show more variation depending on the networks seed point (Figure 72) whereas M21 shows a huge range in predictions depending on what value was used to seed the network (Figure 73).

This suggests that the data fit for M21 has more local minima/maxima that will cause the network to converge on an incorrect 'answer'. This could indicate that M21 will be more difficult to predict and should be represented in the test portion of the dataset

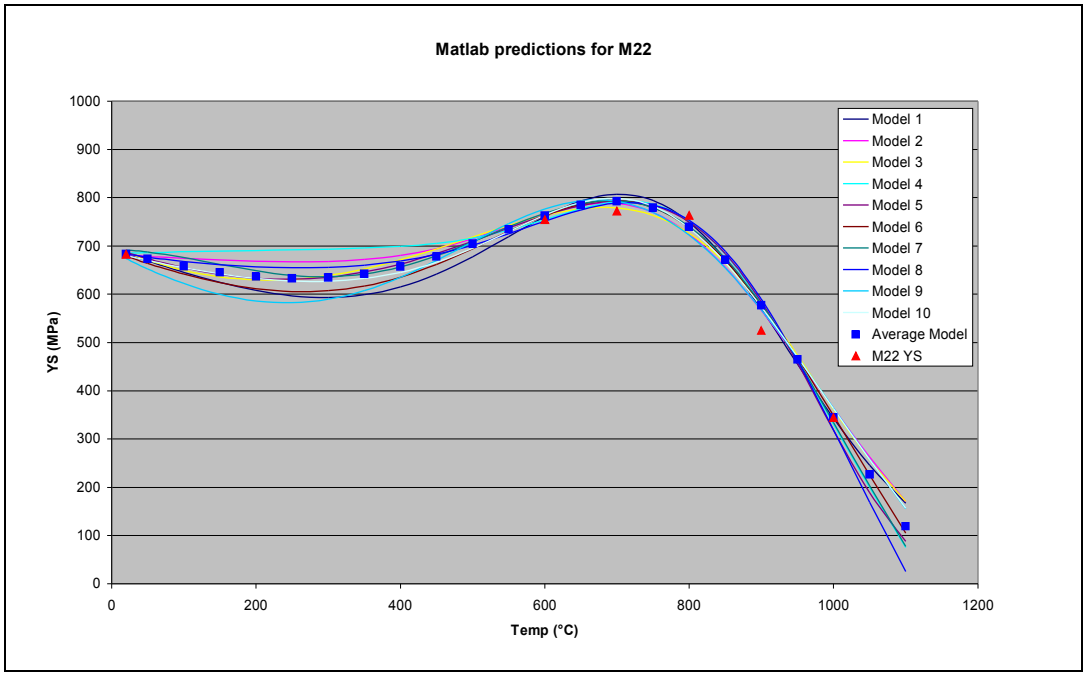

Figure 71 –YS predictions for M313 with 10 networks all using different seed points in Matlab.

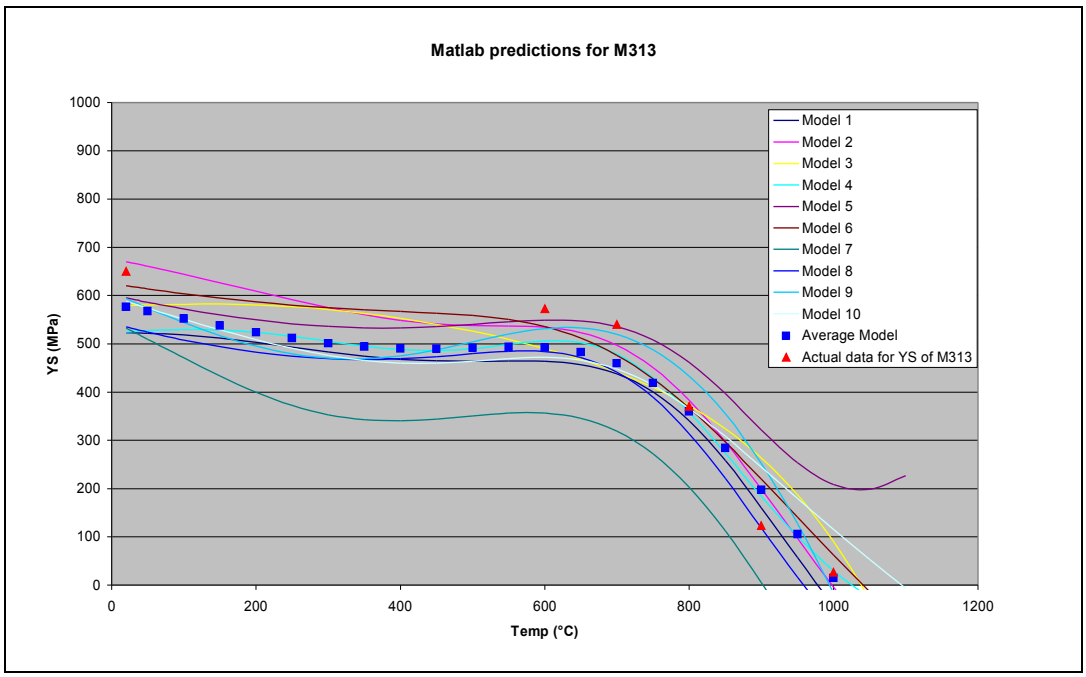

Figure 72–YS predictions for M22 with 10 networks all using different seed points in Matlab.

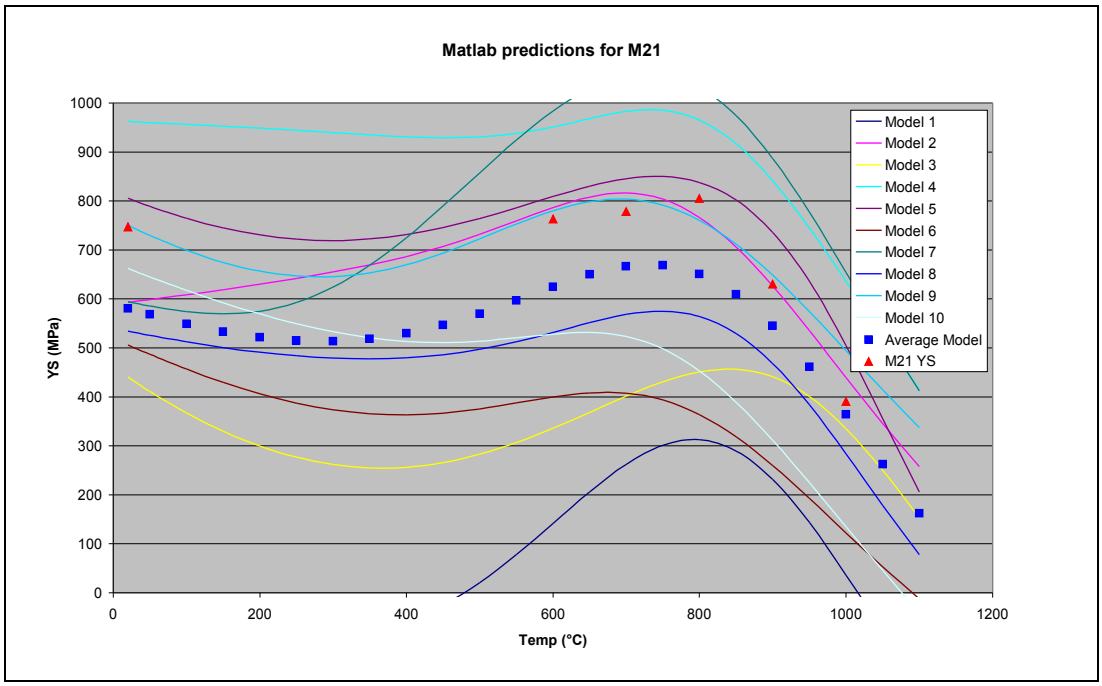

Figure 73 - YS predictions for M21 with 10 networks all using different seed points in Matlab.

The ability of a single model with a given number of hidden units to fit the test data has been analysed **(Figure 74).** The range of HU's in the Neuromat committees was between 6 and 11 for the YS models. The Matlab models began to fit the data with 5 hidden units with 10 and 15 hidden units giving similar performance. Therefore showing good correlation with the models selected by Neuromat.

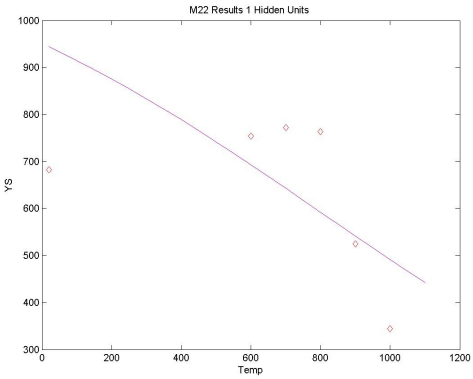

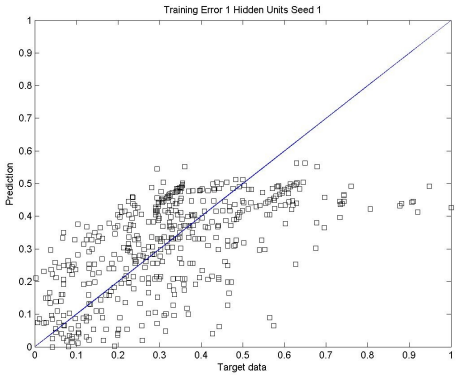

1 hidden unit

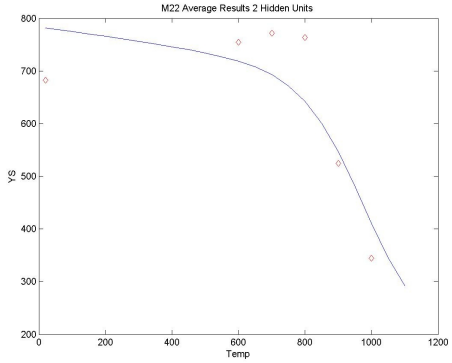

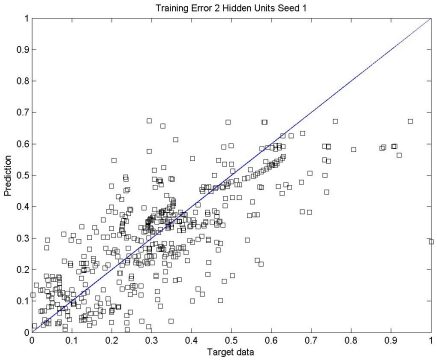

2 hidden units

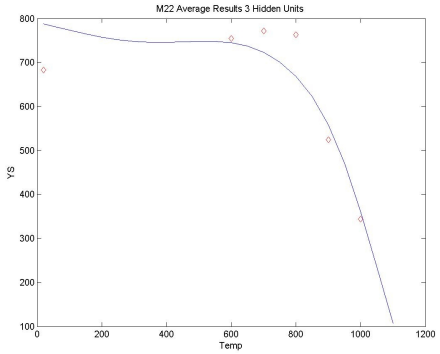

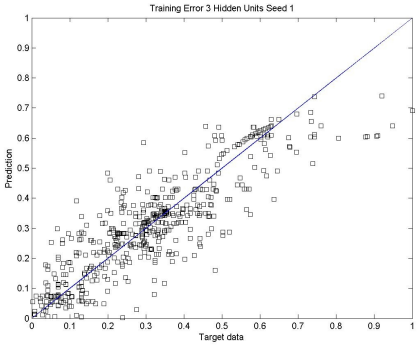

3 hidden units

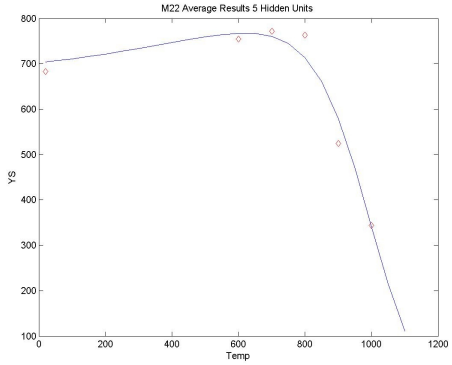

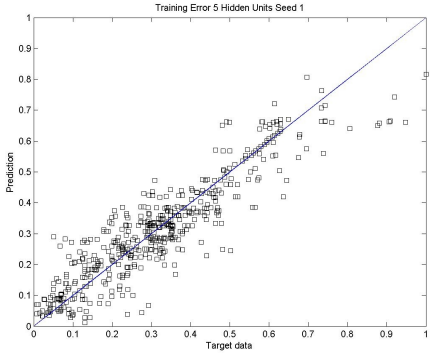

5 hidden units

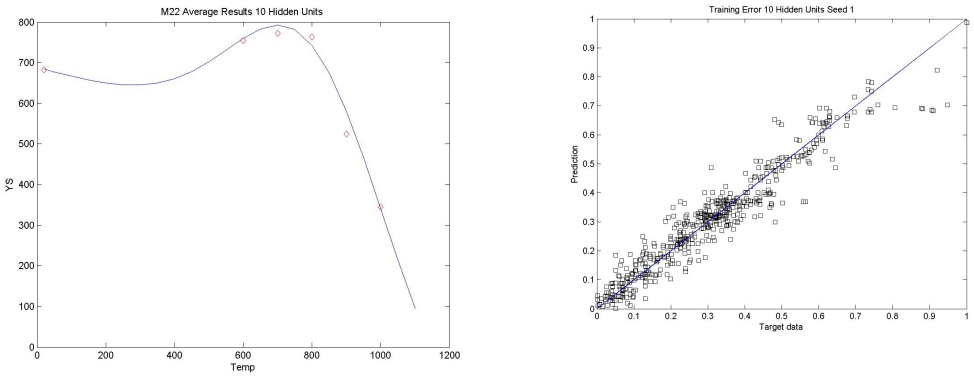

10 hidden units

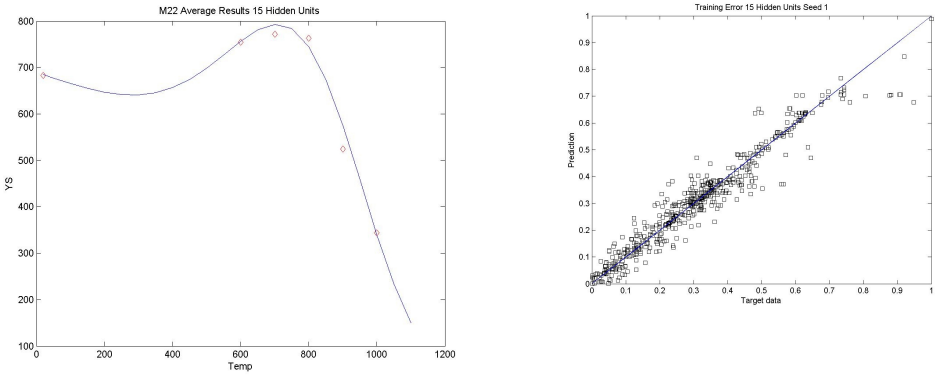

15 hidden units

Figure 74 – Effect of number of hidden units on model data fit (YS dataset) M22 alloy used as example.

5.14 Discussion

It has been shown that, with the current dataset, models can be trained to fit the training data with minimal test error. All the YS models trained since the database cleaning exercise have predicted very well against seen data.

The best model to date is YS_26_04_05. The model gave good predictions in conjunction with sensitivity and significance analysis results that tied in with metallurgical understanding.

The model trained using a 90/10 data split performed as well as models trained using 50/50 data split. Experimentally there was no evident benefit to use either of these methods in preference. In theory a 90/10 split will provide the model with more training data thus increasing the certainty of predictions. This assumes that the 10% data used for testing is representative of the whole dataset and not artificially skewed.

There is insufficient data in input column CHT2. 97% of data is set to (1) – furnace cool. The effect of this input is, on average, quite high this is unlikely to be a real effect. With such a small amount of data spread, the model is susceptible to coincidental linking of variables. For example if the 3% of data where CHT2 is not 'furnace cool' coincided with just one or two alloys of high strength, the model would assign an artificially high significance.

It is probable that some models will predict seen data well, have sensible significance values but perform poorly on unseen data or predict incorrect trends in the sensitivity analysis. This could be brought about by an input having a large effect in the 'wrong' direction. Significance analysis does not tell us if inputs have a large positive or a large negative effect on YS just the magnitude of that effect.

5.15 Conclusion

Cleaning of the data is important. It is possible to 'add value' to the database by using knowledge of the alloy properties to select 'good' data from 'bad' data or interpolate between values where it is know that the curve is flat.

Inputs that are very highly skewed i.e. 95% or more at one value can adversely affect the learning process. The neural network model benefited from the removal of such inputs such as CHT3 (cooling rate 3). The best model we can hope to come up with should:

- Give good predictions against all seen data.
- Be the closest match to an idealised significance profile.
- Sensitivity analysis should show the correct trends i.e. predictions move in the correct direction with response to changes in composition/hear treatment.

In order to do this a set of rules based on metallurgical understanding should be established. How should the model respond to:

- Compositional changes
- Changes in heat treatment
- Processing types

An idealised significance profile should be formulated to compare the model significance analysis with. This could be in the form of rating ideal significances in tiers:

- **Tier 1 – most important**
  - Test Temperature
  - Heat Treatment 1
  - Al
  - Cr
  -
- **Tier 2 –**
  - Re
  - Fe*

*Iron is a good example of an input to which the response is critical for some alloys (the Inconel alloys) but not important for others. Selecting tier two inputs is therefore not a trivial task and will need to be evaluated on an alloy by alloy basis.

5.16 Low Cycle Fatigue Model

5.16.1 Introduction

The main aim of the QinetiQ neural network program was to work towards developing a neural network model for fatigue life prediction to be used in the alloy development process. Low Cycle Fatigue (LCF) is of primary interest. The previous work using YS and UTS databases has proved invaluable in developing a methodology to apply to the LCF

LCF is a more complicated process to model due to the large number of test variables and model inputs. Fatigue performance data is also subjected to much larger scatter bands than tensile performance tests. Scatter within a tensile test to derive the UTS value for a material may be 20% where as scatter of up to 50% is not uncommon in fatigue testing. Life to crack initiation is hard to predict and model, and can be an appreciable proportion of the total fatigue life.

Fatigue data for materials is less readily published by the alloy manufacturers. The data collection process has relied heavily on reported data in academic papers and data from QinetiQ internal test programs.

Using recommendations drawn form UTS and YS neural network models as a guideline the following approach was used for analysis and subsequent training using the LCF dataset:

- The large amount of scatter present in LCF data meant the data 'cleaning' step developed for UTS and YS models was not used.
- A standard composition was adopted for each alloy. Only tests that were specifically investigating effect of compositional changes were allowed to remain unchanged.
- Statistical analysis was used to check input data spread and start looking at candidates for removal from the input dataset – Much more time has been spent on this step due to the large amount of scatter in the data and the relatively small size of the dataset. It was important that any trends/problems during the modelling process could be attributed to either data issues (such as amount, spread, scatter) or the ability of the network to fit the data provided.

- Testing was carried out using seen and unseen alloys to test the predictive abilities of the network based on the training dataset.
- The ratio of number of variables to lines of input data is anticipated to be the biggest problem in achieving an accurate model. Methods to reduce the number of input variables will be investigated.
- A set of requirements to test the network against are required. Fatigue life is not directly linked to strength so the tests for a 'good' model are likely to be different to those specified for YS and UTS models

5.16.2 Selection of inputs and data collection

A literature review was initially conducted to get an indication of the quantity and quality of data available for fatigue testing. It was decided that only data for strain controlled axial tests would be considered initially for the database.

Inputs regarding alloy composition and heat treatment were chosen to be the same as those used in the other databases previously discussed. Additional inputs were required for fatigue life analysis and were incorporated in the database:

- Cycles to failure (Nf)
- Test temperature (°C)
- Total strain range (%)
- Strain rate (e%/s)
- Frequency
- R-Ratio

Strain range, strain rate and frequency data were collected for each input as some papers quote strain rate and others quote frequency. All the data was kept in the database; for example it is easier to present data in the analysis section by frequency if the test was a fixed frequency test and vice versa if the strain rate is kept constant. In practice, only one of the inputs is required as it is purely a function of the other and the total strain range.

Once the required inputs had been defined, a comprehensive search of the literature was undertaken. It was found that only 30% of papers initially identified actually had enough information to add the data to the database. Many papers used dimensionless

graphs, did not quote the strain range or didn't include any information on the test frequency and waveform used. Due to the nature of academic and industrial papers, a lot of tests were looking at more novel aspects of fatigue testing such as testing in different environments or investigating material coatings – most turbine blades are coated in use.

Prior to further sorting and data analysis, the original database comprised of 700 input lines made up from 38 alloy combinations. A graph of all the data is shown in Figure 75.

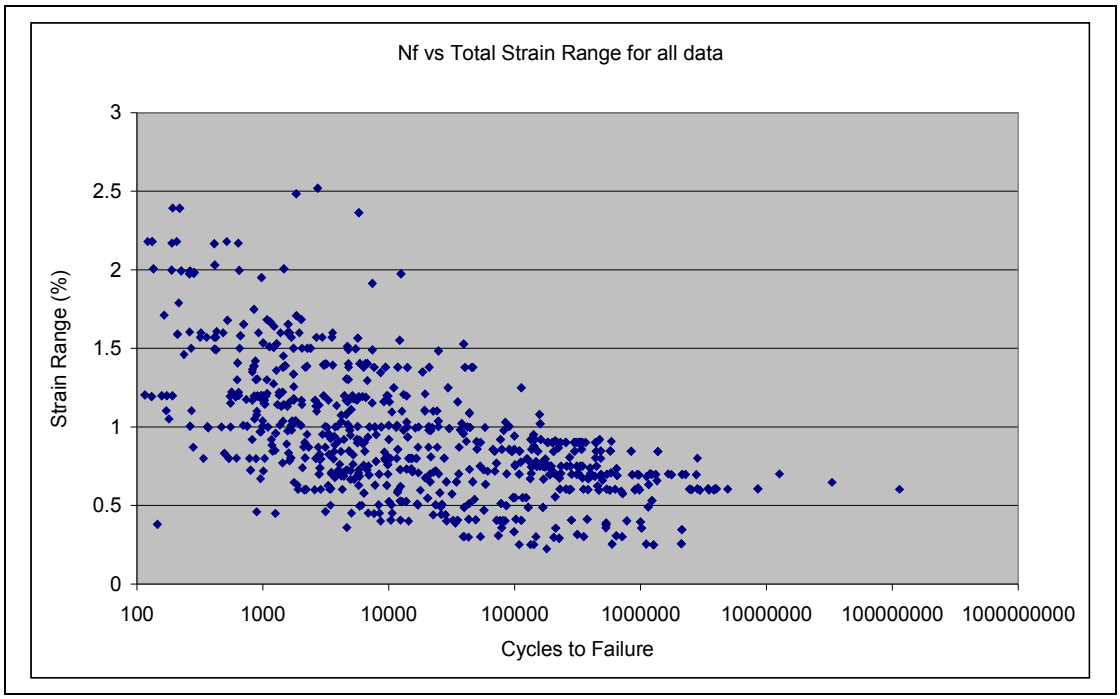

Figure 75 – Total input space (strain range vs. cycles to failure) for LCF database

5.16.3 Analysis of Input Data

Graphs of distribution of input variables and distribution of data by alloy were produced using Minitab. Minitab proved particularly useful for producing graphs of data by alloy as further groupings for temperature, r-ratio and frequency can be included. Minitab is also able to fit a regression line/curve to each group of data. The cubic regression fit has been selected for all graphs. It should be noted that Minitab includes all combinations of variables in the legend even if the particular combination is not present in the raw data.

The alloys Haynes 230 has been used as an example of the data checking process. A graph of strain-life curves has been plotted by temperature and frequency with regression fits to each group (Figure 76). A large amount of scatter is visible in the 427°C range. In this case, the data is further subdivided by reference source (Figure 77

and Figure 78) in order to examine the possible source of the scatter. In this case it can be seen that the 427°C data at 0.33Hz is made up of 2 separate strain life curves from 2 different sources. In this particular case, the data from the Haynes datasheet at 427°C was removed from the database. The gap between this data source and the rest from the same alloy is particularly large.

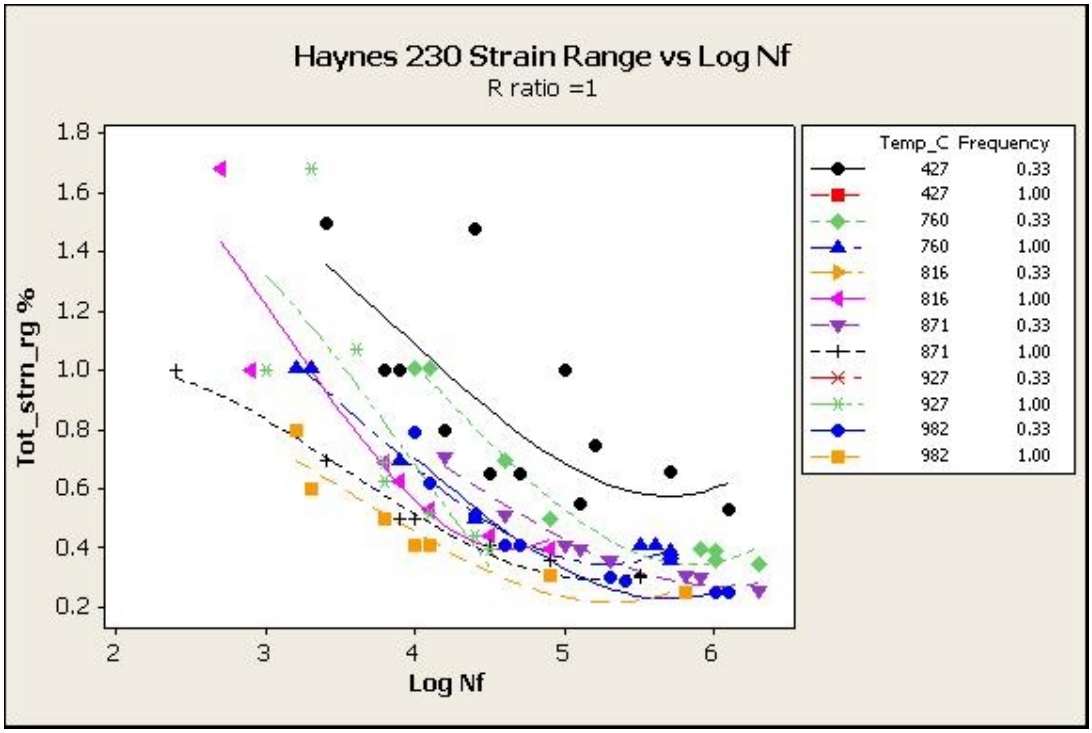

Figure 76 – Spread of training data for Haynes 230 by strain range

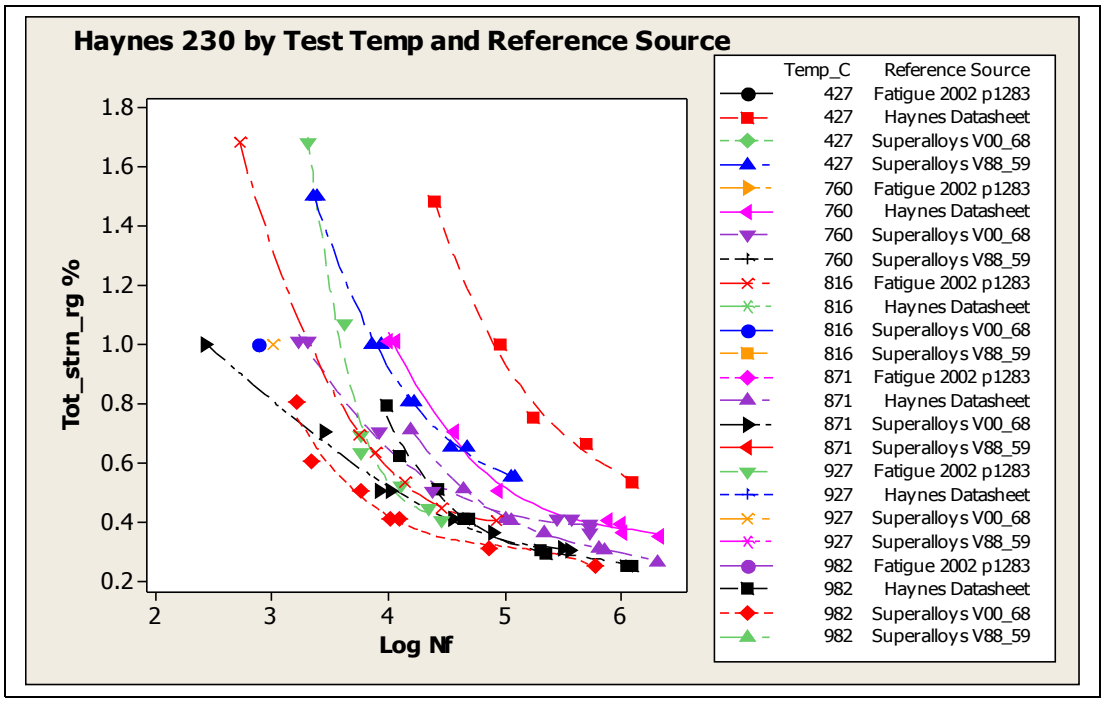

Figure 77 Spread of training data for Haynes 230 by test temperature and Ref source.

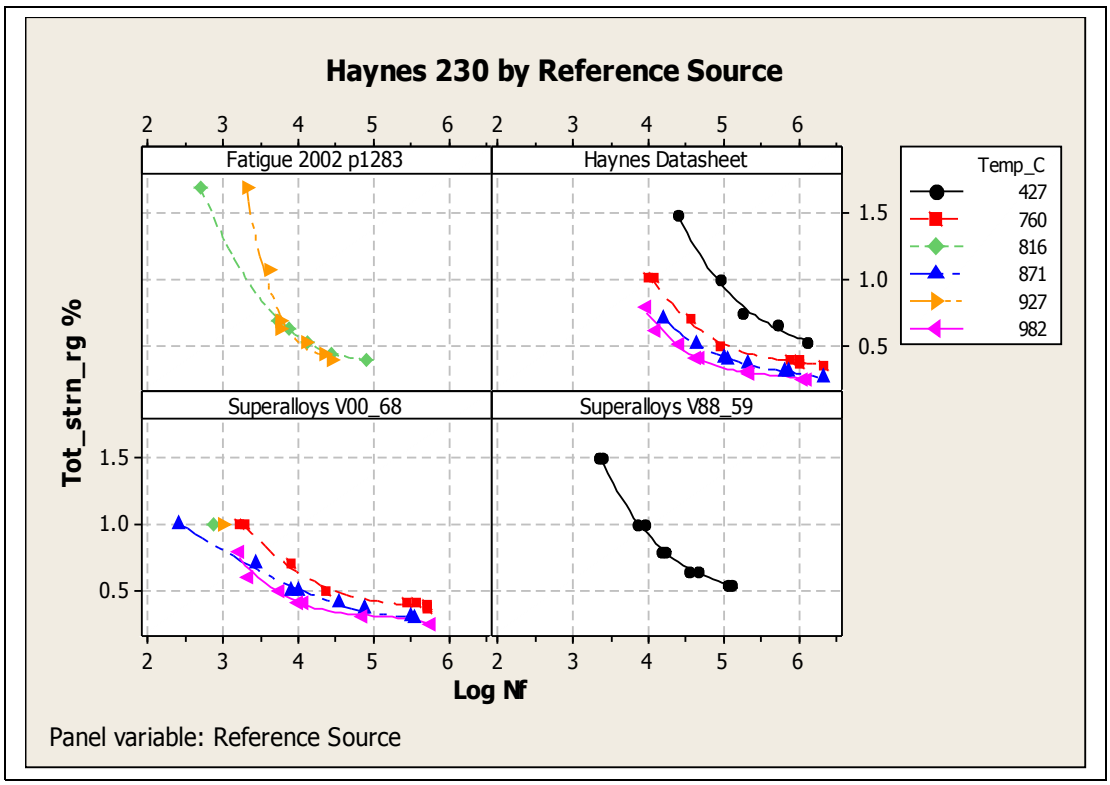

Figure 78 Multi-plots -spread of training data for Haynes 230 by test temperature and reference source

The process of plotting data by alloy has been repeated for all alloys in the database in order to highlight any problems with the data such as wrong values or large amounts of scatter. The data for PW1480 was initially left in the database, on closer examination of the source paper it is apparent that the large amount of scatter (Figure 79) may be due to specimen orientation effects under investigation. This data is a possible candidate for further sorting/removal.

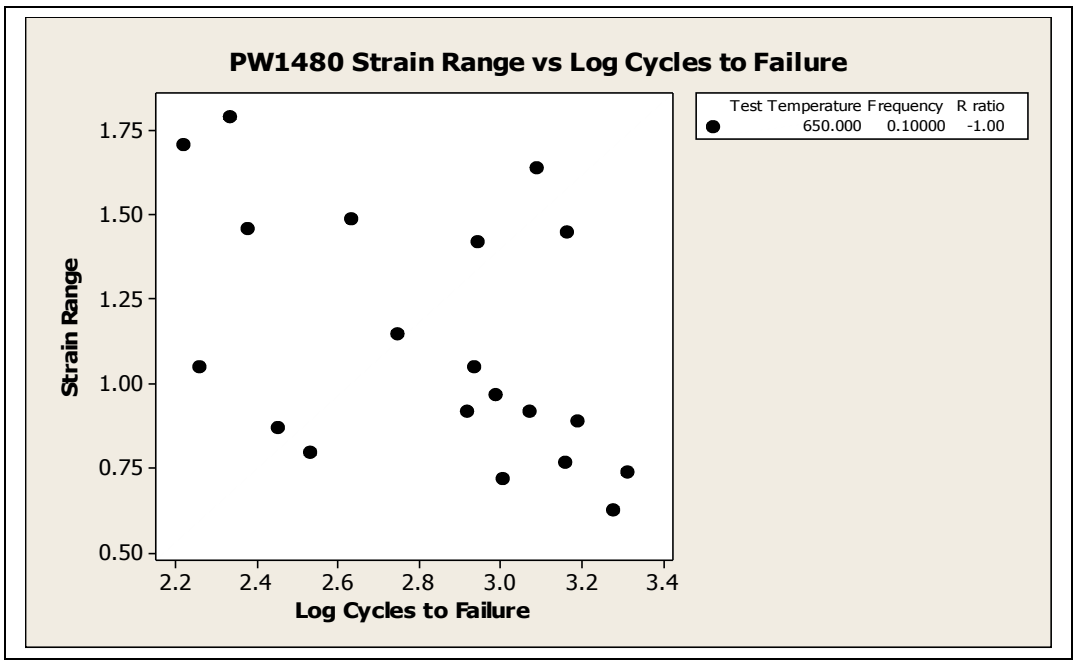

Figure 79 – PWA1480 strain life data

5.16.4 Statistical Analysis

The Minitab software package was used to analyse the data further in conjunction with running the models. The results of the analysis were used to explain trends in the predictions or areas where the models seemed to struggle.

Although Minitab was used to generate detailed statistical data about each input, Matlab has been used to generate input distribution histograms to be included in this report.

Variables with a poor spread of input data are identified as Fe, V, Re, La, Time HT1, Time HT2 and total strain range. It can be seen immediately that the strain range data has been skewed by spurious results at a value of around 400. An amended strain range distribution is given in Figure 84. The treatment of Fe is complicated due to its very different roles depending on the alloy in question; this also explains the spread of data present.

LCF lifetimes (log N_f) within the database can be seen to adopt a normal distribution. R ratio and frequency are also both well spread within the limits of what tests are actually possible.

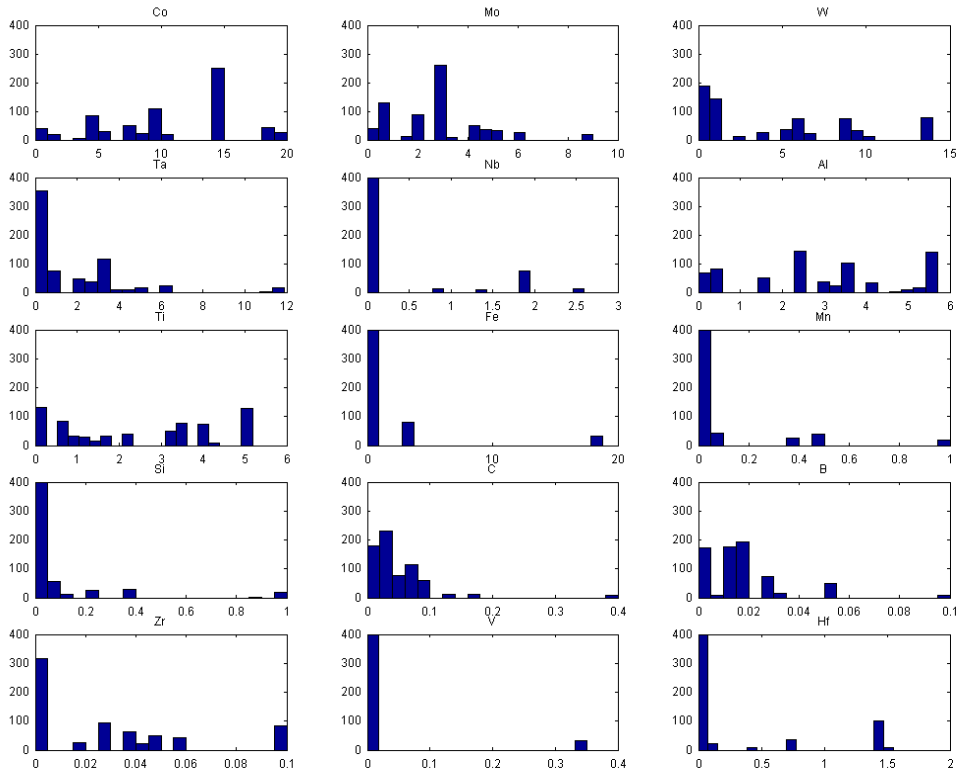

Figure 80 – Distribution of LCF model variables 1

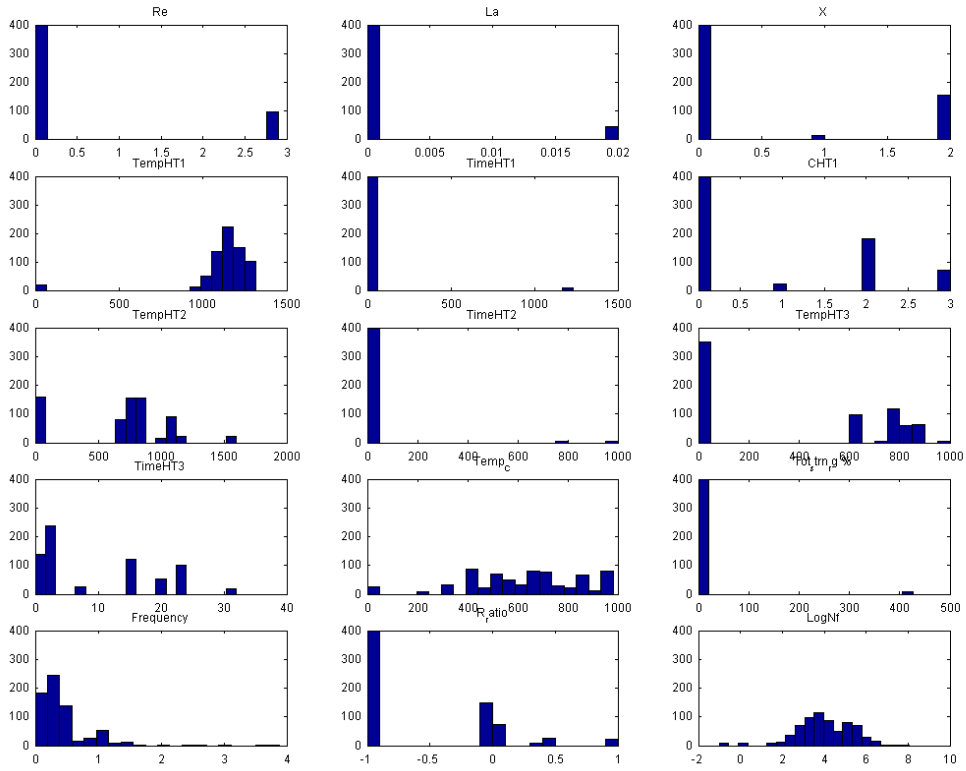

Figure 81 – Distribution of LCF model variables 2

5.16.5 Preliminary models

The first attempt at training a neural network on the LCF database was carried out using Neuromat. At this point the data had been checked for mistakes but no extra data sorting or removal had been carried out. The prediction was carried out against totally unseen data. The source of the data was tests carried out at Southampton University, reported in section 6.6.3.1. Strain range calculations were carried out using FEA as tests were carried out in load control. Although the prediction looks poor (Figure 82), it is comforting to see the prediction passes through data-points in the 1-1.5% strain range.

The significance analysis (Figure 83) shows that the model is not really picking up the correct trends within the model but it does suggest a very high reliance on the strain range input as expected.

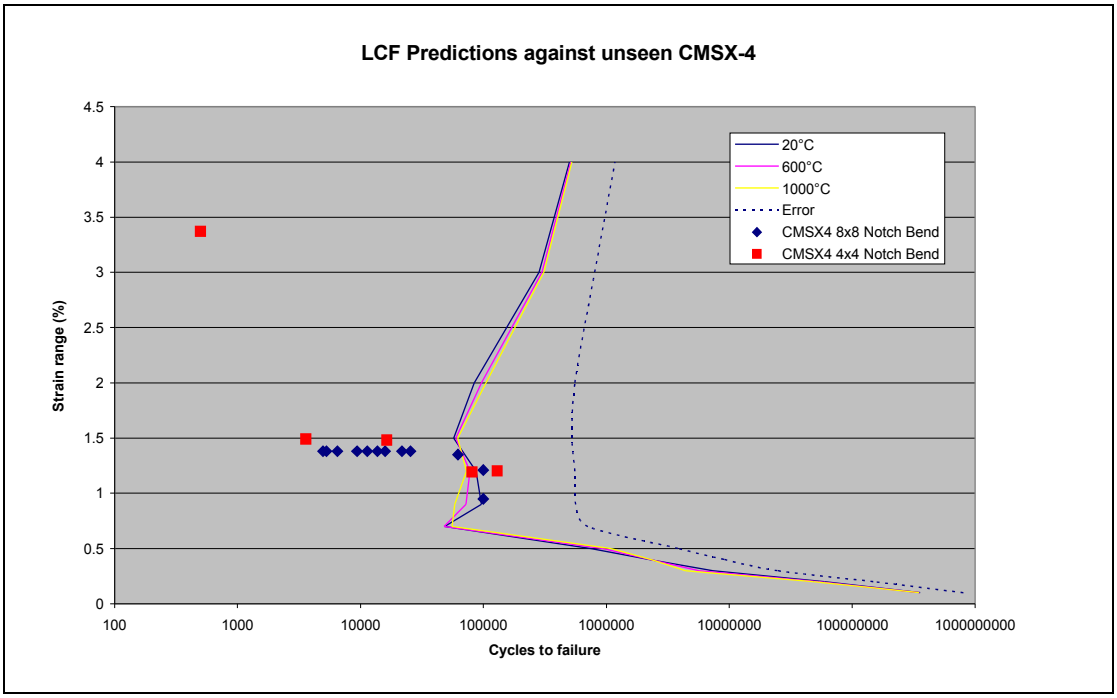

Figure 82 – LCF model predictions against unseen CMSX-4 data

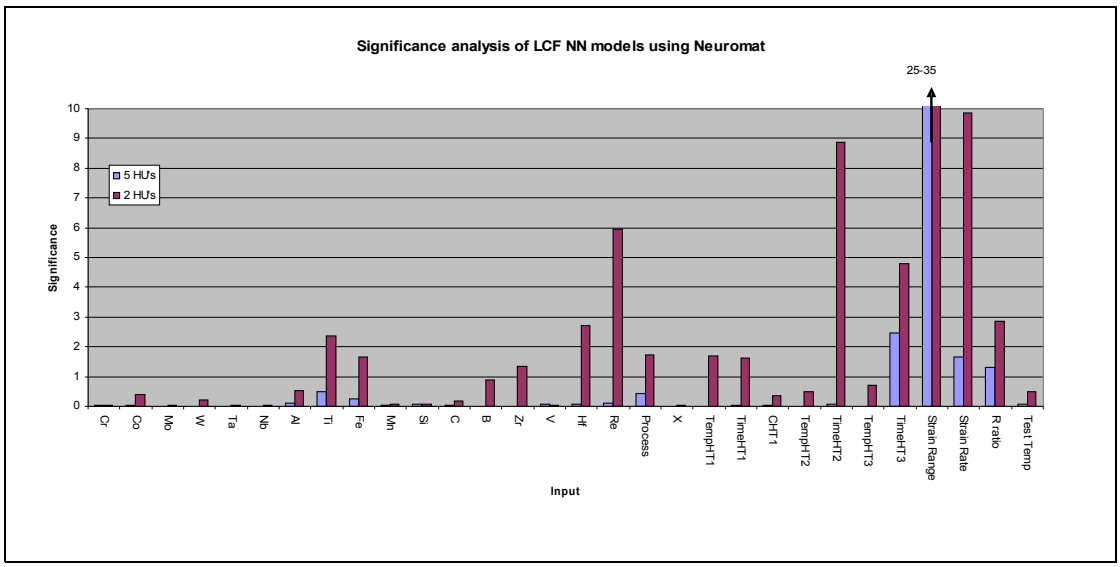

Figure 83 – LCF model significance of inputs

5.16.6 Discussion

The initial model shows reasonably good correlation at 1-1.5% strain range. Above 1.5% strain, models were unable to predict well. This is not surprising as a large percentage of the training data is in the range of 0% - 1% with most of the data clustered between 0% and 0.5% (Figure 84).

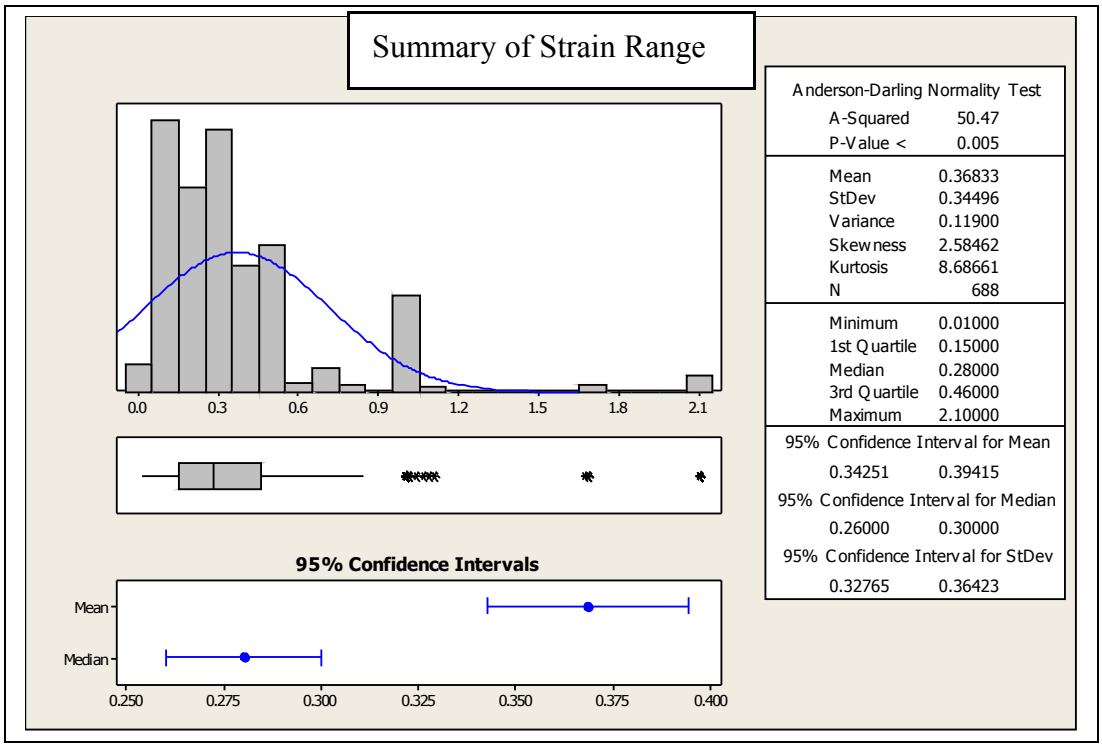

Figure 84 - Analysis of strain range distribution

Strain range appears to be by far the most significant input. This in itself is a function of a material's properties. Other inputs seem to have too high a significance value, whereas test temperature is predicted to be not as influential.

It is suggested in the literature that the model should be trained using Log N_f, rather than Nf, this is implemented in future models.

5.16.7 LCF model 2nd attempt

Models are now trained using Log N_f as an input instead of N_f. An initial simple test dataset was constructed using only CM186 data. In order to demonstrate that a model could be trained using the large number of inputs in the LCF model a simple 10 hidden unit model was trained in Matlab and predictions were made. The results (Figure 85) show a very good fit to the training data as expected and gave the confidence to train a model using the full database.

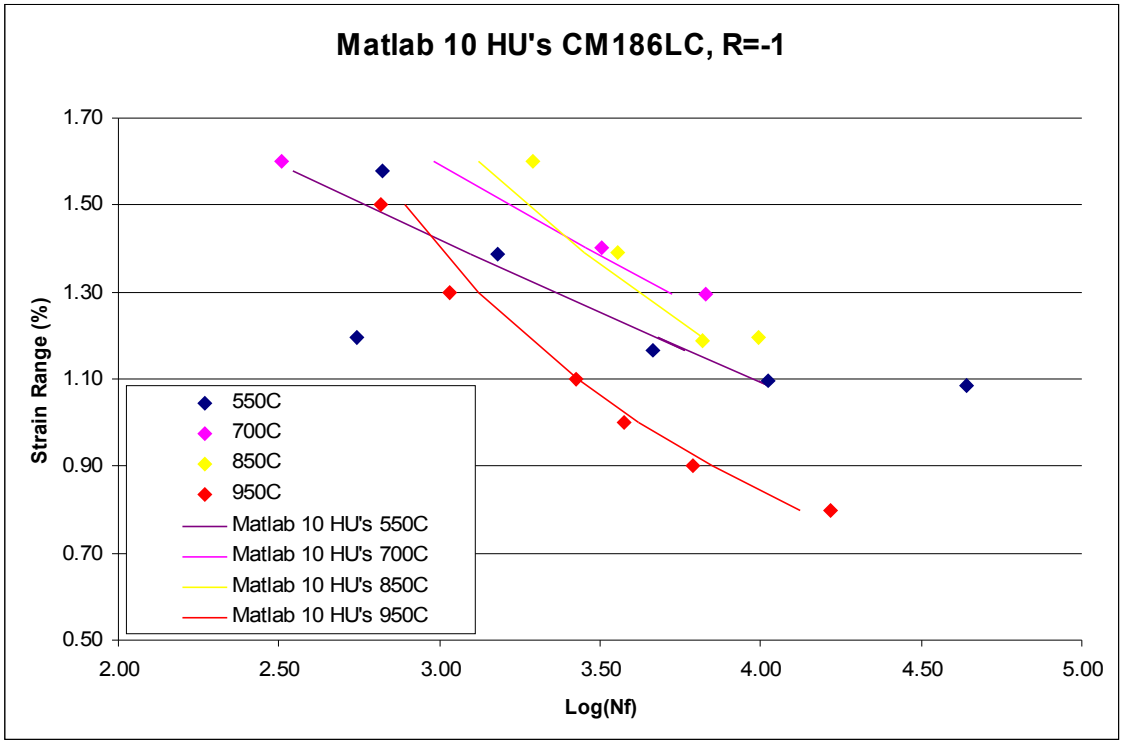

Figure 85 – Matlab neural network demonstrating data fit to CM186 data

Matlab is now used to demonstrate it is possible to use the neural network model to fit seen data having been trained on the full database. All curves are very close to being on top of one another (Figure 86) and do not show much dependence on temperature. That said, the test data does not show any conclusive temperature effect either.

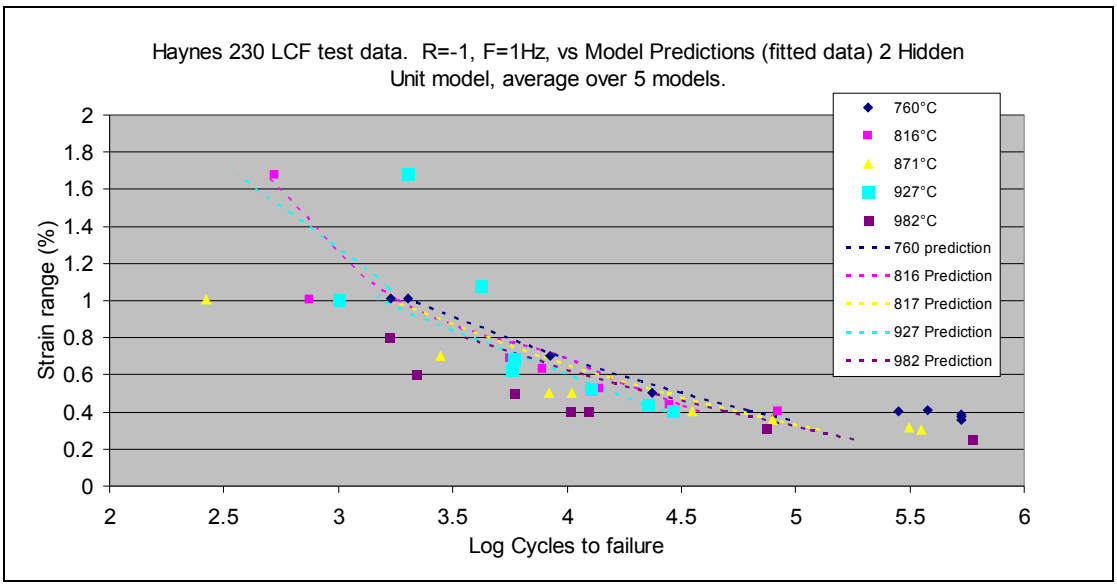

Figure 86 – LCF model predictions for seen data Haynes 230

Removal of input lines

Reducing the number of input variables reduces the size of the modelling space thus making it easier for the model to fit the remaining data. Inputs that are known to have no effect or that do not vary from record to record should be removed

Input variables CHT2, CHT3 are the first candidates for removal from the dataset due to the lack of data spread within the database (mostly set to 0). It is arguable that the data lines with non zero values for these inputs should be removed. However, the lines of data have been left in to preserve the size of the training dataset.

Certain elements included in the composition are referred to as tramp elements[xlix] for example Mn and Si. The values in the database are maximum allowable values where the ideal value would be zero. These elements are not in there by design and would not be specified when designing a new alloy. It is felt they do not add anything to the model at this current level of complexity and are another candidate for removal.

Fe is also named as a tramp element but due to the inclusion of Inconel alloys (as discussed earlier) it must be left in the database.

Model Results

Initial Predictions using an LCF model trained in Neuromat show a very good fit for CMSX-4 (seen data) at an R ratio of 0.05. On examination of input significances for this model, strain range and test temperature are now showing as the two most significant inputs as would be expected. Two other inputs with high significances are Vanadium and the duration of the 3rd heat treatment. The effect of heat treatments is

with respect to fatigue life is likely to be different for polycrystalline and single crystal alloys where the heat treatment effects grain size and γ' size respectively.

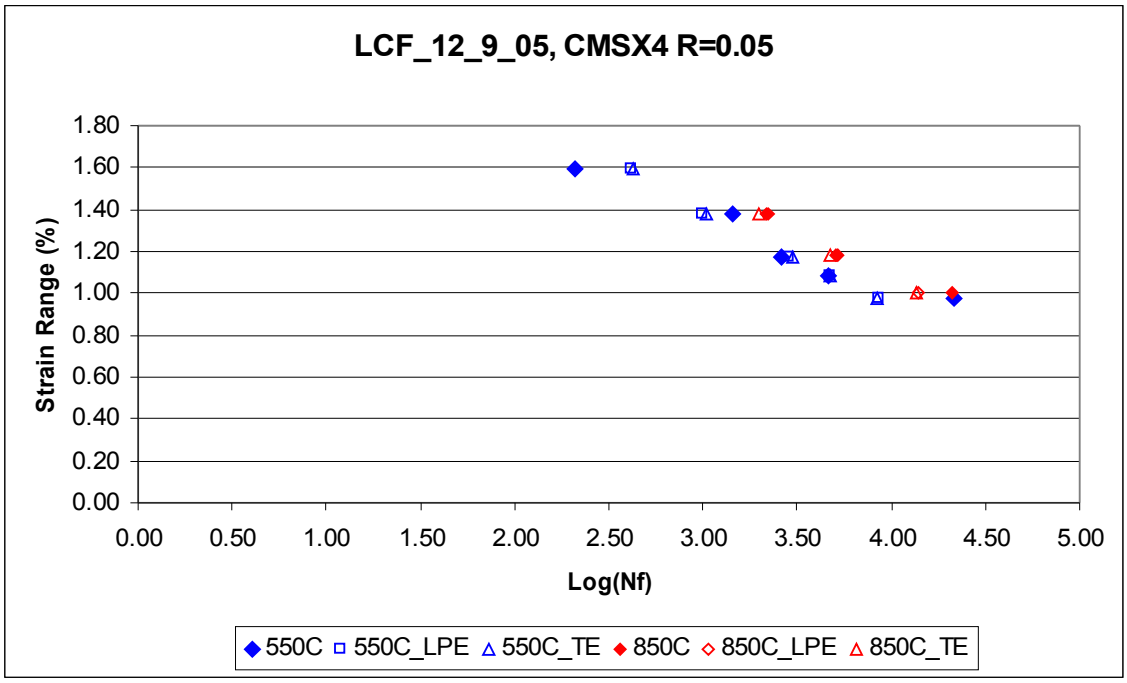

Figure 87 – Neuromat LCF predictions for seen data CMSX-4

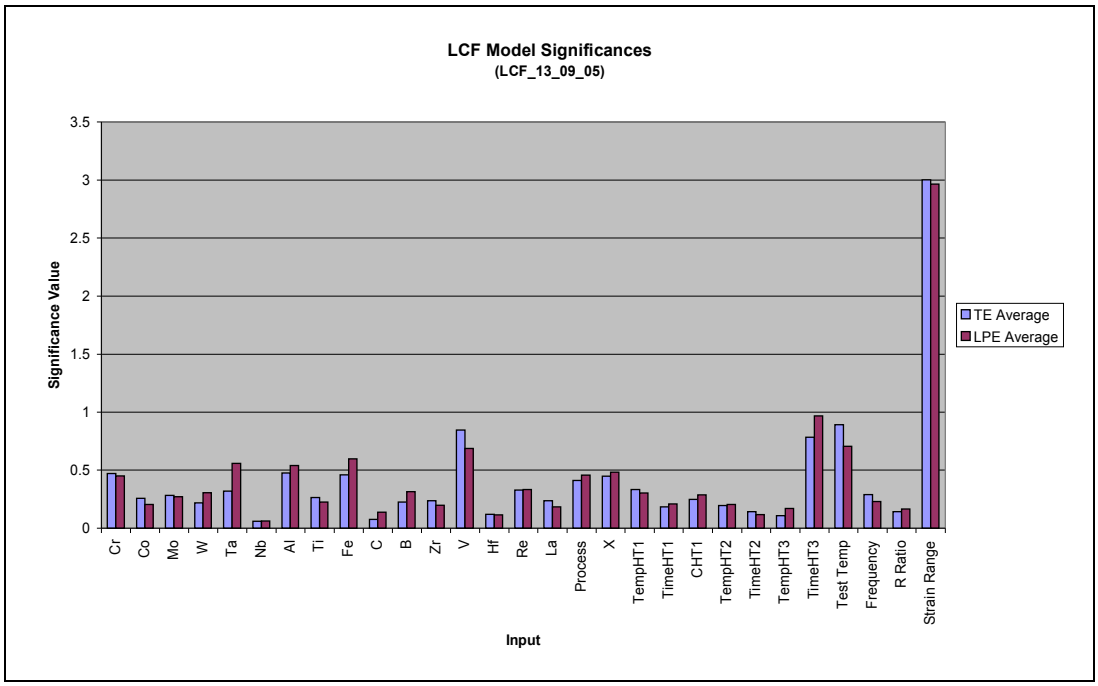

Figure 88 – Input significances for model trained on reduced input dataset

Further tests show that good agreement can be achieved between Neuromat models and relatively simple models trained in Matlab. Figure 89 to Figure 92 show direct comparisons between Neuromat and Matlab models for alloy CM186LC. This alloy was chosen as there is a relatively small amount of scatter in the input data and there is

data for various temperatures at two different R ratios. Both models were able to capture the temperature and R ratio effects satisfactorily.

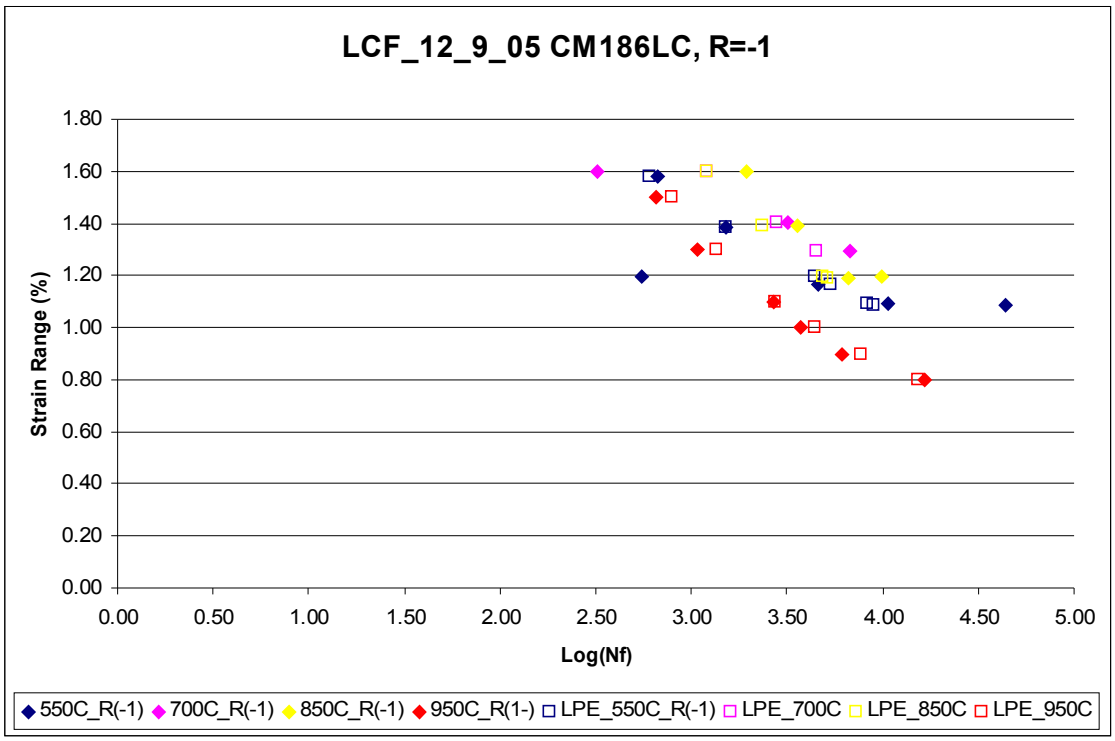

Figure 89 – Neuromat LCF predictions for seen data CM186LC R=-1

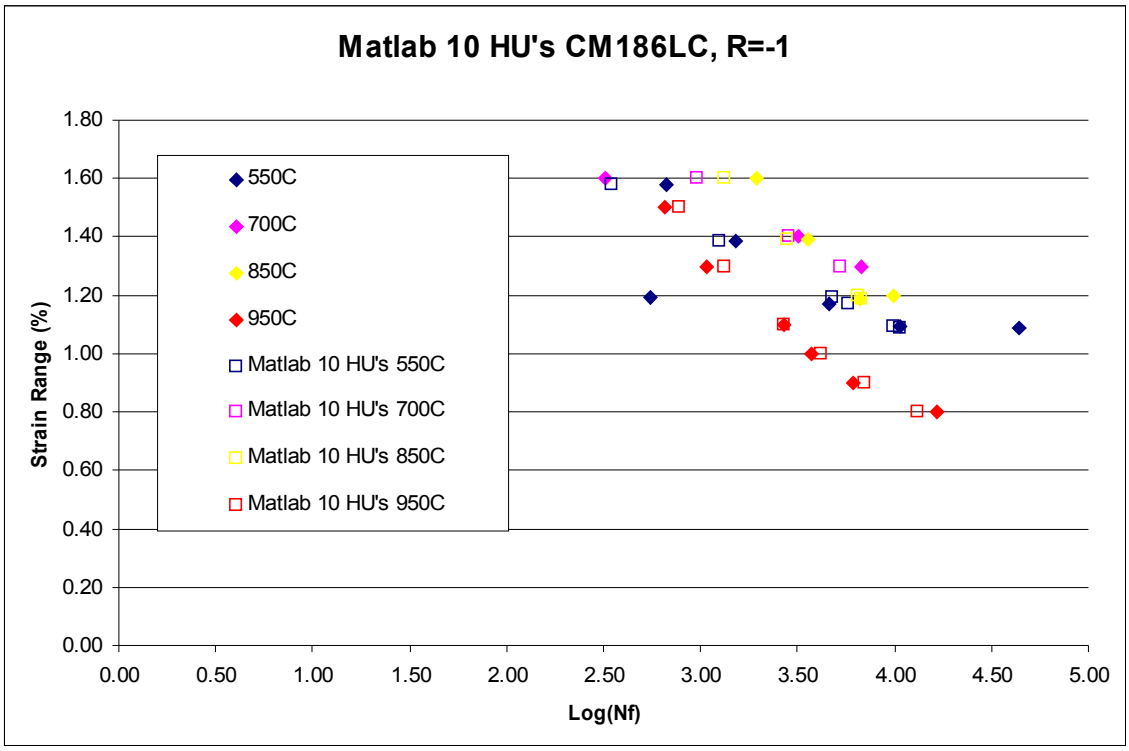

Figure 90 – Matlab LCF predictions for seen data CM186LC R=-1

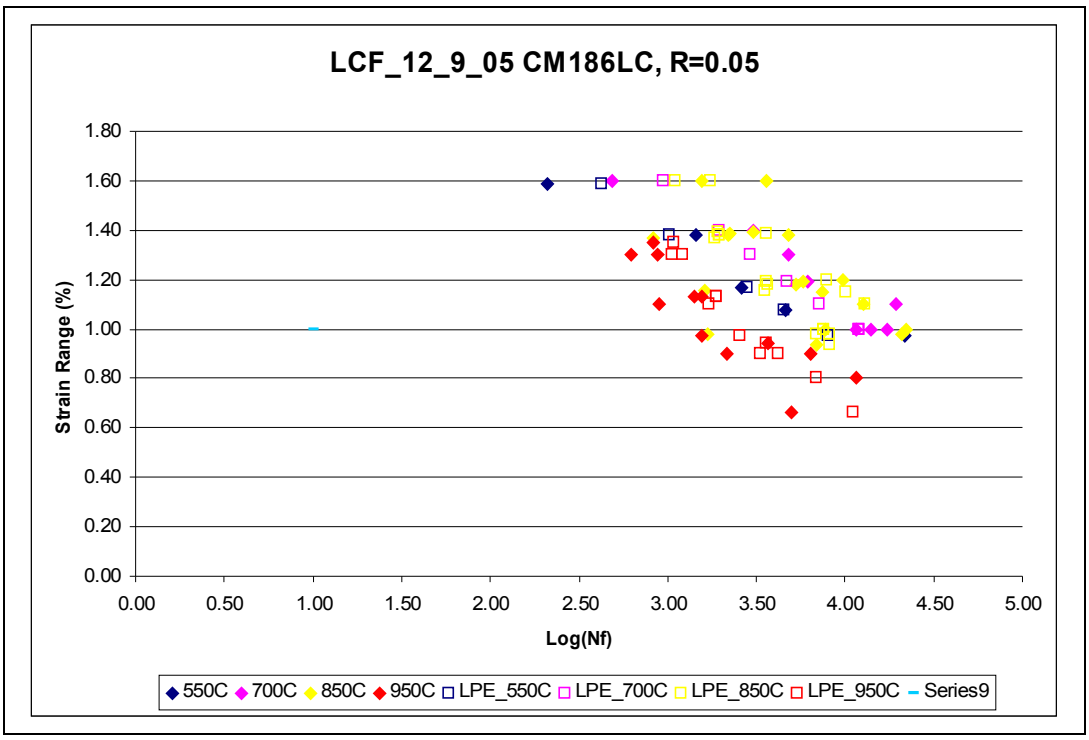

Figure 91 – Neuromat LCF predictions for seen data CM186LC R=0.05

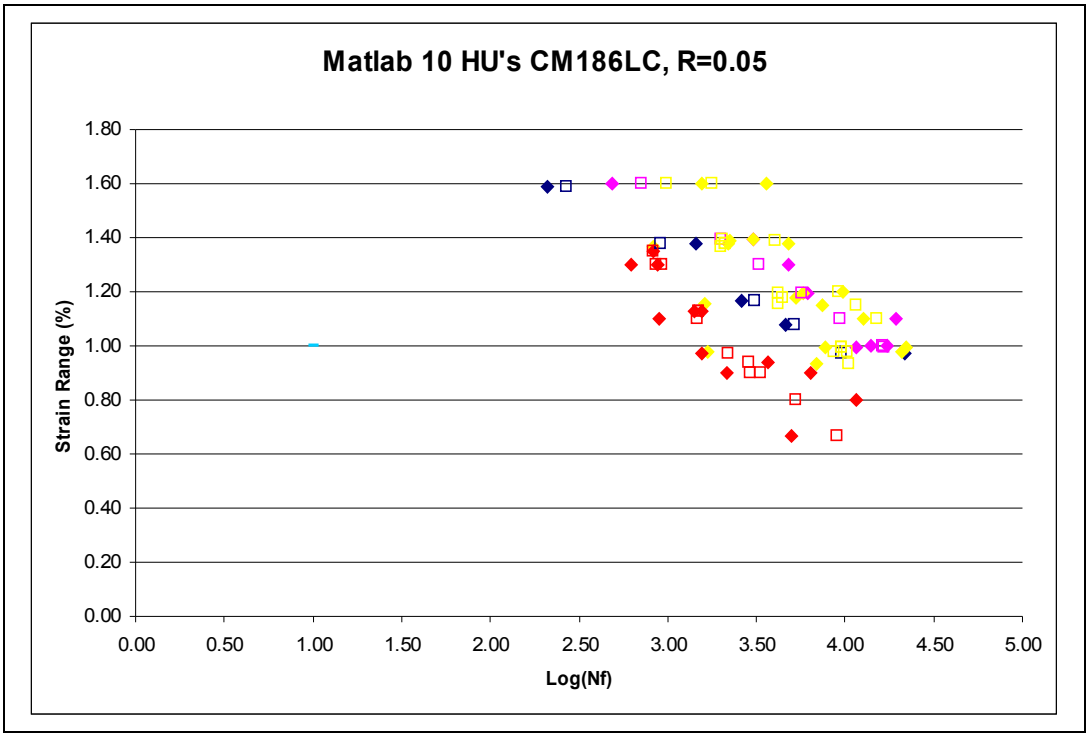

Figure 92 – Matlab LCF predictions for seen data CM186LC R=0.05 (Key as in Figure 91)

5.16.8 Discussion

There is a large difference between the amount of scatter in the test data in Figure 86 vs Figure 87, Figure 89 and Figure 91. The models fit extremely well when there is not much scatter in the input data. When there are large amounts of scatter the fit is still good, the order in which the curves are presented with respect to temperature is not always as expected. When the input data is examined it is not surprising due to the amount of scatter in the training data.

Models trained in Matlab with a set number of HU's are performing as well as Neuromat models with an 'optimum' number of HU's.

Predictions have only been carried out at points where there are datapoints in the training set to compare with. When there is a large amount of scatter in the predicted values, a line of best fit has been applied to the results using the line fitting tool in Excel.

The predictions should really be made in the form of a continuous line as the model can predict points at any strain range. This is the way predictions were performed using the UTS and YS models. Using this process will highlight over fitting of models to data with large amounts of scatter. The desired output from the model should be in the form of a strain life curve.

The models have been seen to improve by reducing the number of inputs. This was done by removing inputs that were not felt to contribute to the performance of the alloy (tramp elements) or inputs with very little or no variation in data.

Although the LCF models have not been tested on any unseen data, the fit to seen data it very good. It is felt that there is not yet enough data in the training dataset to provide meaningful results against unseen data.

Another proposed method to reduce the number of inputs would be to look at the Smith Watson Topper parameter[l] to condense information about R ratio and frequency.

5.17 Final Conclusions

Neural network models are able to fit to seen LCF data well although overfitting to data with a large amount of scatter is a problem. To improve the models, more data is required. The distribution histograms should be used as a starting point to determine where data is sparse.

Further investigation is required as to the method of inputting data, whether the raw data is used or a curve fitting process is used prior to training. Further predictions should be made at strain range values throughout the entire range to check for overfitting and poor generalisation. Sensitivity analysis is required. To do this, inputs must be identified that have a known effect on fatigue life. Temperature is currently the only input that has been examined this way.

The UTS and YS models showed benefits from 'human intervention' i.e. the removal of some data that was clearly outside the expected range for the material, collapsing of data, adoption of nominal compositions and the addition of data where the curve was know to be flat.

Due to the nature of fatigue data there is a lot more inherent scatter. Collecting, analysing and sorting the data prior to training takes more precedence than with the UTS and YS models.

On analysis of the fatigue data it is apparent that some input data curves do not fit the expected pattern. For example, when plotting SN curves for Haynes 230 (Figure 86) it would be expected that the curves would be ordered by temperature. Where curves cross or are in completely the wrong order, this data may not be valid to train the neural network.

There is no disputing that the data is real but when the neural network is picking out trends should it be helped along by using known information about fatigue performance trends with temperature or R ratio to improve the data?

The best training database should be a combination of data from literature and accumulated knowledge from metallurgy and test experience. This is where QQ can add value to the process over and above collecting large amounts of data to train a neural network. It has already been shown that large amounts of data alone are not

enough. The UTS database has been steadily improved whilst removing data as the process evolved.

6 Fatigue testing

6.1 Introduction

A turbine blade root contains notches that locate into a “fir-tree” root fixing (Figure 9) in the turbine disc. Fatigue initiation in these stress concentrating features is of some concern. Fatigue crack initiation can occur at relatively low service temperatures in this area (e.g. 650°C). The main purpose of this chapter is therefore to establish the critical factors controlling the notch fatigue life of turbine blade single crystals. When a turbine blade is cast, the primary orientation along the blade (usually in the <001> direction) is controlled to within certain limits, however the secondary orientation (i.e. the orientation of any notches) is not generally controlled. A programme of study is proposed with the following broad aims:

- To establish the critical factors controlling the notch fatigue life of turbine blade single crystals.
- To study the nucleation, early fatigue crack growth and final fatigue crack growth regimes.
- To produce simulation models to predict the initiation, growth and coalescence or growth to final failure of such fatigue cracks.
- To investigate the effect of secondary orientation on fatigue behaviour.
- To assess the possible use of this within a design procedure.

The aims of the work are to investigate fatigue crack initiation and early crack growth in the notch root of single crystal alloys. The notched specimen geometry has been defined such that the stress concentration is similar to that found in a fir tree notch root on a turbine blade, with a stress concentration ~2. All tests were conducted for a <001> tensile axis with two differing nominal crack growth directions <110> (orientation A) and <100> (orientation B) as shown in Figure 18. Testing was conducted at room temperature, 650°C and 725°C. The high temperature tests are within the range of temperatures that the notch root experiences in service. Room temperature testing has been conducted in order to identify temperature effects and to establish loading levels likely to achieve lifetimes ~10,000 cycles. The LCF regime was identified as important in discussion with sponsors (QinetiQ and ALSTOM). It was also an experimental requirement to allow replication approaches to track crack

initiation and surface features of crack growth within a reasonable test duration (~ 3 weeks at the frequencies chosen).

The Engineering Doctorate (EngD) work forms part of a co-operative research programme (CRP) between the School of Engineering Sciences, University of Southampton and the Structures, Materials and Propulsion Laboratory, Institute for Aerospace Research, NRC, Canada. The material under investigation at CNRC is PWA1484.

A complementary postdoctoral programme (Dr Mark Joyce) is studying the long crack propagation behaviour of the same CMSX-4 orientations under equivalent test conditions (R-ratio, frequency, temperature, orientation) thus conventional long crack propagation behaviour will also be available for comparisons with the short crack initiation and growth data produced in this package of work.

René N5 was made available by GE in order to provide a comparison with the work being conducted using CMSX-4

6.2 Materials

The CMSX-4 material was supplied by ALSTOM Power in the form of cylindrical cast bars. The bars were between 130mm and 160mm in length and 12mm in diameter. The bars were cast in the <001> and <111> directions and the misalignment for each individual bar was given. Table 5 gives the details for each casting supplied. θ and ρ refer to the primary (bar axis) and secondary (perpendicular to the bar axis) orientations with respect to <001> directions. For <001>, the secondary orientation is not controlled, and variations in ρ have no real relevance, the maximum misorientation from the <001> tensile/bar longitudinal direction can be seen to be 8 degrees. In the case of the <111>, ρ should ideally be 45°. The heat treatment details for the batch are given in Table 6. Although bars were also supplied in the <111> direction they have not yet been used and are not discussed further in this report. NB the specific details of heat treatment are commercially proprietary and examiners are asked to maintain confidentiality.

René N5 material was supplied courtesy of General Electric.

PWA1484 was sourced and tested at CNRC. Once testing and analysis was completed at CNRC the test specimens were passed over University of Southampton for further

metallurgical analysis and microscopy. The compositions of all 3 materials are given below:

CMSX-4	Cr	Co	W	Mo	Nb	Ta	Hf	Ti	Al	Re	Ni
Min (%)	6.2	9.3	6.2			6.3	0.07	0.9	5.45	2.8	Bal
Max (%)	6.6	10	6.6	0.6	0.1	6.7	0.12	1.1	5.75	3.1	

Rene N5	Cr	Co	W	Mo	Nb	Ta	Hf	Ti	Al	Re	Ni
Nom	7.48	7.72	6.38	1.5		7.13	0.15	-	6.18	2.85	Bal

PWA 1484	Cr	Co	W	Mo	Nb	Ta	Hf	Ti	Al	Re	Ni
Nom	5.0	10.0	6.0	2.0	-	9.0	0.1	-	5.6	3.0	Bal

6.3 Material Characterisation

6.3.1 Sample preparation

Samples sliced from the end of the cast bars were used for basic material characterisation and for determination of secondary orientation of the bars. A thin slice was removed using a Buehler Isomet 4000 Linear Precision Saw with a 11-4207 abrasive wheel and mounted in conducting bakelite. The sample was then polished using an automatic polisher as detailed:

- 120 grit paper @250 rpm contra rotating, 20lbs pressure, 5 minutes
- 600 grit paper @250 rpm contra rotating, 20lbs pressure, 5 minutes
- 1200 grit paper @250 rpm same rotation direction, 20lbs pressure, 5 minutes
- 4000 grit paper @250 rpm same rotation direction, 20lbs pressure, 5 minutes
- 3μm Diamond paste on dp nap cloth, 150rpm same rotation direction, 15lbs 4 minutes.
- OPS solution on dp nap cloth, 150 rpm same rotation direction, light pressure, 1 minute.

Nimonic etch (100ml distilled water, 40ml hydrochloric acid, 10ml nitric acid, 5g copper II sulphate) was used to preferentially etch the γ'. Examination of the samples was performed using an optical microscope and a Jeol JSM-6500F FEG SEM in both secondary electron imaging (SEI) and backscattered electron imaging (BEI) mode. Plain polished specimens were used in the scanning electron microscope (SEM) when observing the sample in backscatter mode.

6.3.2 Hardness testing

Specimens were tested using the micro Vickers hardness method. Lines of indent tests were performed at various loads across each sample to assess the hardness of dendritic and interdendritic regions. Testing was carried out to BS EN ISO 6507

The following equation was used to calculate the hardness value of each indent:

$$HV = 1.854 \frac{p}{d^2} \qquad \text{Equation 31}$$

Where,
P - the applied load [kg]
d - the average diagonal [mm].

6.3.3 Oxidation Study.

In service, CMSX-4, René N5 and PWA1484 would normally be coated with a suitable oxidation resistant coating. Information about the formation of oxide on uncoated samples at the temperatures of interest is sparse. Therefore an assessment of oxide formation was performed.

Material left over from specimen machining was cut into ~8mm square samples. Plain polished samples, and polished and etched samples were prepared and exposed at 650°C for 1, 2, 4, 8, 16, 32, 64, 128 and 256 hours in a furnace fitted with a calibrated thermocouple. The test specimens were placed in ceramic crucibles and a sample location map was used to ensure that samples with different time exposures were clearly identified. it was anticipated that any identification marks would be obscured during the oxidation process and every attempt was made to remove sources of contamination.

All samples were weighed before and after thermal exposure using a calibrated set of electronic scales accurate to 0.0001g. Oxidised samples were examined in the SEM starting with the two extremes (1 and 256 hours). Selected samples were sectioned so that the oxide thickness could be observed. The sectioning and plating procedure is documented in section 6.3.4

In the case of the PWA1484, samples were cut from the end of test specimens supplied by CNRC.

6.3.4 Sectioning and Ni Plating

The surface of interest (oxidised sample or fracture surface) was protected with a layer of nickel plate before cutting any samples. The Ni plating was performed in the following solution:

500 ml H_2O
150 g Nickel sulphate
20 g Nickel chloride
20g Boric acid

A 99.9% Ni anode was used. The superalloy acts as the cathode. The solution was warmed to 55-60°C on a hot plate and agitated using a magnetic stirrer. A voltage of 3v was applied across the system. A diagram of the test apparatus is given in Figure 93.

Once plating was completed, a thin slice or section was removed from the plated sample using a Buehler Isomet 4000 Linear Precision Saw with a 11-4207 abrasive wheel. The sample was then mounted in bakelite and polished and etched using a Nimonic etch.

6.3.5 Porosity Analysis.

Preparation of the notch root is discussed in the following section. The notch root was photographed after polishing and prior to etching to record the surface porosity distribution for all tested samples. An optical microscope was used to systematically photograph the surface after which the micrographs were pasted together to provide an overview of the notch. This composite picture was then used to generate a binary image of the porosity in order to carry out Finite Body Tessellation Analysis (FBTA) on the image. FBTA is a technique developed at Southampton which can capture information on size, aspect ratio, clustering and alignment of secondary phases based on grey-scale differences (i.e. ideal for assessing pore distribution), further details of the FBTA technique can be found in a paper by Boselli et al.[li]

Surface replicas were taken prior to testing to provide a record of the location of surface porosity prior to testing. Further porosity analysis was performed on plain polished mounted specimens to provide statistical data on the porosity size and distribution.

6.4 Finite Element Model

Finite element modelling was employed for two purposes. A simple elastic model was used to specify an appropriate notch geometry for the required stress concentration, whilst maintaining the necessary notch diameter to allow polishing preparation of the notch root. A more elegant elasto-plastic solution was obtained to allow estimation of the stress/strain fields in the notch root for a given loading. (Initial Finite element models written by Dr. Mark Joyce using ANSYS as part of CRP)

6.4.1 CMSX-4 Model geometry

Constraints on material supply meant that the sample dimensions were limited to 8mm x 8mm x 50mm for CMSX-4. The notch geometry was selected to have a minimum radius of 2mm as previous work had demonstrated that notches of this radius could be polished adequately for acetate replication. The sample was loaded in 3 point bend as specified in the test conditions.

The notch was required to produce a stress concentration factor of ~2 at its root. With a fixed notch radius, the stress concentration factor is dependent on the notch depth; therefore, this factor was made variable in the FE model. To ensure good approximation of the notch root stress/strain fields a reasonably dense mapped mesh using 8 node quadrilaterals was employed. The exact number in any given model varied depending on the depth of the notch, but was typically around 1275. Figure 94 shows the overall mesh, together with the loading and constraints. Figure 95 shows the mesh detail around the notch.

6.4.2 Elastic model - (determination of notch depth)

For this model only the elastic properties supplied by Alstom, given in Table 3, were considered. A simple constraint was applied to a single node to simulate the lower roller, whilst an arbitrary point load of 100N was applied to simulate the upper roller. The notch depth was varied from 0.25mm to 1.5mm in 0.25mm increments and the magnitude of the notch root stress field was assessed at each stage. Stress concentration factors were derived by comparing the computed Von Mises stress values with the stress evolved on the top surface of an un-notched bar, these results are given in (Table 4). The results show that a notch depth of 1.25mm gave a stress concentration factor of ~2.

6.4.3 Elasto-plastic model - (evaluation of notch root stress/strain fields)

At the load levels required to cause fatigue crack initiation, it is likely that the material in the region of the notch root will be deforming plastically. In order to estimate the stress levels in this region under such conditions a more complex elasto-plastic analysis is appropriate. The basic model geometry and mesh from the earlier elastic model was retained, the notch depth now fixed at 1.25mm. The material model was changed to include isotropic monotonic plasticity data supplied by ALSOTM. This was implemented using a multi-linear curve. Loading was applied monotonically from zero to a maximum of 6000N. This was applied in 10N increments and the model allowed to converge fully (typically only 1-2 iterations required). At each increment the magnitude of the notch root stress and strain fields were assessed, these results are shown in (Figure 96). It is recognised that the model is based on monotonic stress-strain behaviour at 650°C for the <100> orientation and does not take into account any cyclic softening/hardening or plastic anisotropy effects and simply simulates a simple loading step.

6.4.4 Sub-sized CMSX-4 specimens

A further set of test specimens 4mm x 4mm x 50mm have also been modelled. Minor changes were made to the model to account for the different geometry

6.4.5 René N5

The finite element modelling process was modified for René N5 with a test sample geometry of 10mm x 10mm by 50mm. No data for René N5 material properties was made available so the CMSX-4 material model was used to provide a best estimate of the loads required for a similar strain range in the Notch root.

6.4.6 PWA 1484

A finite element model also used to estimate the strain range in the notch root of PWA 1484 specimens tested by CNRC in order to compare them with CMSX-4 and René N5 test data generated at Southampton. The model was run in Abaqus and used stress strain data for PWA 1480 in absence of any data available for PWA 1484 (Figure 97.). PWA1484 test specimens supplied by CNRC were measured using a digital vernier, the

FEA model was based upon the average measurements of the test specimens. The mesh was constructed using 20 noded brick elements with a large amount of refinement around the notch root (Figure 98). Mesh quality checks were performed on the meshed bar and a mesh convergence study was performed.

6.5 Fatigue Testing

6.5.1 Specimen Preparation

The longitudinal, cast direction, of each bar of CMSX-4 was known to be <001>, but the secondary orientation, the nominal crack growth direction, had to be determined prior to machining. The orientation A tensile axis is in the <001> direction and the nominal crack growth direction is <110>. For orientation B, the tensile axis is in the <001> direction and the nominal crack growth direction is in the <010> direction (Figure 99). The orientation directions were determined after etching the ends of the cylinders with Nimonic etch. This revealed the dendritic structure, the dendrite arms are known to grow along <100> type directions and hence reveal the <100> directions perpendicular to the cylinder axis (Figure 100).

The specimens were machined using electrical discharge machining (EDM). An initial specimen size of 8mm x 8mm x 50mm was selected in order to make best use of the material supply. A 4mm diameter notch was machined half way along the specimen bar with the centre point of the radius set 0.75mm above the surface of the bar (Figure 101).

The EDM process left behind a highly oxidized surface layer that required polishing away to reveal the microstructure before testing could take place. A dental felt coated with diamond paste was used to polish the notch. The specimen was clamped in a stage with X and Y adjustment possible via thumb screw and the notch was lined up with the dental felt. Enough pressure was applied to cause the felt to deform slightly, a lubricant (metadie) was used and the drill was oscillated up and down by hand during polishing. Three grades of diamond paste were used (6μm, 3μm and 1μm) to obtain the polished finish. The process is very lengthy and has proved damaging to the bearings in the pillar drill. This process was modified to include a 4000 grit paper first stage. A dental felt pin was slotted to take the paper which is then wound around the pin to give an approximate diameter of 2mm. Using the grinding paper speeds up the process considerably.

Figure 102 shows the quality of the finish after polishing and subsequent etching (dendrite orientation in the notch can be clearly seen). The polished surfaces were

etched to allow crack interactions with the microstructure on the surface to be assessed. Identical processes were used for the preparation and testing of sub-sized CMSX-4 samples and René N5 examined later in the project.

6.5.2 Testing Procedure

Notch fatigue experiments were performed on an Instron 8501 servo hydraulic testing machine fitted with an ESH high temperature vacuum chamber. Tests were carried out on the notched specimens in symmetric three point bend as detailed in (Figure 101). During all testing the load ratio was 0.1. The preliminary test to establish appropriate loading levels to obtain a lifetime ~10,000 cycles was conducted using a triangular waveform at 20Hz, in air, at room temperature. Further tests were conducted at 650°C using a 1-1-1-1 trapezoidal waveform (Figure 103). Loading levels were assessed with reference to the FE model discussed earlier. High temperatures were achieved with the use of four quartz lamps mounted within the testing chamber. The lamps and reflectors were positioned around the specimen with the maximum concentration of heat at the centre of the chamber where the specimen was mounted. Temperature control was via an ESH power cabinet fitted with a Eurotherm 815 set point controller. Specimen temperature was measured by means of an R type Pt-Rh thermocouple spot welded within a couple of millimetres of the notch. Chamber temperature was controlled to within +/- 1°C. The chamber was heated to test temperature then allowed to soak for 20 minutes before testing commenced. During this time the specimen was held at minimum load.

Interrupted/replica tests were stopped at a pre-determined number of cycles in order to take a replica. Lamps were shut off immediately after the test stopped cycling and the specimen was held at minimum load. The chamber was not opened until the specimen temperature had fallen below 150°C. Once the chamber had been opened, a large desk fan was used to blow air into the chamber and facilitate cooling. Before taking a replica, the load level was increased to mean load in order to open any surface cracks slightly. Replicas were taken using a Struers RepliSet-F1 kit, the silicon rubber compound required a temperature of less than 35°C to set satisfactorily. The specimen was then returned to minimum load and the chamber was reheated as outlined above. Replication intervals were decreased at the onset of surface cracks appearing.

6.5.3 Fractography

Detailed systematic assessment of each fracture surface was carried out. Initial overviews were taken both with a Wild macroscope and in the JEOL FEG-SEM, to assess gross macroscopic features and to help pinpoint initiation sites and notch surface fracture features. High magnification shots were taken of all initiation areas and of typical crack propagation features, for comparison with long crack specimen fractography carried out in the partner programme in the CRP. The SEM was also used in BEI mode to give topographical and compositional scans of the fracture surface. Energy dispersive x-ray (EDX) compositional mapping was conducted on sites of particular interest on the fracture surface using the FEG SEM in BEI mode in conjunction with Oxford Inca 300 software.

Temp (°C)	E (GPa)	ν	σ_{yield} (MPa)	$\sigma_{0.2\%}$ (MPa)	σ_{UTS} (MPa)	Elong. (%)
20	115	0.4	680	900	1050	5
650	106.9	0.4	700	943	1200	8.77
750	100	0.4	730	980	1200	10

Table 3 - Elastic and plastic properties used in modelling

Notch depth (mm)	Stress concentration factor
0.25	1.32
0.5	1.53
0.75	1.69
1	1.83
1.25	1.98
1.5	2.13

Table 4 - Stress concentration factor variation with notch depth

Identity	Type	θ	ρ
BAVF A1	<001>	2.3	32.1
BAVF A4	<001>	2.3	2.2
BAVF A6	<001>	4.5	29.0
BAVF A8	<001>	4.0	24.8
BAVF A11	<001>	7.9	44.3
BAVF A12	<001>	6.4	33.6
BAVF A14	<001>	4.9	34.4
BAVF A15	<001>	5.3	32.6
BAVF A16	<001>	3.7	2.6
BAVF A17	<001>	5.2	38.0
AWLSA 3B	<111>	51.4	42.6
AWLSA 4B	<111>	51.4	43.5
AWLSA 5B	<111>	52.5	44.0
AWLSA 8B	<111>	50.7	41.8
AWLSA 9A	<111>	50.3	44.5

Table 5 - CMSX-4 Bar Identities and Primary Orientations

Standard service heat treatment employed to produce CMSX-4

- *x hrs @ x°C → raise temperature*
- *x hrs @ x°C → raise temperature*
- *x hrs @ x°C → raise temperature*
- *x hrs @ x°C → raise temperature*
- *x hrs @ x°C → raise temperature*
- *x hrs @ x°C → raise temperature*
- *x hrs @ x°C → raise temperature*
- *x hrs @ x°C → rapid gas fan quench in argon*
- *x hrs @ x°C → air cool*
- *x hrs @ x°C → air cool*

Table 6 - Heat treatment data supplied by Alstom (NB the specific details of heat treatment are commercially proprietary y)

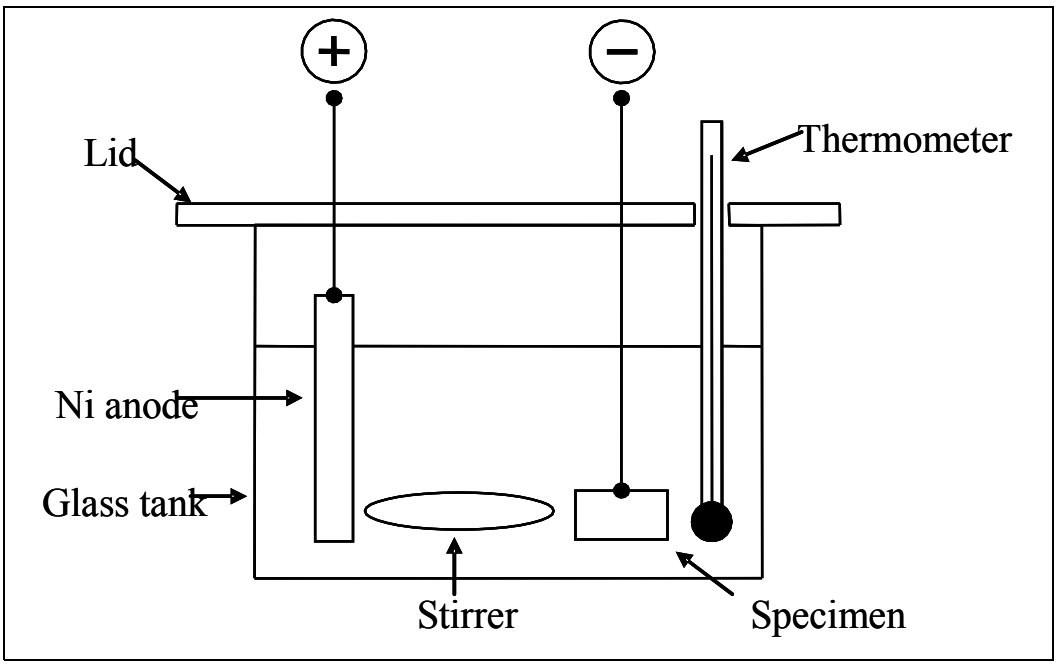

Figure 93 – Ni plating apparatus

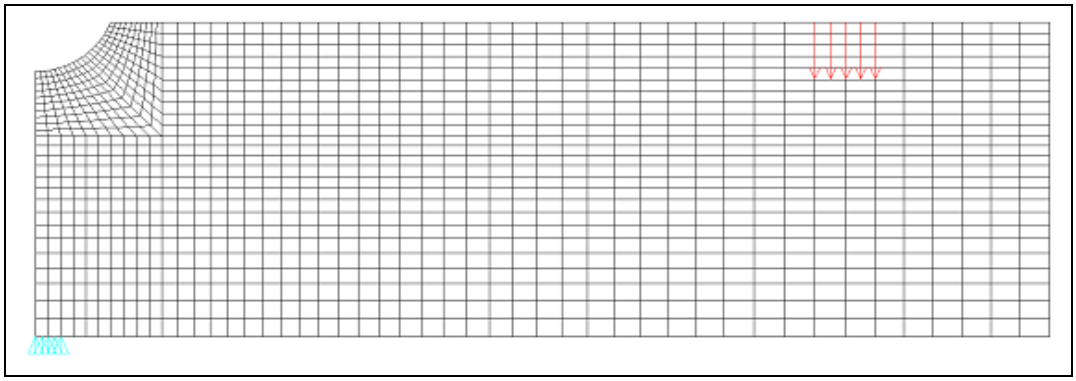

Figure 94 - Meshing, loading and constraint strategy. Note distributed constraints shown (used in elasto-plastic model only) (after Mark Joyce)

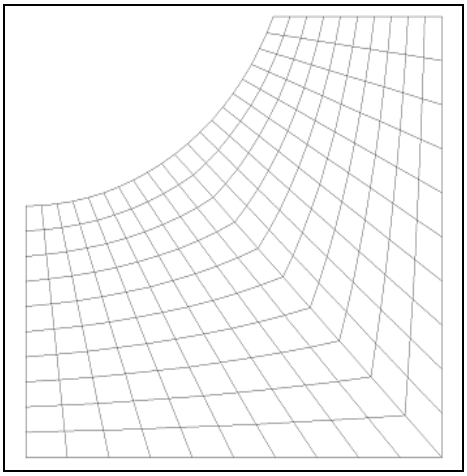

Figure 95 - Notch root mesh detail – 8 node mapped quadrilaterals employed to accurately assess notch root fields (after Mark Joyce)

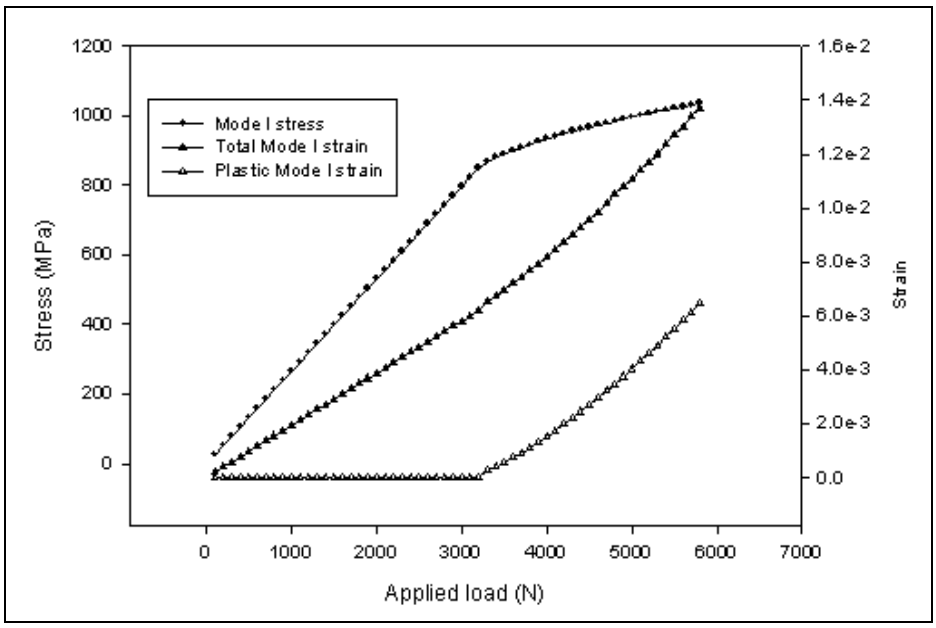

Figure 96 - Mode I stresses and strains predicted at notch root in CMSX-4 at 650°C. (after Mark Joyce)

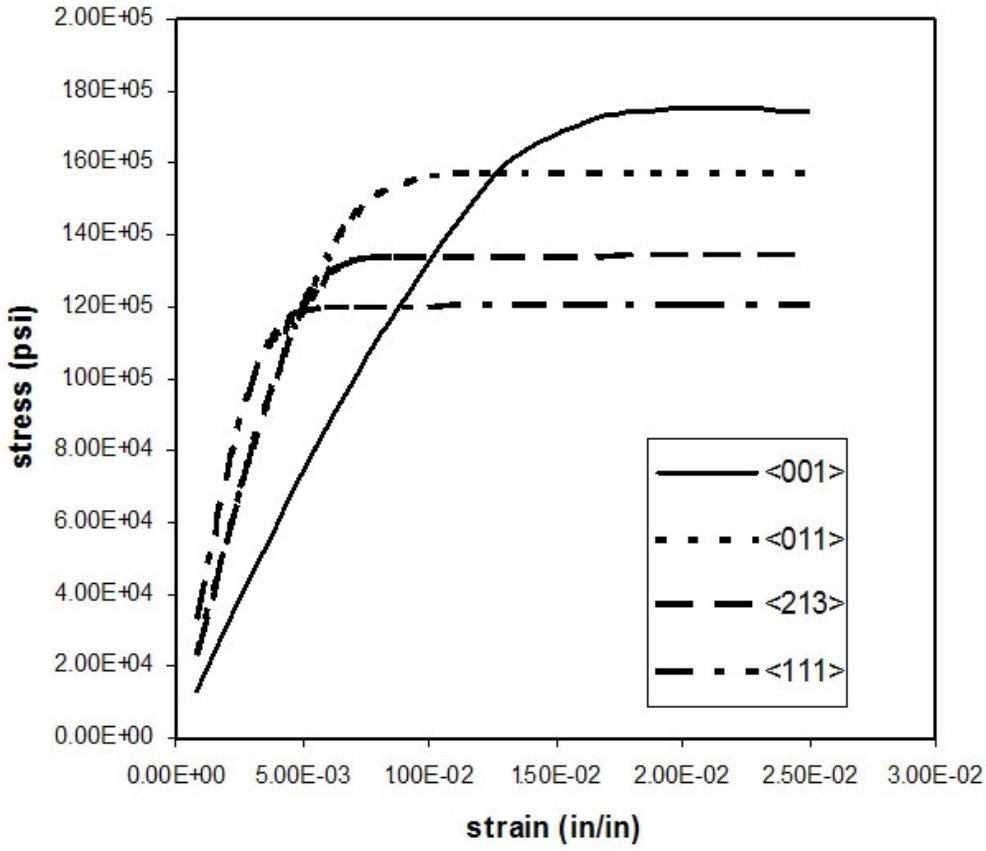

Figure 97 – Stress/strain behaviour for PWA1480

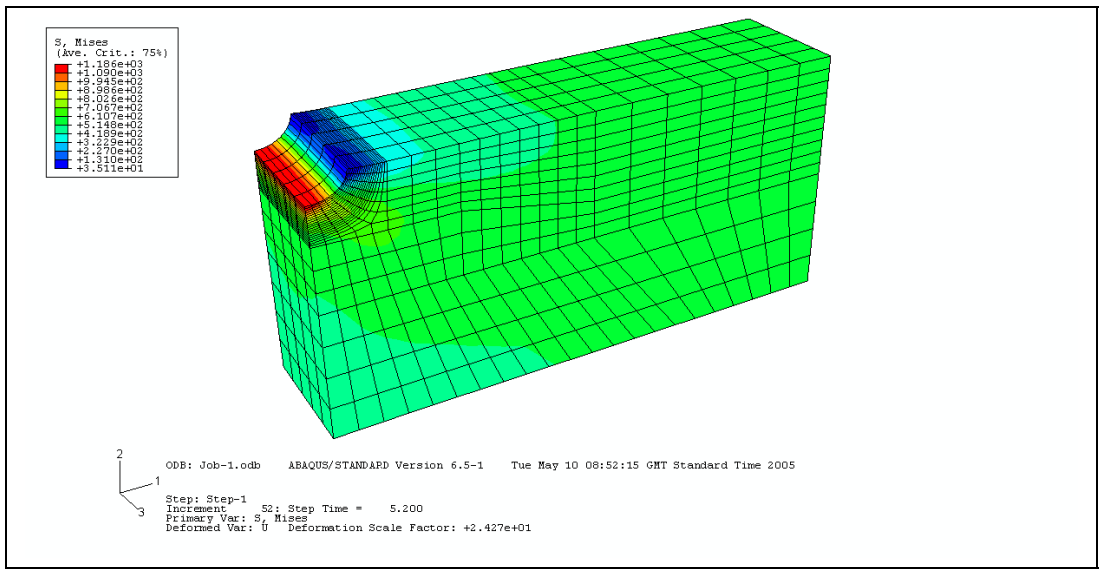

Figure 98 - Abaqus FEA model of PWA 1484 test bar with detail of mesh refinement around notch root.

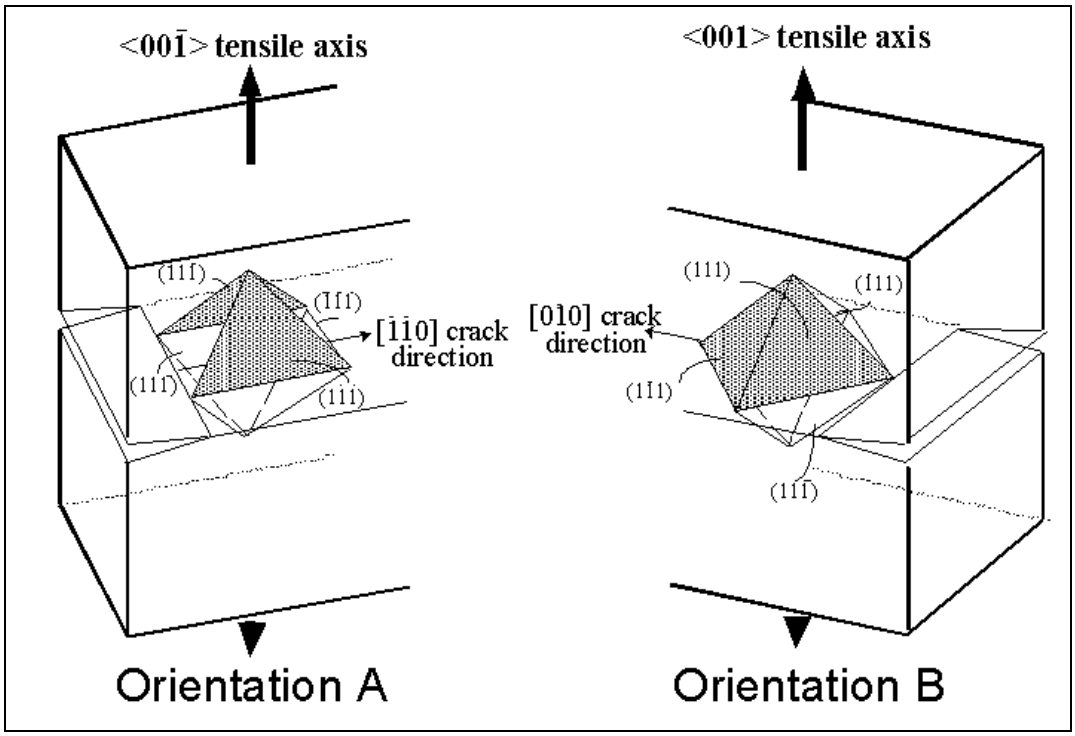

Figure 99 - Definition of secondary orientations A and B and their nominal crack growth directions

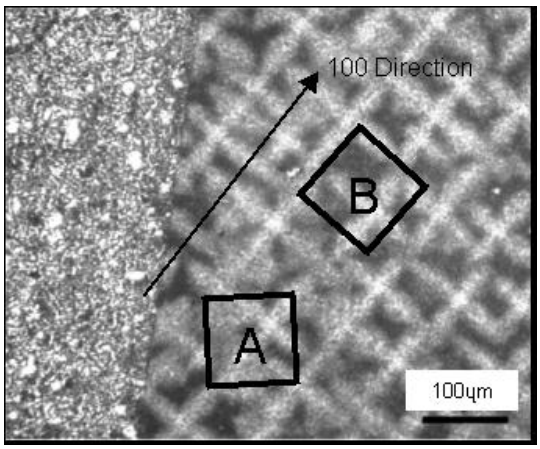

Figure 100 - Secondary orientation with relation to dendrites taken from end of cast bar

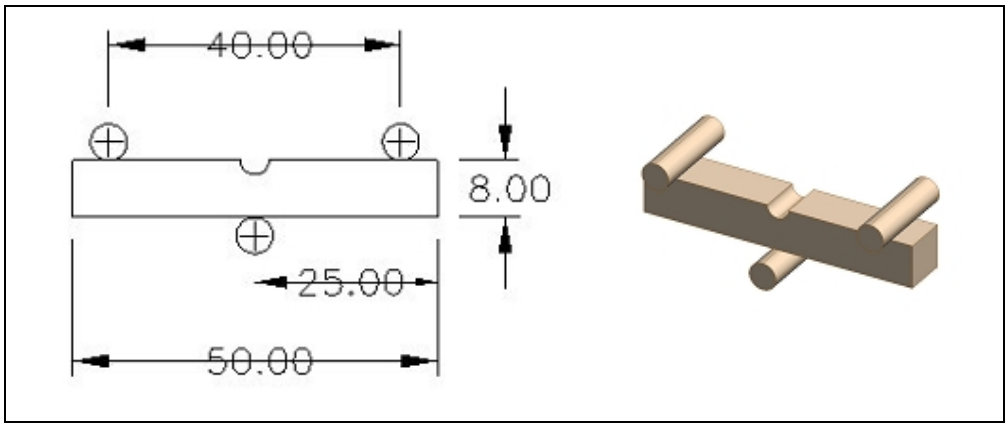

Figure 101 - Short crack test specimen geometry

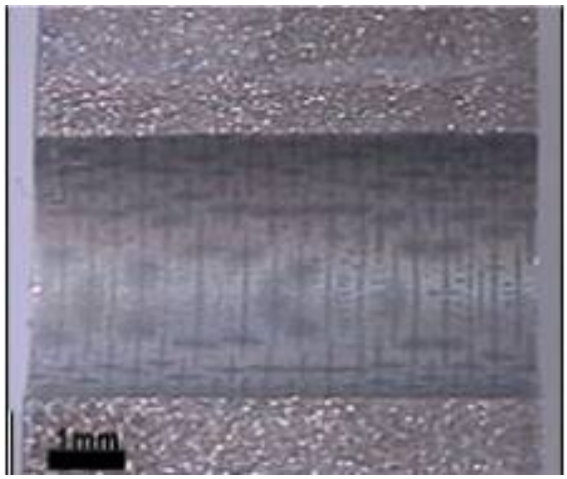

Figure 102 - Etched and polished notch (orientation B)

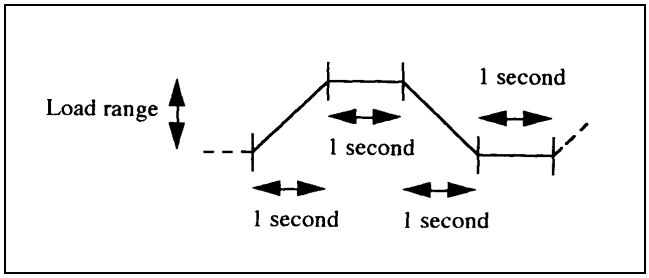

Figure 103 - Trapezoidal 1-1-1-1 waveform.

6.6 Results

6.6.1 Material Characterisation

6.6.1.1 Macrostructure.

Dendrites can be observed on polished etched specimens of each alloy (Figure 104, Figure 105 & Figure 106). Dendrite orientation has been used to determine the orientation of test specimens (A or B) during manufacture (Figure 100) as described in Chapter 6.5.1.

Dendrite spacing is of the order of 10μm for each alloy. Dendrites in CMSX-4 are more clearly defined. There is a sharper transition between the dendritic and interdendritic regions in CMSX-4 than is seen in PWA1484 and René N5.

EDX analysis has been carried out on CMSX-4 to determine segregation of elements for comparison with the literature 220. EDX plots show higher concentrations of Re and W (~20% rel) within dendritic areas (Figure 107 & Figure 108). These values agree with the ratios shown in the literature 220.

Porosity is observed to be interdendritic in nature, Figure 109 shows an example of porosity in an etched sample of René N5 with porosity clearly occurring in the lighter, interdendritic, regions.

Porosity is visible on plain polished specimens of all 3 alloys. Collages of optical microscope images (Figure 110) have been processed using tessellation analysis software (Figure 111) to provide statistical information on the porosity distribution of each alloy (Table 7, Table 8 & Table 9). A total area of ~28mm² was analysed over a sample of 3 test bars for each alloy. CMSX-4 samples had the highest porosity levels of 1.3% with an average aspect ratio of 1.2 and an aspect ratio range of 1 to 5.1. All 3 alloys had a maximum pore aspect ratio of 4.5 or more. The size (2D section area) of the pores ranges between 3μm² and 2240μm².

Hardness testing has been completed on CMSX-4 and René N5 using a micro-hardness Vickers test. Rows of hardness indents on etched samples have been divided into results for dendritic and interdendritic regions. Results are presented in Table 10. Although there was a lot of scatter in individual results, CMSX-4 shows a marked increase in the average hardness values in the dendritic regions over the interdendritic regions. The standard deviation of the results was of the same order of magnitude as the difference between the averages but on closer examination of the data there were some

obvious outliers possibly caused by indenting a hard phase or at the site of a pore. René N5 shows the same trend but the difference between the average results was much less and too small to be considered statistically significant.

Slip bands are clearly visible around hardness indents. Figure 112 and Figure 113 show examples of slip bands in CMSX-4 and PWA1484 respectively. For slip bands to be visible it was necessary to view them on plain polished samples.

6.6.1.2 Microstructure.

On a polished and etched sample of CMSX-4 the finer scale γ/γ' microstructure is clearly visible. A Nimonic etch was used to reveal the γ matrix and confirm the high γ' fraction (Figure 114). The triangular sections of the matrix are consistent with what would be expected for a {111} section through a cuboidal γ' array. The same sample was also observed in the plain polished condition using backscattered electron imaging (Figure 115). The light areas indicate heavier elements are concentrated in the γ matrix as indicated by the literature[lii].

Compositional analysis conducted using EDX was unable to determine the compositional differences between the γ and γ'. The interaction volume over which compositional values are averaged is an order of magnitude larger than the γ' channels.

SEM images of PWA1484 and René N5 (Figure 116 & Figure 117) confirm high γ' fractions. The same etching procedure was used for all three alloys. PWA1484 appears to have thicker γ channels, and therefore a lower percentage γ' is deduced in comparison to CMSX-4 and René N5.

6.6.2 Oxidation Studies.

An oxidation study has been carried out on all 3 alloys. Plain polished samples and polished and etched samples were examined by SEM after timed exposure in a furnace at 650°C. An initial oxidation study was carried out by the author. Three further studies incorporating weight measurements for all three alloys were carried out.

6.6.2.1 CMSX-4

Heavy oxidation was observed on CMSX-4 samples after just one hour. The γ matrix is clearly visible on a polished specimen (Figure 118). The etched sample also exhibited

rapid oxidation, after one hour the γ matrix had become much thicker and less well defined (Figure 119).

After 256 hours the polished sample had oxidised further, the oxidised γ matrix is clearly more prominent than after 1 hour exposure (Figure 120). On the etched samples, oxidation was so heavy in places that the γ matrix almost completely obscured the etched out γ' (Figure 121).

Oxidation was not consistent across the surface of each specimen. Small blemishes and areas of lighter and heavier oxidation can be observed. Light areas of the same order as the dendrite spacing are visible on the etched sample after 256 hours. No cracks were observed on any of the oxidation samples unlike the test specimens that later suffered from heavy cracking within the oxide layer. Sections through oxidised samples show the oxide layer is both additive and penetrative. The oxide layer is in region of 2-3μm thick with an actual increase of ~2μm with respect to the original substrate surface (Figure 122 & Figure 123).

6.6.2.2 ReneN5

After one hour exposure at 650°C a polished specimen exhibited a similar amount of oxidation as that seen in the CMSX-4 (Figure 124). Oxidation was not uniform throughout the sample with some areas experiencing more preferential oxidation than others being observed. Under SEM observation, areas of lighter speckled marks were found in the interdendritic regions of a polished sample after 1 hour (Figure 125), showing that the compositional differences between the dendrite centres and the interdendritic regions may be the reason for the varying degrees of oxidation thus the dendrites are effectively shown up by thermal etching. Figure 126 & Figure 127 show small light coloured globular protrusions, possibly oxidised carbides, around the edges of the dendritic regions. Weight gain from oxidation on René N5 was generally less than CMSX-4.

6.6.2.3 PWA1484

There are no micrographs of oxidation of PWA1484. Observations from the recorded masses are that all but one sample of PWA1484 gained weight. The weight gain of the PWA1484 samples was less than the CMSX-4

6.6.2.4 Summary

The small size of the samples meant that the accuracy of the weighing equipment (0.0001g) was insufficient to accurately record the small changes in mass. Average mass change results were lost within the experimental scatter and are not presented.

In general, the results show that visually René N5 oxidises in the same manner as CMSX-4, with the γ matrix showing preferential oxidation. This is expected as dendrites have the largest portion of Re which is relatively stable. Weight gain from oxidation on René N5 was generally less than CMSX-4. It was expected that due to the low chromium content of CMSX-4 and the comparatively higher Cr content in René N5, oxidation resistance would be better in the latter. Interdendritic carbides are clearly visible on samples of René N5 but are less prominent in CMSX-4. .PWA1484 also shows higher resistance to oxidation than CMSX-4.

6.6.3 Fatigue Testing Results

6.6.3.1 Fatigue Test Lifetimes.

Data is presented for a total of 31 fatigue tests. A total of 14 fatigue tests have been completed using the original 8mm x 8mm x 50mm CMS4 samples. Further samples of 4mm x 4mm x 50mm were produced to increase the number of tests possible from the batch of CMSX-4 available. Test data from 5 small CMSX-4 bars is presented with the help of undergraduate project student Amira Kawar.

During the test program, a small quantity of René N5 became available for testing and has been used for comparison with the CMSX-4 as a similar 2nd generation superalloy. Testing and analysis of 6 fatigue tests has been carried out on (10mm x 10mm x 50mm) specimens with the help of undergraduate project student Irene Lee.

Fatigue testing using PWA1484 was carried out at CNRC as part of the collaborative research programme between University of Southampton Dept and CNRC,. Test data for 6 axial fatigue tests has been supplied by CNRC along with test specimens in order to perform microscopic analysis on the fracture surfaces courtesy of Dr Xijia Wu..

All test data and results are presented in Table 11, Table 12, Table 13 & Table 14. A strain life graph of cycles to failure for each test is given in Figure 152.

CMSX-4 8x8

Tests, 1,2 and 3 were used to establish a suitable lifetime in order to conduct interrupted replica tests, misoriented specimens were chosen for these calibration tests. A target lifetime in the order of 10,000 was identified. The data generated from the FE model was used to select a suitable load/strain condition for the first test.

The first test ran for 100,000+ cycles. Towards the end of the test the load was increased. This increased load value was used as a starting point for the next test but further increases were required in order achieve an acceptable lifetime to failure. An effective calculated strain range of 1.35% gave a lifetime of 62,000 cycles. All further tests using 8mm x8mm bars of CMSX-4 were tested at an estimated strain range of 1.38%.

Initial results for orientation A and B in air showed favourable lifetimes with respect to conducting replica tests. At 650°C in air the orientation A specimen had a considerably longer lifetime. At 725°C in air the effect of orientation swapped over, with the orientation B specimen giving a longer lifetime.

In Vacuum, orientation A tests had longer lifetimes that orientation B at 625°C and 725°C.

A replica test was attempted at 650°C. Heavy oxidation was observed on the notch surface after a short period of time. This heavy oxidation masked any cracks that may have initiated on the notch surface. Cracks in the oxide layer of the notch appeared and disappeared throughout the duration of the test thus making replica records very difficult to interpret. This replica test was stopped after ~8000 cycles at which point ~30 replicas had been taken. The test was then run to failure without any further interruptions

CMSX-4 4x4

Considerably less scatter is observed in the test lifetimes of 4x4 test specimens in comparison to the larger 8mm x 8mm specimens. Further investigation into the specimen geometry shows that the variation in dimensions is much higher than the stated accuracy of the EDM tooling used to produce the test specimens. Specimen dimensions have been checked using digital vernier calliper and stress and strain values have been altered accordingly. Some specimens were rejected due to tapering of the bar thus leaving predominantly orientation B test pieces. The variation in cycles to failure for each of the tests cannot be accounted for by the variation in geometry alone.

René N5

A total of 6 bars have been tested to date; 3 bars of orientation A and 3 of orientation B. The first 3 tests conducted on orientation B bars produced lifetimes of ~3000 cycles. Lifetimes for orientation A samples showed the largest scatter with the lowest lifetime cycle being 3346 and the highest being 11,490. Of the 6 tests conducted on René N5 bars, orientation A samples tended to have longer lifetimes than orientation B.

PWA1484

Testing of PWA1484 was carried out at CNRC. All testing was carried out in load control at 1Hz in axial tension at several strain ranges. Tests had much longer lifetimes in general and the scatter observed showed overlap between the different strain ranges tested.

6.6.3.2 Fracture Surface Overviews.

Figure 128 through to Figure 151 show series of fracture surface overviews for specimens tested to failure in the form of exploded views. The main fracture surface is in the centre, surrounded by the appropriate side and top profiles so the extent of out-of-plane faceting can be fully appreciated in each case.

CMSX-4 8x8

Room temperature test fracture surfaces (Figure 128) exhibit large facets on the fracture surfaces. Facets have formed along the {111} planes.

At 650°C in air, fracture surfaces appear less faceted than the room temperature tests (Figure 129 & Figure 130). Side facets have formed but the fracture surface is relatively smooth in the middle of the specimen. The orientation B specimen appears more faceted that orientation A. Facets on Orientation A specimen run parallel to the sides of the fracture surface, whilst the orientation B specimen has facets that intersect the sides at 45°. Major initiation points can be identified even on these low magnification overviews.

At 725°C in air the fracture surfaces look similar to those at 650°C (Figure 131). Side facets are however slightly smaller. There is a smooth region in the centre of the

fracture surface. Some initiation points can still be identified (although they are less distinct).

At 650°C in vacuum fracture surfaces are similar to those tested in air (Figure 132). Side facets are comparable in size. The fracture surface is not obscured by oxidation and dendrites are observed on the initial fracture area before the onset of extended slip band cracking.

At 725°C in vacuum fracture surfaces have much larger side facets. In both cases the side facet from one side only dominates the fracture surface (Figure 133 & Figure 134). The orientation A sample has a similar area of 'smooth' fracture surface compared to the air test. The orientation B sample exhibits a massive facet that cuts through most of the notch. The faceted area has a very smooth/shiny fracture surface.

Small 4x4 bars were all tested at 650°C in air. Side facets take up a larger proportion of the fracture surface than on the 8mm x 8mm samples. 'Smooth' areas of initial crack growth are similar in appearance to the larger test samples (Figure 135 & Figure 139).

The orientation A samples appear less faceted whereas the facets on bar 17 (Figure 136) almost meet in at the centre of the fracture surface.

René N5

The fracture surfaces obtained from the testing show much similarity with the CMSX-4 fracture surfaces with orientation B bars appearing more faceted than those from orientation A. The fracture surfaces appear to be relatively smooth in the middle of each specimen where it appears that initial crack growth has taken place (Figure 140 Figure 145).

The orientation of the dendrites can be seen on the fracture surfaces with the dendritic structure appearing in the shape of a'+' or 'x' depending on orientation.

PWA1484

All the specimens showed extremely large, effectively single, facets at 45° to the tensile axis. These edges do not show 'zig-zag' faceted growth except for one sample. The initiation sites could be clearly identified through the macroscope (Figure 146 to Figure 151).

The fracture surfaces in all the PWA1484 samples tend to be smoother along the macroscopic facets when compared to the sections near the notches. Dendrites can be observed on some of the fracture surfaces. The fracture surfaces are shinier than either the CMSX-4 or the René N5 samples thus suggesting less oxidation of the fracture surface.

6.6.3.3 Detailed Fractography –

CMSX-4 Tests in Air

Room temperature tests exhibit multiple surface initiation points. Figure 153 and Figure 154 give an example of an interdendritic pore that caused initiation of the critical crack. River-lines were observed on fracture surfaces and were used to trace back to the major, and minor crack initiation sites.

An example of a pore on the notch surface that did not initiate a crack is given (Figure 155) also note the etched microstructure on the surface and within the pore clearly showing the narrow γ-matrix channels retained after the etching away of the γ' precipitates. The circular appearance of such pores on the top surface gives little indication of the 3D nature of these complex casting defects. The fracture surface shows the critical pore cross-section that initiates failure to be angular and elongated.

At high temperatures, Initial crack propagation was smooth with river lines (Figure 156 B) pointing back towards major and minor initiation points (Figure 156 A). The fracture surface was obscured by oxidation. As the crack progressed further through the specimen, alternating slip band cracking was observed (Figure 156 C) along {111} slip planes at high crack tip stresses.

At 650°C heavy oxidation of the notch root was observed during and at the end of the first test to failure (Figure 157 and Figure 158). Cracks were observed in the oxide layer, both during, and at the end of the test. The cracks appeared to penetrate the substrate at times (Figure 159 and Figure 160) but did not initiate the major fatigue crack. Further evidence of this is seen in Figure 161, Figure 162 & Figure 163.

Crack initiation at high temperatures occurred at sub surface pores in all cases; 650°C and 725°C orientations A and B. An example of a fracture surface at 725°C orientation A is show in Figure 164 with crack initiation locations marked. Although large cracks are seen in the surface oxide they do not appear to be the primary cause of failure (Figure 165).

All initiating sub surface pores were encircled by a halo, examples of which are given in (Figure 166 to Figure 169). The halo is generally circular in shape with its uppermost boundary touching, or coming very close to, the surface of the notch. Subsurface pores were predominantly irregular shapes consistent with interdendritic spacing both in size and shape. The texture of the fracture surface within the halo differs from that seen in the surrounding area. This is better observed using backscattered electron imaging (Figure 170) to look at topographical features on the fracture surface. Using this method several new crack initiation points were identified.

A compositional scan also picked up differences within the halo region compared with the surrounding area (Figure 171) and shows an enriched area within the halo. This feature was observed at several other halo initiation sites. The compositional scan has been broken up into individual elements in order to identify depleted areas (Figure 172 to Figure 180).

Further down the fracture surface 2-4mm away from the notch root alternating slip band cracking is observed along {111} slip planes at high crack tip stresses (Figure 181 & Figure 182).

Due to the high levels of oxidation it was necessary to section the fracture surface to reveal more detail of the interaction between the microstructure and the fatigue cracks. Figure 183 provides details of where the cuts were made and the locations of the subsequent figures. The oxide layer is seen to be thicker in the notch root than on the fracture surface (Figure 184) with the notch root oxide in the order of 1 – 1.5μm. At high magnification the cracks can be seen to following slip bands and cutting the γ' precipitate (Figure 185). In Figure 186 several slip bands are observed. The crack is caused to deviate due to the proximity of a pore and swaps from travelling along one slip band to another. At this location closer to the fracture surface, some signs of oxidation along the crack can be observed. A section through 'rooftop' facets formed at high ΔK levels (Figure 187) shows a heavily oxidised secondary crack extending along a slip band from one of the facets.

CMSX-4 Tests in Vacuum

Four tests were conducted on CMSX-4 samples in vacuum. A minimum vacuum level of $1x10^{-5}$ mbar was achieved for each test. From initial observation there were no signs of oxidation during the tests – this was expected but confirmed the quality of the vacuum achieved.

Dendrites are immediately visible on the fracture surface under an optical microscope and SEM (Figure 188). Crack initiation occurs at porosity both at the surface (Figure 189) and subsurface (Figure 190 & Figure 191) although it is much harder to pinpoint subsurface initiation due to the lack of the halo feature around the porosity which is presumed to be caused by an oxidation phenomenon – this is discussed more detail in section 6.8

Much more detail is present on the fracture surface in comparison to the tests conducted in air. The interaction of slip bands with pores is observed and the presence of striations can be seen on some of the larger faceted areas of the fracture surface (Figure 192). At high ΔK levels the effect of porosity on highly micro-faceted crack propagation is observed (Figure 193).

Without a difference in oxidation around a pore on the fracture surfaces is more difficult to categorise porosity initiation sites as surface or subsurface. Figure 194 appears to be an example of surface initiation with Figure 190 & Figure 191.showing examples sub surface porosity initiation all on the same fracture surface (OA, Vacuum, 650°C).

René N5 Tests in Air

An overview of an orientation A fracture surface is shown in Figure 195 (OA, 650°C, Air, 3346 cycles). The major initiation sites are clearly visible and were also identified by the river lines which appear to lead back to major and minor sites of initiation. These sites were then examined in detail with the points of interest labelled A to D as depicted in Figure 195.

Subsurface pores were found at locations A, B and D and a relatively large surface pore of approximately 7.5μm in length was located at site C. A circular 'halo' was found around the pore at site D (Figure 203) with its uppermost boundary nearly reaching the notch surface. It was also noted that the texture of the surface within the halo differed from the surrounding area. The subsurface pores were found to be consistent in size with the interdendritic spacing.

An example of an orientation B specimen is given in Figure 204. Initiation from porosity is seen to occur at sites A,B, D and E (Figure 205 to Figure 208). At the initiation site located at site C, river lines lead to what appears to be an oxidised carbide (Figure 209 Figure 210)

The characteristic subsurface pore and halo feature is present on most of the fracture surface samples, two examples of which are given in Figure 211 & Figure 212.

PWA1484 Tests in Air

Examples of 2 PWA1484 fracture surfaces are give in Figure 213 to Figure 220. Figure 213 shows an overview of a fracture surface with the main initiation point labelled. SEM images at successively higher resolutions (Figure 214 Figure 215 Figure 216) trace the initiation point back to a dark phase most likely to be a secondary carbide. The smooth surface area of this sample is relatively small. A large number of pores are visible on the side facet (Figure 214) but there is no sign of cracks initiating from porosity.

A second example of a PW1484 fracture surface is given in Figure 217. Dendrites are clearly visible in Figure 218. The main initiation point is visible as a half circular area (Figure 219) with river lines running back towards the initiating feature, which in this case is an interdendritic pore (Figure 220).

6.6.3.4 Collection of Porosity Data

It is apparent that porosity is one of the main factors that controls fatigue life in alloy 3 alloys and may be a source of some of the scatter seen in the fatigue life data.

Several parameters that describe the pore size and location have been defined (Figure 221 and Figure 222) and used to collect data about initiating pores on all fracture surfaces. The irregular shape of the pores made taking measurements quite difficult and potentially very subjective. For each pore, a centroid was estimated. From this point, the depth of the pore (d) was recorded. The greatest distance across the pore, tip to tip, passing through the centre was recorded as the major dimension (x). The minor dimension (y) is measure at 90° to the major axis and is taken as an average dimension as indicated by the dashed lines The tessellation analysis software (TAP) was used to measure the area of the pore from a digital image and provide data about the aspect ratio. The aspect ratio defined in TAP is the maximum chord length divided

by the perpendicular width. Tables of results containing the porosity information are presented for each alloy in Table 15.

CMSX-4	Obj Area (μm²)	Obj Aspect Ratio	Obj Angle (rad)	No. NNs	NN Dist (μm)	Mean NND (μm)	NN Angle (rad)
Mean	542.1	1.2	0.7	5.8	67.9	195.6	0.8
Median	440.0	1.1	0.7	6.0	56.8	194.0	0.8
Mode	3.0	1.1	0.8	5.0	6.9	99.1	0.2
Standard Deviation	503.2	0.3	0.4	1.4	58.2	70.9	0.5
Minimum	3.0	1.0	0.0	2.0	4.8	12.0	0.0
Maximum	2241.9	5.1	1.6	10.0	268.5	374.8	1.6
Sum	375667.4	849.4	471.3	4017.0	47047.4	135585.1	562.6
Count	693	693	693	693	693	693	693
Total area analysed	28.79 mm²						
% porosity	1.30%						

Table 7 CMSX-4 porosity data (3 samples taken)

René N5	Obj Area (μm²)	Obj Aspect Ratio	Obj Angle (rad)	No. NNs	NN Dist (μm)	Mean NND (μm)	NN Angle (rad)
Mean	105.2	1.5	0.6	5.7	56.8	181.3	0.8
Median	14.9	1.3	0.5	6.0	35.6	173.8	0.8
Mode	3.0	1.0	0.0	5.0	3.5	#N/A	0.5
Standard Deviation	222.3	0.6	0.5	1.9	63.7	92.6	0.4
Minimum	3.0	1.0	0.0	2.0	3.5	4.1	0.0
Maximum	1443.7	4.8	1.6	12.0	319.9	438.6	1.6
Sum	79499.4	1136.6	434.1	4311.0	42962.4	137071.4	592.3
Count	756	756	756	756	756	756	756
Total area analysed	27.42 mm²						
% porosity	0.29%						

Table 8 René N5 porosity data (3 samples taken)

PW 1484	Obj Area (μm²)	Obj Aspect Ratio	Obj Angle (rad)	No. NNs	NN Dist (μm)	Mean NND (μm)	NN Angle (rad)
Mean	241.2	1.4	0.6	5.7	45.9	142.6	0.8
Median	50.7	1.1	0.6	6.0	31.1	138.6	0.9
Mode	3.0	1.0	0.0	5.0	3.5	41.7	1.1
Standard Deviation	406.1	0.6	0.5	1.7	45.5	80.8	0.5
Minimum	3.0	1.0	0.0	2.0	3.5	3.5	0.0
Maximum	3704.7	4.5	1.6	11.0	217.4	369.9	1.6
Sum	274239.3	1611.0	676.8	6495.0	52178.2	162155.1	953.4
Count	1137	1137	1137	1137	1137	1137	1137
Total area analysed	28.64 mm²						
% porosity	0.96%						

Table 9 PWA1484 porosity data (3 samples taken)

	Vickers Hardness Value		
	Dendritic Region		**Interdendritic Region**
CMSX-4			
A {110}	342	>	318
B {100}	356	>	295
C {111}	323	>	298
René N5			
A {110}	336	>	313
B {100}	350	>	349
C {111}	348	>	346

Table 10 – Average Vickers Hardness Values for CMSX-4 and René N5

Test ID.	Wave-form	Temp (°C)	Air/ Vac	Orient-ation	Pmax (KN)	"Δε" (%)	Cycles to Failure
1	20Hz	21	Air	X	4.9	0.95	100,000+
2	1-1-1-1	650	Air	X	5.7	1.21	100,000+
3	1-1-1-1	650	Air	X	6.1	1.35	62,000
6	1-1-1-1	650	Air	B	6.2	1.38	6500
4	1-1-1-1	650	Air	A	6.2	1.38	25,500
14	1-1-1-1	650	Vac	B	6.2	1.38	9,378
16	1-1-1-1	650	Vac	A	6.2	1.38	15,871
9	1-1-1-1	725	Air	A	6.2	1.38	5,271
11	1-1-1-1	725	Air	B	6.2	1.38	13,717
7	1-1-1-1	725	Vac	A	6.2	1.38	11,363
12	1-1-1-1	725	Vac	B	6.2	1.38	4,960
8	5Hz	21	A	A	6.2	1.38	21,661
13	1-1-1-1	650	Air	B	6.2	1.38	46,665
15	1-1-1-1	650	Air	B	6.2	1.38	9,632

Table 11 CMSX 8mm x 8mm Fatigue Test Results

Test ID.	Wave-form	Temp (°C)	Air/ Vac	Orient-ation	Pmax (KN)	"Δε" (%)	Cycles to Failure	Images
16	1-1-1-1	650	Air	A	Overload	3.37	500	Figure 135
17	1-1-1-1	650	Air	B	1	1.49	3592	Figure 136
24	1-1-1-1	650	Air	B	0.85	1.19	81,000	Figure 137
28	1-1-1-1	650	Air	B	1.2	1.54	130,792	Figure 138
29	1-1-1-1	650	Air	B	0.8	1.48	16,386	Figure 139

Table 12 CMSX-4 4mm x 4mmm Fatigue Test Results

Test ID.	Wave-form	Temp (°C)	Air/ Vac	Orient-ation	Pmax (KN)	"Δε" (%)	Cycles to Failure	Images
1	1-1-1-1	650	Air	B	12.26	1.38	3,325	Figure 140
2	1-1-1-1	650	Air	B	12.26	1.38	2,573	Figure 141
3	1-1-1-1	650	Air	B	12.26	1.38	3,507	Figure 142
4	1-1-1-1	650	Air	A	12.26	1.38	4,945	Figure 143
5	1-1-1-1	650	Air	A	12.26	1.38	3,346	Figure 144
6	1-1-1-1	650	Air	A	12.26	1.38	11,490	Figure 145

Table 13 René N5 10mm x 10mm Fatigue Test Results

Test ID.	Wave-form	Temp (°C)	Air/ Vac	Orient -ation	Pmax (KN)	"Δε" (%)	Cycles to Failure	Images
P28-A	1Hz	520	Air	B	12.26	1.26	58495	Figure 146
P28-B	1Hz	520	Air	B	12.26	1.26	121110	Figure 147
P24-B	1Hz	500	Air	B	12.26	1.19	127649	Figure 148
P22-B	1Hz	480	Air	B	12.26	1.12	136206	Figure 149
P22-A	1Hz	480	Air	B	12.26	1.12	154284	Figure 150
P26-A	1Hz	500	Air	B	12.26	1.19	182001	Figure 151

Table 14 PWA1484 axial tension tests (CNRC) Fatigue Test Results

Bar/Pore details	Area (μm²) From TAP	Aspect Ratio (a/c) From TAP	Major Axis (μm)	Minor Axis (μm)	Depth (μm)	Area (μm²) From TAP	Aspect Ratio (a/c) From TAP	Major Axis (μm)	Minor Axis (μm)	Depth (μm)
			Side A					Side B		
CMSX4-1	1011	1.09	40	13	0					
CMSX4-2										
CMSX4-3	494	6.5	100	10	80					
CMSX4-4	1351	3.7	100	25	250					
CMSX4-6	2639	1.7	90	10	130					
	735	1.2	30	40	25					
	645	2.5	75	10	40					
CMSX4-7	1933	2.9	128	24	47					
CMSX4-8	715	1.8	40	15	0					
	495	1.5	30	10	0					
	438	1.8	25	10	0					
CMSX4-9	1903	2.0	50	30	200					
	842	2.0	60	60	350					
	550	1.5	30	20	50					
	860	1.2	60	10	125					
	426	2.1	50	10	90					
CMSX4-11	1062	2.0	50	5	350					
	791	1.5	80	10	45					
CMSX4-12	1230	4.2	92	33	40					
CMSX4-14	2554	2.4	90	28	0					
CMSX4-15										
CMSX4-16	3095	1.7	128	40	0					
	5563	1.5	147	83	114					
Bar 13_AK_OB_pore A	1106.8	5.7	72.9	4.8	44.2	1031.5	4.1	68.8	4.8	44.2
Bar 16_AK_OB										
Bar 17_AK_OB_ pore A	591.6	1.4	19.2	9.8	16.3	555.0		19.2	9.2	15.2
Bar 17_AK_OB_pore B	228.2	1.3	10.9	6.7	10.7	213.3	1.4	10.3	6.6	9.1
Bar 17_AK_OB_pore C	273.1	1.9	17.8	4.9	19.6	298.2	1.9	18.8	5.1	23.8
Bar 17_AK_OB_pore D						1418.4	1.6	40.0	11.3	86.7
Bar 24_AK_OB_pore A	1243.6	1.4	32.5	12.2	246.7	1405.5	1.6	33.3	13.4	260.0
Bar 28_AK_OB_pore A	223.5	3.2	23.0	3.1	22.3	134.5	5.0	20.2	2.1	20.0
Bar 29_AK_OB_pore A	576.5	1.3	19.7	9.3	40.7	571.8	1.7	19.6	9.3	*N/A*
P22-A	552.1		18.4	9.5	24.7					
P22-B	2185.5	3.5	58.3	11.9	90.0					
P24-A	175.8	1.4	9.1	6.2	36.4					
P26-A	348.3	1.7	11.5	9.6	32.0					
P28-A	1185.5	1.9	30.6	12.4	92.6					
P28-B	1292.5	2.7	52.8	7.8	50.0					
Bar 1_IL_OB_Pore A	312.7	1.2	10.9	9.1	11.6	279.4	3.1	20.8	4.3	10.3
Bar 1_IL_OB_Pore B						1672.3	2.8	53.0	10.0	59.1
Bar 1_IL_OB_Pore C	107.4	1.3	7.3	4.7	38.2	106.2	1.1	6.7	5.1	42.7
Bar 1_IL_OB_Pore D	1488.1	3.0	47.8	9.9	62.6	347.5	1.3	17.1	6.5	28.0
Bar 1_IL_OB_Pore E(2)						398.7	1.7	16.3	7.8	15.7
Bar 1_IL_OB_Pore E	412.1	1.8	18.2	7.2	16.7	531.9	1.2	17.4	9.7	52.2
Bar 1_IL_OB_Pore F						234.1	1.2	10.0	7.5	23.3
Bar 1_IL_OB_Pore G	187.8	1.1	8.3	7.2	27.3	681.8	1.4	26.5	8.2	48.7
Bar 1_IL_OB_Pore H	172.1	3.5	15.2	3.6	23.9					
Bar 1_IL_OB_Pore I	210.4	1.2	9.5	7.0	13.6	210.4	1.2	9.5	7.0	13.6
Bar 1_IL_OB_Pore J	268.3	1.1	10.0	8.5	14.7					
Bar 1_IL_OB_Pore K	257.5	1.1	9.8	8.4	15.9	551.9	2.2	25.0	7.0	29.1
Bar 1_IL_OB_Pore L	45.8	1.1	4.5	3.2	6.0					
Bar 1_IL_OB_Pore M	141.4	1.2	7.0	6.4	15.0	282.6	3.0	20.0	4.5	8.0
Bar 1_IL_OB_Pore N	1419.2	1.3	35.0	12.9	20.7	240.5	1.4	10.2	7.5	7.3
Bar 1_IL_OB_Pore O	50.1	1.4	5.1	3.1	6.3	265.4	1.7	14.0	6.0	22.2
Bar 1_IL_OB_Pore P(1)	357.8	1.6	15.9	7.2	90.9					
Bar 1_IL_OB_Pore P(2)	362.1	1.6	20.5	5.6	53.6					
Bar 10_IL_OA_Pore A	373.6	1.4	13.6	8.7	28.8	6208.1	1.3	77.1	25.7	
Bar 10_IL_OA_Pore B	1341.8	3.9	60.9	7.0	25.5	1429.7	1.9	32.3	14.1	21.0
Bar 10_IL_OA_Pore C(1)						591.0	5.6	58.1	3.2	26.5
Bar 10_IL_OA_Pore C(2)						332.0	1.2	12.3	8.6	15.3
Bar 10_IL_OA_Pore C	2052.1	2.2	53.3	12.3	17.1					
Bar 10_IL_OA_Pore D	7347.4	1.3	81.6	28.7	81.6	626.4	1.8	20.7	9.7	50.7
Bar 10_IL_OA_Pore E	375.0	1.3	11.8	10.1	12.7	375.0	1.3	11.8	10.1	12.7
Bar 11_IL_OA_Pore B	457.0	1.2	18.7	7.8	41.3	457.0	1.2	18.7	7.8	41.3

Table 15 – Data from all initiating pores in all 3 alloys

Figure 104 CMSX-4 dendrites (100) orientation

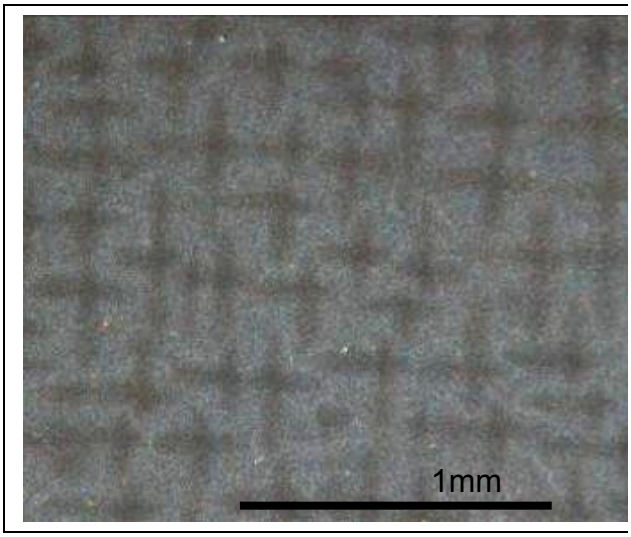

Figure 105 PWA1484 dendrites (100) orientation

Figure 106 - René N5

Figure 107 SEI Image

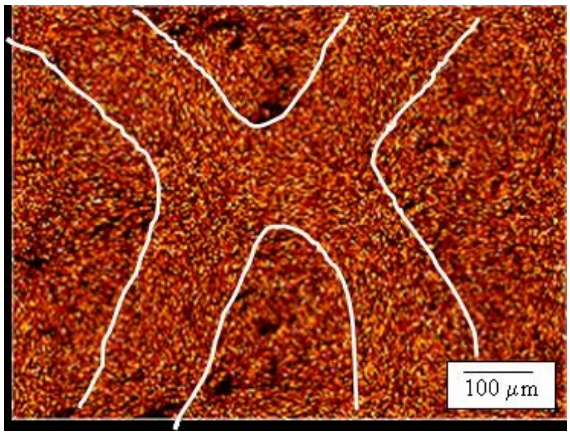

Figure 108 Rhenium Concentration

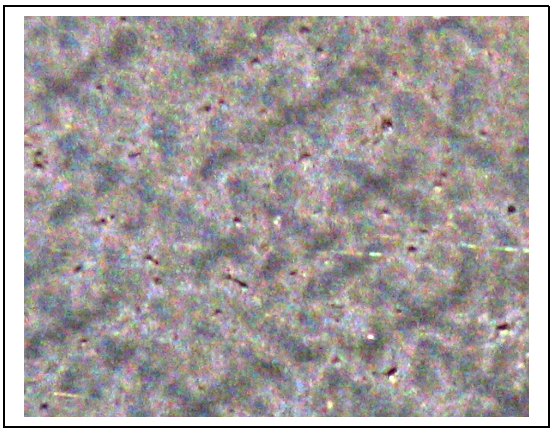

Figure 109 - Example of interdendritic porosity in RenéN5

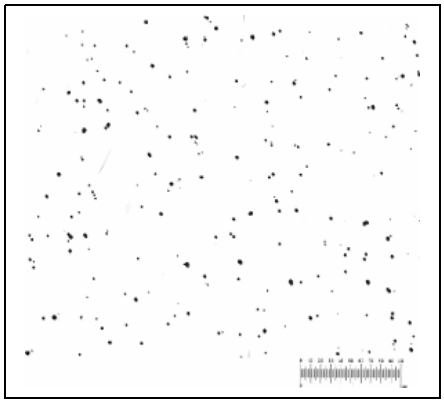

Figure 110 Sample of porosity in CMSX-4 used for porosity analysis (collage of 4 separate images)

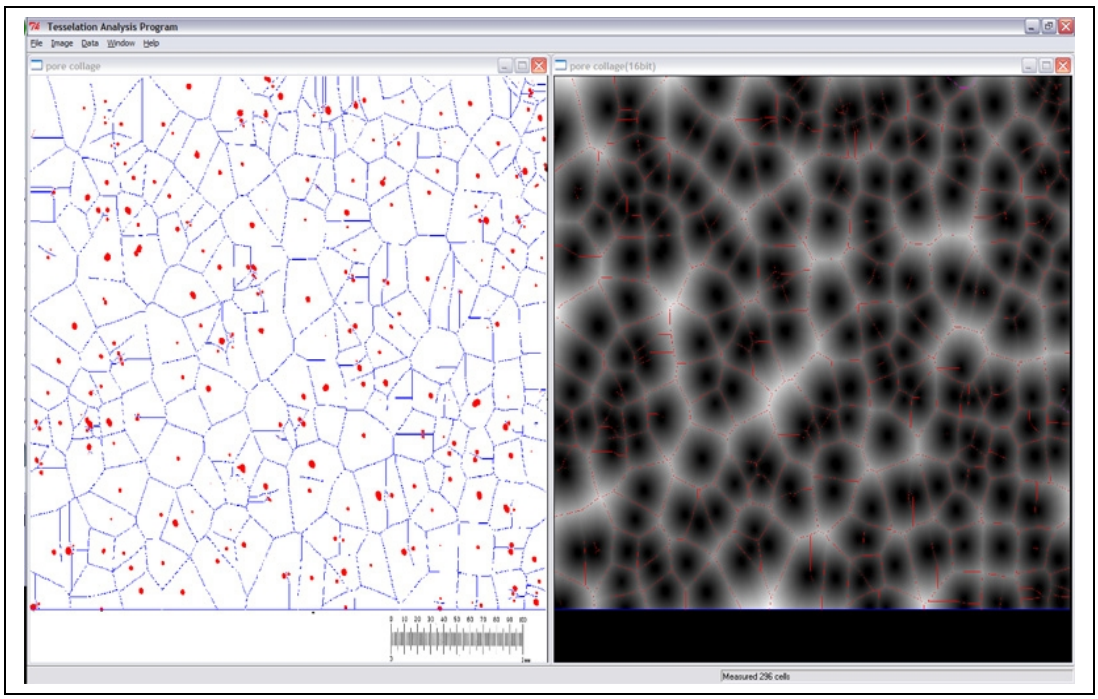

Figure 111 – Example of FBTA cell gathering for CMSX-4 porosity

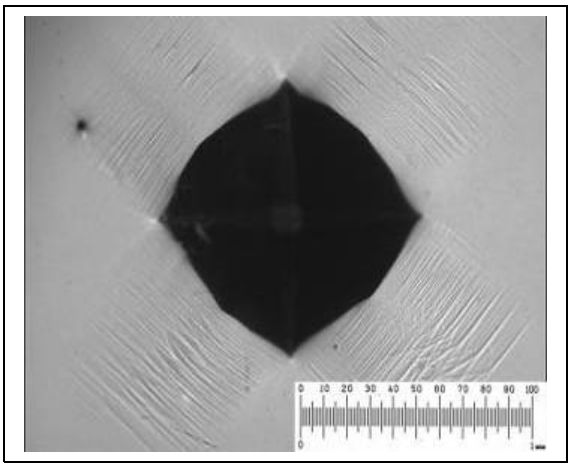

Figure 112 CMSX-4 - Slip bands around a hardness indent

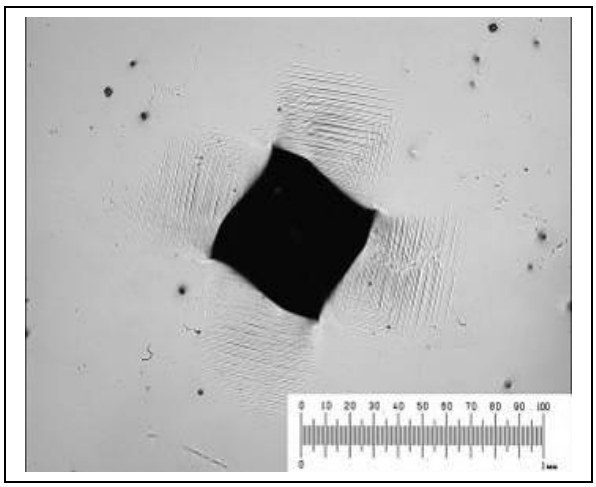

Figure 113 PWA1484 - Slip bands around a hardness indent

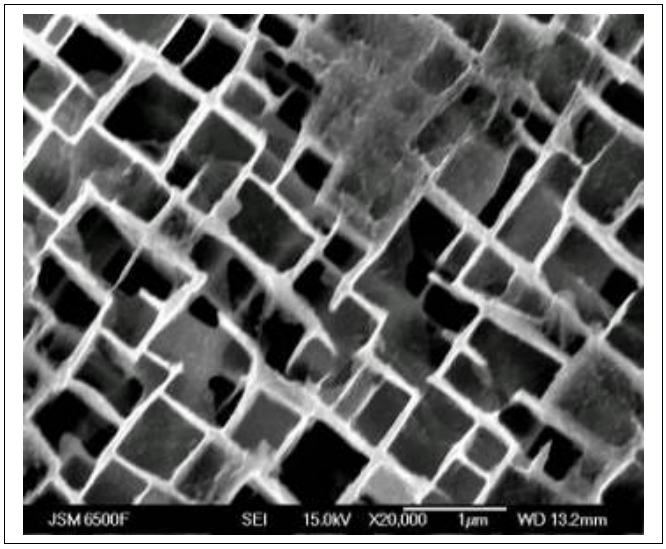

Figure 114 CMSX-4 etched surface {001} orientation using FEG-SEM

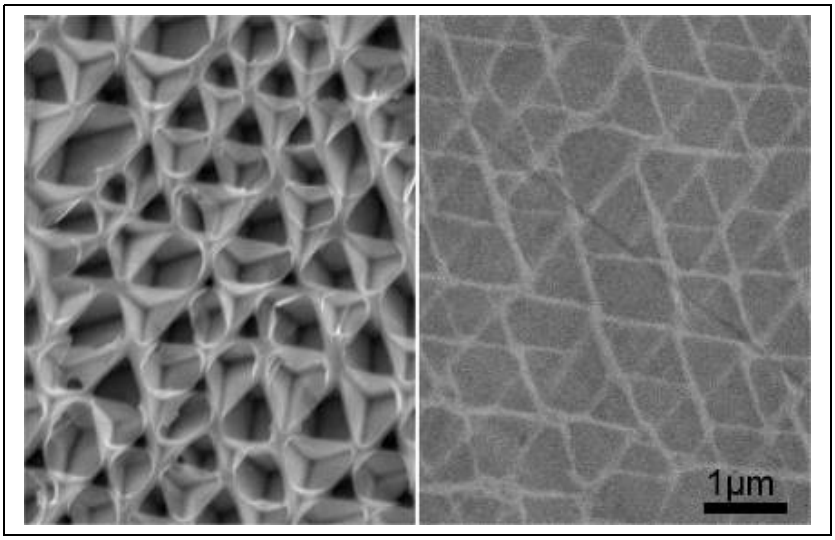

Figure 115 SEM images Etched surface (left) Backscattered electron image (right) 111 plane

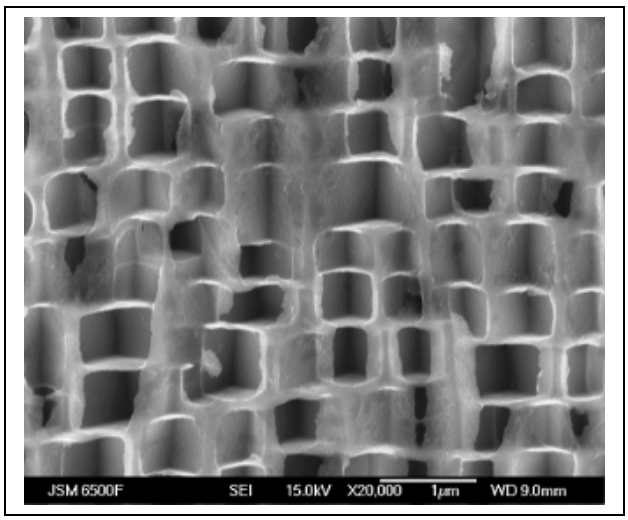

Figure 116 SEM image Etched surface of René N5 γ matrix (110) orientation A

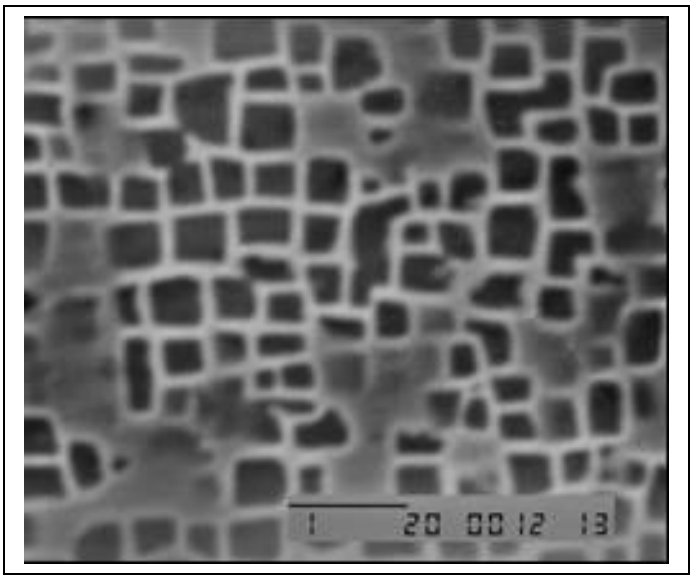

Figure 117 SEM image Etched surface of PWA1484 γ matrix (110) orientation A

Figure 118 SEM images – Polished CMSX-4 after 1 hour exposure at 650°C (A) Preferential oxidation of γ matrix (B) Surface blemish (C) γ obscured

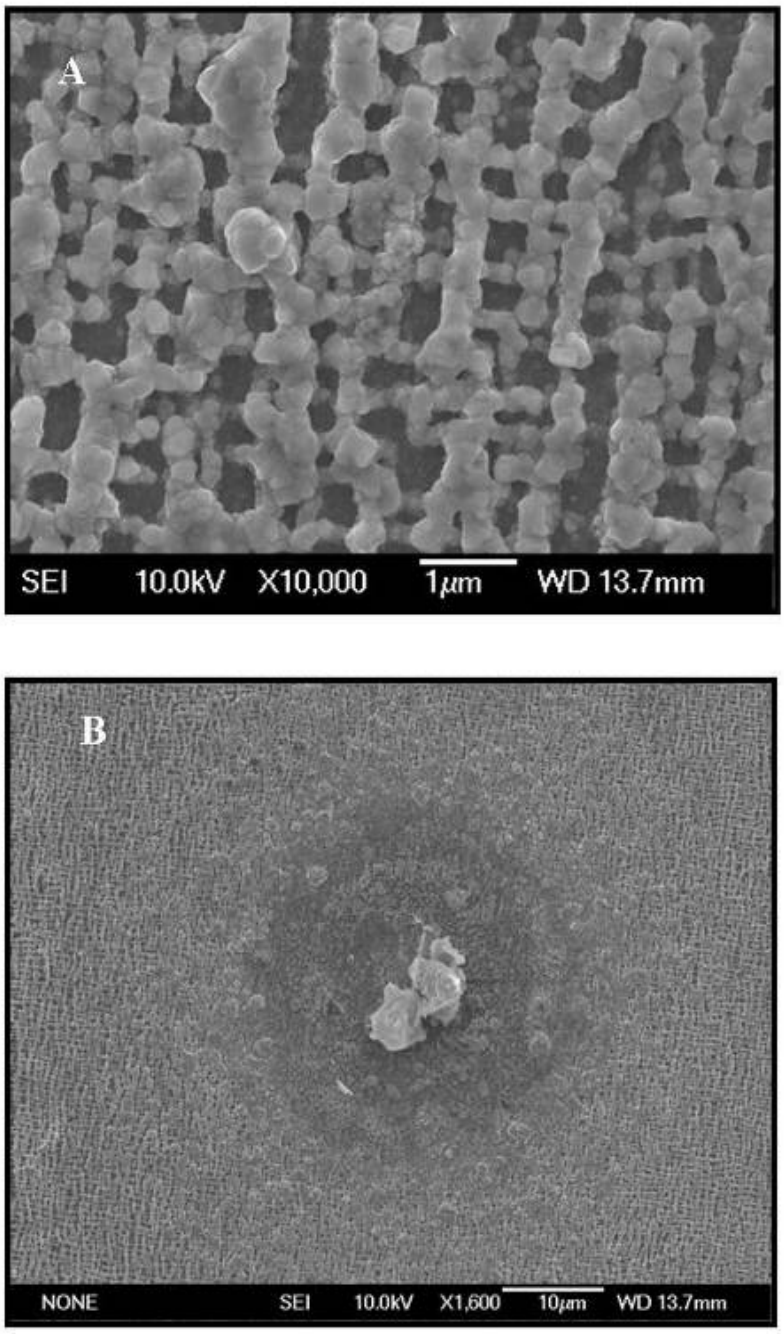

Figure 119 SEM images – Polished CMSX-4 after 256 hours exposure at 650°C
(A) Preferential oxidation of γ matrix (B) Surface blemish

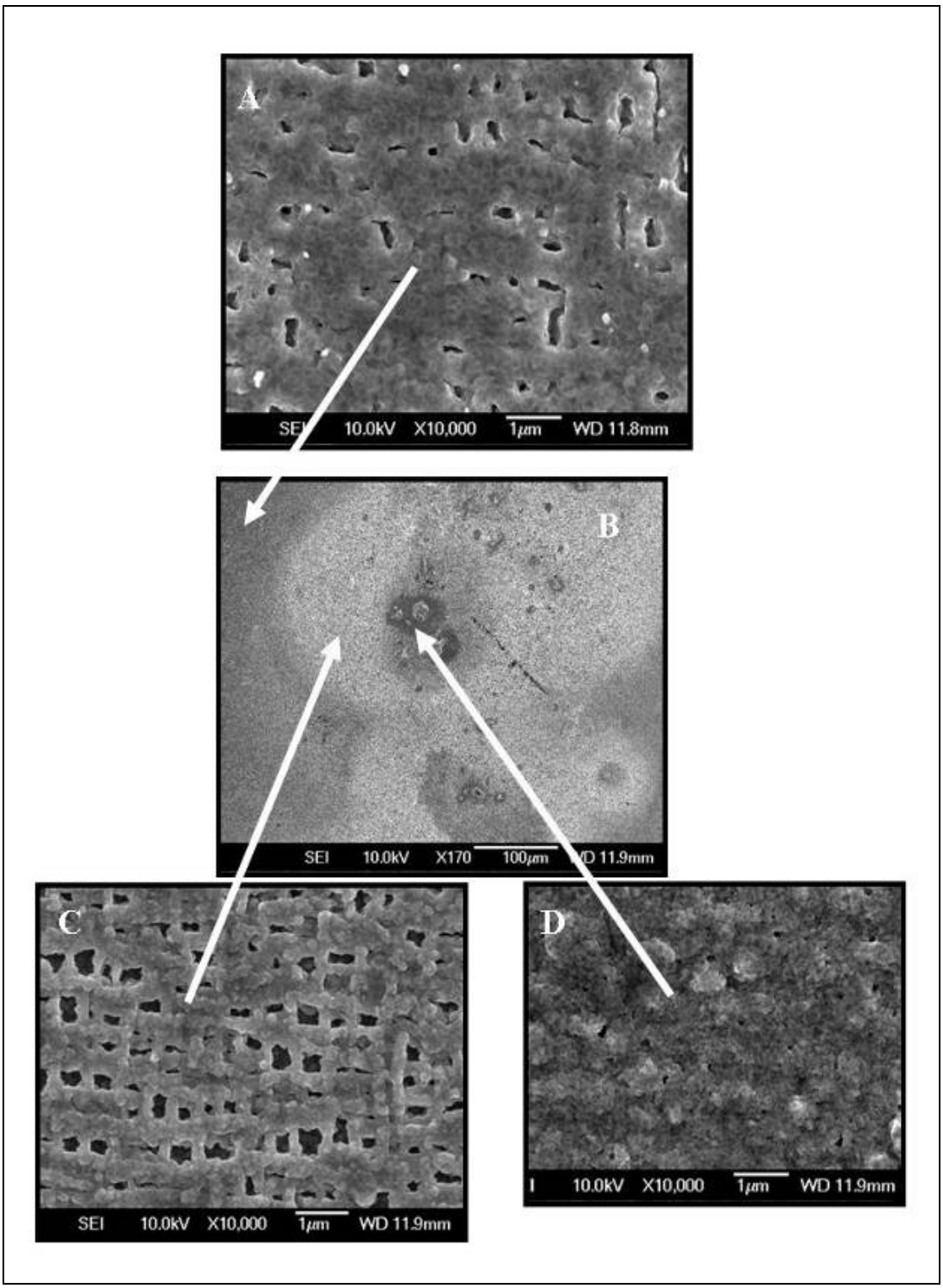

Figure 120 SEM images – Polished and etched CMSX-4 after 1 hour exposure at 650°C (A) Heavily oxidised γ matrix (B) overview (C) Oxidised γ (D) γ totally obscured

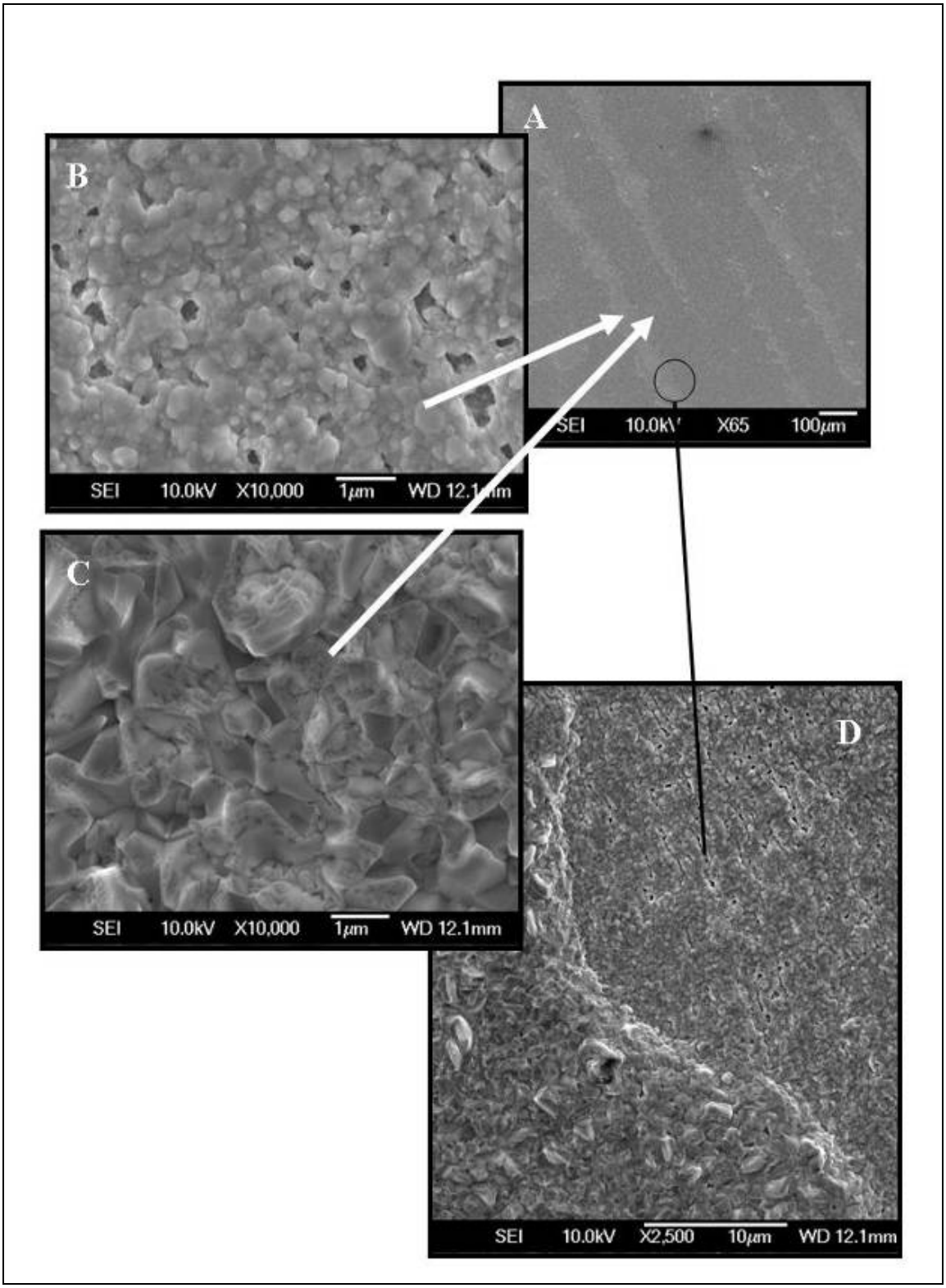

Figure 121 SEM images – Polished and etched CMSX-4 after 1 hour exposure at 650°C
(A) Light areas consistent with dendrite spacing (B) Heavily oxidised γ matrix (C) γ totally obscured
(D) transition between light and dark area in (a)

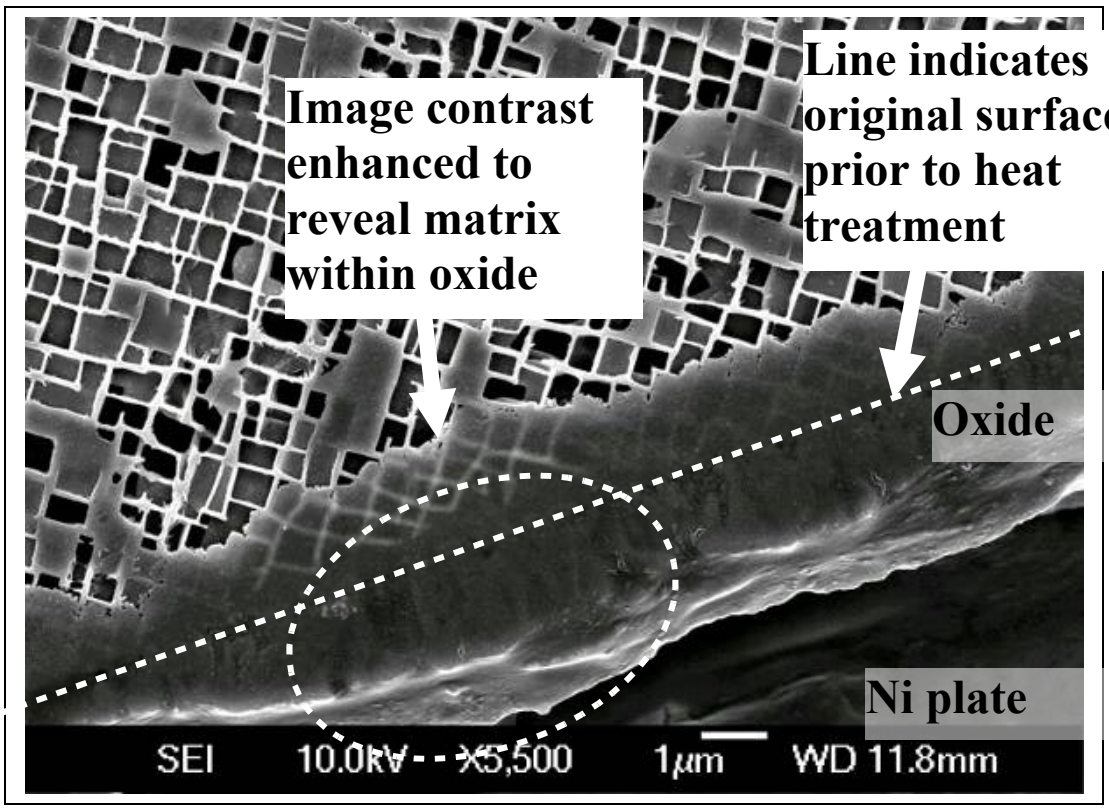

Figure 122 SEM image - Slice from oxidised sample showing oxide thickness.

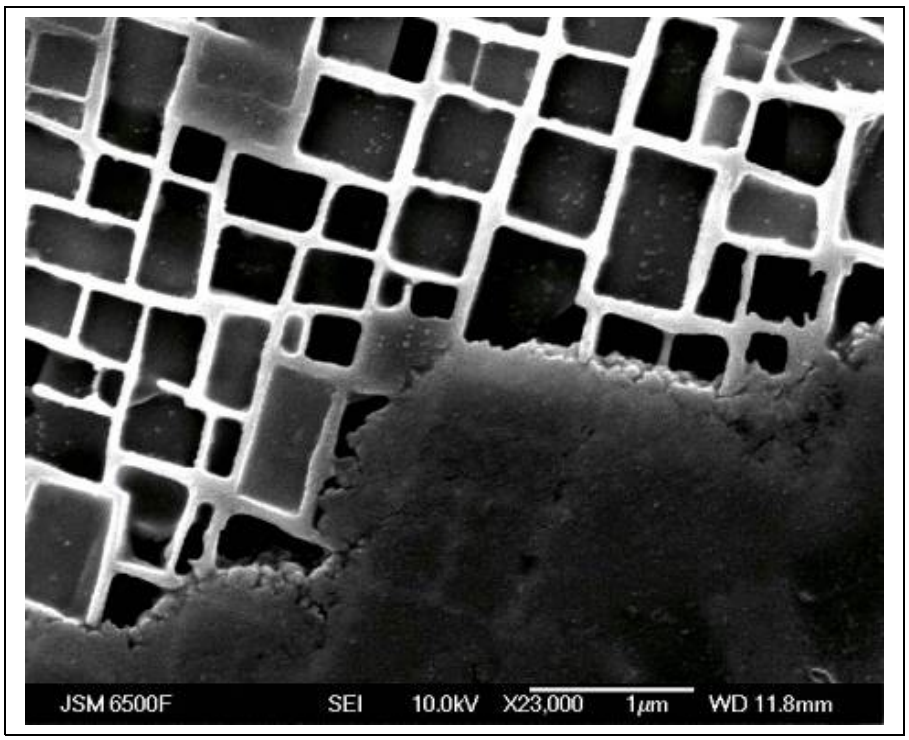

Figure 123 SEM image – As Figure 122, higher magnification

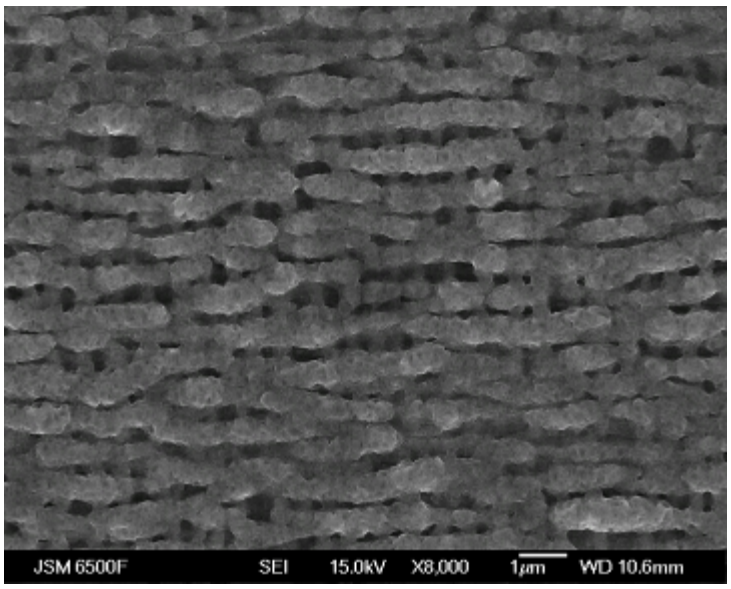

Figure 124 - Preferential oxidation of γ' on an polished sample of Rene N5

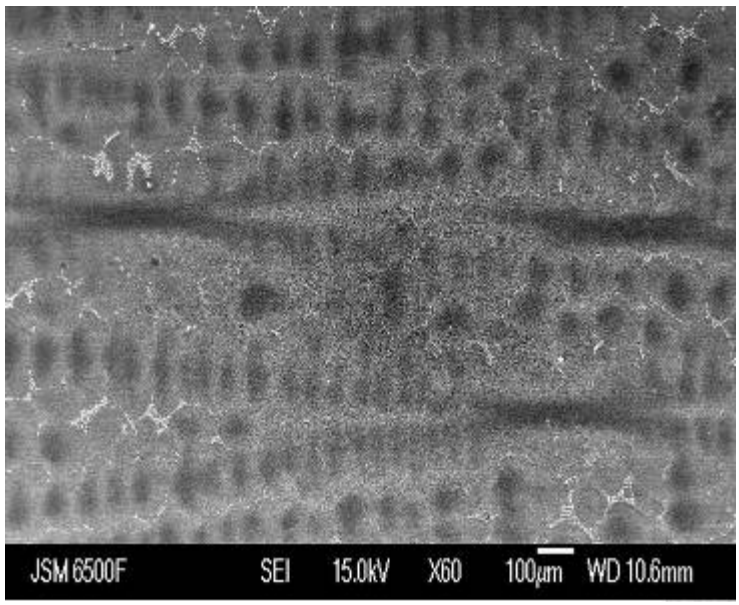

Figure 125 - oxidised carbides on Rene N5 oxidation sample (1)

Figure 126 - oxidised carbides on Rene N5 oxidation sample (2)

Figure 127 - - - oxidised carbides on Rene N5 oxidation sample (3)

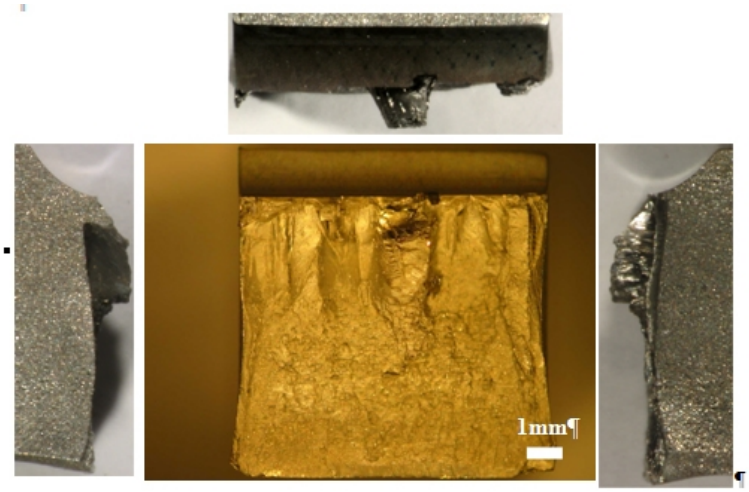

Figure 128 Orientation A, Air, 21°C
Test to failure– 21,661 cycles

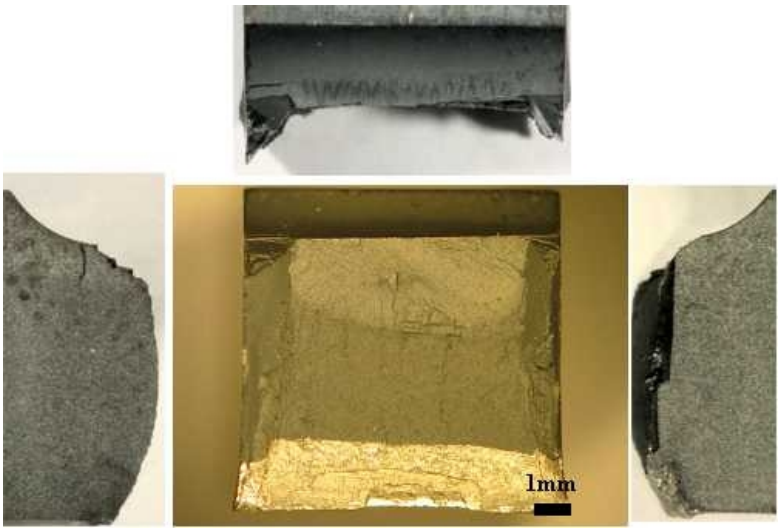

Figure 129 Orientation A, Air, 650°C
Test to failure – 25,500 cycles

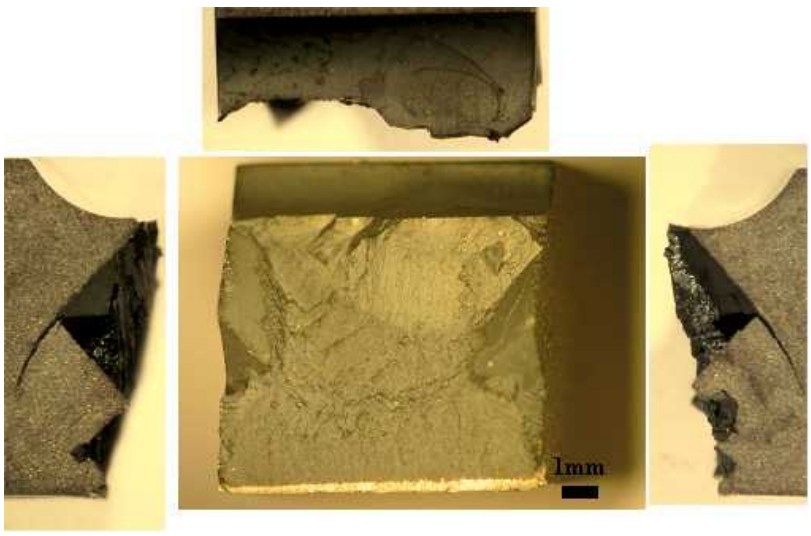

Figure 130 Orientation B, Air, 650°C
Test to failure – 6,500 cycles

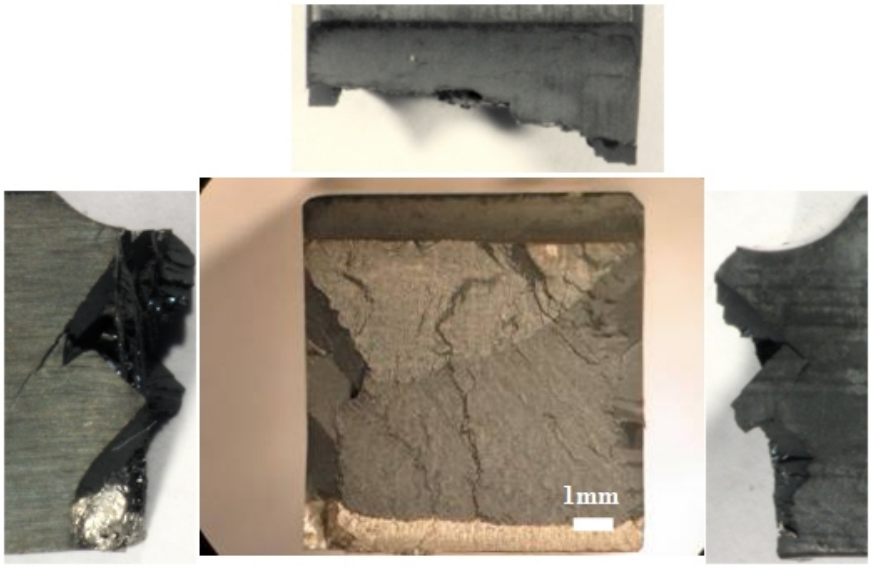

Figure 131 Orientation B Air, 725°C
Test to failure – 13,717 cycles

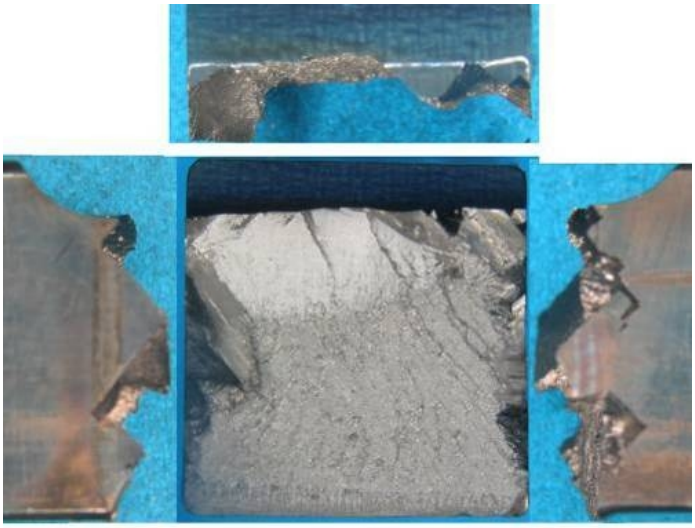

Figure 132 Orientation B, Vac, 650°C
Test to failure – 9,378 cycles

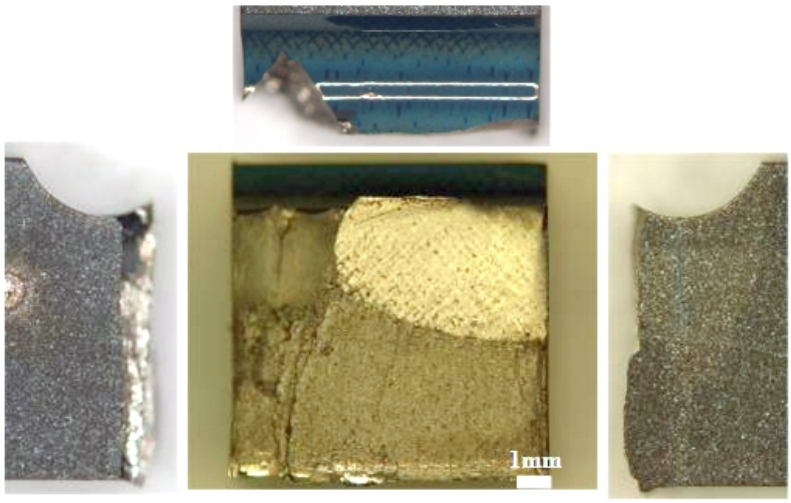

Figure 133 Orientation A, Vacuum, 725°C
Test to failure – 11,363 cycles

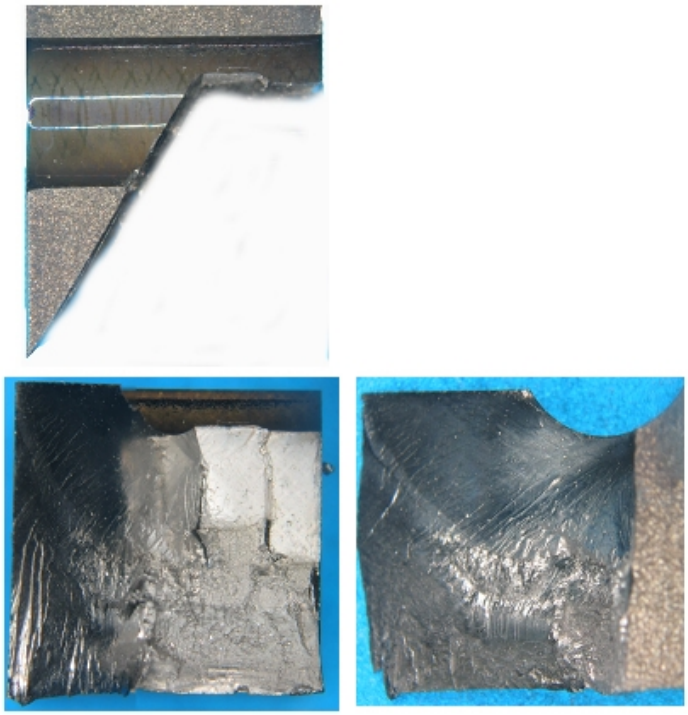

Figure 134 Orientation B Vacuum, 725°C
Test to failure – 4,960 cycles

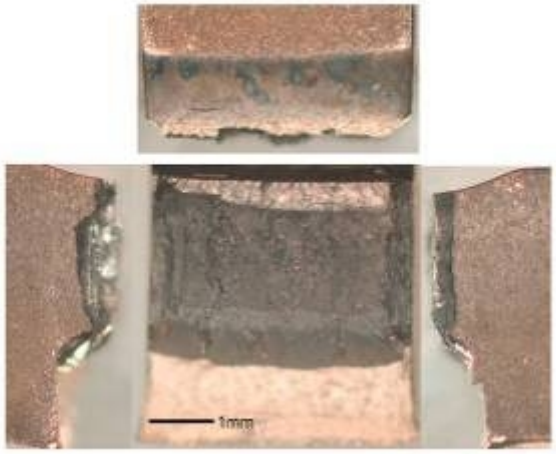

Figure 135 CMSX-4 Bar 16 OA
Δε=3.37 %, 500 cycles to failure

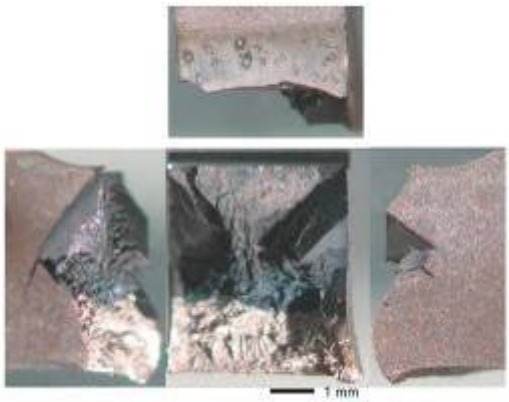

Figure 136 CMSX-4 Bar 17 OB
Δε=1.49 %, 3592 cycles to failure

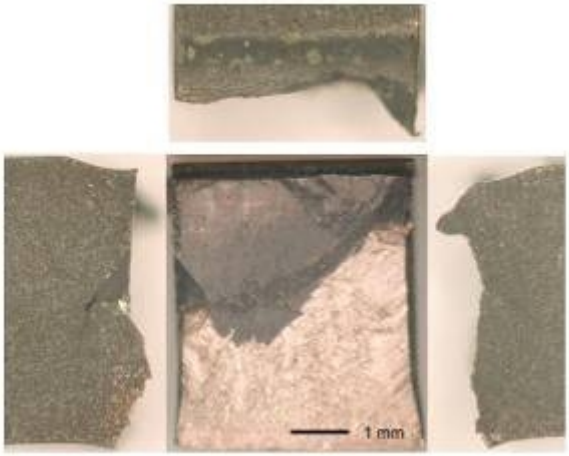

Figure 137 CMSX-4 Bar 24 OB
Δε=1.19 % 81000 cycles to failure

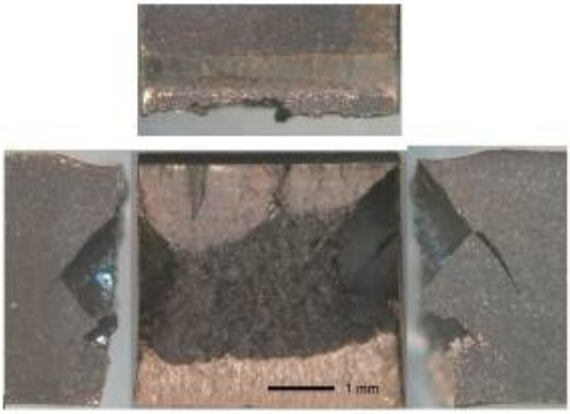

Figure 138 CMSX-4 Bar 28 OB
Δε=1.54 % 130792 cycles to failure

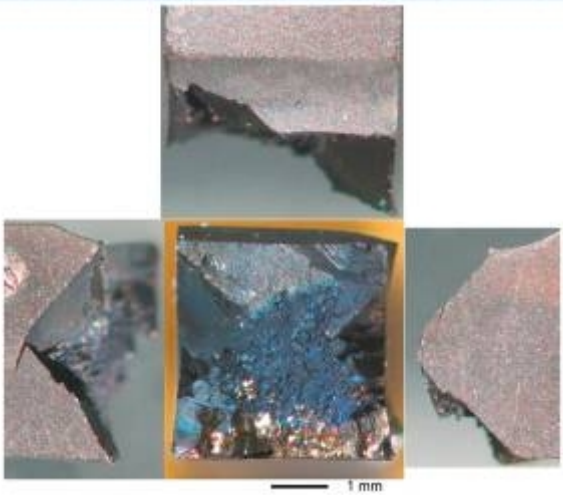

Figure 139 CMSX-4 Bar 29 OB
Δε=1.48 %, 16386 cycles to failure

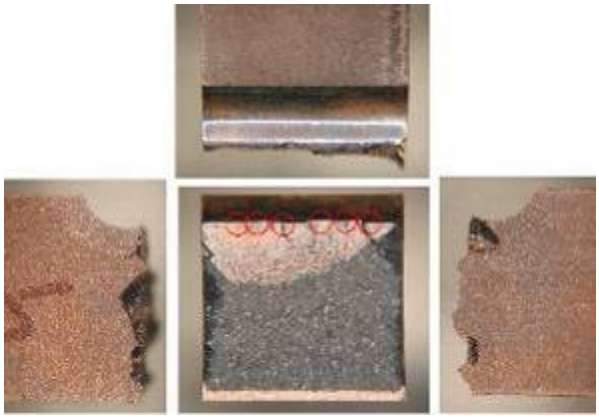

Figure 140 René N5 Bar 1 OB
Δε=1.38 %, 3325 cycles to failure

Figure 141 René N5 Bar 2 OB
Δε=1.38 %, 2573 cycles to failure

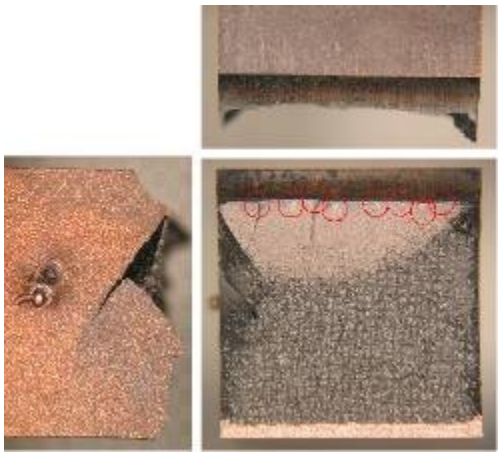

Figure 142 René N5 Bar 3 OB
Δε=1.38 %, 3507 cycles to failure

Figure 143 René N5 Bar 4 OA
Δε=1.38 %, 4945 cycles to failure

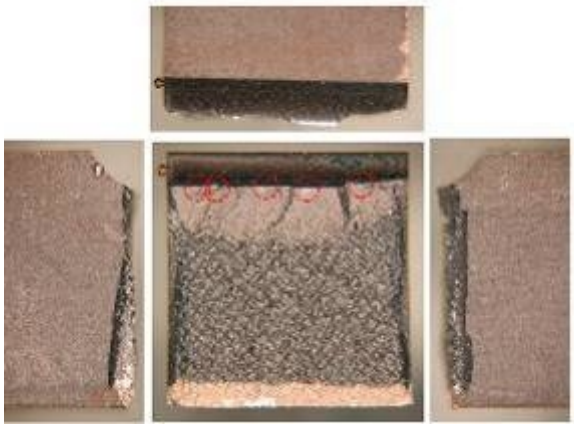

Figure 144 René N5 Bar 5 OA
Δε=1.38 %, 3346 cycles to failure

Figure 145 René N5 Bar 6 OA
Δε=1.38 %, 11490 cycles to failure

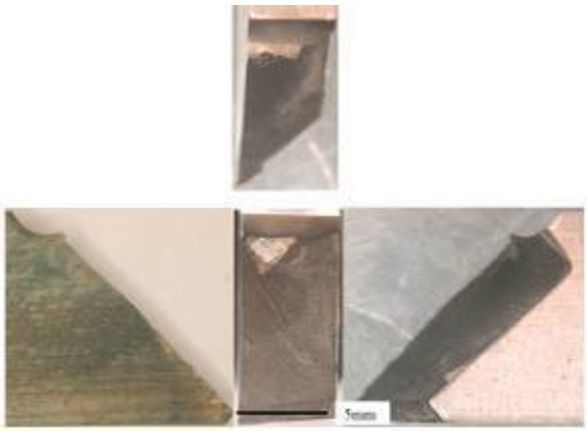

Figure 146 BAR P28-A, OB
Δε=1.26 %, 58495 cycles to failure

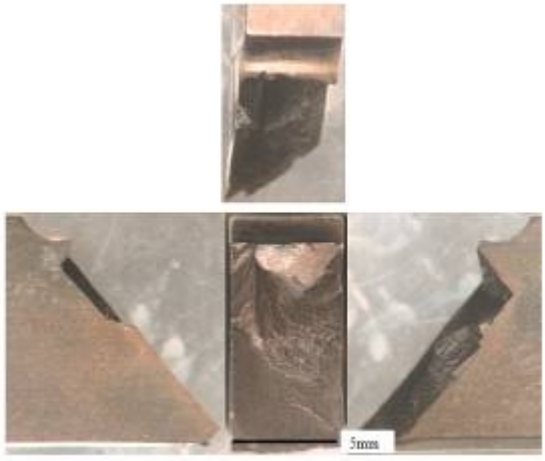

Figure 147 BAR P28-B, OB
Δε=1.26 %, 121110 cycles to failure

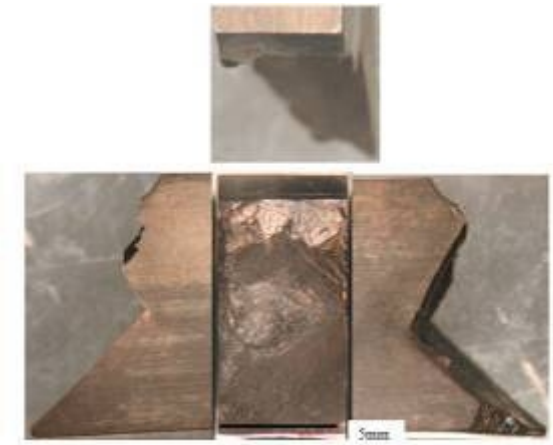

Figure 148 BAR P24-A, OB
Δε=1.19 %, 127649 cycles to failure

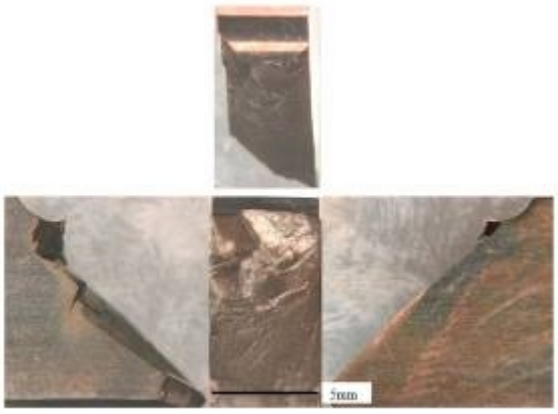

Figure 149 BAR P22-B, OB
Δε=1.12 %, 127649 cycles to failure

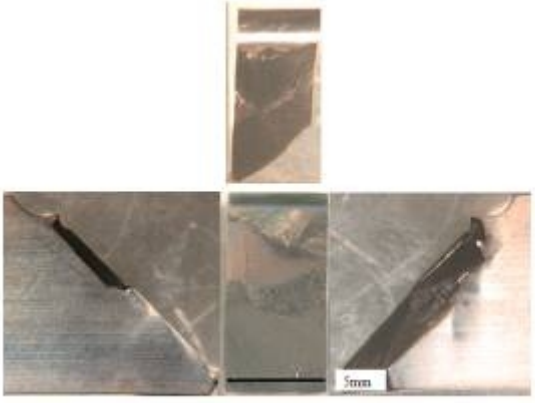

Figure 150 BAR P22-A, OB
Δε=1.12 %, 154284 cycles to failure

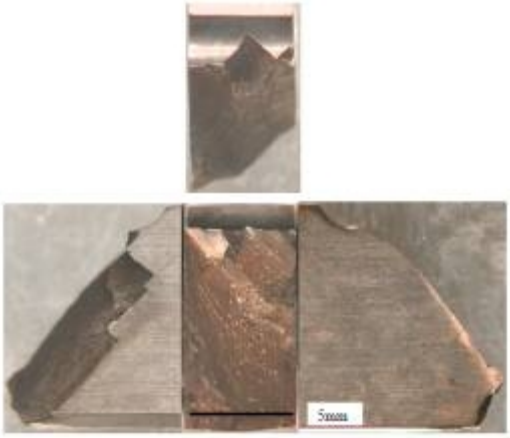

Figure 151 BAR P26-A, OB
Δε=1.19 %, 182001 cycles to failure

Figure 152 – Strain Life data for all fatigue tests.

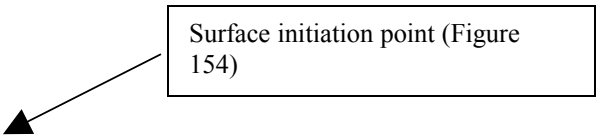

Figure 153 SEI micrograph - Bar 1 - Orientation X, Fracture surface (a).

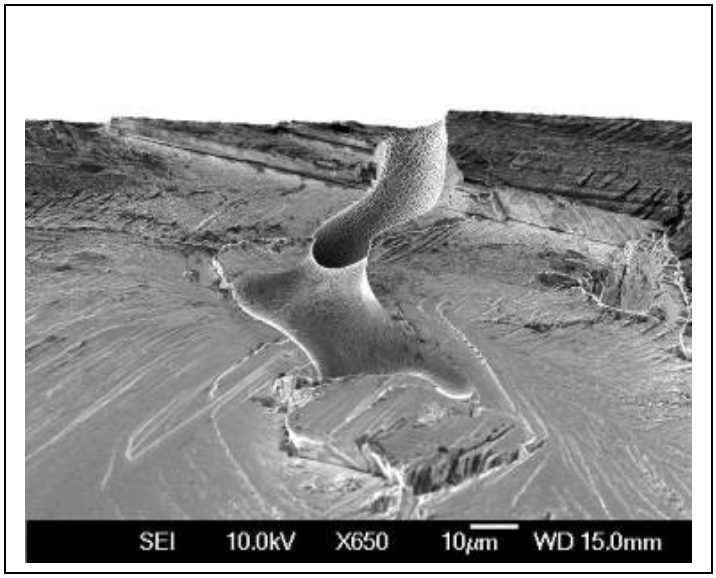

Figure 154 SEI micrograph Interdendritic surface pore identified as major initiation point as marked on Figure 153

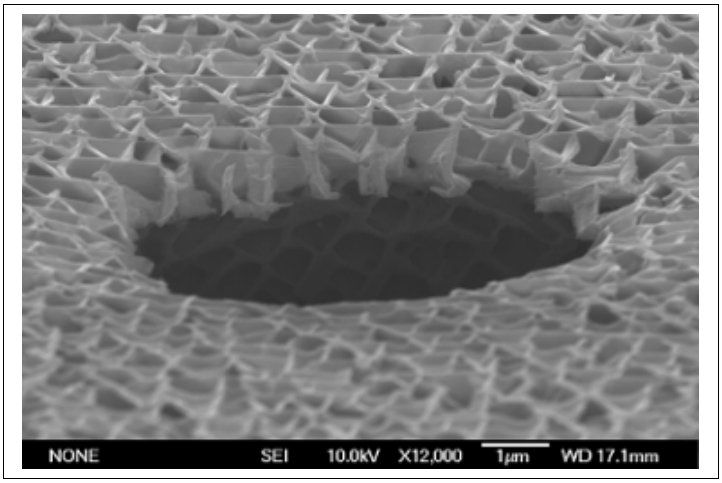

Figure 155 SEI micrograph of Pore on surface of etched notch from CMSX-4 room temperature test.

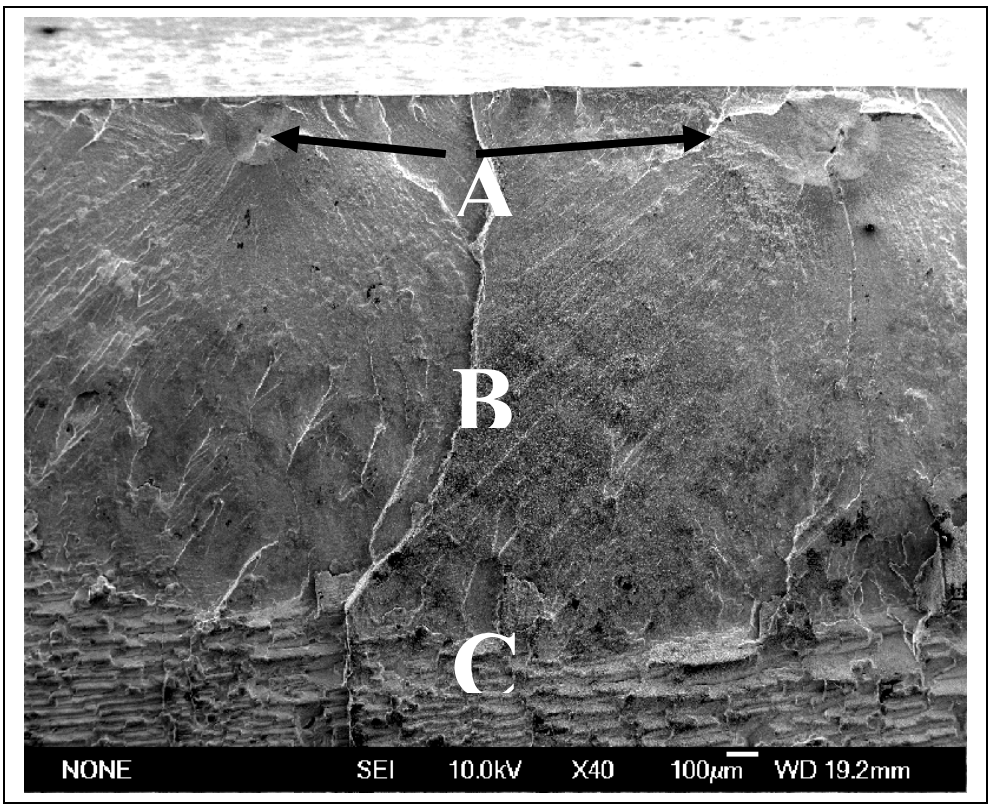

Figure 156 SEI micrograph Example of fracture surface features OA, 725°C, Air, 5271 cycles

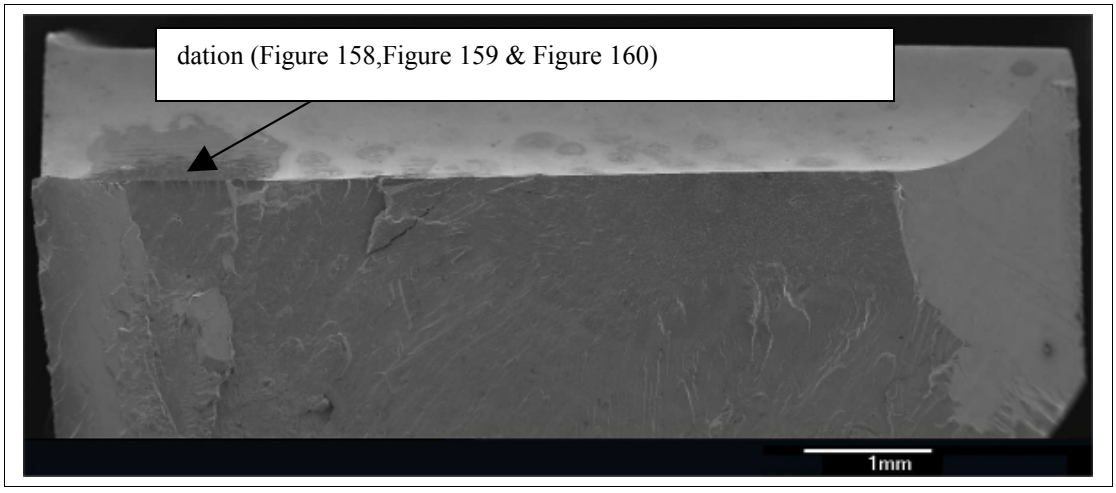

Figure 157 Bar 2 - SEI micrograph overview Bar 2 orientation X, Air, 650°C, 100,000 cycles.

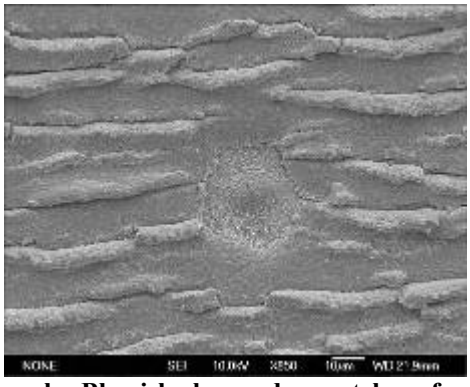

Figure 158 SEI micrograph - Blemish observed on notch surface after testing at 650°C

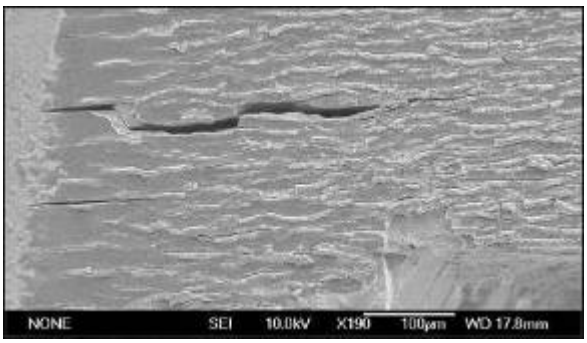

Figure 159 SEI micrograph - Large penetrating crack in oxide layer observed on notch surface after testing at 650°C.

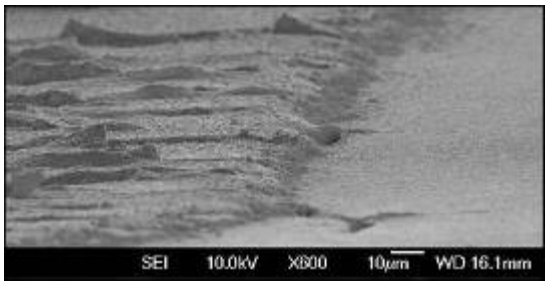

Figure 160 SEI micrograph image – As Figure 159 side on.

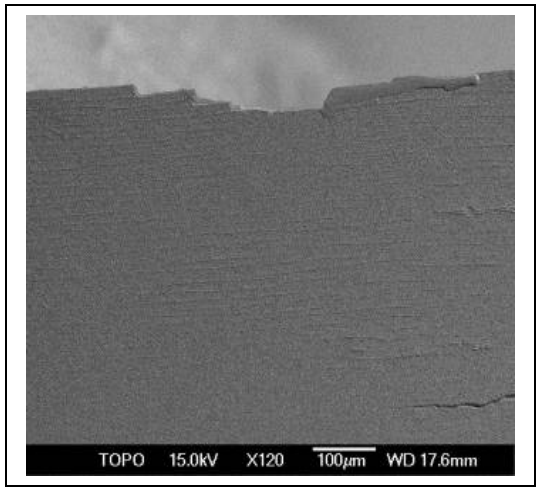

Figure 161 BEI Topographical Scan of cracks in notch root oxide layer

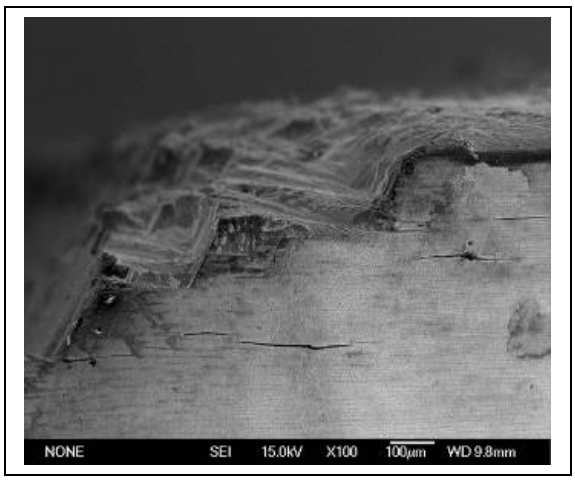

Figure 162 SEI micrograph of cracks in notch root oxide layer

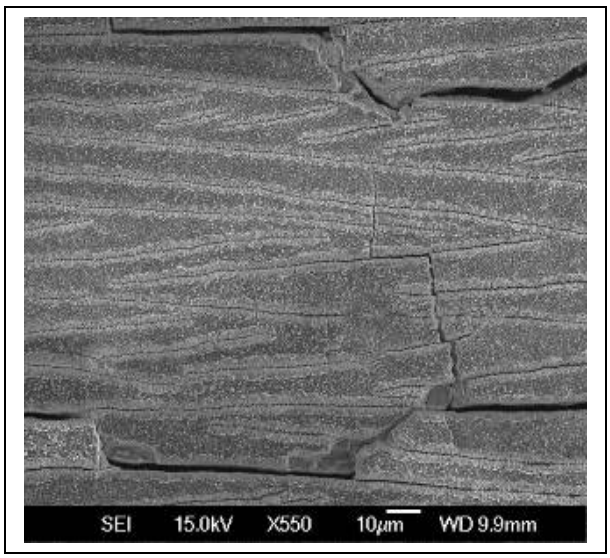

Figure 163 SEI micrograph of cracks in notch root oxide layer

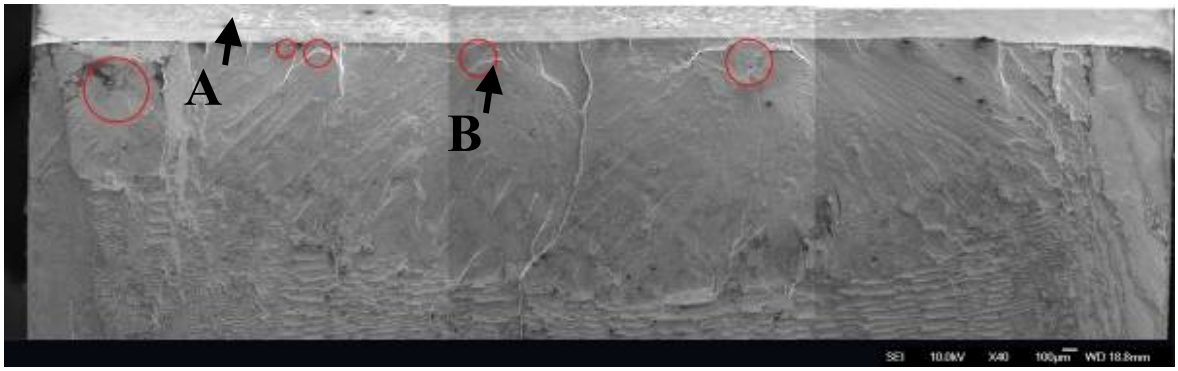

Figure 164 SEI micrograph – Fracture surface overview ,OA, 725°C, Air, 5271 cycles.

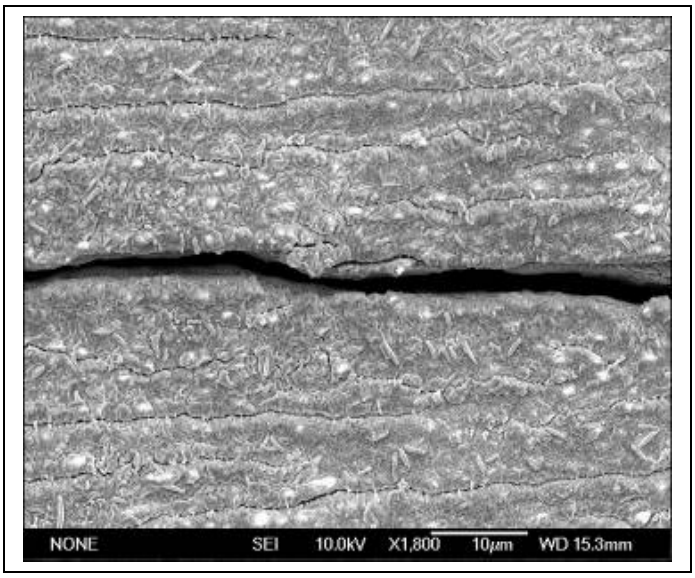

Figure 165 SEI micrograph – Crack in notch surface (Figure 164 location A)

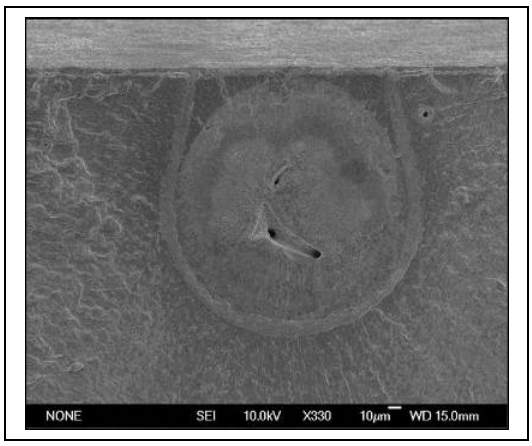

Figure 166 SEI micrograph – Subsurface 'halo' crack initiation point (Figure 164 location B)

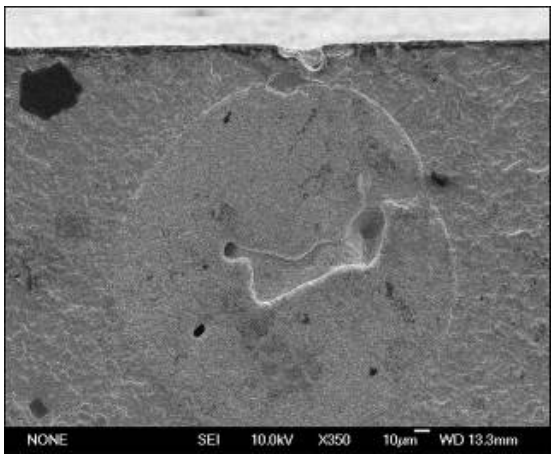

Figure 167 SEI micrograph Sub-surface initiation point Orientation B, 650°C, 1-1-1-1, 6,500 cycles

Figure 168 - SEI micrograph Subsurface initiation point Orientation A, 725°C

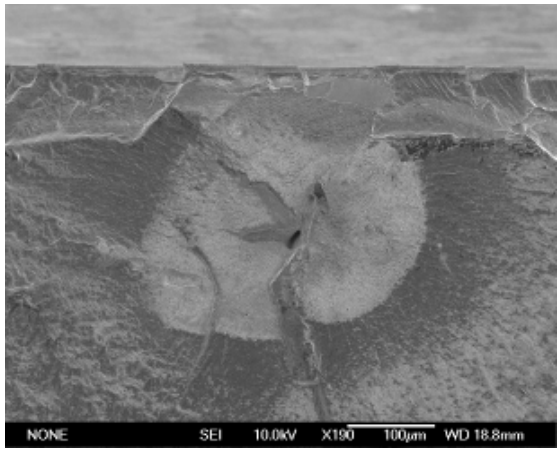

Figure 169 - SEI micrograph Subsurface initiation point Orientation A, 725°C

Figure 170 - BEI Topographical Scan. Sub-surface initiation point Orientation A, 725°C

Figure 171 - BEI Compositional Scan. Sub-surface initiation point Orientation A, 725°C

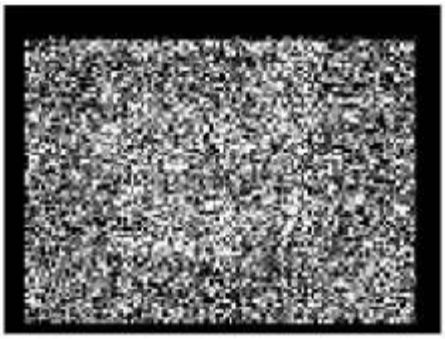

Ni Ka1

Figure 172 - EDX plot for Nickel, from Figure 171

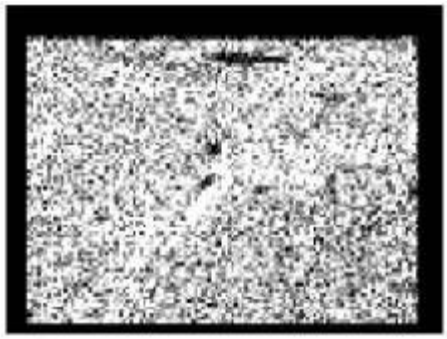

O Ka1

Figure 173 - EDX plot for Oxygen, from Figure 171

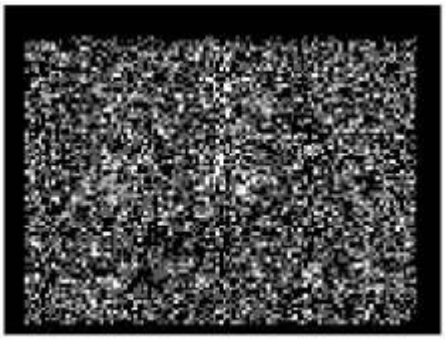

Co Ka1

Figure 174 - EDX plot for Nickel, from Figure 171

C Ka1_2

Figure 175 - EDX plot for Nickel, from Figure 171

Ti Ka1

Figure 176 - EDX plot for Titanium, from Figure 171

Cr Ka1

Figure 177 - EDX plot for Chromium, from Figure 171

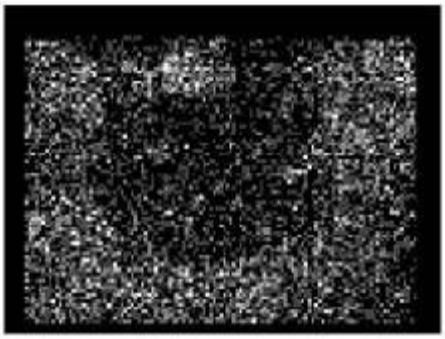

Si Ka1

Figure 178 - EDX plot for Silicon, from Figure 171

Al Ka1

Figure 179 - EDX plot for Aluminium, from Figure 171

Figure 180 - EDX plot for Tungsten, from Figure 171

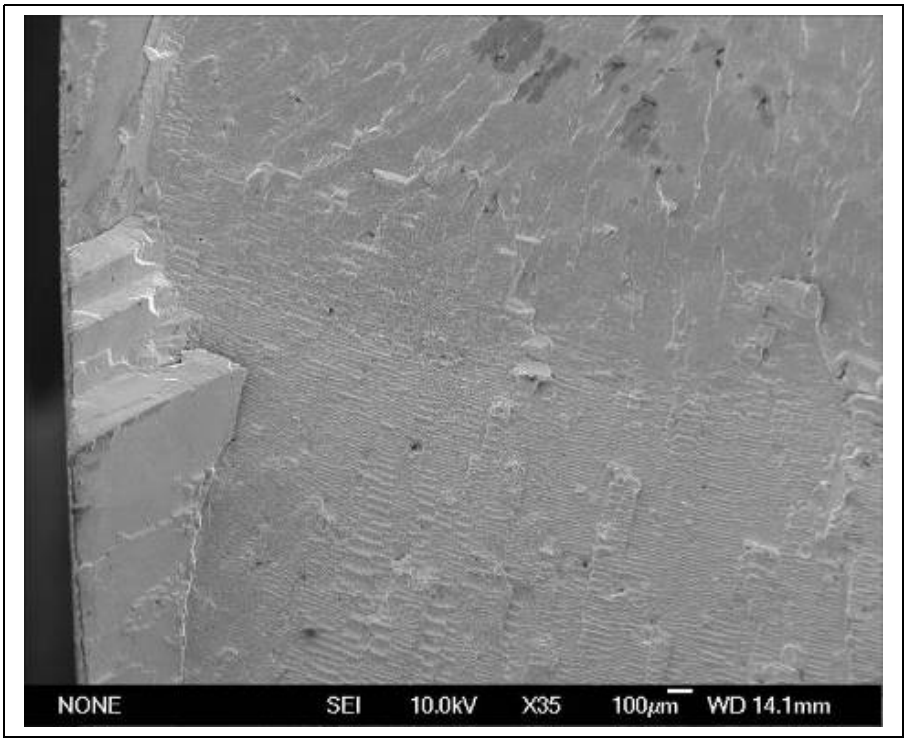

Figure 181 SEI micrograph crack propagation in CMSX-4 OA

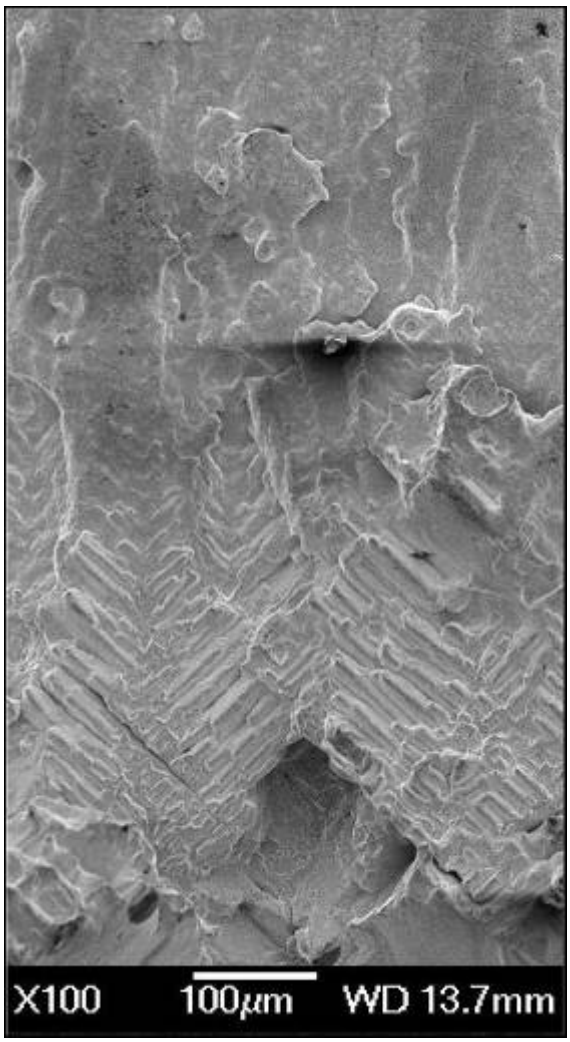

Figure 182 SEI micrograph crack propagation in CMSX-4 OB

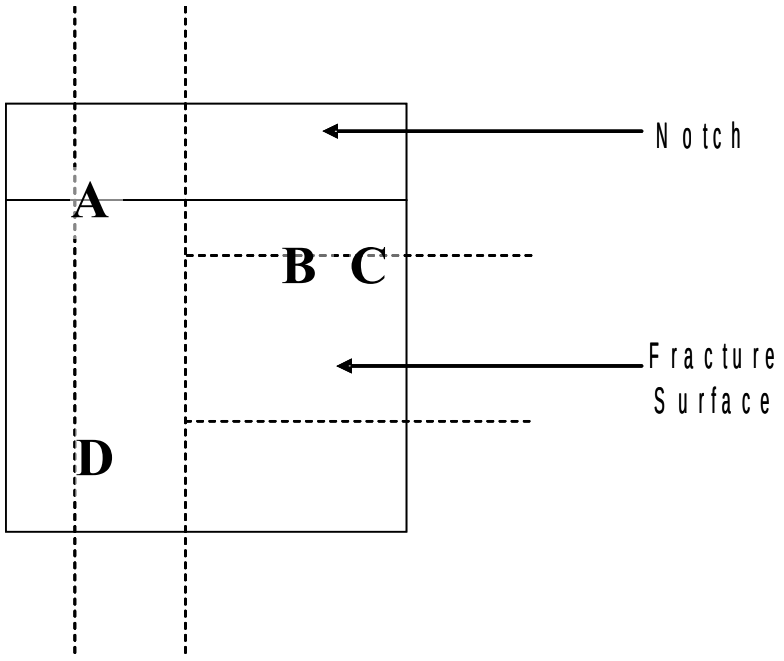

Figure 183 – Detail of sectioning and location of Figure 184, Figure 187Figure 185Figure 186.

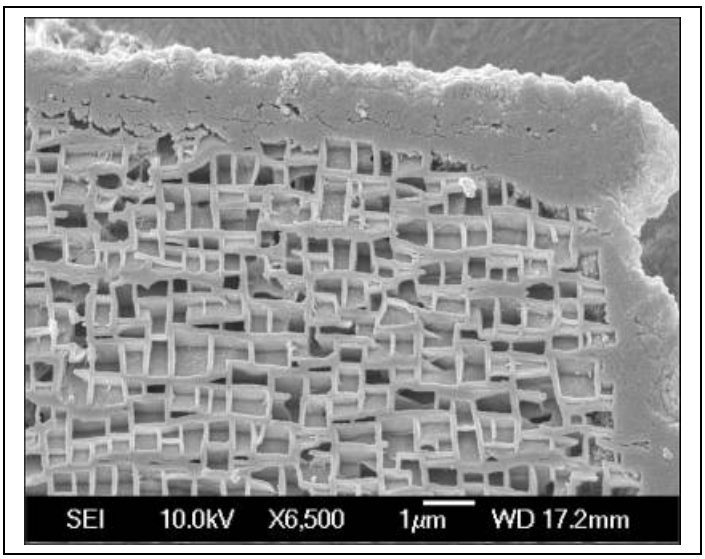

Figure 184 SEI micrograph (Location A) oxide layer in notch root

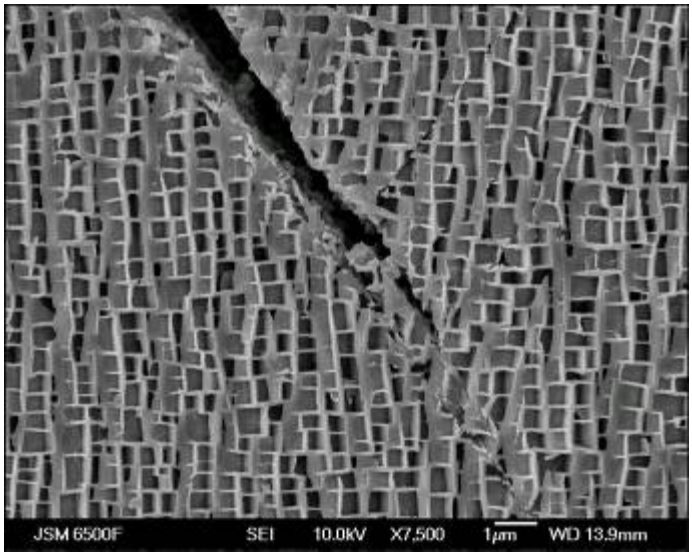

Figure 185 SEI micrograph (Location B) Crack following a slip band, cutting through g'

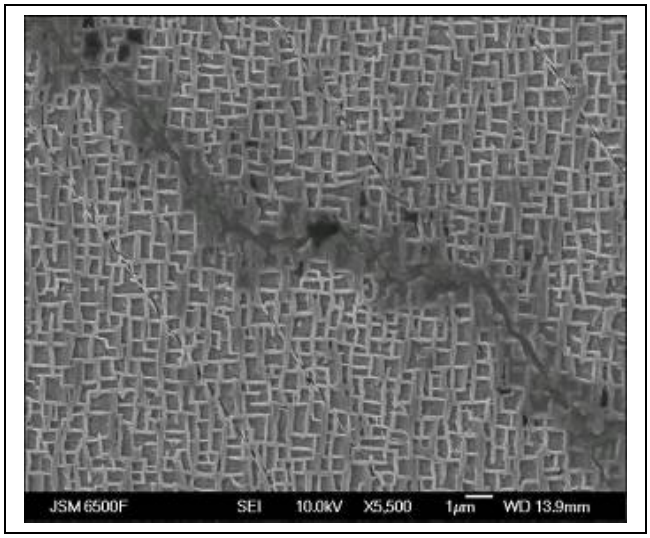

Figure 186 SEI micrograph (Location C) Crack deviation around pore before continuing along slip band

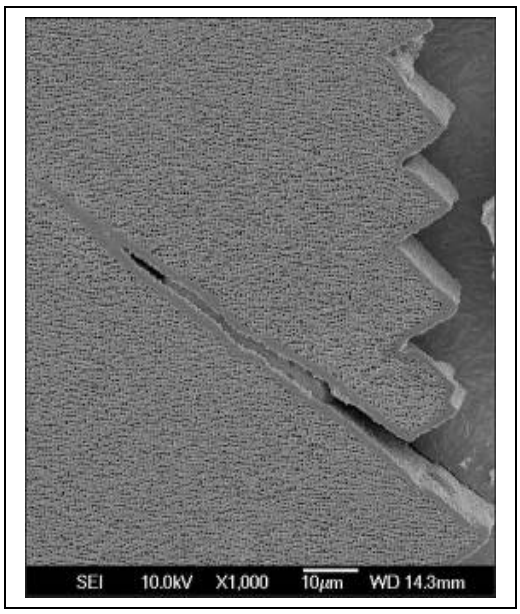

Figure 187 SEI micrograph (Location D) oxide layer on fracture surface exhibiting 'rooftop' faceting

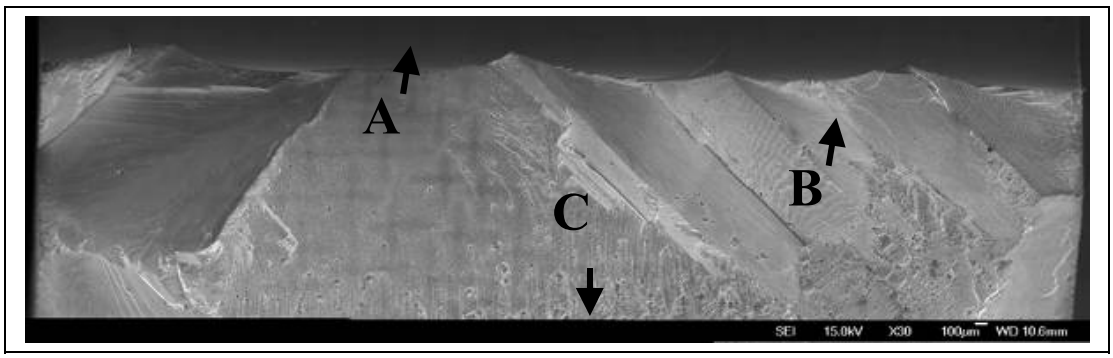

Figure 188 – SEI micrograph fracture surface overview 650°, OB, Vacuum.

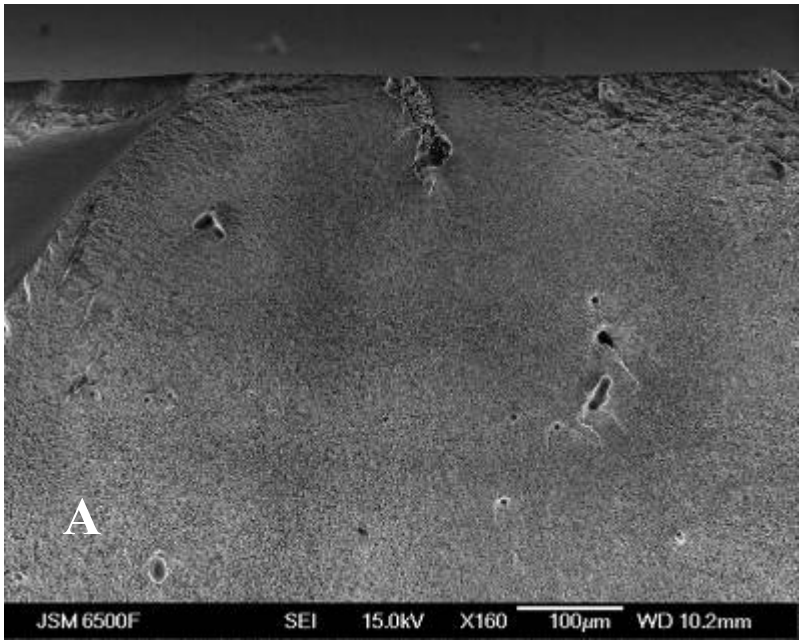

Figure 189 SEI micrograph – initiation pore 650°, OB, Vacuum

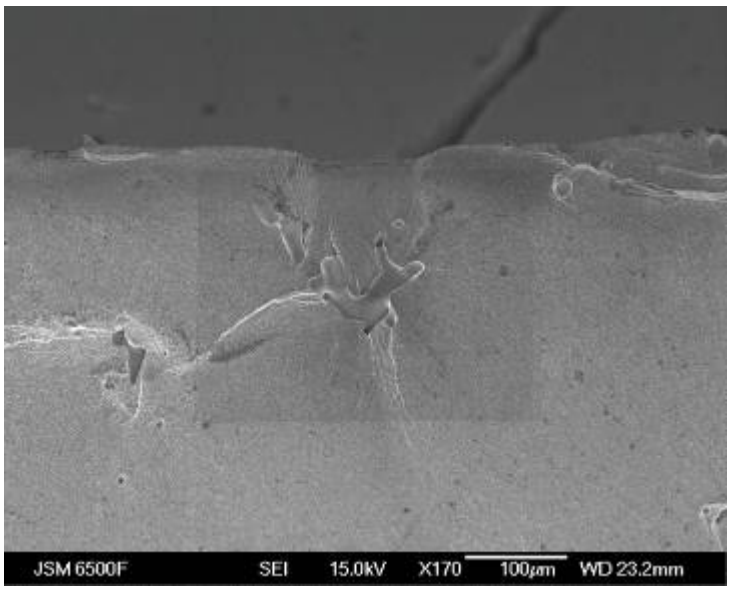

Figure 190 SEI micrograph – initiation pore 650°, OA, Vacuum

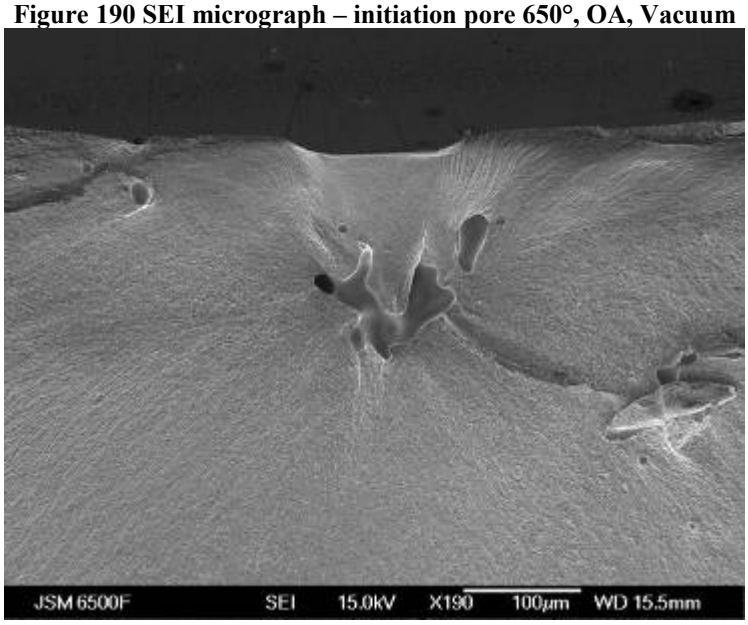

Figure 191 SEI micrograph – initiation pore 650°, OA, Vacuum

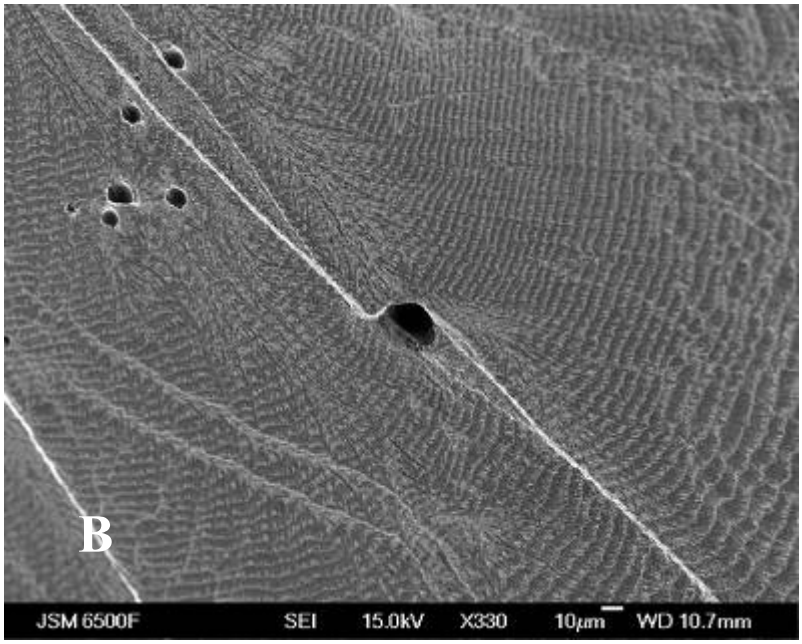

Figure 192 SEI micrograph – Slip bands, pore and striations, 650°, OB, Vacuum

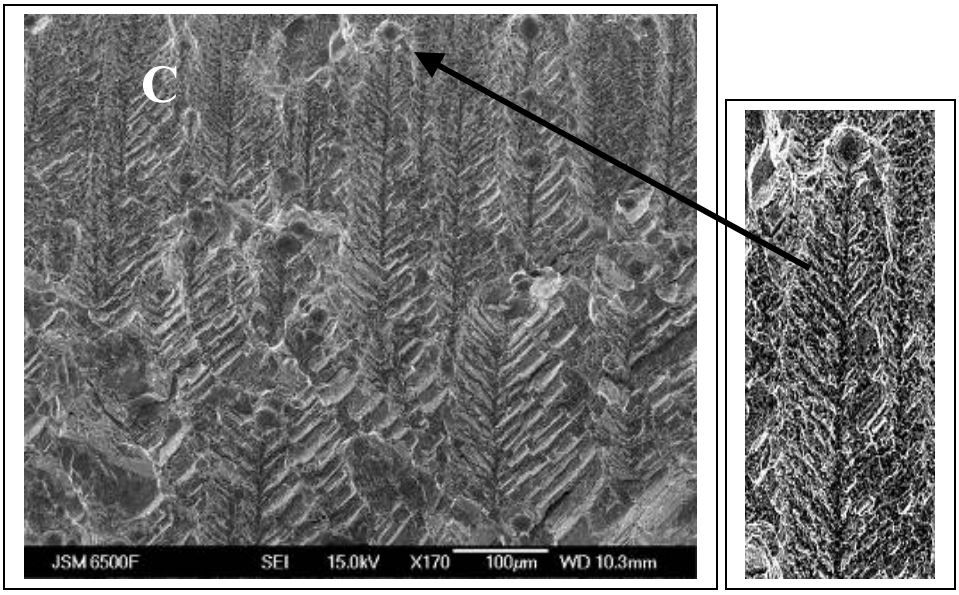

Figure 193 SEI micrograph – Fast fracture region with porosity, 650°, OB, Vacuum

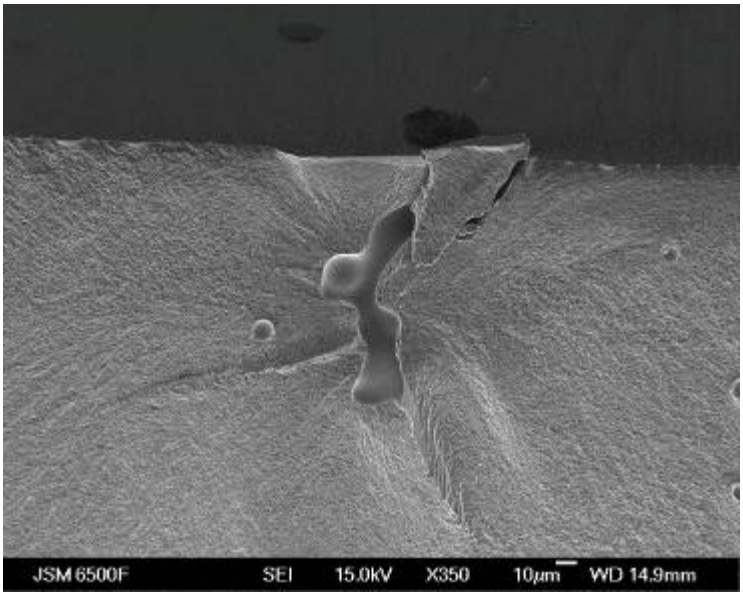

Figure 194 SEI micrograph – initiation pore 650°, OA, Vacuum

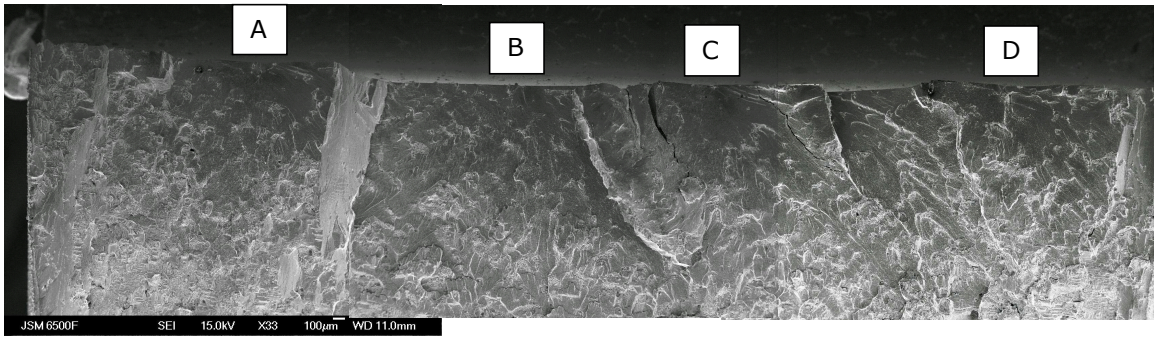

Figure 195 SEI micrograph overview – René N5 ffracture surface OA, 650°C, Air. Test to failure 3346 cycles

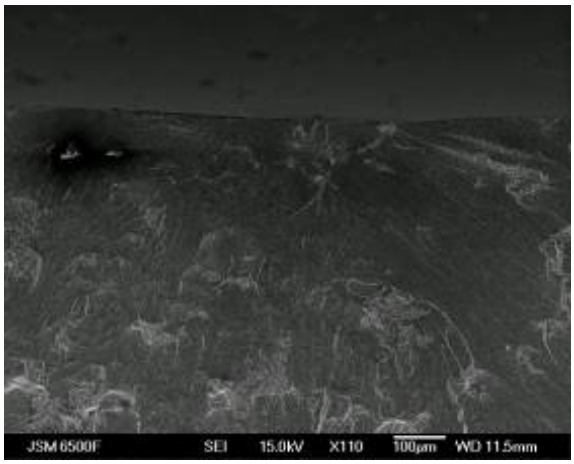

Figure 196 - SEI micrograph Initiation site A (Figure 195)

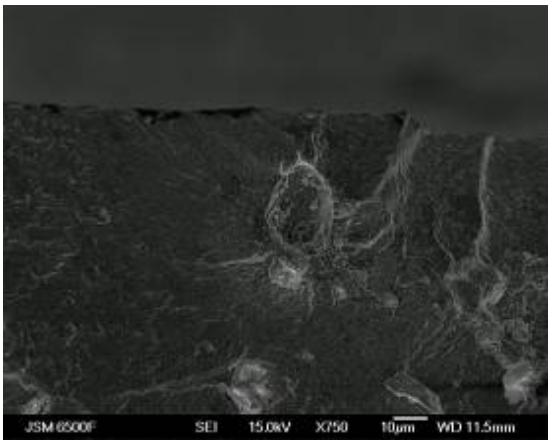

Figure 197 - SEI micrograph Detail of initiating pore from Figure 196

Figure 198 - SEI micrograph Initiation site B (Figure 195)

Figure 199 - SEI micrograph Detail of initiating pore from Figure 198

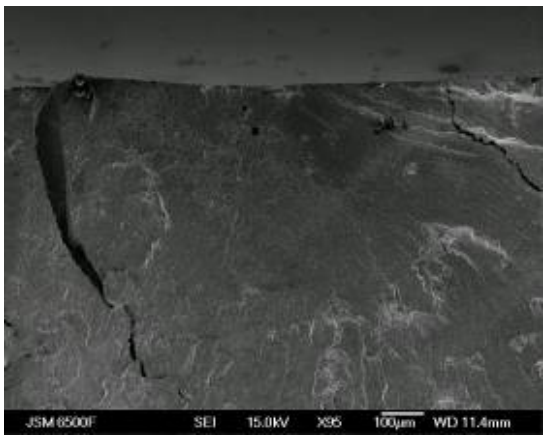

Figure 200 - SEI micrograph Initiation site C (Figure 195)

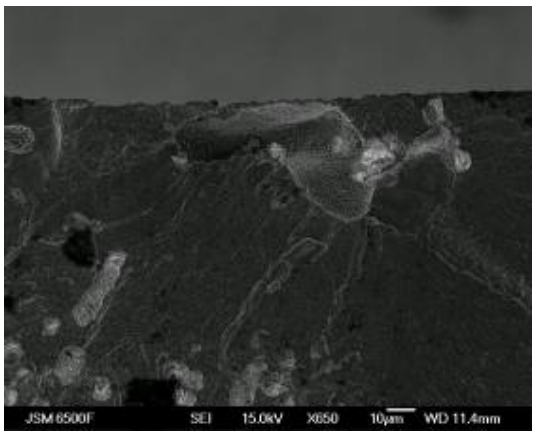

Figure 201 - SEI micrograph Detail of initiating pore from Figure 200

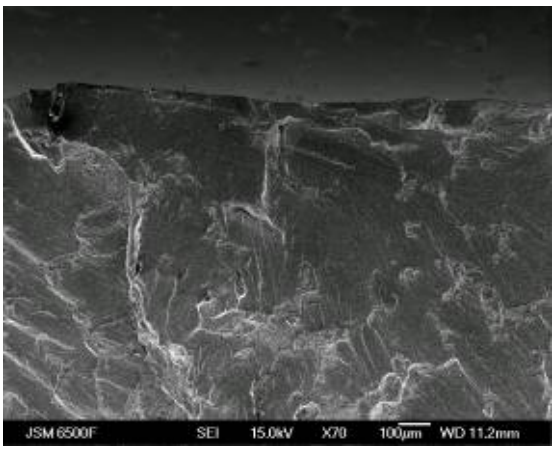

Figure 202 - SEI micrograph Initiation site D (Figure 195)

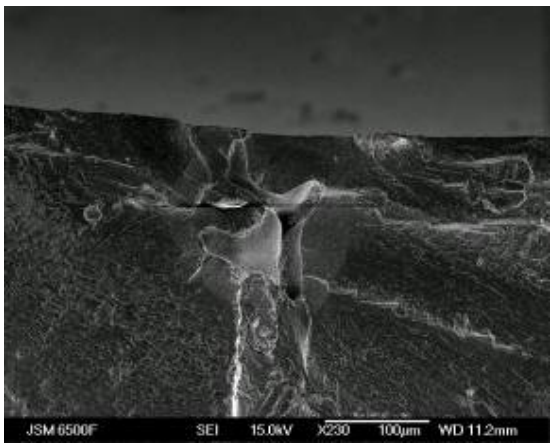

Figure 203 - SEI micrograph Detail of initiating pore from Figure 202

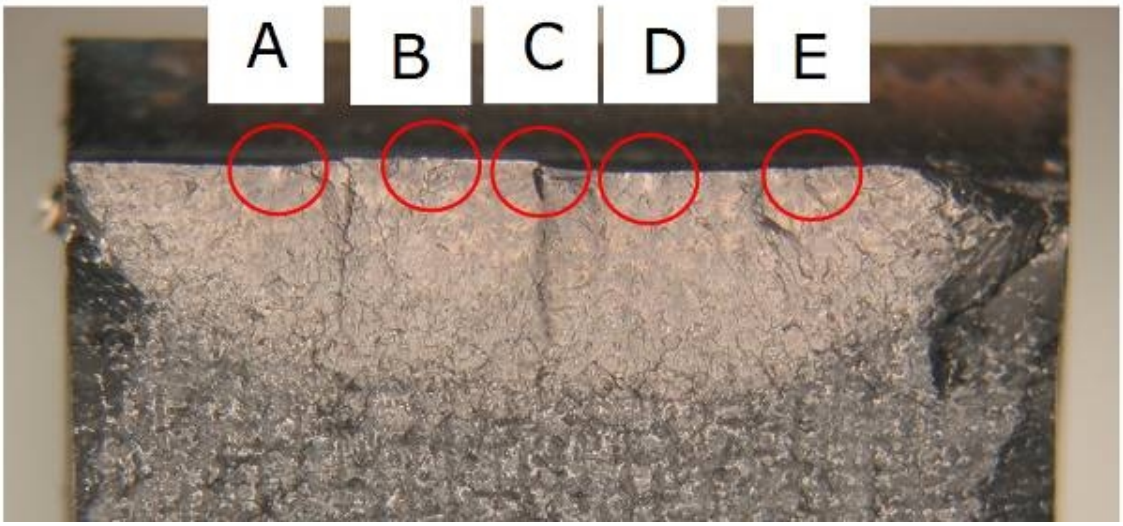

Figure 204 Rene N5 fracture surface overview, OB.

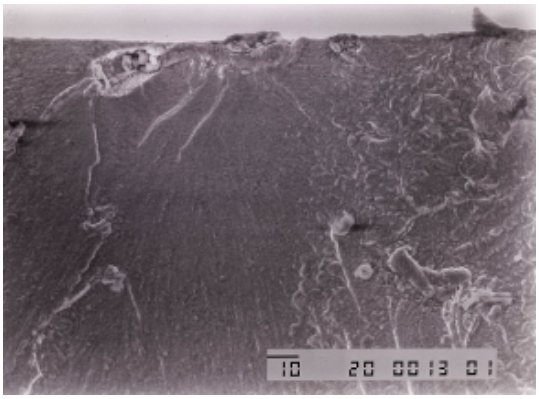

Figure 205 - SEI micrograph at location A (Figure 204)

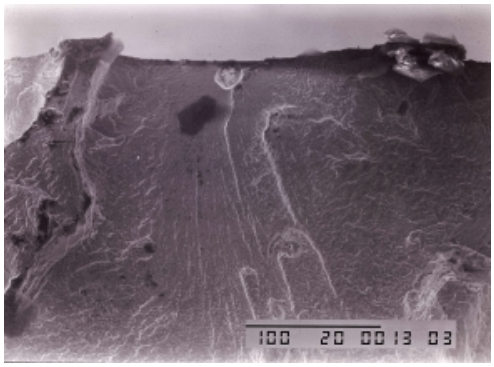

Figure 206 - SEI micrograph at location B (Figure 204)

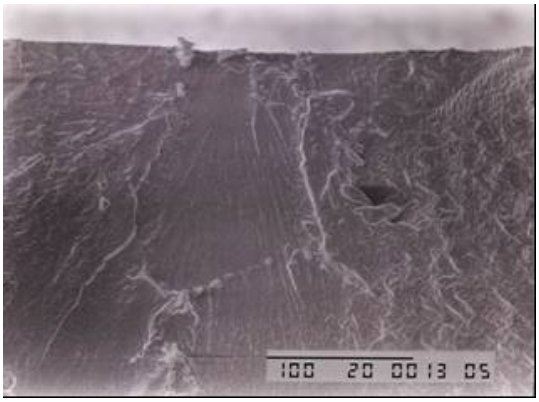

Figure 207 - SEI micrograph at location D (Figure 204)

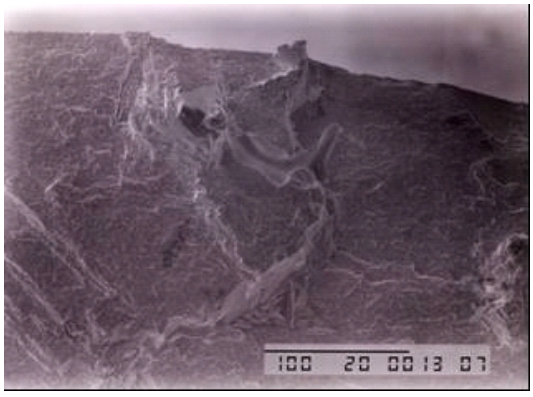

Figure 208 - SEI micrograph at location E (Figure 204)

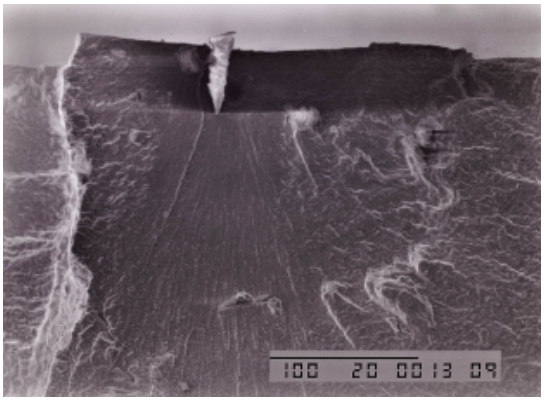

Figure 209 - SEI micrograph at location C (Figure 204)

Figure 210 - SEI micrograph Detail of C (Figure 204)

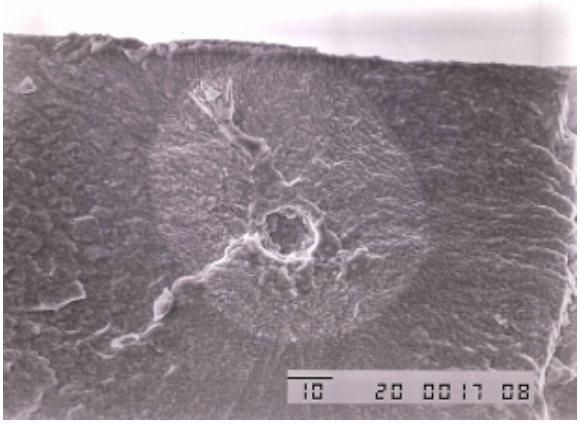

Figure 211 - SEI micrograph orientation B with Nf of 3325 cycles

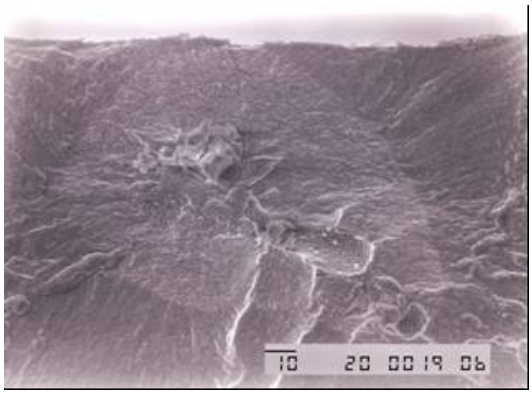

Figure 212 - SEI micrograph orientation B with Nf of 3507 cycles

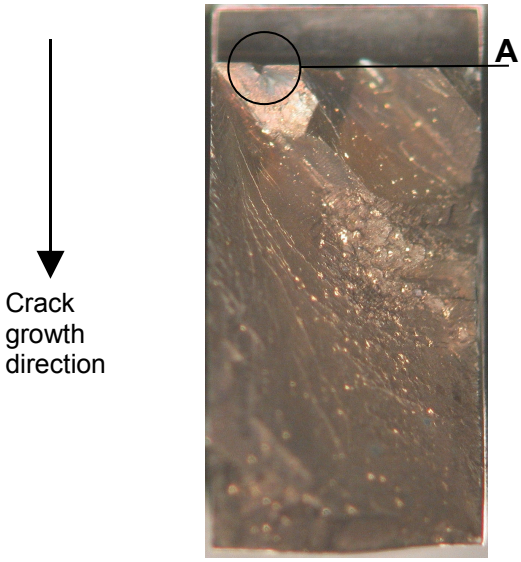

Figure 213 Overview of fracture surface Bar P26-A, Orientation B, Nf = 182001.

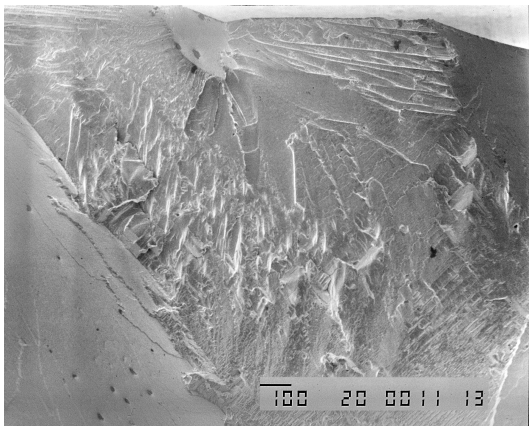

Figure 214 SEI micrograph of the major initiation site in region A (Figure 213)

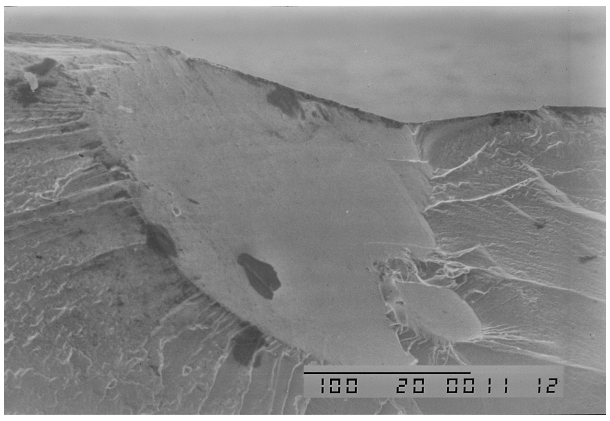

Figure 215 SEI micrograph at initiating facet region A (Figure 213)

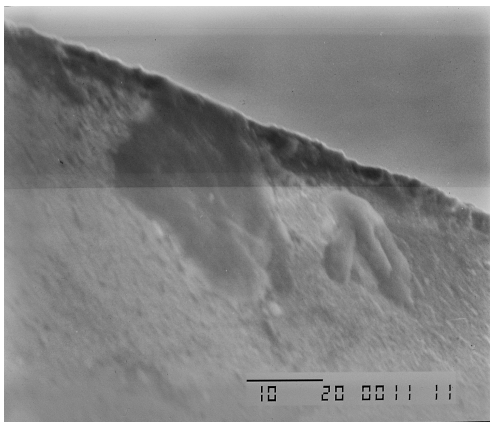

Figure 216 SEI micrograph detail of the dark phase in Figure 215 (possible oxidised carbide) that initiated first crack.

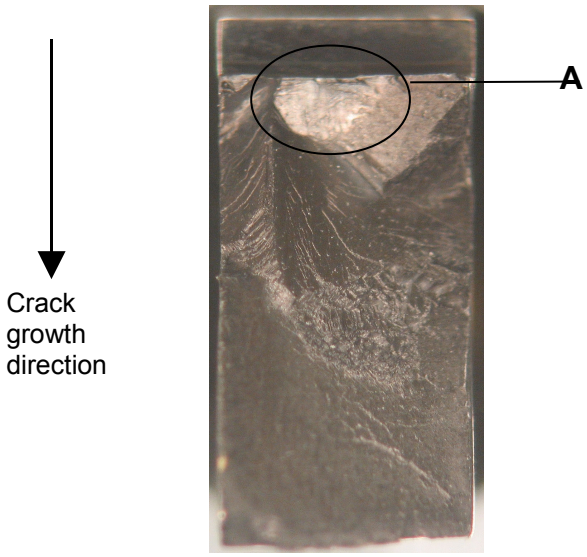

Figure 217 - Overview of fracure surface Bar P26-A, Orientation B, Nf = 182001:

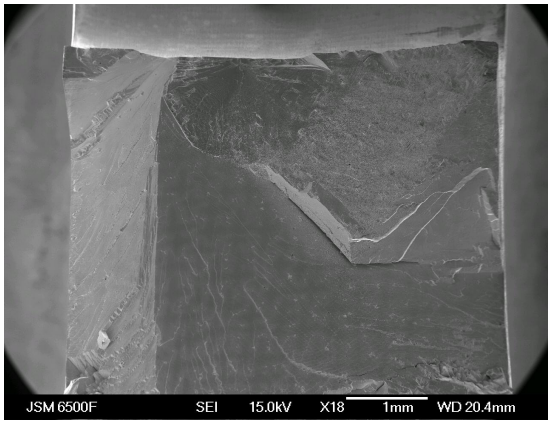

Figure 218 SEI micrograph overview of the major initiation site in region A (Figure 217)

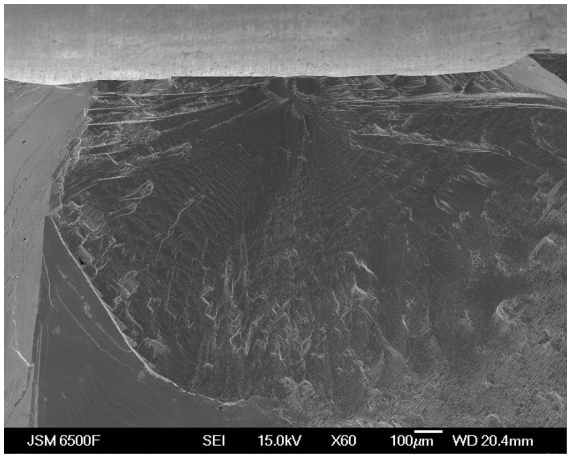

Figure 219 - SEI micrograph of the initiation site in region A (Figure 217)

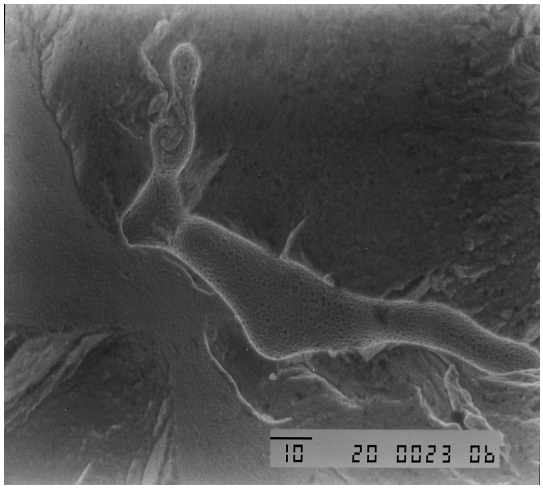

Figure 220 - SEI micrograph of initiating pore in Figure 219

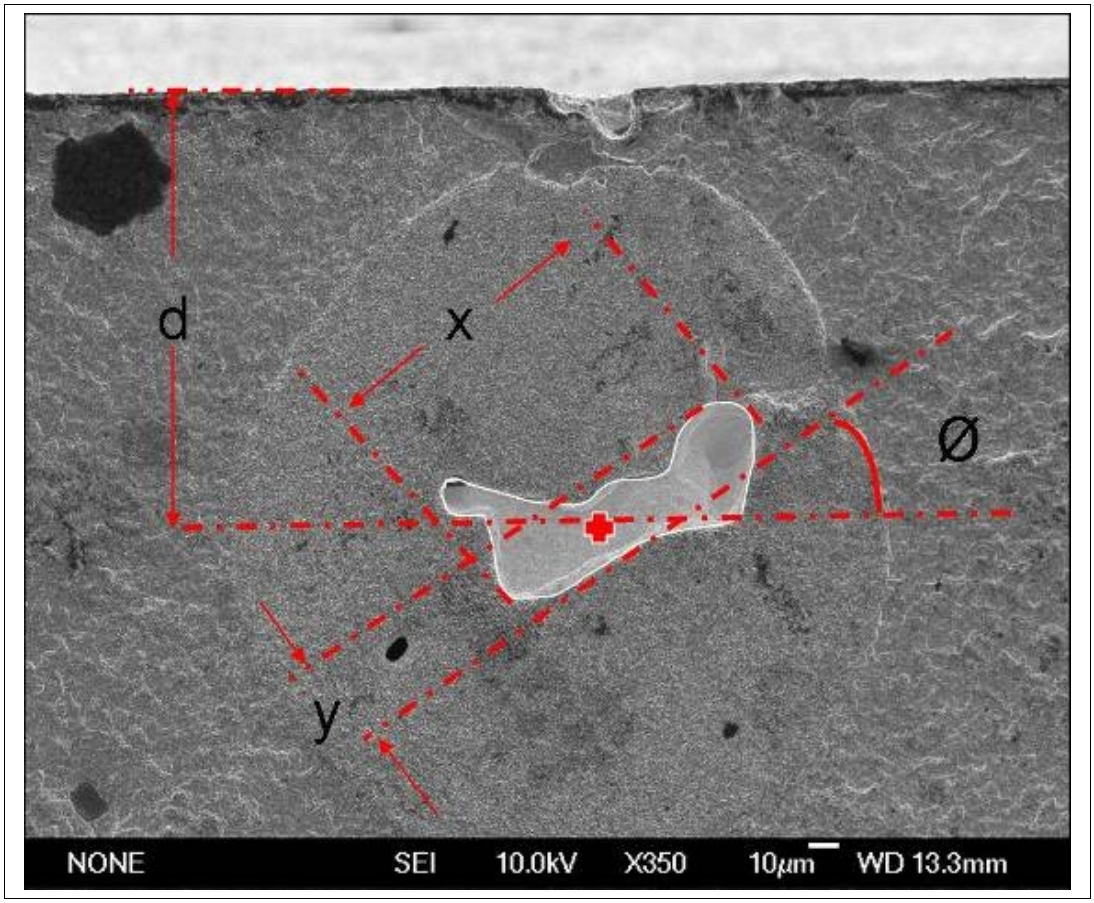

Figure 221 Pore measurement details

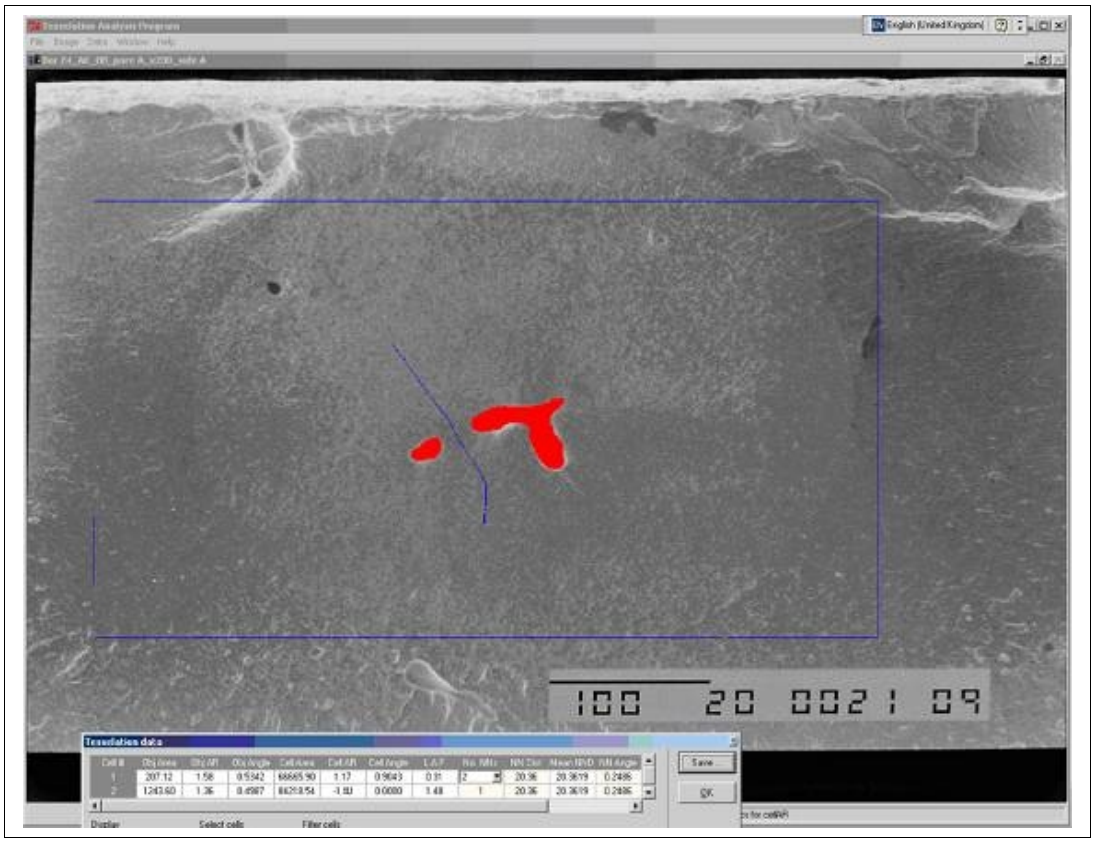

Figure 222 Pore area calculation using TAP software

6.7 Discussion & Analysis of Results

6.7.1 Fatigue Life Data

Comparison of test data with data supplied by Alstom is shown in Figure 223. The data from notch bend tests at Southampton consistently tends towards the higher boundary of the data provided by Alstom. This may reflect the consistent surface finish achieved by polishing the notch root on all tests conducted as part of this work

6.7.2 Fractography

CMSX-4 samples have been tested at a variety of temperatures and as temperature is increased, smooth areas in the centre of the fracture surface are larger. At higher strain ranges and lower temperatures a more crystallographic, highly faceted crack growth mode is observed. The increase in strain range is likely to set up more extended slip band cracking. When cracks initiate at typical stress concentrating features sufficient local stress will be generated to produce long slip bands with repeated cutting of γ'. This is also reflected in the fact that at longer crack lengths a transition to overall faceted crack growth was observed indicative of extended slip-band cracking. This was correlated with a high ΔK (50 MPa√m) value in the long crack propagation studies carried out by Mark Joyce[220]. At lower temperatures more planar slip processes are expected leading to more faceted fracture surfaces (as observed)

For all 3 alloys the orientation of the {111} facets differs between orientations A and B as expected. This facet orientation causes orientation B fracture surfaces to appear more faceted than orientation A. In orientation A samples the facets run parallel to the sides of the fracture surface, whereas with orientation B they intersect the sides at 45°. The angled appearance of the orientation B facets gives the illusion of orientation B samples being more faceted. The actual area taken up by side facets in the high temperature tests appears similar between the 2 orientations.

In CMSX-4 and René N5, oxidation obscures the detail of the fracture surface in the notch root at 650°C. A build up of cracked oxide scale in the notch root makes replication techniques difficult.

Crack initiation in most tests has occurred at surface or subsurface pores, this agrees with observations in the literature 219[,219,]. At room temperature, initiation is observed to be from pores at the notch surface. Porosity analysis of the notch surface is of limited use in characterising pores that extend below the surface. Most interdendritic

pores have complex 3D geometrical shapes due to the nature of their formation. These complex shapes do break the notch surface but only appear as circular or oval pores.

It is not yet fully understood why cracks do not initiate at the notch surface at higher temperatures. Cracks in the surface oxide do penetrate the substrate but do not initiate the critical crack. There may be sufficient oxidation of the surface pores to effectively plug them up therefore reducing the stress concentration induced by the pore - similar to oxide induced closure effects. The stress/strain fields below the notch surface may change/redistribute at higher temperatures thus making sub surface initiation more likely. Tests on CMSX-4 in vacuum revert back to a mix of surface and subsurface initiation.

An oxidation study showed that moderate to heavy oxidation occurs in a relatively short space of time at 650°C in both René N5 and CMSX-4. The γ matrix becomes visible on polished specimens after 1 hour exposure due to preferential oxidation of the γ matrix. This can be confirmed by looking at an etched specimen after 1 hour thermal exposure. After 256 hours, varying levels of oxidation are observed on each sample. No pores are visible on the surface after thermal exposure. A section through an oxidised pore would provide valuable information on the oxidation process and possibly provide an insight as to why cracks do not initiate at the surface at high temperatures. Compositional differences caused by debris picked up during the casting process may be the cause of some of the more extreme surface blemishing.

Sectioning of CMSX-4 samples showed the oxide layer to be thicker in the notch root than on the fracture surface. This is likely to be a function of exposure time. Fracture surface sections show that oxidation occurs at crack boundaries as they propagate into the specimen, oxidation assisted crack propagation is seen. Oxidation test samples show that the oxide layer protrudes into the substrate as well as causing growth on top of the substrate. Preferential oxidation of the matrix is seen both on the sample surface and below the surface. Oxide thickness is greater on the oxidation study samples in comparison with the notch bend bars. The main difference being that study samples were not subjected to any stress during oxidation. This suggests a certain amount of spallation from the notch surface occurs during testing. The presence of multiple surface cracks certainly backs up this argument. Despite the cracks in the oxide layer, more than 90% of the critical cracks in all high temperature air tests initiated at sub surface pores. With this in mind it was apparent that characterisation and analysis of all initiating sub surface pores was required. Although this is still a 2D

approach, it is looking at pores on the critical fracture path rather than distributions on the notch surface.

6.7.3 Analysis of porosity initiating fatigue cracks

Data of all initiating pores has been collected as discussed in the previous section. Raw data is presented in (Table 15). Where both fracture surfaces have been analysed for test sample, an average value over the two fracture surfaces has been calculated. A main initiating pore has been identified where possible for each test where multiple initiation points were recorded. On many of the fracture surfaces, a main initiation point is difficult to identify. In the absence of an obvious major initiating point, the largest pore (area) has been identified. Several other values have been calculated from the raw data on a test by test basis:

- Total area of initiating pores per test bar (from TAP measurement)
- Average area of initiating pores per test bar (from TAP measurement)
- Aspect ratio of each pore (from manual measurements) = major axis / minor axis
- Average major axis of initiating pores per test bar.
- Average minor axis of initiating pores per test bar.
- Elliptical area of each pore (area of an ellipse using Major and Minor axis)
- Aspect ratio of each pore (from Major and Minor Axis)
- Average depth of initiating pore per test bar.

The major and minor axes were also recalculated on the basis of the measurements from the TAP software. Using the area of an ellipse as an approximation for the pore shape, values for A and C were calculated from the area and aspect ratio values returned from the software:

$$\text{TAP Area} = \pi \times a \times b \qquad \textbf{Equation 32}$$

$$\text{TAP Aspect Ratio} = a/b \qquad \textbf{Equation 33}$$

$$\text{Therefore: } b = \sqrt{\frac{TAPArea}{\pi . r}} \qquad \textbf{Equation 34}$$

And

$$a = \text{Aspect Ratio} \times b \qquad \textbf{Equation 35}$$

Scatter plots have been systematically generated to show the effect of each variable on cycles to failure. Plots were generated for every pore, average pore and main pore values.

The variable that shows the greatest correlation with cycles to failure is the sum area of initiating pores (Figure 224). The major outlier highlighted in Figure 224 relates to a CMSX-4 test, orientation A, 650°C in Vacuum. Plotting just the area of the main initiating pore areas shows no correlation with fatigue life (Figure 225).

6.7.4 Effect of shape of initiating porosity

Porosity data collected from plain polished samples has been compared with the data from porosity that was characterised as an initiating pore (Table 16). For all three alloys the maximum and mean area of the initiating pores is far greater than that seen in the data collected from plain polished specimens. The average and maximum aspect ratio of initiating pores is greater for CMSX-4 and PWA1484 although it is less for ReneN5

A simple analysis of pore aspect ratio has been conducted using Scott and Thorpe's approximation for a semi-elliptical surface crack[liii] under pure bend loading conditions. A pore area was selected that was representative of those observed to initiate cracks. The ratio of a/c was varied whilst keeping the area of the pore constant. A pore with high aspect ratio with major axis parallel to the notch surface gives the highest value of K_d (stress intensity at the maximum depth position) Figure 226.

6.7.5 CMSX-4 long crack data

Long crack testing has been carried at 650°C and 725°C using CMSX-4 to complement the program of work. Testing was carried out by Mark Joyce as part of the collaborative research project as discussed in the introduction. Methodology and results from the long crack testing are described in detail in the literature[liv]. The long crack data will be used to compare with fatigue test lifetime trends and to help develop a simple lifing model. The long crack test matrix is given in Table 17, data has been generated for orientation A and B samples in air at 650°C and 725°C with tests also completed in vacuum at 650°C. Results from the tests in the form of crack growth rate vs. ΔK are presented in Figure 227.

At 650°C, fatigue crack propagation in air was seen to be faster in orientation B than in A, particularly at lower ΔK levels. Under vacuum, fatigue crack propagation rates in orientation A were seen to be similar to that in air at high ΔK. At 725 C crack growth rates were generally faster than at 650°C.

Examples of long crack test fracture surfaces are given in Figure 228 (OA, Air, 650°C) and Figure 229 (OA, vacuum, 650°C). Comparisons have been made between short crack fracture surfaces and long crack fracture surfaces along with relevant crack propagation data for ΔK. Measurements were taken from several short crack fracture surfaces to ascertain the size of the crack at the onset to rooftop cracking. Using Scott and Thorpe approximation for an elliptical crack in pure bend 220, ΔK is found to be ~ 50 MPa√m for the crack measurements as shown in Figure 230 and Figure 231 using an FEA stress estimate at the notch root.

This result fits with long crack data where Mark Joyce measured ΔK to be in the region of 50 MPa√m at the transition to rooftop cracking in his SENB specimens (Figure 228 & Figure 229).

6.7.6 Lifing Model

Crack initiation at high temperature is seen to occur at subsurface pores and is characterised by a halo around the pore where initial crack growth has occurred in vacuum. The proposed mechanism that causes this halo effect is due to the crack initiating and propagating in vacuum until it breaks the surface of the sample and is exposed to air. Initial crack propagation conditions are that of fatigue crack propagation in vacuum. Once air can enter the crack, the initial fatigue area within the halo undergoes oxidation, *after* failure has occurred. The boundary of the halo marks the point at which the crack continues to propagate, but now under combined fatigue and oxidation conditions. The two mechanisms described give rise to the change in texture and composition of the oxidised fatigue crack that are visible in SEI and BEI modes with the FEG SEM. Similar halo effects have been seen in polycrystalline disk alloys[lv]

An initial modelling approach has been implemented. The model uses a simplified pore geometry representative in size and shape of those observed on existing fracture surface. FE analysis or fracture mechanics is required to calculate K values around the pore. An estimation of the evolution of the crack shape from the pore to the circular crack path (as confirmed by the halo) via K-calculations indicated a circular shape was adopted very soon after initiation. Data from crack propagation work in vacuum can be used to

estimate the number of cycles before the subsurface crack reaches the surface by Paris law integration approaches. Crack growth data from air tests is then be used in conjunction with K calibrations based on Scott and Thorpe 220 in order to calculate the last component of the fatigue lifetime, again using Paris law integration approaches.

The model was developed as part of the collaborative research project with CNRC and has been written by Dr Xijia Wu using C++. The model code has been included in APPENDIX 3

The model was written for the 8mm x 8mm CMSX-4 notch bend tests at the strain calculated for theses tests. The model uses some important initial assumptions:

- The crack initiation is caused by an initial elliptical flaw
- That the sample has no initiation life.
- The initial sub-surface flaw is in vacuum conditions.
- The initial growth direction is controlled by the orientation of the pore therefore orientation B growth rate data in vacuum is applied to minor and major axis of the ellipse
- The subsurface crack adopts a circular morphology
- The surface crack adopts a semi-circular morphology upon breaking the surface.
- Growth to failure is controlled by data from long crack tests in air.

A schematic of the proposed crack growth model is given in Figure 232 where steps 1-2 take place in vacuum conditions before the crack breaks the surface (3) and adopts the semi circular morphology.

The model assumes that the crack begins to propagate from the 1st cycle. The initial growth occurs in a uniform stress field. For a subsurface pore, K values around the ellipse are calculated using the following equations:

$$K = F_{sn}\sigma\sqrt{\frac{\pi a}{Q}}\sqrt{\cos^2\psi + \left(\frac{a}{c}\right)^2\sin^2\psi}$$

Equation 36

$$Q = E^2(k) \approx 1 + 1.46\left(\frac{a}{c}\right)^{1.65}$$

Equation 37

Where F_{sn} is a boundary correction factor, which in case of the CMSX-4 8x8 bars is 1.1[lvi]. It is found that, numerically, the crack propagates more rapidly from the blunt

sides of the ellipse (value of *c* increases) thus rapidly forming a circular crack. This agrees with the proposed theory based on the fractography results. The model evaluates K then performs 100 iterations before re-evaluating K. At the end of each loop, the values for *a* and *c* are compared to the depth *d*. If either *a* or *c* are greater than or equal to *d*, the pore has broken the surface. During subsurface growth, crack propagation distance per cycle is calculated using the Paris equation (Equation 38 & Equation 39) where *C* and *m* are calculated from experimental data for long crack growth in vacuum for an orientation B sample.

$$a = 1.85 \times 10^{-7} \times K_a^{4.25} \quad \text{Equation 38}$$

$$c = 1.85 \times 10^{-7} \times K_c^{4.25} \quad \text{Equation 39}$$

Once the crack has reached the surface it is assumed that the crack becomes a semi-elliptical crack with depth *a* and width *2a* (at this point the crack is circular so *a*=*c*). The stress intensity factor is calculated using a weight function for a through edge crack. The model now uses orientation specific data for crack growth in air to continue growing the crack until a critical value of K is reached and the specimen fails. The critical K value is based on results from Mark Joyce and has been initially set at 60MPa√m

A flow chart describing the modelling process (Figure 234) shows the various loops the model takes as it assesses whether crack growth is occurring subsurface (therefore using vacuum crack propagation data) or has broken the surface (at which point the air crack growth data is used for the correct specimen orientation).

The model inputs are *a*, *c* and *d* in mm, *C* and *m* material constants derived from vacuum and air crack growth and a critical K value at which the bar fails. Crack growth rate data is input in mm/cycle. A comma separated text input file containing the 9 columns of data for each pore is read in to the model which then returns a two column output file with the subsurface crack growth life and the total number of cycles to failure.

6.7.6.1 Sensitivity to Pore Geometry

Minitab software has been used to perform a full factorial design of experiments (DOE) analysis using idealised porosity geometry. The test matrix uses three levels for pore geometry and depth with a 2 level field for sample orientation. The test matrix is not shown, but is a full factorial design incorporating every possible combination of the 3

inputs giving rise to 54 combinations. Statistical data from initiating porosity has been used to select the maximum, middle and minimum values for pore dimensions *a* and *c* and the pore depth *d*. Interaction plots have been created for both the internal life (Figure 235) and the total life (Figure 236) predicted by the model. Each shows the effect of two variables with respect to fatigue life (right hand axis). The scale for one variable is given along the top, with the second variable inferred through the legends (far right). Certain combinations where *a* is less than *c* are not plotted as *a* (the major axis) must always be greater than *c* by definition.

The internal life model shows that the depth of the pore has most effect when *a* and/ or *c* are small with a large depth giving rise to a longer lifetime. The top left graph for the effect of *a* vs. *c* indicates that the aspect ratio has comparatively small effect. Orientation will not have any effect on internal life as orientation B vacuum data is always used.

Interaction plots for total life show that the greatest effects occur when *a* and/or *c* are small. This time the trend is reversed. Small pores at the surface show the largest number of cycles to failure.

Response surface plots have also been used to identify the relationship between parameters. Comparing *a* and *c* with cycles to failure again shows that aspect ratio has very little effect in comparison with the major dimension of the pore (Figure 237). Having established that the major dimension has the greater effect it is plotted against the pore depth (Figure 238) which again shows that a small pore close to or at the surface will equate to the longest life. Plotting predicted internal life against predicted cycles to failure shows a linear relationship for lifetimes greater than 10,000 cycles. At shorter lives the relationship does not hold true

6.7.6.2 Sensitivity to Paris Constants and K level at failure

The model sensitivity to material constants has also been analysed. A full factorial DOE experiment has been designed to look at the effect of the Paris constants *C* and *m* and the critical value of K for specimen failure on the lifetime of an *average* sized pore in a CMSX-4 notch bend bar. The experiment design values used are given in Table 18 A 3 level experiment with 5 inputs generated 243 results. The average effects of each input are given in Figure 240. The effect of *m* and *C* constants both in air and in vacuum on total life appear to conform to an inverse power law relationship with small values tending towards infinite life as would be expected. At very long lives, changes

in crack growth rate in vacuum shows a greater effect on total life. The effect of the critical K value at which failure occurs appears to be linear although it may be levelling off at high values of K. An interaction plot for all 5 factors is given in Figure 241.

6.7.6.3 Fatigue life model results.

The fatigue life model has been presented with all porosity data for all initiating pores. Data from long crack tests has been used for CMSX-4 data (Figure 242). Vacuum crack growth rates for 650°C has been used for the 725°C predictions in absence of actual data. PWA1484 and René N5 were modelled using CMSX-4 data in air at 650°C.

Results have been presented in the form of a scatter plot of actual cycles to failure vs. predicted cycles to failure with x=y representing a perfect prediction. It should be noted that the current form of the model calculates the stress field for an 8mm x 8mm CMSX-4 notch bend bar. All tests were carried out at similar estimated strain ranges so have been included in the analysis but results are likely to be less accurate. Results for CMSX-4 8mm x 8mm notch bend bars are presented in Figure 243. The model shows good agreement with the test data

Figure 244 shows predicted values for all test data. Large icons are used to represent the main initiating point for each test bar with small icons used to represent all minor initiation points for each test. CMSX-4 tests (now including the small sized specimens) still show good correlation with actual test results with 5 of the tests lying very close to the actual values. All René N5 tests were over predicted and all PWA1484 test were under predicted.

The model has also been run using pore data collected from measurements taken by hand. The model using data generated from TAP (Figure 243) performs much better with data points lying closer to the actual test results.

6.7.7 Fatigue life modeling using Neural Networks

Neural network models have been trained using output data from the Paris lifing model described in the previous chapter or using raw data from fatigue tests. The neural networks were run within MATLAB software and used the same scripts described in chapter 5.2.9. Only small changes in the script were required to allow for different numbers of variables in the input file and to change and labelling in graphs

generated as part of the training process. Examples of Matlab scripts used are given in APPENDIX 2.

6.7.7.1 Training a Neural Network to emulate the lifing model

The lifing model described in section 6.7.6 has already been used to generate a large dataset of results for various pore geometries for statistical analysis (6.7.6.1). This dataset is of sufficient size to use to train a neural network model. A Matlab script was used to train models ranging from 1 to 20 HU's using the dataset. The neural network model produced a good fit to the data with just 4 HU's (Figure 245) with very little improvement shown with higher numbers of hidden units (Figure 246).

6.7.7.2 Training a Neural Network on test data

The amount of data collected for initiating pores is relatively small in comparison to the number of variables. Subsets of variables have been used to train neural networks to see how well they can fit to the data. Based on metallurgical understanding and the analysis of porosity data with respect to lifetime, the most important variables have been selected:

- Strain range
- Sum area of pores
- Test temperature
- Material type

Combinations of the above variables were presented to the neural network with respect to test lifetime in each case. There are a large number of combinations of inputs so only the most significant ones will be discussed. Using just the sum area and material type produced a relatively poor fit (Figure 247). The strain range for most tests is related directly to the material type so it could be expected that a reasonable fit would be achieved. Adding the strain range as a separate input allowed the neural network to achieve a much better fit to the data (Figure 248). The significance of the inputs (Figure 249) shows strain range to have the largest effect with the sum area and material type having smaller effects (both of a similar magnitude).

The addition of test temperature produced almost exactly the same results (Figure 250) in comparison to the fit achieved without. The variation of test temperatures in the input data is very small and confined to tests conducted using CMSX-4.

CMSX-4	Sample Data - Pore Area (μm²)	Initiating Pores - Pore Area (μm²)	Sample Data - Apect Ratio	Initiating Pores - Aspect Ratio
Mean	542.1	1206.1	1.2	2.2
Median	440.0	842.0	1.1	1.8
Mode	3.0		1.1	
Standard Deviation	503.2	1119.8	0.3	1.3
Minimum	3.0	179.0	1.0	1.1
Maximum	2241.9	5563.0	5.1	6.5

René N5	Sample Data - Pore Area (μm²)	Initiating Pores - Pore Area (μm²)	Sample Data - Apect Ratio	Initiating Pores - Aspect Ratio
Mean	105.2	1037.5	1.2	2.2
Median	14.9	1185.5	1.1	1.9
Mode	3.0		1.1	
Standard Deviation	222.3	809.7	0.3	0.9
Minimum	3.0	175.8	1.0	1.4
Maximum	1443.7	2185.5	5.1	3.5

PW 1484	Sample Data - Pore Area (μm²)	Initiating Pores - Pore Area (μm²)	Sample Data - Apect Ratio	Initiating Pores - Aspect Ratio
Mean	105.2	655.4	1.2	1.8
Median	14.9	457.0	1.1	1.6
Mode	3.0		1.1	
Standard Deviation	222.3	750.2	0.3	0.8
Minimum	3.0	45.8	1.0	1.1
Maximum	1443.7	3986.9	5.1	5.6

Table 16 – Comparison of Average Porosity Data vs. Critical Porosity Data

Sample ID	Orientation	Temperature (°C)	Environment	Comments
OALC1	A	650	Air	Completed
OALC2	A	650	Vac	Completed
OALC3	A	725	Air	Completed
OALC4	A	725	Vac	Not Completed
OBLC1	B	650	Air	Completed
OBLC2	B	650	Vac	Completed*
OBLC3	B	725	Air	Completed
OBLC4	B	725	Vac	Not Completed

Table 17 – Long crack data test matrix

A	C	D	Paris M Vac	Paris M Air	Paris C Vac	Paris C Air	K crit
30	15	175	2	2	1.00E-10	1.00E-10	20
30	15	175	3	3	1.00E-09	1.00E-09	40
30	15	175	4	4	1.00E-08	1.00E-08	60

Table 18 – 5 factor, 3 level design for sensitivity to material constants

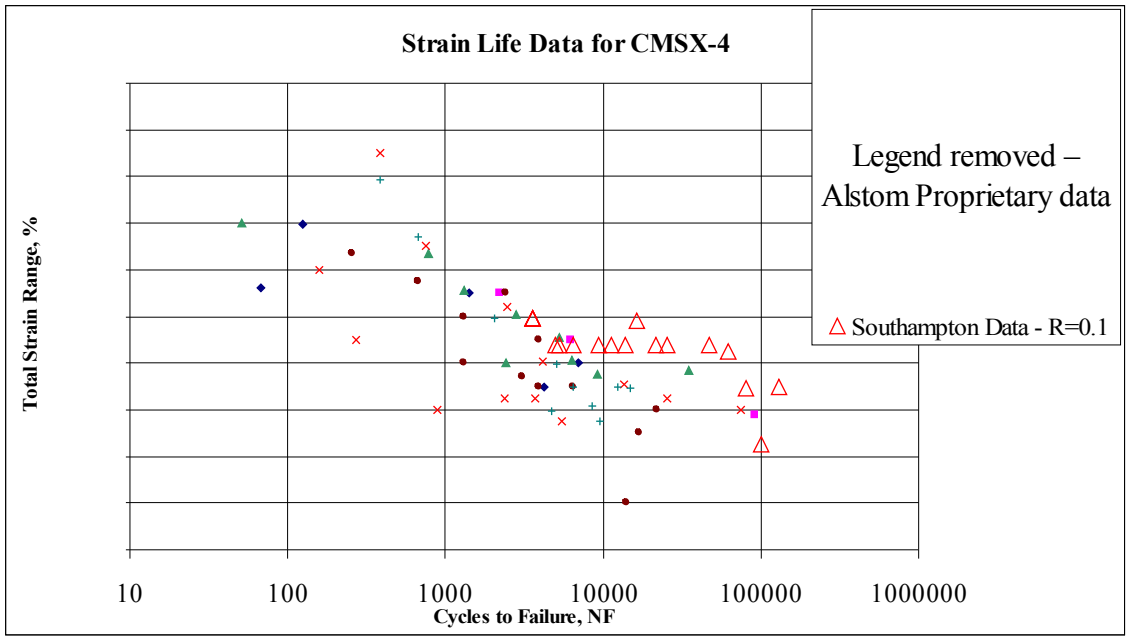

Figure 223 – Comparison of Southampton data with Alstom test data.

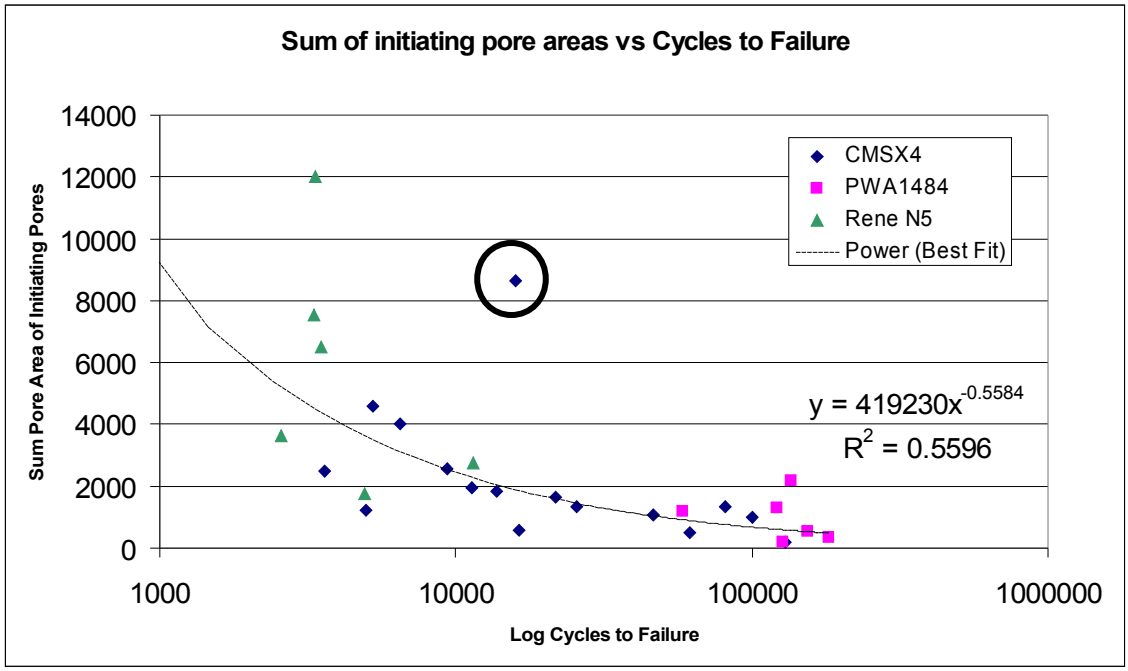

Figure 224 – Sum area of initiating pores vs. cycles to failure

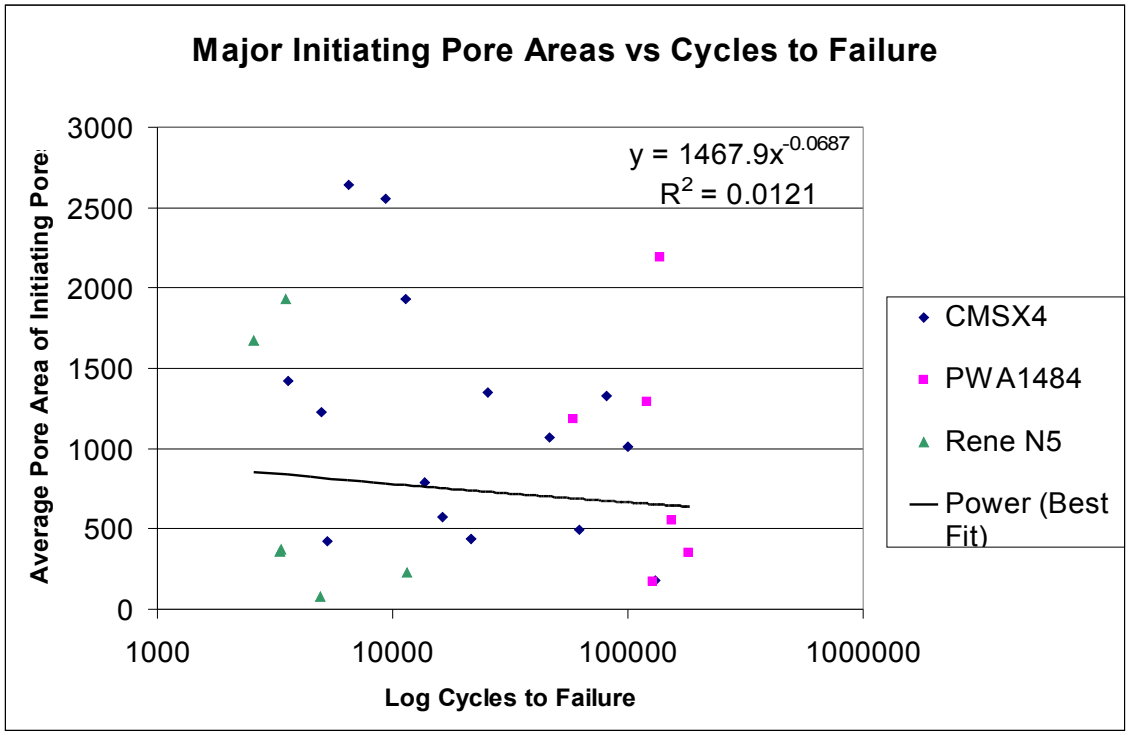

Figure 225 – Major initiating pore vs. cycles to failure

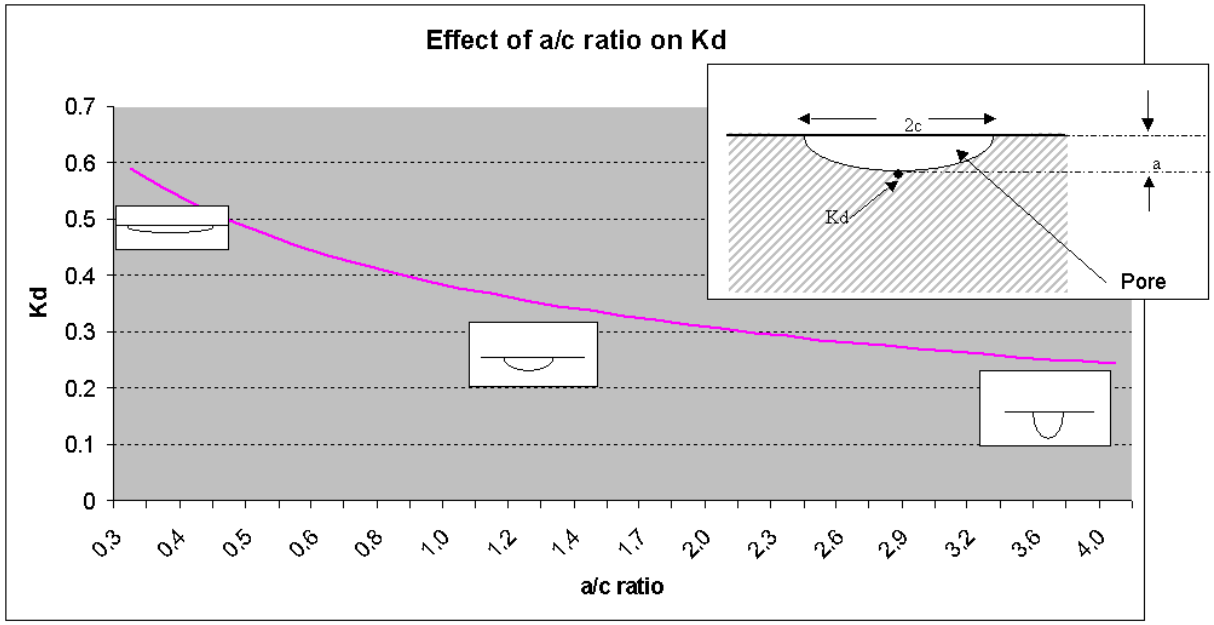

Figure 226 - effect of a/c ration on effective K_d (a simple analysis using Scott and Thorpe)

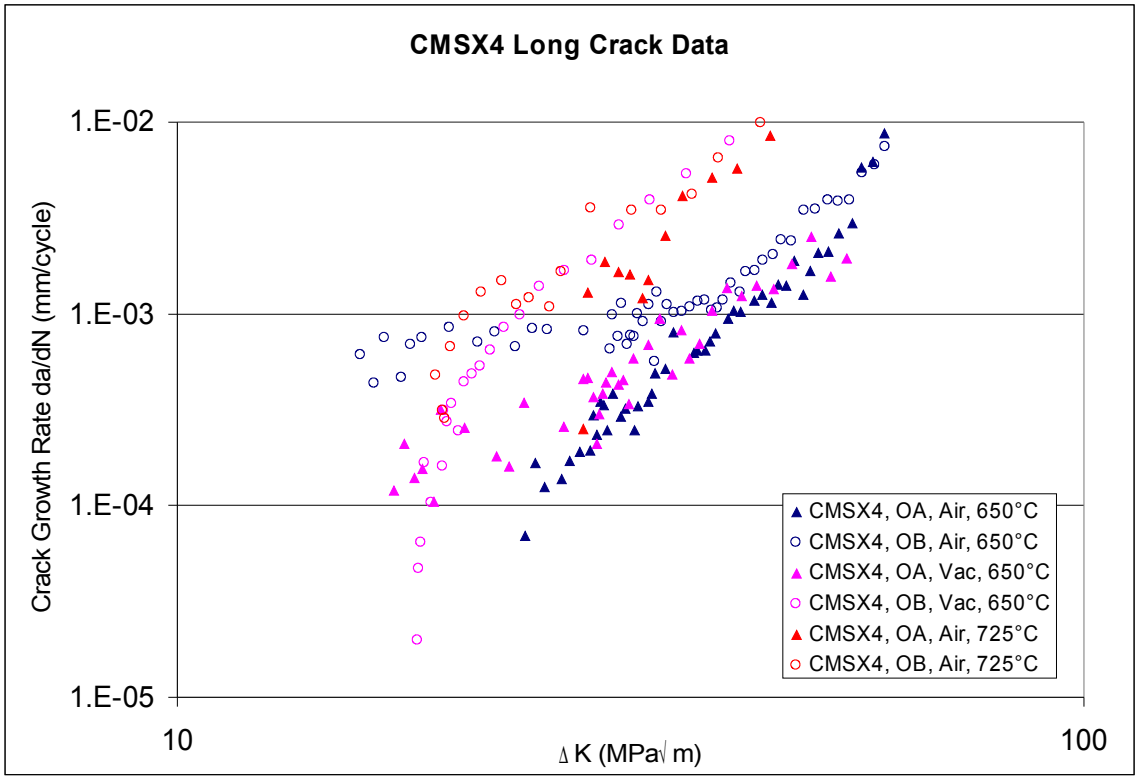

Figure 227 - CMSX-4 Long Crack Data (after Mark Joyce[220])

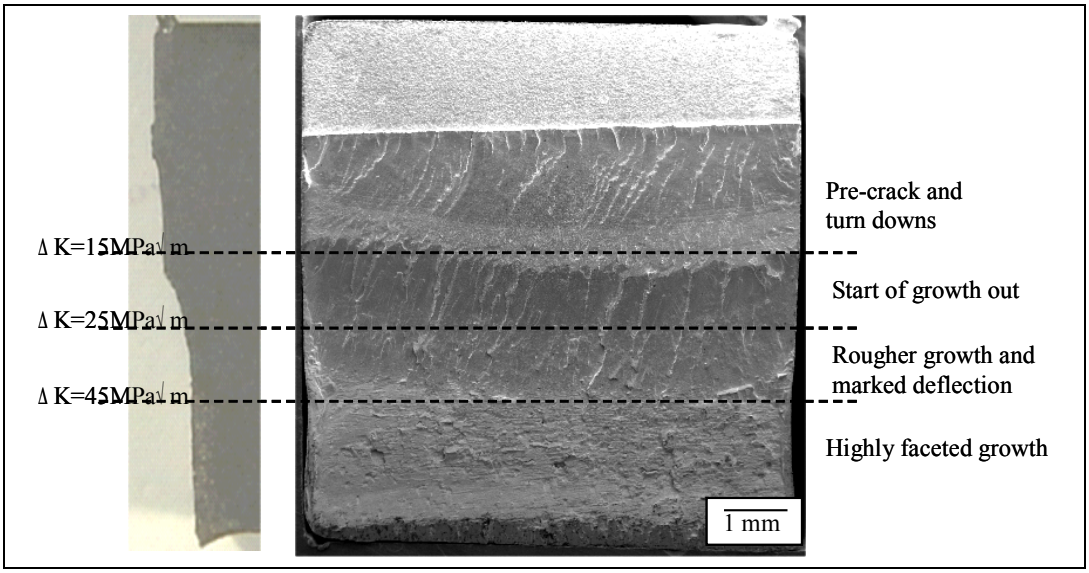

Figure 228 Orientation A, Air fracture surface (after Mark Joyce[220])

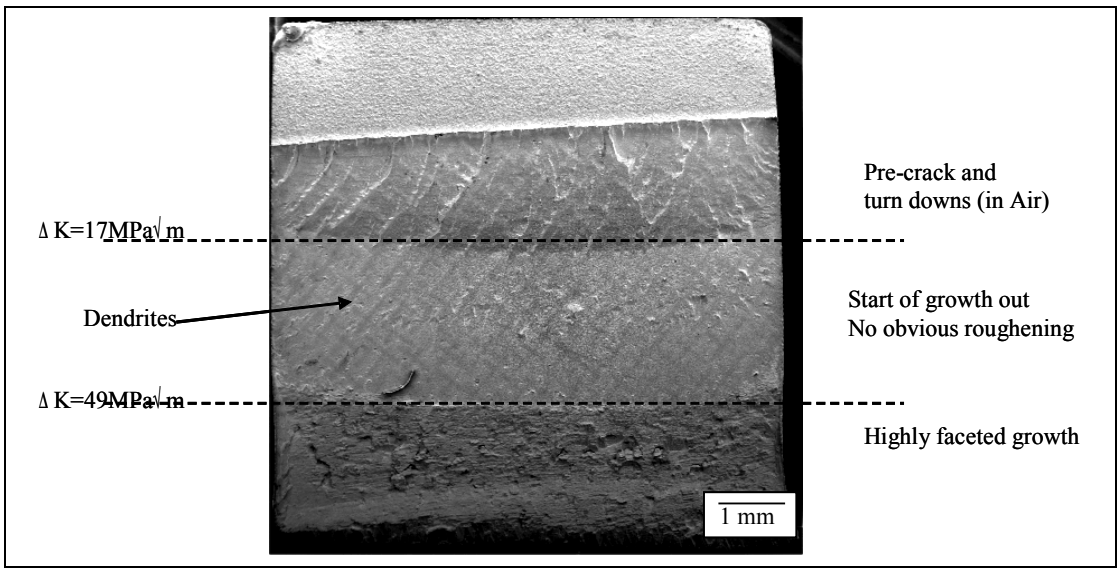

Figure 229 Orientation A, Vacuum fracture surface (after Mark Joyce[220])

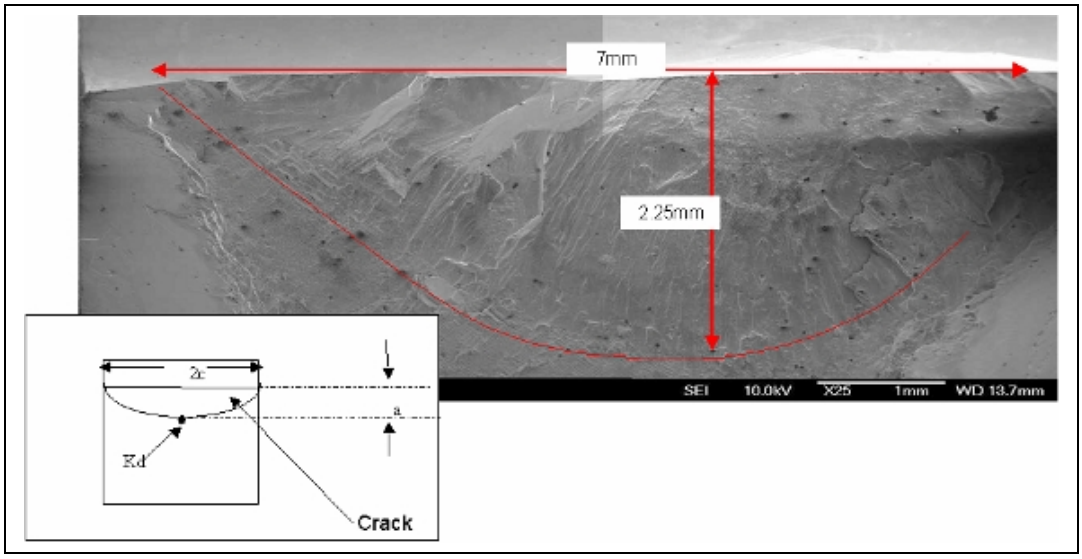

Figure 230 – Crack measurements for S&T analysis – OX 650°C air

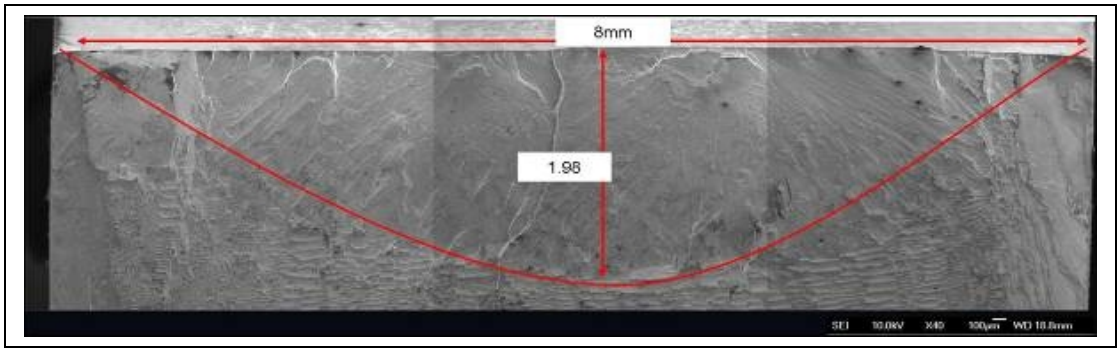

Figure 231 – BAR OA, 725°C, Air, 5271 cycles

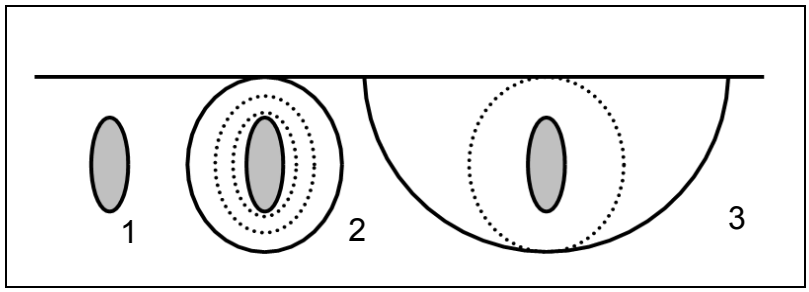

Figure 232 – Schematic of crack propagation from subsurface pore

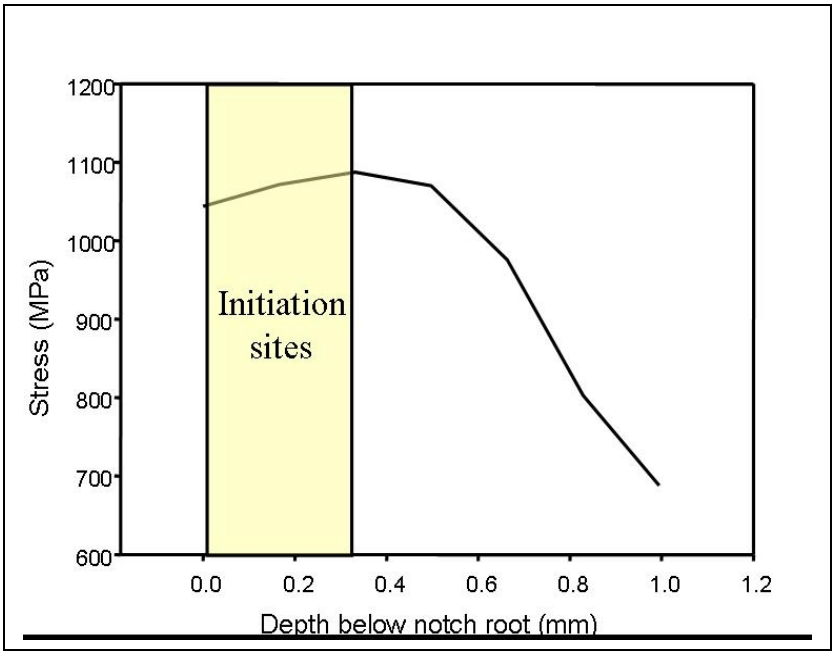

Figure 233 Stress fieled in notch root of CMSX-4 notch bend bar

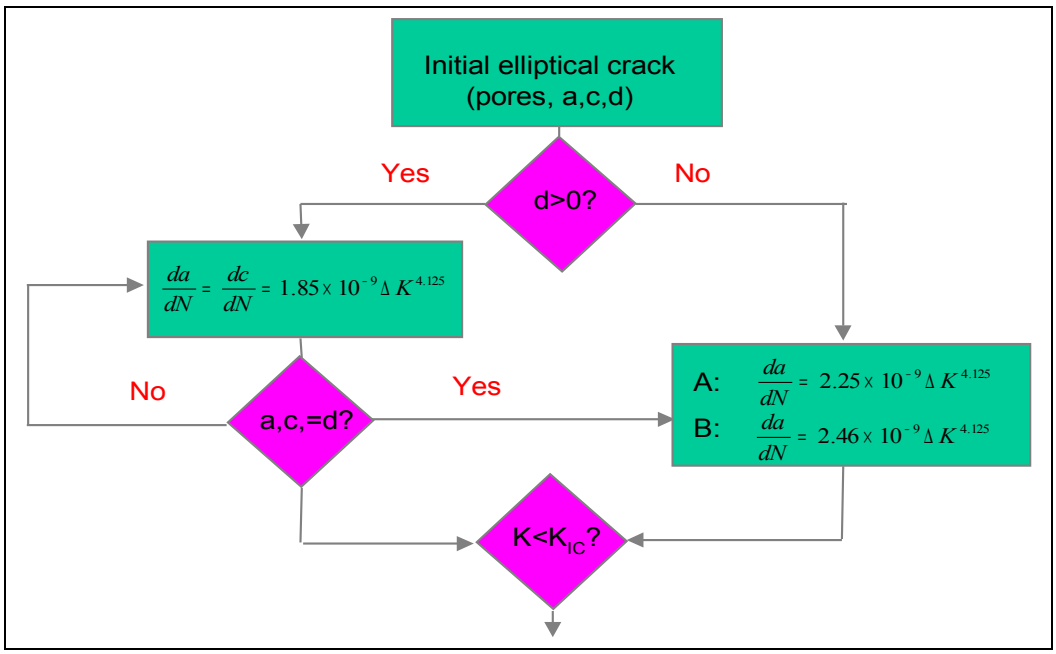

Figure 234 – Flow chart for Notch Fatigue Model

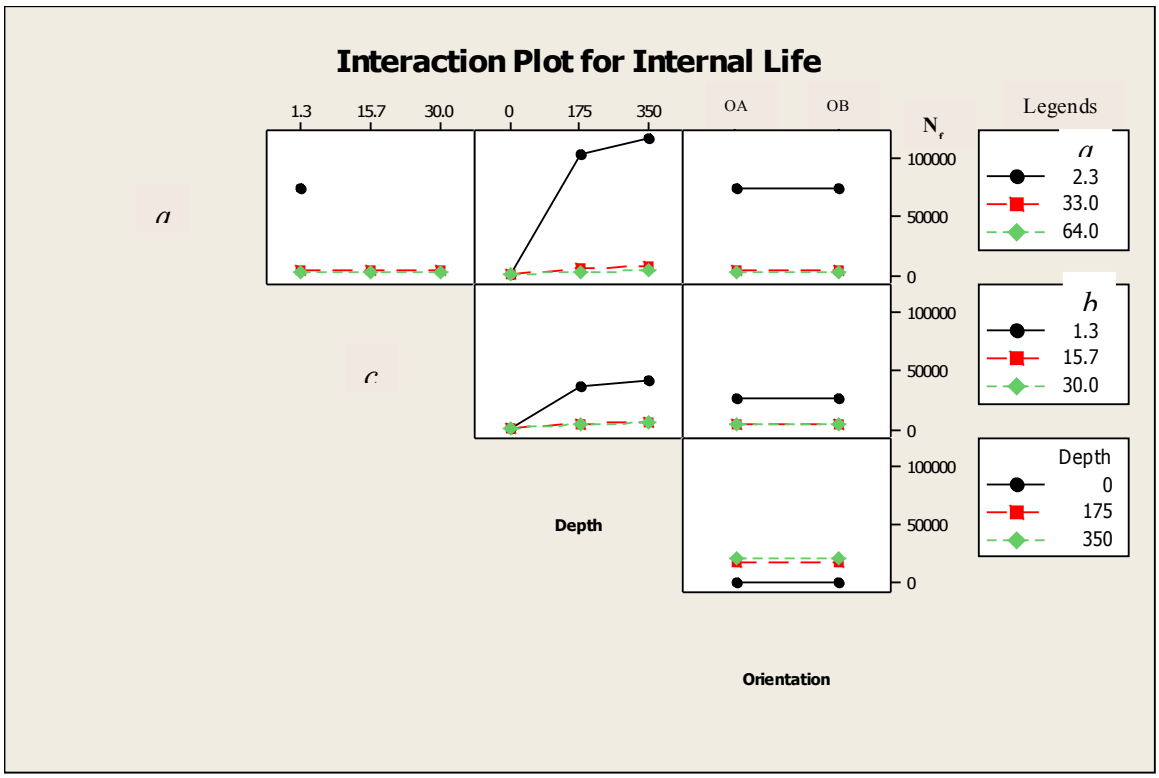

Figure 235 - Interaction plot for *a*, *c* and *d* with respect to subsurface life

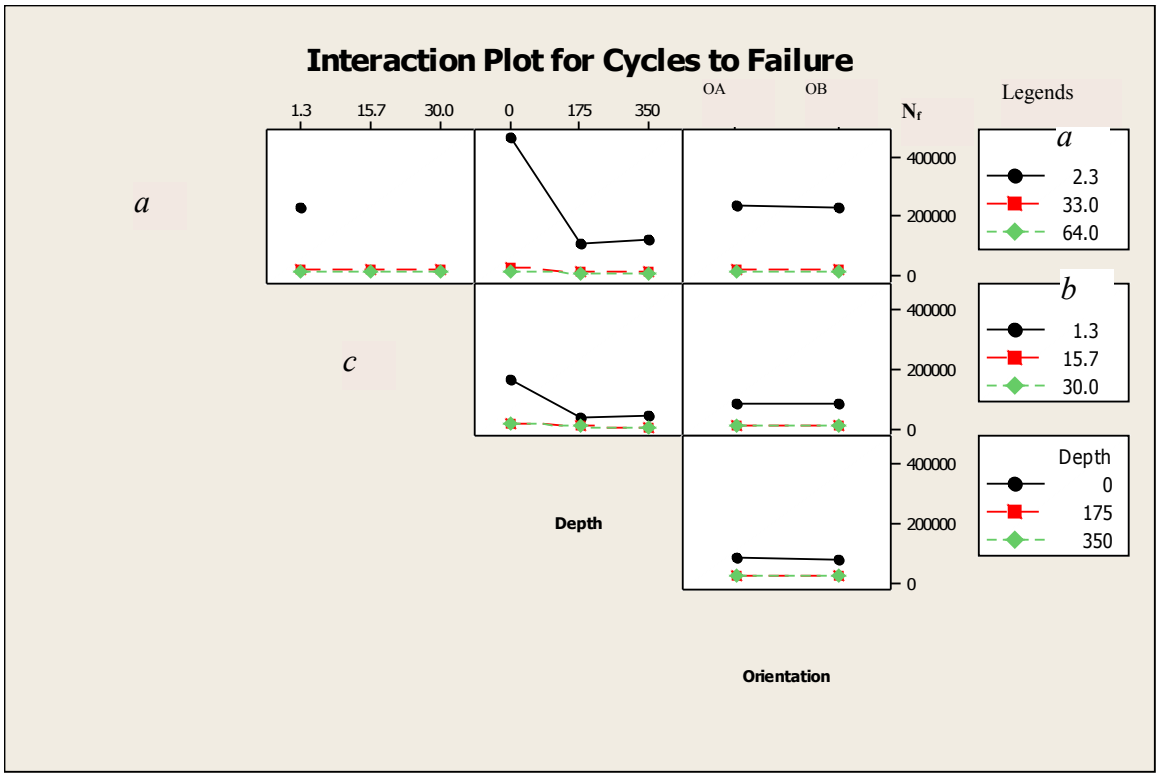

Figure 236 - Interaction plot for *a*, *c* and *d* with respect to total life

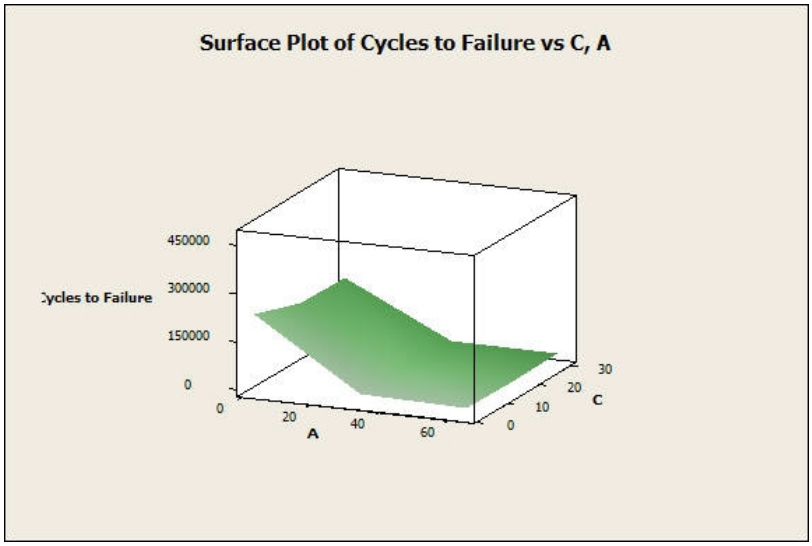

Figure 237 – Surface plot for relationship between *a*, *c* and total cycles to failure

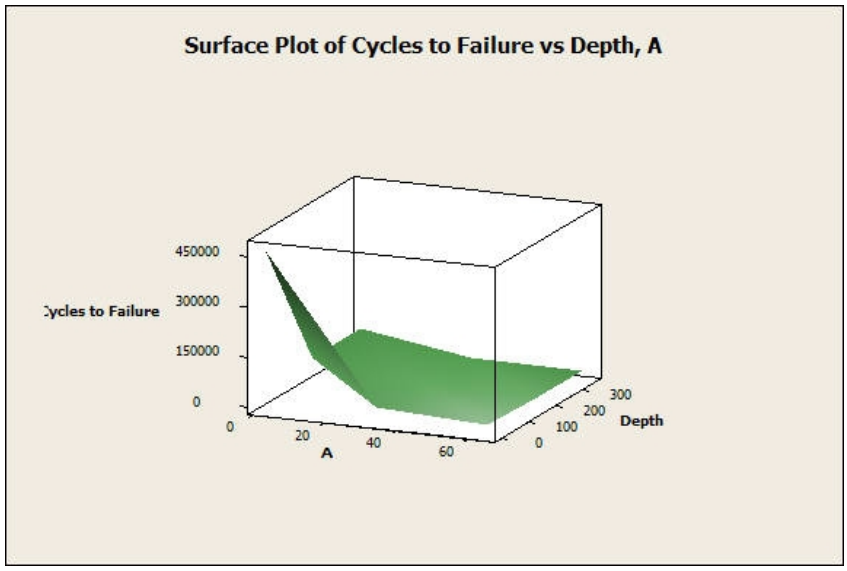

Figure 238 – Surface plot for relationship between *a*, *d* and total cycles to failure

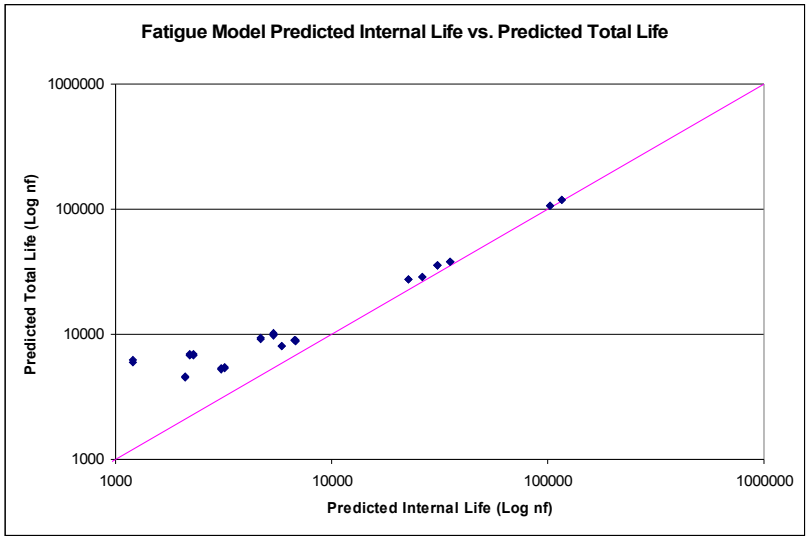

Figure 239 – Correlation between predicted internal life and total predicted cycles to failure

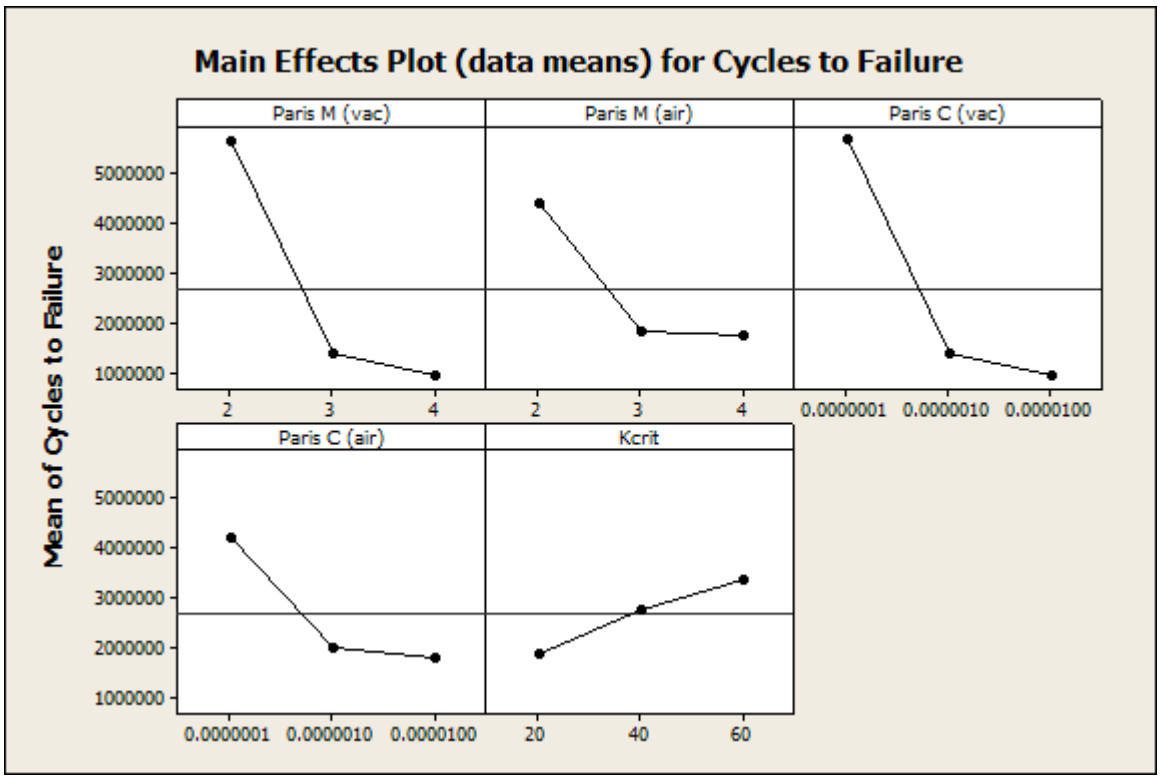

Figure 240 – Average effects for change in material properties vs cycles to failure for an average sized pore

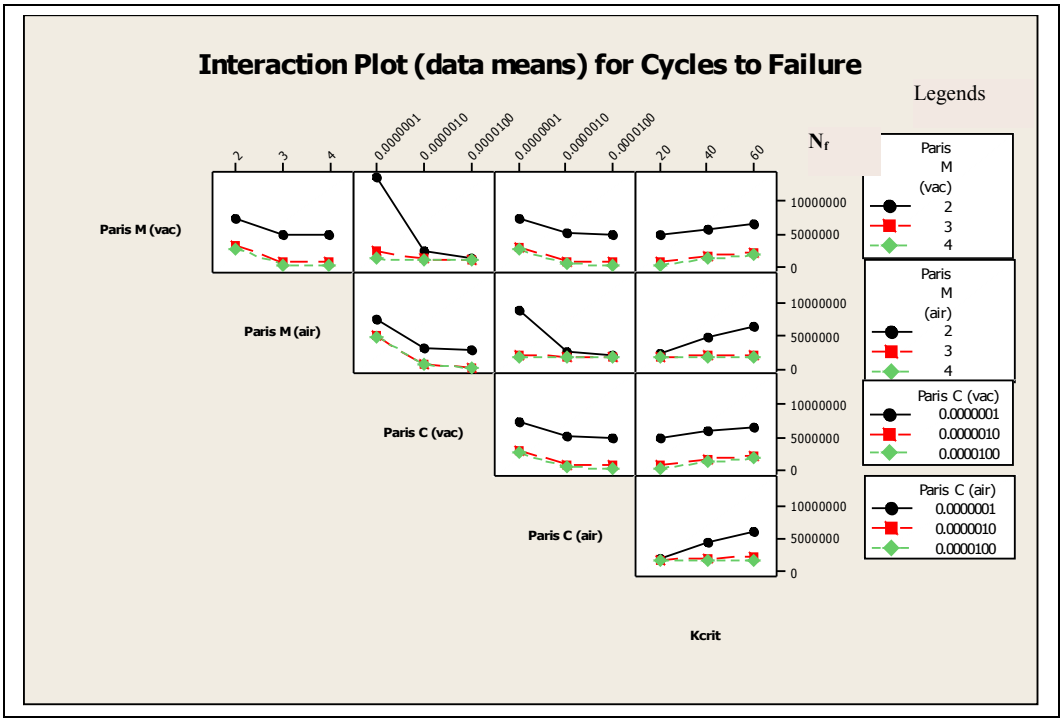

Figure 241 – Interactions plot for m_{vac}, m_{air}, C_{vac}, C_{air}, K_{crit} Vs. Cycles to failure

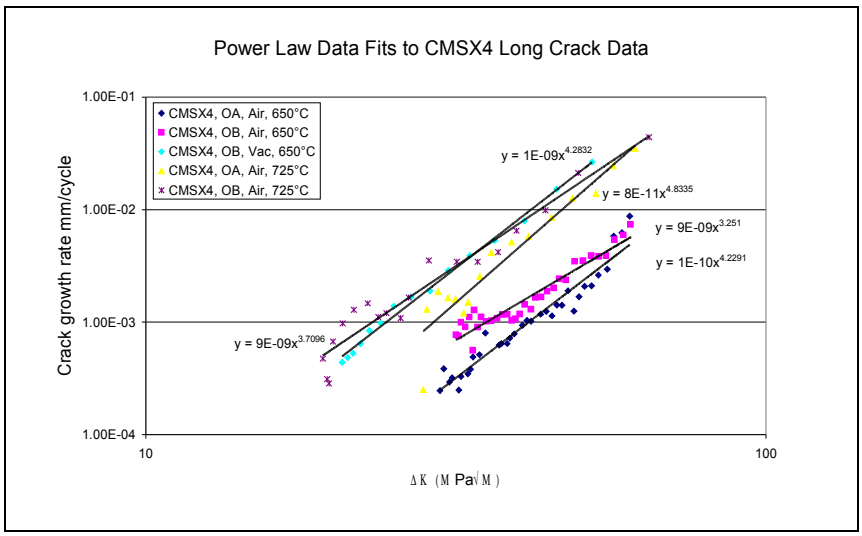

Figure 242 – Power law fits in Excel to long crack data supplied by Mark Joyce

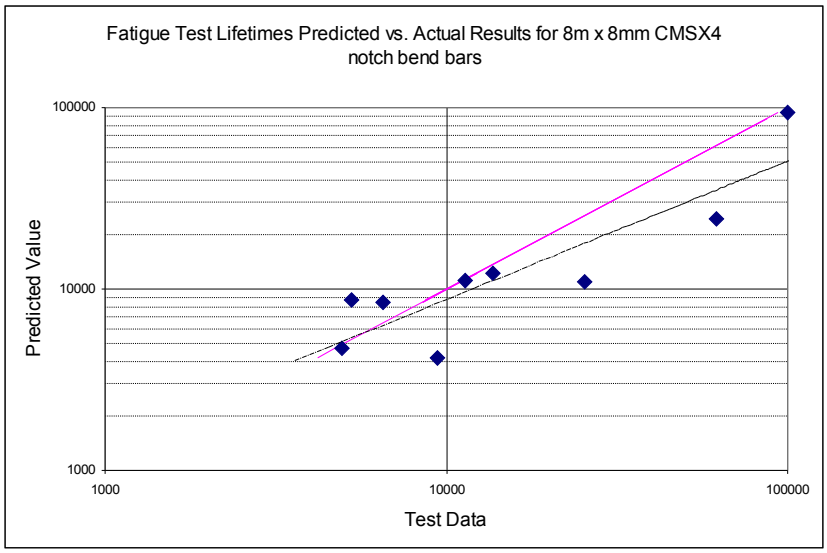

Figure 243 - Predicted results vs. actual test results for 8mm x 8mm CMSX-4 Notch Bend Bars

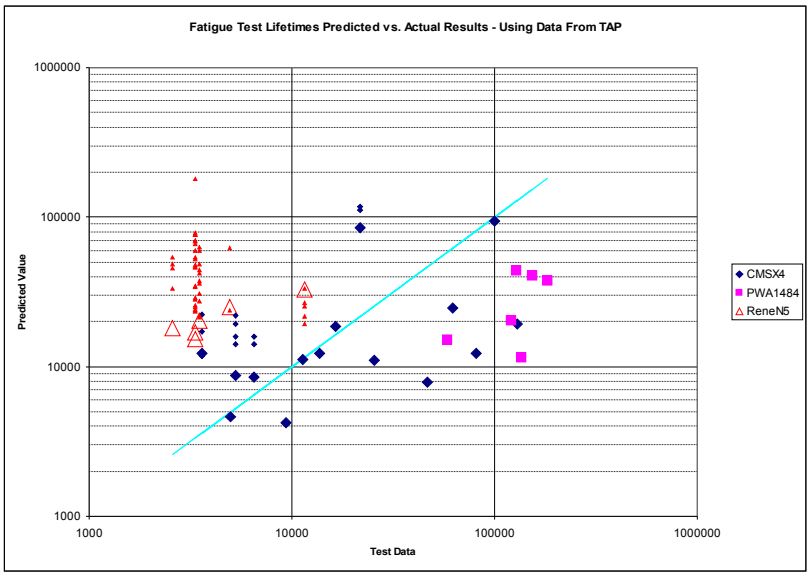

Figure 244 – Predicted results vs. actual test results (Large data points = main initiating pore, small data points = all other initiating pores for each bar)

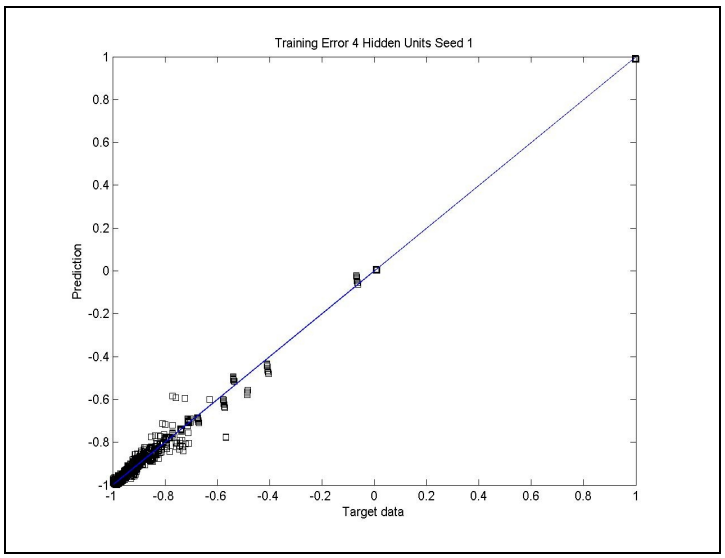

Figure 245 – Training vs target data for 4 HU neural network using results from fatiue lifing model.

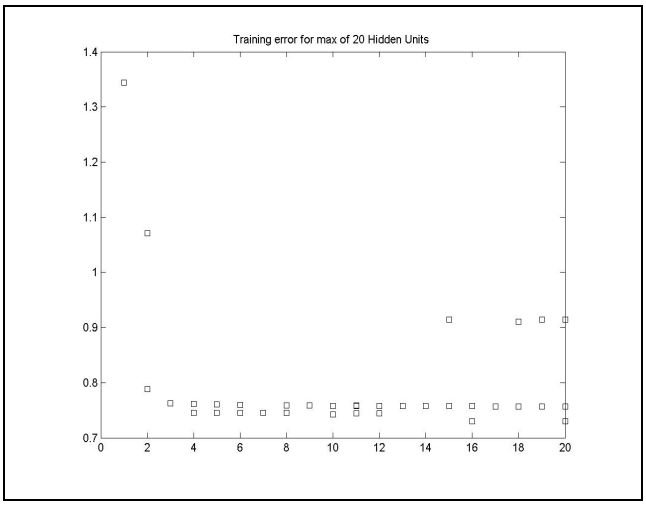

Figure 246 – Training error for neural networks using 1-20 HU's.

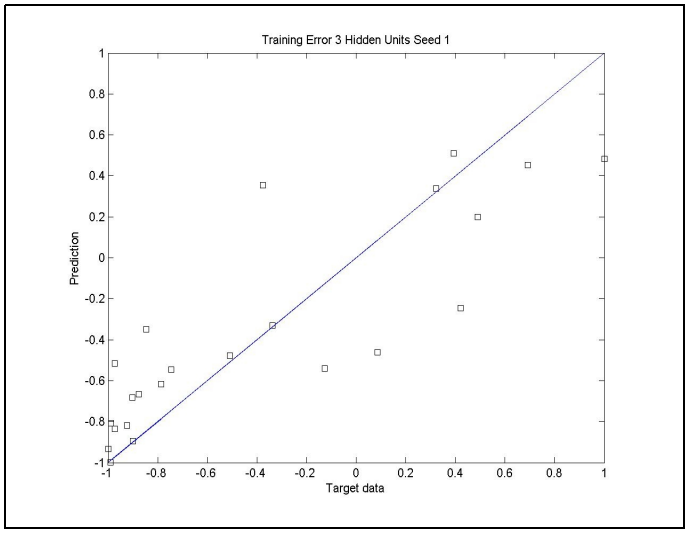

Figure 247 - Training vs target data for 3 HU neural network. Inputs = Material and Sum Area

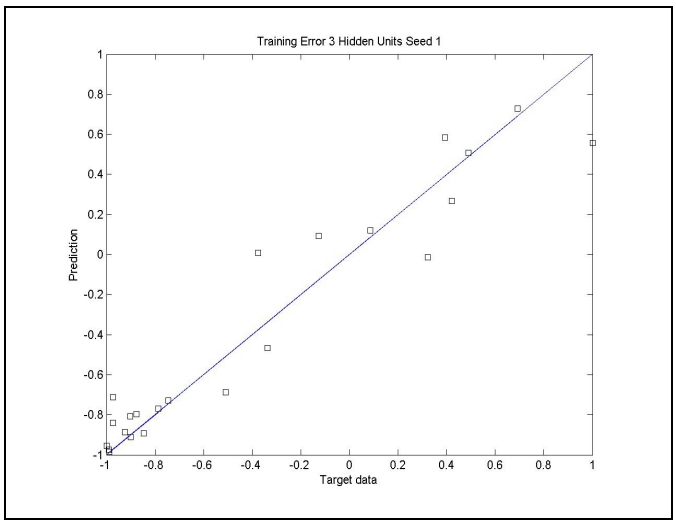

Figure 248 - - Training vs target data for 3 HU neural network. Inputs = Material, Sum Area and Strain Range.

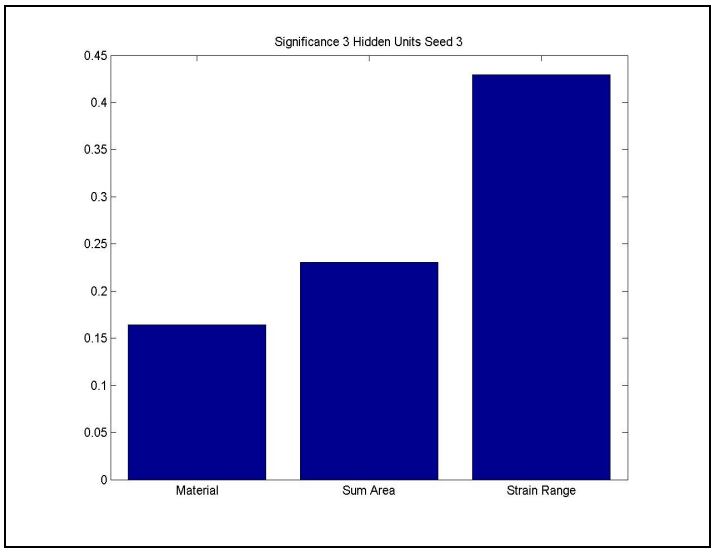

Figure 249 – Significance of inputs for 3 HU model in Figure 248

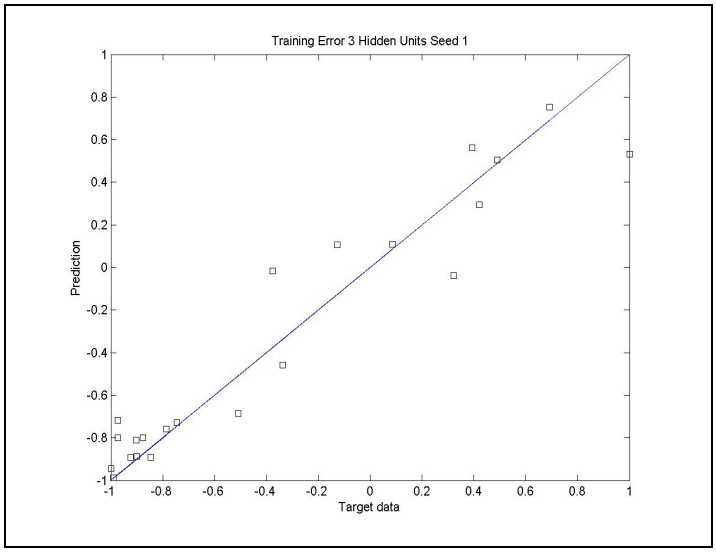

Figure 250 - Training vs target data for 3 HU neural network. Inputs = Material, Sum Area, Test Temperature and Strain Range.

6.8 Discussion

Pore measurements have been recorded for all initiating pores. Pore shape was classified very broadly into either circular, or oval. Pores were measured along the major long axis (a) and along an arbitrary 'short' axis (c) perpendicular to the long axis. The depth of the pore (d) was measured from the centre of area of the pore.

Finite body tessellation analysis has been used to analyse the complicated 2D shapes of the porosity in order to get an accurate measure of area. This process also generates an aspect ratio which was used to re-calculate the minor axis measurement

Comparisons of statistical porosity data shows that the average pore size is greater for pores on the fracture surface in comparison to a prepared polished surface. This indicates that cracks form on intersections with the greatest cross sectional area of each pore.

It was shown that the sum area of all initiating pores has the greatest correlation with fatigue life, more so than plotting just the main initiating pore area. The sum area will indirectly account for coalescence effects and therefore provides the more accurate correlation with test life. All other variables show little correlation with life. Pore aspect ratio was expected to be an important factor in the initiation of fatigue cracks but the simplified oval approximation of the pore does not bear enough resemblance to the actual pore shape for this to be assessed.

Comparisons have been made between CMSX-4 short crack fracture surfaces and Mark Joyce's long crack fracture surfaces along with relevant crack propagation data for ΔK. Measurements were taken from several short crack fracture surfaces to ascertain the size of the crack at the onset to rooftop cracking Using Scott and Thorpe approximation for an elliptical crack in pure bend220 ΔK is found to be 54 MPa√m for the crack measurements. This result fits with long crack data where Mark Joyce measured ΔK to be in the region of 50 MPa√m at transition to rooftop cracking in his SENB specimens. This simple approximation for the crack geometry and loading is useful, as it shows reasonable correlation between the Scott and Thorpe ΔK calculation and the fractography calibration. This result implies that the notch stress field gradient in the CMSX-4 8mm x 8mm bend bars has a limited effect at these crack sizes.

Analytical work has been carried out to understand the effects of sub surface pore geometry. A pore with high aspect ratio with major axis parallel to the notch surface gives the highest value of K_d (stress intensity at the maximum depth position). More detailed approximations for elliptical subsurface cracks by Rooke and Cartwright[lvii] have been investigated. The aim was to conduct a simple 2D analysis of

an elliptical subsurface crack and analyse the combined effects of depth, a/c ratio and rotation. The Rook and Cartwright solution was not flexible enough to suitably model porosity conditions. Analysis is also still 2D.

6.8.1 Fatigue life modeling

Using observations from fracture surfaces, a modelling approach to capture initiation from a geometrical feature, such as a pore, has been proposed. Crack initiation at high temperature is seen to occur at subsurface pores and is characterised by a halo around the pore when testing in air. The proposed mechanism that causes this halo effect is due to the crack initiating and propagating in vacuum until it breaks the surface of the sample and is exposed to air. Initial crack propagation conditions are that of fatigue crack propagation in vacuum. Once air can enter the crack, the initial fatigue area within the halo undergoes oxidation, *after* failure has occurred. The boundary of the halo marks the point at which the crack continues to propagate, but now under combined fatigue and oxidation conditions.

Development of a fatigue lifing model based upon initiation from porosity features has allowed a theoretical sensitivity study to be carried out. The effects of pore dimension and material constants have been analysed separately. Internal life is mostly dependant on depth of pore when pore size is small. This combination gives rise to the longest crack growth distance required for the subsurface crack to reach the surface. This observation is reversed when looking at total life, where small pores close to the surface generate the longest total life. Crack growth rate data in vacuum for CMSX-4 is faster than that in air so it follows that a small initiation point from which the majority of the crack growth is in air will yield the longest lifetime.

The major dimension a is seen to be the next most important factor in the model but did not appear to be coupled with the c dimension to the extent expected. A long thin pore is not much better or worse that a long fat pore. It has been shown numerically that crack growth in a sub surface ellipse occurs more quickly in the c direction thus causing the void to be circular. Any coupling between variables is more likely to come from the relationship between area and lifetime rather than aspect ratio and lifetime.

Sensitivity to crack growth rate constants m and C is high with longer lifetimes as either value is decreased. Relationships between m and lifetime and C and lifetime are of a power law type with small values of m and C tending towards infinite lifetimes. It is therefore important that there is confidence in crack growth rate data used for the

model. It is suggested that repeat long crack tests may be beneficial to generate more accurate material constants although short crack growth laws are probably even more appropriate but considerably more difficult to obtain. The effect of changing the critical K value appeared to be linear over the range of values tested. Effect plot did suggest that the value was starting to flatten off at high K levels. This is expected because at the these K levels crack propagation is so fast that changes in the critical failure level will have little effect on the total life.

The model has been presented with data for all pores identified as initiation points from all 3 alloys. Crack growth rate data from CMSX-4 has been used for all cases in absence of any more relevant data. Predicted results for 8mm x 8mm CMSX-4 bars show good correlation with actual test results. With the exception of two tests, the model is under predicting lifetimes. Differences between the predicted value and actual value are thought to be due to two reasons:

- The model assumes instant initiation from the critical pore. This is possible but is unlikely to occur in *all* cases. The number of cycles to initiation cannot be captured in this model and can be treated as a probabilistic function. Confidence limits could be added in one direction (increased life) to indicated to possible increased in life due to initiation. These values can only be determined experimentally although the geometry of the pores is expected to have an effect.

- The model does not use short crack data, using a Paris law approximation will result in faster crack growth at low ΔK regions. The Paris growth law will also under predict growth rate as the sample approached failure but the number of cycles accumulated during this stage is low so the effect is much smaller.

When presented with data for PWA1484 and René N5 the model is less accurate. Lifetimes for René N5 are constantly over predicted. This alloy showed the greatest number of initiating pores on each fracture surface. Multiple initiations and coalescence will yield shorter lives than those predicted from a single pore in the model. Modifications are required to allow for multiple initiation points in the model. As two small cracks approach each other a larger semi elliptical crack will be formed. Rules for this coalescence can be added in a future model. The effect of multiple cracks on the stress field is more complicated and may require changes to the underlying fracture mechanics equations.

Crack shape evolution during progression from subsurface initiation to circular subsurface crack (halo) to semi elliptical crack and coalescence with nearby neighbours could possibly be monitored by running another test. Running a test that alternated between high and low frequency or between high and low R ratio could generate beachmarks defining the crack front at various points throughout crack growth.

Lifetimes for PWA1484 are consistently over predicted. The crack growth rate data is incorrect (CMSX-4 data has been used). Data for PWA1484 has been found in the literature and substituted into the model but did not improve the accuracy of the predictions. PWA1484 testing was performed in axial tension. Therefore the assumptions of stress gradient are different for this type of sample. The stress value calculated in the model will be much less accurate for this sample geometry and is likely to cause the greatest difference between actual and predicted results. The model requires modification for this particular specimen geometry before more crack growth rate data is added.

Predictions for all 3 alloys are dependent on the predicted stress value to drive the crack growth rate. FE analysis shows that the notch region becomes plastic at maximum load. An estimation of the stress has been made but could be refined by performing tensile tests to generate stress strain curves to feed into an FE model to predict notch field stresses. This process could be refined further by performing cyclic stress strain tests in order to assess the amount of plastic hardening/softening that takes place during the first few cycles. This data will also allow for re –assessment of the strain range for each test and may move Southampton data closer to the Alstom test data as shown in (Figure 223)

Neural networks have been trained on artificial data from the lifing model and on real data collected from fatigue tests using Matlab. It has been demonstrated that a neural network can be trained on data from the fatigue lifing model with only a small error in the resulting predictions. However, when actual test data is used, the neural network was unable to fit the data to the same degree. This could be attributed to two factors, both of which are likely to have an effect. Firstly, the model cannot account for the crack initiation life, this has been discussed with relation to the fatigue lifing model already. The neural network model would benefit from error bars as generated by Neuromat software to give an indication of the amount uncertainty present in the predictions. This would provide a good measure of variability of initiation life within the tests. In order for this to be successful the neural network will require a much larger training set before any meaningful conclusions can be drawn. Secondly, although there

are a large number of variables that affect fatigue life, only a small combination of variables was used for each model. In order to use a larger number of input variables, the size of the input dataset would need to be increased substantially. The size, location and number of initiating pores cannot be predefined before testing so methods such as DOE cannot be used to pre-define a test matrix.

6.9 Conclusions

Crack initiation was dominated by inter-dendritic <100> aligned micro-porosity, which is directly affected by the secondary orientation of the sample, although no clear effect of secondary orientation on overall notch fatigue life has been found

Surface oxide cracks did not appear to initiate critical fatigue cracks. At high temperature in vacuum, initiation occurs from pores at or close to the notch surface, whereas at high temperatures in air, initiation occurs almost exclusively at sub-surface pores, indicating a possible in-filling of surface pores by oxidation.

Scatter in lifetimes can be partially modelled by a multi-part Paris type lifing approach, modelling initial sub-surface crack growth from a pore under vacuum conditions and subsequent crack growth under air once the crack breaks through to the surface. Vacuum long crack propagation rates at 650˚C indicate that apparent vacuum lifetime improvement is not necessarily due to slower propagation. Development of the model requires more realistic crack growth laws, allowing for crack coalescence and to be tested more extensively against increased amounts of experimental data.

A neural network model is able to capture the complicated relationships within the fatigue lifing model but unable to fit to real test data presented with respect to a reduced number of test variables. A neural network approach will also benefit from a larger spread of test data.

7 Final Conclusions

Fatigue life estimation for a given alloy has been carried out using two different approaches

Both sections of work hope to address some of the factors which influence the fatigue life of superalloys and the inherent scatter in fatigue life data. The first approach uses neural network models to fit patterns in data in order to predict material performance based upon a set of inputs (composition and processing parameters). At this level, the model does not have any 'knowledge' of metallurgy or microstructural evolution of the alloys concerned.

The contribution of the work presented comes from methodologies developed for the selection of training data in the first instance combined with defining a set of tests for the trained model. A model trained on a small amount of 'good' data will give better predictions than a model trained using a much larger dataset including 'bad' data. The decision as to which data should be included in the model has been based on metallurgical knowledge and experience gained from actually using the training datasets. Initial neural network models were re-trained multiple times with small changes to the training dataset and the effects on the output recorded for each change made. The sensitivity tests are then required to judge if the model is picking up real trends in the data that can be explained by our physical understanding of the problem. Without these processes, the neural network modelling is reduced to a data fitting exercise. The processes are now being used by QinetiQ as part of their neural network modelling method.

Supporting work with Matlab has been carried out to complement the work carried out using Neuromat. This work has not questioned the theories behind the neural network modelling process employed by Neuromat. An understanding of each step in isolation was achieved buy using Matlab scripts to generate a more transparent modelling process that both increased the knowledge of the process and validated the results that were generated using Neuromat.

Models have been shown to perform well against known and unknown data from the literature and the next step for QinteiQ is to use them to help develop a new alloy composition and validate the results via physical testing. Once validated, this modelling processes could bring huge cost savings in alloy development by providing a screening process before committing to produce test samples of new materials.

The second approach tackles a much more specific problem with a more a mechanistic approach. Using observations from tests, a model has been described and developed using fracture mechanics theory and data derived from tests. The model has been successful in increasing understanding of the role of porosity in the fatigue life of a notched test specimen. This process has helped explain a proportion of the scatter seen in fatigue test results. The modelling process has been backed up by microscopy to illustrate the mechanisms present during the fatigue initiation process. A lot of care has been taken to remove sources of scatter where possible. Statistical analysis methods used to analyse the input data for the neural networks have also been used to look for patterns in test data with particular emphasis on porosity size and distribution.

Although both sections of work have started off quite separate, the information generated as a result of the LCF testing and modelling can know begin to be used in conjunction with the neural network model. A lifing model that is able to take more general information about porosity shape distributions and volumes could be used as another input to the higher level neural network modelling approach thus addressing another source of scatter in the data.

Lessons learnt from each section of work have benefited the other. Knowledge of testing methodologies and practices proved very useful when searching for, and filtering through, data presented in technical papers. Results from LCF tests using a variety of alloys have helped highlight factors, such as porosity distribution, which directly affect the scatter in fatigue life but as yet are not incorporated into the neural network modelling process. Modelling techniques and scripts that were developed as part of the neural network program have been applied to data generated as a result of LCF testing at Southampton

8 Further Work

Further work to improve the LCF neural network should concentrate on manipulation of the input data to in order to present the model with 'clean' data with a possible reduction in the number of inputs. The following experiments should be carried out:

- Reduce 'scattered' input to a series of SN curves. Theoretically there should be no numerical discontinuities in this data so interpolation can be used to provide a set number of points per alloy curve.
- Predictions should also be in the form of SN curves, not predictions against isolated points
- Investigate the use of the Smith Watson Topper parameter to condense information about R ratio and frequency.
- Investigate grouping other inputs into a single parameter, such as γ' formers Al and Ti.

The fatigue lifing model would benefit from the following information

- Crack growth rate data for Rene N5 and PWA 1484
- More accurate stress calculation for test bars of different geometry – This could be achieved using FEA or extension of the current methodology.

Further developments to the model should look at implementing multiple initiation from porosity with separate cracks growing and coalescing to produce one large crack.

A statistical input based on the probability distribution for the size and shape of pore for a given alloy could be used to generate results with a accompanying levels of scatter. This information can then be used as an input to the LCF neural network modelling process.
This would require upfront optical or 3D topological analysis of each alloy to define the porosity distributions

APPENDIX 1 – Matlab neural network training script for YS models.

```
%Neural network training
%Matlab script written by Mark Miller.

clear       %clears current workspace

%----------------MODEL PARAMETERS---------------

humin = 5;      %Min number of hidden units
humax = 22;      %Max Number of hidden units
ep = 100;    %Number of training epochs
x = 20;      %Number of seed points to use


%----------------PROCESS INTPUT DATA---------------------

   load('Input workspace.mat');        %loads matlab workspace
containing all input data
   YS = YS_InputData_26Apr05';       % Takes transpose of
"YS_InputData" matrix and names it "YS"'
   p=YS([1:29],:);                     % Creates matrix containing
training data "p"
   [pn, pmin, pmax] = premnmx(p);      % Creates pn, pmin, pmax - used
to normalise data
   t= YS(30,:);                        % Creates matrix containing
target data "t"
   [tn, tmin, tmax] = premnmx(t);      % Creates tn, tmin, tmax - used
to normalise data

   Test = Testdata';                   % Take transpose of "Testdata"
and name it "Test"
   TestN = tramnmx(Test, pmin, pmax);  % Normalise data using pmin and
pmax generated from training set
   vinputs = vinputs';
   vtargets = vtargets';
   Test.P = tramnmx(vinputs, pmin, pmax);  % Normalise data using pmin
and pmax generated from training set
   Test.T = tramnmx(vtargets, tmin, tmax);  % Normalise data using
pmin and pmax generated from training set

   TrainingErrors = [];                     %creates array to store
Training MSE of each model
   %TestErrors = []                         %creates array to store
Test MSE
   %of each model - Not in use yet.

   %-------------------------First loop to initialize NN for given
numer of
   %Hidden
Units-----------------------------------------------------------

   for hu=humin:1:humax;                    %loop between min number
and max number of HU's in steps of 1

      Results = Testdata(:,29);           %Add line of data containing
temperatures to results matrix

      name1 = int2str(hu);                %create text string for
number of hidden units
      name2 = ' Hidden Units ';
      HuName = [name1, name2];
```

```
      Mkdir (HuName);                      %Create new folder to store
results.
       cd (HuName);                         %Make new folder working
directory

      % ---------------------------NN ARCHITECTURE-------------------

      net=newff(minmax(pn),[hu,1],{'tansig','purelin'},'trainbr');
%create network

      net.trainparam.show = 10;           % Updates graphs every 10
epochs
      net.trainparam.epochs = ep;         % Train network for (ep)
epochs


      %----------------------------Sub Loop to train one model for a
given number of Hidden Units-----
      % Trains network and make predictions using unseen data.
Process repeats x
      % no. times.

      for seed=1:1:x;                       % Repeat training x times

           name1 = int2str(seed);        %create string for seed
number
           name2 = 'Seed ';
           SeedName = [name2 name1];


            net = init(net);                    % Initialise network
            eval(['Initnet' num2str(hu) num2str(seed) ' = net']);
% Record initial network in matrix called "initnet(i)"


            net = train(net,pn,tn,[],[],[],Test);             % Train
network - Network plots predictions error against test data.

            name1 = 'Training data ';                         %
Creates name for graph and saves as jpeg
            name = [name1 HuName SeedName];
            print ('-djpeg', name);
            close

            % Calculate Training errors

            ErrN = sim(net,pn);                              % Perfrom
prediction for all original input data
            e = tn-ErrN;                                     %calculate
matrix 'e' (targets - predicted values)
            perf = mse(e);                                   % Mean
squared error of 'e'
            TrainingErrors = [TrainingErrors perf];          % Add mean
squared error value to Training Error matrix

            plot(tn,ErrN,'ks',tn,tn);                         %Plots
targets vs predicted
            axis([0 1 0 1]);
            xlabel('Target data');
            ylabel('Prediction');
            name1 = 'Training Error ';
            name = [name1 HuName SeedName];
            title(name);
```

```
            print ('-djpeg', name);
            close


            % Make predictions

            aTestN = sim(net,TestN);            % Perfrom prediction
"aNim" contains normalised predictions
            aTest = postmnmx(aTestN, tmin, tmax);   % Un-normalize
data
            Ans = aTest';                       % Transpose results
matrix
            Results = [Results Ans];            % Adds predicted
results to results file

            eval(['Network' num2str(hu) num2str(seed) ' = net']); %
Rename trained network

      end

      %--------------------PLOT GRAPHS OF INDIVIDUAL MODEL
PREDICTIONS----------------------------
      last = x+1;  %Last line of data predictions
      aver = x+2;  %line containing data predictions

      MeanRes = mean(Results(:,2:last)')';              %Adds mean
results to predictions results file
      Results = [Results MeanRes];

      %Plot results against actual data.  Actual data in 2 column
matrix,
      %temp and YS.

      name1 = 'M313 Results ';
      name = [name1 HuName];
      plot((Results(1:23,1)),(Results(1:23,2:last)),(M313(:,1)),
(M313(:,2)),'rd');
      xlabel('Temp');
      ylabel('YS');
      title (name);
      print ('-djpeg', name);
      close

      name1 = 'M22 Results ';
      name = [name1 HuName];
      plot((Results(24:46,1)),(Results(24:46,2:last)),(M22(:,1)),
(M22(:,2)),'rd');
      xlabel('Temp');
      ylabel('YS');
      title (name);
      print ('-djpeg', name);
      close

       name1 = 'M21 Results ';
      name = [name1 HuName];
       plot((Results(47:69,1)),(Results(47:69,2:last)),(M21(:,1)),
(M21(:,2)),'rd');
      xlabel('Temp');
      ylabel('YS');
      title (name);
      print ('-djpeg', name);
      close
```

```
      %------------------------PLOT GRAPHS OF MEAN
(COMMITTEE)PREDICTIONS------------

       name1 = 'M313 Average Results ';
      name = [name1 HuName];
      plot((Results(1:23,1)),(Results(1:23,aver)),(M313(:,1)),
(M313(:,2)),'rd');
      xlabel('Temp');
      ylabel('YS');
      title (name);
      print ('-djpeg', name);
      close

       name1 = 'M22 Average Results ';
      name = [name1 HuName];
      plot((Results(24:46,1)),(Results(24:46,aver)),(M22(:,1)),
(M22(:,2)),'rd');
      xlabel('Temp');
      ylabel('YS');
      title (name);
      print ('-djpeg', name);
      close

       name1 = 'M21 Average Results ';
      name = [name1 HuName];
      plot((Results(47:69,1)),(Results(47:69,aver)),(M21(:,1)),
(M21(:,2)),'rd');
      xlabel('Temp');
      ylabel('YS');
      title (name);
      print ('-djpeg', name);
      close

       cd ..

       %-----------------------------------------------------------------
------

       eval(['Results' num2str(hu) ' = Results']);         %Renames
results file corresponding to number of HU's
   end

   name1 = 'Results';
   name = [name1 HuName SeedName];
   save(name);                          %Workspace is saved one all
training finished.
```

APPENDIX 2 – Summary of data collected for LCF neural network model

Alloy	Reference Source
Alloy 10 B1	NASA
Alloy 10 B1	NASA
Alloy 10 B2	NASA
Alloy 10 C1	NASA
Alloy 10 C2	NASA
Alloy 10 D1	NASA
Alloy 10 D2	NASA
Alloy 10 E1	NASA
Alloy 10 E2	NASA
APK-6	Superalloys 92 Conference Proceedings
C263	QinetiQ Data - CPLife
CM186LC	QinetiQ Data - COST522 WP1.1
CM247LC DS	Superalloys 96 Conference Proceedings
CM247LC DS	V96_37.pdf
CMSX-4	DSLife report - NLR-CR-2002-551
CMSX-6	Superalloys V96_34
CMSX-6	V96_34.pdf
GH4049	International Journal of Fatigue 21 (1999) 791–797
GH4049	The influence of temperature on low cycle fatigue behavior of nickel base superalloy GH4049.pdf
HASTELLOY X	Fatigue 2002 p1283
HASTELLOY X	Superalloys 88 Conference Proceedings
Haynes 230	CPLife - tested at Alstom
Haynes 230	Fatigue 2002 p1283
Haynes 230	Haynes Datasheet
HAYNES 230	Superalloys 2000 Conference Proceedings
HAYNES 230	Superalloys 88 Conference Proceedings
IN 718	Superalloys 92 Conference Proceedings
IN738 LC	Fatigue '96 p807
Low Co Waspaloy	Superalloys 92 Conference Proceedings
Mar-M-247(WLB)	Superalloys 84 Conference Proceedings
Mar-M-247(WLK)	Superalloys 84 Conference Proceedings
Mar-M-247(WST)	Superalloys 84 Conference Proceedings
Mar-M-247(WWS)	Superalloys 84 Conference Proceedings
Mar-M-247(WWS)	Superalloys 84 Conference Proceedings
MERL76	Superalloys 96 Conference Proceedings
PWA 1480	Materials Science and Engineering, A 108 (1989) 189-202
RR1000 R44	QinetiQ Data
SC 16	Superalloys 96 Conference Proceedings
SC16	Fatigue '96 p807
SRR99	Superalloys 96 Conference Proceedings
U720	U720 report (special metals)
U720 PM	NASA
U720 PM	TM-2000-209418.pdf

Alloy	Reference Source
U720 PM	TM-2002-211571.pdf
U720HC	QinetiQ Data MANDATE - FP4
U720LC	QinetiQ Data MANDATE - FP4
U720Li	QinetiQ data - ARP4
U720Li LG	QinetiQ data - ARP4
U720PM	QinetiQ Data MANDATE - FP4

APPENDIX 3 C++ Code for Fatigue Lifing Model
Written By Dr Xijia Wu and Modified by Mark Miller

```
#include <math.h>
#include <stdio.h>


#define BUF_SIZE 512
static const double pi=3.1415926;


double T1(int n)
{
   if(n==0) return pi/2;
   else if(n==1)
         return 1;
   else
         return T1(n-2)*(n-1)/n;
}

double g1(double r_at)
{
   return 0.46+3.06*r_at+0.84*pow((1-r_at),5)+0.66*pow(r_at*(1-
r_at),2);
}
double g2(double r_at)
{
   return -3.52*r_at*r_at;
}
double g3(double r_at)
{
   return 6.17-28.22*r_at+34.54*r_at*r_at-14.39*pow(r_at,3)
            -pow((1-r_at),1.5)-5.88*pow((1-r_at),5)-
2.64*pow(r_at*(1-r_at),2);
}
double g4(double r_at)
{
   return -6.63+25.16*r_at-31.04*r_at*r_at+14.41*pow(r_at,3)
             +2*pow(1-r_at,1.5)+5.04*pow(1-r_at,5)+1.98*pow(r_at*(1-
r_at),2);
}

/* Array of function pointers containing the above 'g' functions */
double (*g[4])(double)={&g1,&g2,&g3,&g4};

double SIFofThruEdgeCrack(double a, double r_at, int n)
{
   double sif=0.0;

   /* Call each 'g' function in turn */
   for (int i=0; i<4; i++) {
         sif+=g[i](r_at)*T1(n+i);
   }
   sif*=2*pow(a/1000,n)/sqrt(pi)/pow((1-r_at),1.5)*sqrt(a);

   return sif;
}


/* Perform the main calculation
 *
 * ORT = orientation, 'A' or 'B'
 */
```

```
   int doCalculation(double a, double c, double d, double PMvac,
double PMair, double PCvac, double PCair, double Kcrit, char ORT, int
*internal, int *total)
   {
      double R=0.1;
      double stress,strain,Q,K1,K2,K3,a1,r_at;
      double s0[7]={1.0716,0.26292,-1.0854,0.62811,-0.16191,0.01962,-
0.00009125};

      stress = 0.0;
      for (int i=0; i<7; i++) {

            stress += s0[i]*pow(d/1000,i);
      }

      int ni=100;
      int I=0;
      int J=0;

      do {

            Q=1+1.46*pow(a/c,1.65);

            if (a < d && c < d) {
                  K1=stress*sqrt(pi*a/Q);
                  K2=stress*sqrt(pi*a/Q)*a/c;

                  a += PCvac*pow(K1,PMvac)*ni;
                  c += PCvac*pow(K2,PMvac)*ni;

                  J=I;
            }
            else
            {
                  c=a;
                  a1=a/Q;
                  r_at=a/7500/Q;
                  K1=0.0;
                  for (int i=0; i<7; i++) {

                        K1+=s0[i]*SIFofThruEdgeCrack(a1,r_at,i);
                  }
                  K2=K1;
                  switch (ORT)
                  {
                  case 'A':
                        a+=PCair*pow(K1,PMair)*ni;
                        break;
                        /* NAB TODO: break;??? */
                  case 'B':
                        a+=PCair*pow(K1,PMair)*ni;
                        break;
                  }
            }


            I++;

      } while ((K1 < Kcrit) && (K2 < Kcrit));

      *internal = J*ni;
      *total = I*ni;

      return 0;
```

```
   }

   /* Read a line from the input file that describes the pore.
      pSrc = source file pointer
      a, c, d, ORT = data read from source file */
   int readLine(FILE *pSrc, double *a, double *c, double *d, double
*PMvac, double *PMair,  double *PCvac, double *PCair, double *Kcrit,
char *ORT)
   {
       int retVal = 0;
       char buf[BUF_SIZE];

       if (fgets(buf, BUF_SIZE, pSrc) != NULL)
       {
           int scannedNos;

           /* Check that this line fits the expected format. */
           scannedNos = sscanf(buf, "%c,%lf,%lf,%lf,%lf,%lf,%lf,%lf,
%lf", ORT, a, c, d, PMvac, PMair, PCvac, PCair, Kcrit);
           if (scannedNos == 9)
           {
               retVal = 1;
           }
       }

       return retVal;
   }

   /* Entry point for the appliction.
    * argc = count of command line parameters
    * argv[] = array of command line parameters as strings.
    * argv[0] = program name as invoked on command line. */
   int main(int argc, char* argv[])
   {
       if (argc < 3)
       {
           printf("Usage: %s SOURCE DEST\n", argv[0]);
       }
       else
       {
           FILE *pSrc;
           FILE *pDst;
           char ORT;
           double a,c,d,PMvac,PMair,PCvac,PCair,Kcrit;

           pSrc = fopen(argv[1], "r");
           if (!pSrc)
           {
               printf("Unable to open SOURCE file %s\n", argv[1]);
               return 1;
           }

           pDst = fopen(argv[2], "w+");
           if (!pDst)
           {
               printf("Unable to open DEST file %s\n", argv[2]);
               fclose(pSrc);
               return 1;
           }

           while (readLine(pSrc, &a, &c, &d, &PMvac, &PMair, &PCvac,
&PCair, &Kcrit, &ORT) != 0)
           {
               int internal, total;
```

```
                doCalculation(a, c, d, PMvac, PMair, PCvac, PCair,
Kcrit, ORT, &internal, &total);
                printf("internal %d, total %d\n", internal, total);
                fprintf(pDst, "%d,%d\n", internal, total);
            }

            fclose(pSrc);
            fclose(pDst);
        }

        return 0;
    }
```

[i]K. GURNEY, "An introduction to Neural Networks" *Routledge 2001, ISBN 1-85728-503-4*

[ii] F. Rosenblatt, "The Perceptron: A Probabilistic Model for Information Storage and Organization in the Brain", *Cornell Aeronautical Laboratory, Psychological Review*, v65, No. 6 (1958) pp. 386-408

[iii] Neuromat ® Model Manager and Neoromat ® Predictor User Guide

[iv] J. T. YAO, "Sensitivity analysis for data mining". *Fuzzy Information Processing Society, 22nd International Conference proceedings 24-26 July 2003 pp.272 – 277*

[v] S. SARLE, "How to measure importance of inputs?" *ftp://ftp.sas.com/pub/neural/importance.html, SAS Institute Inc., Cary, NC, USA*

[vi] C. DUMORTIER, and P. LEHERT, "Statistical Modelling of Mechanical Tensile Properties of Steels by Using Neural Networks and Multivariate Data Analysis" *ISIJ Int., Vol. 39 (1999) No. 10, pp. 980-985*

[vii] R. C. THOMSON, F. J. PEREZ-PEREZ, A. D. WARTERS. and G. THEWLIS, "A Neural Network Approach to the Prediction of Submerged Arc Weld Metal Chemistry" *ISIJ Int., Vol. 39 (1999) No. 10, pp. 1096-1105*

[viii] T. WATANABE, K. OMURA, M. KONISHI, S. WATANABE and K. FURUKAWA "Mold Level Control in Continuous Caster by Neural Network Model" *ISIJ Int., Vol. 39 (1999) No. 10, pp. 1053-1060*

[ix] M. EVANS, "Method for improving parametric creep rupture life of 2 center dot 25Cr-1Mo steel using artificial neural networks" *Mater. Sci. Technol. Vol 15 (1999), pp647-658*

[x] Y. HUANG and P. L. BLACKWELL, "Prediction of Mechanical Properties of Superplastic Inconel 718 using Artificial Neural Networks" *Mater. Sci. Technol. (2002) pp.1104-1108*

[xi] H. K. D. H. BHADESHIA "Neural networks in material science" *ISIJ International, Vol 39 (1999) pp966-979*

[xii] J. M. SCHOOLING, M. BROWN and P. A. S. REED, "An example of the use of neural computing techniques in materials science – the modelling of fatigue thresholds in Ni-Base superalloys" *Mater. Sci. Eng. A-Struct. Mater. Prop. Microstruct. Process. Vol 260 (1999) pp. 222-239*

[xiii] J. JONES and D.J.C. MACKAY "Neural Network Modelling of the Mechanical Properties of Nickel Base Superalloys" *Proceedings of the 8th international symposium on Superalloys, TMS, Warrendale, (1996) pp 417-424*

[xiv] J. WARDE and D.M. KNOWLES "Application of Neural Networks to Mechanical Property Determination of Ni Base Superalloys" *ISIJ International, Vol 39 (1999), No.10 pp 1006-1014.*

[xv] J. WARDE and D. M. KNOWLES, "Use of Neural Networks for Alloy Design" *ISIJ International, Vol, 39 (1999), No. 10, pp. 1015-1019*

[xvi] F. TANCRET and H. K. D. H. BHADESHIA "Design of a creep resistant nickel base superalloy for power plant applications Part 1 – Mechanical properties modelling" *Mater.Sci. Technol., 2003, 19, 283 – 290.*

[xvii] F. TANCRET and H. K. D. H. BHADESHIA "Design of a creep resistant nickel base superalloy for power plant applications Part 2–Phase diagram and segregation simulation" *Mater.Sci. Technol., 2003, 19, 291 - 295.*

[xviii] F. TANCRET and H. K. D. H. BHADESHIA "Design of a creep resistant nickel base superalloy for power plant applications Part 3 – Experimental Results" *Mater.Sci. Technol., 2003, 19, 296 - 302.*

[xix] F. TANCRET and H.K.D.H. BHADESHIA, "An affordable creep-resistant nickel-base alloy for power plant" *Proceedings of the 6th International Charles Parsons Turbine Conference, September 2003, Dublin, pp 525-535*

[xx] H. FUJll, D. J. C. MACKAY and H. K. D. H. BHADESHIA, "Bayesian Neural Network Analysis of Fatigue Crack Growth Rate In Nickel Base Superalloys" *ISIJ International, Vol. 36 (1996), No. 11, pp. 1373-1382*

[xxi] Neuromat website www.neuromat.com

[xxii]Cambridge University materials dept. website http://www.msm.cam.ac.uk/phase-trans/

[xxiii] V. VENKATESH, H.J. Rack "A neural network approach to elevated temperature creep–fatigue life prediction" *International Journal of Fatigue 21 (1999) 225–234*

[xxiv] S. SURESH, "Fatigue of Materials" Cambridge *University Press, ISBN 0-521-57847-7.*

[xxv] L. F. COFFIN, "A study of the effects of cyclic thermal stress on a ductile metal" *Transactions of the American Society of Mechanical Engineers 76, (1954), p 931-950.*

[xxvi] S. S. MANSON, "Behaviour of materials under conditions of thermal stress" *National Advisory Commission on Aeronautics, Report 1170 (1954) Cleveland: Lewis flight propulsion laboratory.*

[xxvii] T. L. ANDERSON, "Fracture Mechanics, fundamentals and applications" Second Ed, CRC Press, 1995 ISBN 0-8493-4260-0.

[xxviii] C. E. INGLIS, "Stresses in a plate due to the prescence of cracks and sharp corners" *Transactions of the Institute of Naval Architects 55 (1913), p 219-41.*

[xxix] J. C. HEALY, L. GRABOWSKI, C. J. BEEVERS, "Short-fatigue-crack growth in a nickel-base superalloy at room and elevated temperature" *International Journal of Fatigue, v 13, n 2, (Mar 1991), p 133-138.*

[xxx] T DENDA, P. L. BRETZ, J. K. TIEN, "Inclusion size effect on the fatigue crack propagation mechanism and fracture mechanics of a superalloy" *Metall Trans A, v 23A, n 2, (Feb 1992), p 519-526.*

[xxxiii] K. SADANANDA, "Environmental effects on high temperature crack growth" Key Eng Mat, v 20-28, n pt 1-4, (1987), pt 3, p 2301-2317.

[xxxiv] B.H. KEAR, H. G. F. WILSDORF, *Trans. AIME, 224, 382 (1962).*

[xxxv] K. HARRIS, G. L. ERICKSON, S. L. SIKKENGA, W. D. BRENTNALL, J. AURRECOECHEA, K. G. KUBARYCH, "Development of two rhenium-containing superalloys for single-crystal blade and directionally solidified vane applications in advanced turbine engines" *Journal of Materials Engineering and Performance, v 2, n 4, (Aug 1993), p 481-488.*

[xxxvi] A SENGUPTA, S K PUTATUNDA., "Influence of dynamic strain aging on the near-threshold fatigue crack growth behavior of a new single crystal nickel-based superalloy" *Scripta Metallurgica et Materialia, v 31, n 9, (Nov 1 1994), p 1163-1168.*

[xxxvii] D.L. ANTON, F.D. LEMKEY, in M.Gell, C.S. Kortovich, R.H. Bricknell, W.B. Kent and J.F, *Superalloys 1984 (1984), p. 601.*

[xxxviii] U. GLATZEL, "Neutron scattering experiments with a nickel base superalloy. Part II: analysis of intensity profiles" *Scripta Metallurgica et Materialia, v 31, n 3, (Aug 1 1994), p 291-296.*

[xxxix] R, VOELKL, U GLATZEL, M FELLER-KNIEPMEIER , "Measurement of the lattice misfit in the single crystal nickel based superalloys CMSX-4, SRR99 and SC16 by convergent beam electron diffraction" *Acta Materialia, v 46, n 12, (Jul 24 1998), p 4395-4404.*

[xl]. W. SCHNEIDER, J. HAMME and H. MUGHRABI, *Superalloys 1992, 589 (1992).*

[xli] D. W. MACLACHLAN, D. M. KNOWLES, "Fatigue behaviour and lifing of two single crystal superalloys" Fatigue and Fracture of Engineering Materials and Structures" *v 24, n 8, (August 2001 2001), p 503-521.*

[xlii] J. C. HEALY, L. GRABOWSKI, C. J. BEEVERS , "Short-fatigue-crack growth in a nickel-base superalloy at room and elevated temperature" *International Journal of Fatigue, v 13, n 2, (Mar 1991), p 133-138.*

[xliii] A. DEFRESNE, L. REMY, "Fatigue behaviour of CMSX 2 superalloy [001] single crystals at high temperature. I. Low cycle fatigue of notched specimens" *Materials Science & Engineering A: Structural Materials: Properties, Microstructure and Processing, v A129, n 1, (Oct 1990), p 45-53.*

[xliv] J. TONG, S. DALBY.,J. BYRNE, M. HENDERSON, M. C. HARDY, "Creep, fatigue and oxidation in crack growth in advanced nickel base superalloys" *International Journal of Fatigue, v 23, n 10, (2001), p 897-902.*

[xlv] SCHUBERT F. RIECK T., ENNIS P.J., Superalloys 2000, 341 (2000)

[xlvi] D. J. MACKAY**,** Bayesian non-linear modelling for the energy prediction competition. *ASHRAE transactions 100(2), pp. 1053-1062 (1994).*

[xlvii] SMITHELLS METALS REFERENCE BOOK William F. Gale Terry C. Totemeier
ISBN-13: 978-0-7506-7509-3

[xlviii] M. P. JACKSON and R. C. REED "Heat treatment of UDIMET 720Li: the effect of microstructure on properties" *Materials Science and Engineering A, Volume 259, Issue 1, 15 January 1999, Pages 85-97*

[xlix] E.F. BRADLEY, Superalloys, a Technical Guide (Metals Park, OH: ASM, 1988).

[l] K.N.SMITH, O WATSON, T.H.TOPPER, " A stress strain function for the fatigue of metals", *Journal of Materials, JMLSA.vol.5, 1970 pp 767-778*

[li] BOSELLI, PITCHER, GREGSON, SINCLAIR "Secondary phase distribution analysis via finite body tessellation" *Journal of Microscopy 195 (2), 104–112.*

[lii] U. HEMMERMEIER, M. FELLER-KNIEPMEIER, "Element distribution in the macro- and microstructure of nickel base superalloy CMSX-4" *Mat Sci. Eng. A248 (1998) pp87-97*

[liii] P.M. SCOTT and T.W. THORPE, "A critical review of crack tip stress intensity factors for semi-elliptic cracks" *Fatigue of Engineering Materials and Structures (UK), 4, no.4, (1981) p291-309*

[liv] M. R. JOYCE, X. Wu and P. A. S. Reed "The effect of environment and orientation on fatigue crack growth behaviour of CMSX-4 nickel base single crystal at 650 °C" *Materials Letters*, *Volume 58, Issues 1-2*, *January 2004*, *Pages 99-103*

[lv] J. GAYDA, R. V. MINER, "Fatigue crack initiation and propagation in several nickel-base superalloys at 650°C" *International Journal of Fatigue, v 5, n 3, (Jul 1983), p 135-143*

[lvi] J. Zhao, X. Wu, R. Liu and Z. Zhang "Finite element analysis of a notch root semi-elliptical crack in single crystal superalloy" *Engineering Fracture Mechanics*, *Volume 71, Issues 13-14*, *September 2004*, *Pages 1873-1890*

[lvii] D.P. ROOKE and D.J. CARTWRIGHT, Compendium of Stress Intensity Factors, HM Stationery Office 1976